ESTABLISHING CONTROL OVER VO$_2$ PHASE TRANSFORMATIONS AND

PEROVSKITE QUANTUM CONFINEMENT THROUGH TARGETED

EXPLORATION OF MATERIALS AND PROCESSING DESIGN SPACES

A Dissertation

by

ERICK J. BRAHAM

Submitted to the Office of Graduate and Professional Studies of
Texas A&M University
in partial fulfillment of the requirements for the degree of

DOCTOR OF PHILOSOPHY

Chair of Committee,	Sarbajit Banerjee
Committee Members,	Raymundo Arroyave
	David Russell
	Hong-Cai Zhou
Head of Department,	Simon North

May 2021

Major Subject: Chemistry

ABSTRACT

Establishing mechanistic and causal understanding of a material's function requires the ability to solve the inverse problem of relating function to atomistic properties and to subsequently examine how synthetic processes can be designed to arrive at desired atomistic configurations. Though detailed mechanistic study and data-driven methodology the processing-structure-property relationships of a synthetic design space can be leveraged to converge on the desired functional properties. Through the examples of VO_2 and metal halide perovskites, materials of great current interest due to their desirable properties of a metal-insulator transition (MIT) and high photovoltaic performance respectively, we have established mechanistic understanding and predictivity of relationships between synthesis and materials properties. This work explores chemical doping in the VO_2 system as a vector to modify the MIT properties and establish mechanistic understanding of the modulation observed when doping with tungsten, boron, germanium, and iridium. The interplay of defect dynamics, phase transition kinetics, and crystallographic modification in these doped systems result in mechanisms that lower and raise MIT temperatures, afford control over the MIT hysteresis, create a dynamical response, and stabilize entirely new metastable crystal structures. The synthesis of $CsPbBr_3$ perovskite nanoparticles proves to be a successful case study in the utility and flexibility of machine learning to predict outcomes, such as nanoparticle thickness, from sparse and incomplete data as well as to provide quantitative insight into the mechanisms driving the shape of the reaction landscape.

Sparse expensive synthetic data benefit from machine-learning-directed navigation as it is more efficient and tolerant to uncertainties than simpler experimental exploration methods. The utility of this type of the machine learning and feature analysis when combined with Bayesian learning for chemical and material syntheses has potential for high-quality predictions with small and/or high-dimensional datasets with implications for automated experimentation and engineering where solving the inverse problems may provide human-like insight to automation processes.

DEDICATION

This dissertation is dedicated to my son James Anthony Braham who reminds me every day of the beauty and wonders in this world.

ACKNOWLEDGEMENTS

I would like to thank Prof. Banerjee for always providing support and guidance to every student under his mentorship and for helping me grow into a better student, scientist, and person. I would also like to acknowledge my committee members, Professor Raymundo Arroyave, Professor David Russell, and Professor Hong-Cai Zhou for helping me throughout my time at Texas A&M. I would like to thank our collaborators in the labs of Professors Patrick Shamberger, Raymundo Arróyave, Xiaofeng Qian, and Reza Shahbazian-Yassar, who have each greatly expanded the scope of understanding of the systems explored in each of our projects. I would like to thank Professor Robyn Goacher for her continued guidance before and during graduate school. Lastly, I would like to thank my family and friends for their love and support.

CONTRIBUTORS AND FUNDING SOURCES

Contributors

This work was supervised by a dissertation committee consisting of Professor Sarbajit Banerjee, Professor David Russell, and Professor Hong-Cai Zhou of the Department of Chemistry and Professor Raymundo Arróyave of the Department of Materials Science and Engineering.

DFT calculations in Chapters 2 and 3 were performed by Dr. Ruben Villarreal the advisement of Prof. Raymundo Arróyave. High angle annular dark field transmission electron microscopy in Chapter 2 was performed by Dr. Hasti Asayesh-Ardakani under the advisement of Prof. Reza Shahbazian-Yassar. Synthesis of VO_2 nanostructures, differential scanning calorimetry measurements, and powder X-ray diffraction measurements in Chapters 2 and 3 were performed in collaboration with Dr. Diane Sellers. Transmission electron microscopy in Chapter 2 and Chapter 4 was performed by Dr. Nathan Fleer and working under the advisement of Prof. Sarbajit Banerjee. DFT calculations in Chapter 3 were performed by Baiyu Zhang under the advisement of Prof. Xiaofeng Qian. XANES calculations in Chapter 3 were performed by Dr. Abhishek Parija advisement of Prof. Sarbajit Banerjee and Dr. David Prendergast. XANES spectra in Chapter 3 were acquired by Dr. Luis De Jesus under the advisement of Prof. Sarbajit Banerjee. X-ray photoelectron spectroscopy in Chapter 4 was performed by Dr. Theodore Alivio under the advisement of Prof. Sarbajit Banerjee. The Rietveld refinement in Chapter 4 was performed By Dr. Justin Andrews under the advisement of

Prof. Sarbajit Banerjee. Perovskite nanocrystal synthesis in Chapter 5 was performed by Dr. Junsang Cho and Kristel Forlano. All other work conducted for the dissertation was completed by the student independently.

Funding Sources

TABLE OF CONTENTS

LIST OF FIGURES

LIST OF TABLES

1. INTRODUCTION*

1.1. Overview

Successful design of a functional material requires an understanding of the relationship between materials properties, chemical composition, atomistic structure, and the synthetic processes necessary to arrive at the desired atomistic configuration. Serendipitous discovery of a material with optimal properties or an optimal synthetic process though a guess and check process is rare and an unrealistic strategy for targeted materials design. The design of functional materials presents a challenge of often having high dimensional design spaces with many factors influencing the materials properties and synthetic outcomes while also having a high cost of experimentation making untargeted exploration unfeasible. This challenge can be addressed by developing mechanistic understanding of structure—function correlations of the material property being designed and the underlying physical principles or through efficient data-driven navigation of the design space describing either a synthetic result or a structure-property relationship. Comprehensive mechanistic understanding that links structure and composition to a specific property will aid materials design by providing insight into design features that will have the most impact on the desired outcome, thereby lowering the number of variables that need to be explored to tune a property. In a complementary fashion, data-driven machine learning approaches using existing data can build inference in the inverse direction allowing for the statistical analysis of the most impactful

_____

*Part of this chapter is reprinted (adapted) from E. J. Braham, R. D. Davidson, M. Al-Hashimi, R. Arróyave and S. Banerjee, *Dalton Trans*., **2020**, *49*, 11480. Reproduced by permission of The Royal Society of Chemistry.

features. Mapping the desired properties to processing parameters can help guide the choice of where to sample next beyond "guess and check" or one variable at a time (OVAT) methodology, thereby enabling efficient exploration of materials or synthetic design spaces in search of a desired synthetic outcome or functional property.

This dissertation will explore the complementary use of mechanistic understanding of alloying processes and data-driven inference for improved materials and processing design in two parts. Firstly, chapters 2, 3, and 4 will discuss improving the design of a metal-insulator transition (MIT) material by building mechanistic understanding of the influence of dopants on the transformation temperature and hysteresis of VO_2. Secondly, chapter 5 will discuss mapping a processing design space by using machine learning to predict the quantum confinement of $CsPbBr_3$ perovskite nanoparticles.

1.2. The Rugged Material Design Space of VO_2

VO_2 is an electron correlated transition metal oxide with strongly coupled spin, charge, lattice, orbital, and atomic degrees of freedom, which undergoes a change in physical properties including electrical conductivity, optical transmittance, specific heat, thermal emissivity and magnetic susceptibility when transitioning from the low-temperature M_1 phase to the high-temperature R phase (**Figure 1.1**).[1–6] This switching behavior underpins potential applications in devices such as Mott field-effect transistors, thermal emissivity coatings, optical limiters, infrared modulators, neuromorphic computing elements, and many more.[3,7,8] VO_2 has an equilibrium transition temperature (T_c) of around 67 °C; however, the critical transition temperature, hysteresis width

2
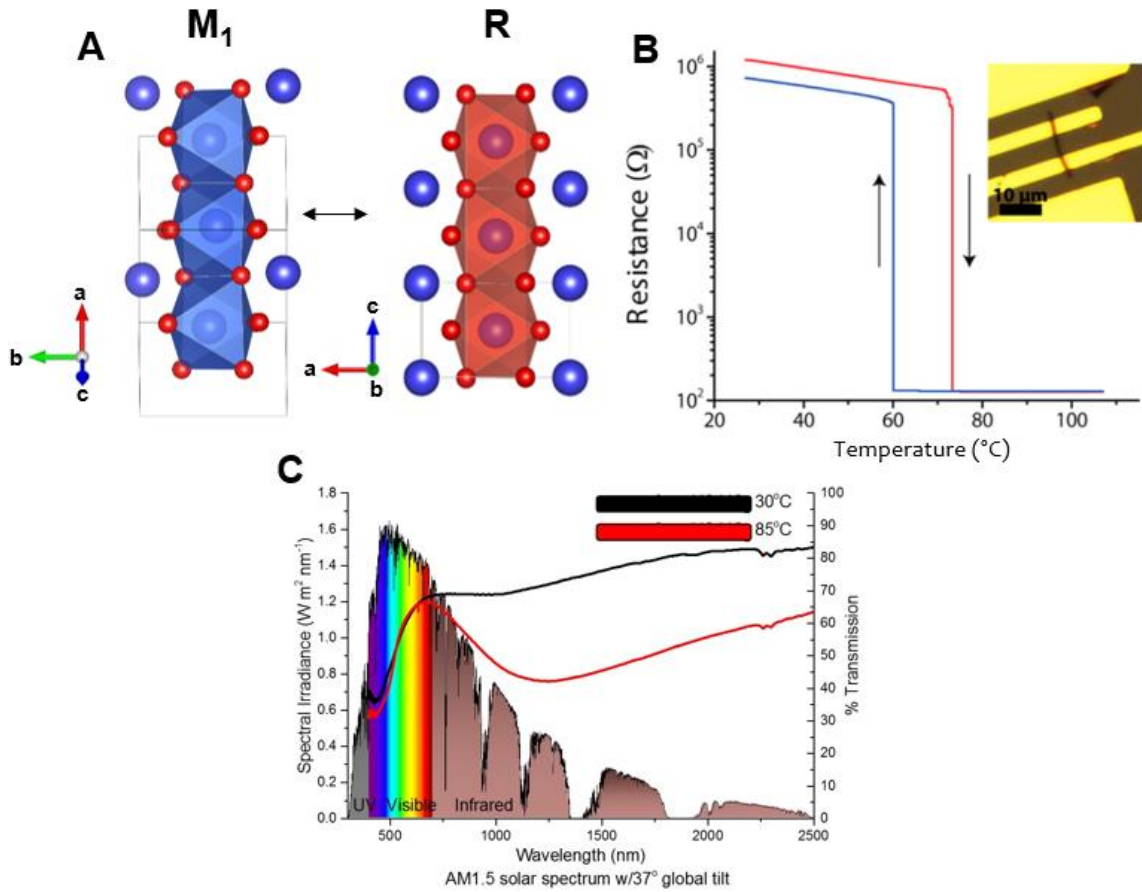
Figure 1.1. A) Crystal structures of the M_1 and R phases of VO_2. B) Resistance change across a single nanowire of VO_2 (optical image in inset) with red indicating the heating transition and blue indicating the cooling transition.[5] Reprinted from ref. 5; Copyright 2014, the American Chemical Society C) Transmission spectra of VO_2 in the M_1 phase (black) and the R phase (red) with a typical solar radiation spectrum plotted on the left axis. To illustrate the infrared blocking capabilities of VO_2.[6] Reprinted from ref. 6; Copyright 2017, the American Chemical Society

between the heating and cooling transition, sharpness of the transition, magnitude of the

transition, as well as the overall dynamics of this phase transition, can be modulated by

factors that alter the coupling between atomistic and electronic structure. The

thermodynamics and kinetics of the solid—solid transformation are amenable to

modulation through incorporation of dopants, point defects, strain and strain induced

extended defects, domain size, and crystallinity. Fine control over the temperatures and

dynamics of this phase transition is crucial for enabling the design of this material for

device applications. **Figure 1.2** shows an illustrated plot of the modulations of the

transition temperature observed in the case of size and the chemical dopants boron and

tungsten as well as the structures of the R and M_1 phase containing a boron dopant.[9]

The martensitic nature of this phase transition, a diffusionless propagation of a

symmetry-changing lattice distortion, allows these compositional and morphological

changes to have a large influence on the nucleation and growth of this transition.[10]
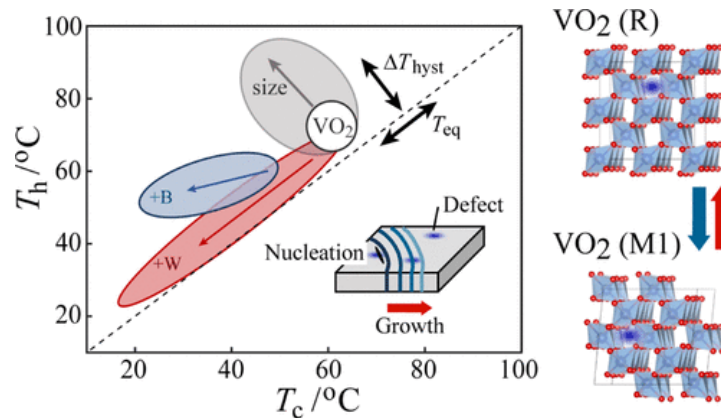
Figure 1.2. (Left) Schematic plot of the modulation of the heating and cooling transition temperatures (T_h and T_c respectively) upon doping and particle size with an illustration of defect-nucleated phase growth. (Right) Crystal structures of the R and M_1 phases of VO_2.[9] Reprinted from ref. 9; Copyright 2020, the American Chemical Society

Incorporation of various elemental dopants is a particularly well studied method

of modulating this phase transition temperature. **Figure 1.3** depicts the observed effect

of 15 unique dopants on the phase and MIT modulation of VO_2 reported in

literature.[8,11–16] Modulation to both higher and lower transition temperature is reported

4

as well as narrowing and widening of the hysteresis between the forward and reverse

transition temperatures. The wide range of observed effects of doping on VO_2 presents a

viable vector for tuning the MIT allowing the phase transformation behavior to be

tailored to a
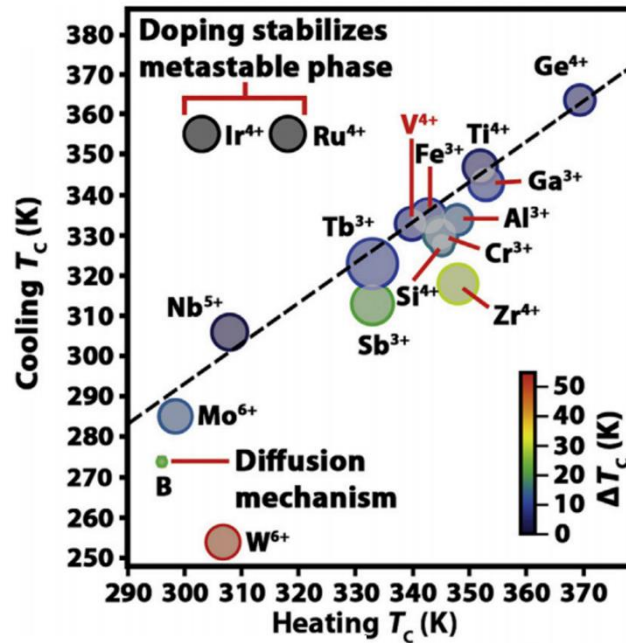
Figure 1.3. Current reported literature values of the heating and cooling transition temperature modulation for 15 unique dopants as well as a color scale representing hysteresis modulation.[8] Reprinted from ref. 8; Copyright 2020, the Elsevier

specific application. Unlocking this potential of VO_2 will require precise synthetic

control and mechanistic understanding of the drastically different effects manifested

when incorporating different elements into the crystal lattice. Currently, mechanistic

understanding of the atomistic structure-property relationship of dopants lies behind a

particularly opaque curtain of the many physical and chemical factors that can

potentially influence the rugged energy landscape of vanadium oxide—for instance, dopants induce (anisotropic) internal strain, aliovalent dopants add electrons or holes to the band structure, alter defect formation energies, and change the potency and distribution of defects that serve as nucleation sites. This complexity and the singularities arising from the strongly coupled spin, charge, orbital, lattice, and atomic degrees of freedom, along with low availability of data makes the VO_2 system poorly suited for building structure-property correlations from experimental data and machine learning models. In this case structure-property insight must be built from comprehensive mechanistic studies of doped and alloyed VO_2 systems to discover the underlying physical factors that must be leveraged to obtain fine control over functional material properties.

This dissertation presents the mechanistic study of four dopant systems with large variation in their effects on VO_2. Chapter 2 presents analysis of the influence of tungsten doping on the hysteresis and T_c of the MIT transition of VO_2 as a result of a change in nucleation mechanism via internal anisotropic strain. Chapter 3 describes the decoupling of the T_c from the hysteresis in a dynamical response mechanism brought about though interstitial boron doping. Chapter 4 presents the finding of iridium doping stabilizing a new metastable tunnel-structured phase of VO_2. Lastly as a technical introduction to the effects of a dopant on VO_2 recent findings on the interplay of germanium doping and oxygen vacancies will be presented in the following introductory section.

1.2.1. The intertwined roles of synthesis, defects, and Ge doping on the Metal-Insulator Transition of VO₂

A broad trend observed in VO_2 doping is that substitutional dopants that have been recorded to raise the equilibrium transition temperature (T_c) higher tend to be of smaller atomic radii and lower oxidation state, such as Ge^{4+} or Ti^{4+},[12,13,17] than those that lower the T_c like Mo^{6+} and W^{6+}.[18,19] Germanium doping in particular has been observed to raise the transition temperature in excess of 90°C for thin films.[12] With the increasing interest of using VO_2 in neuromorphic computing applications that use the

metal—insulator transition as a proxy for neuronal spikes, higher transition temperatures are necessary to enable function operating temperatures typical of data servers of 80-100°C. In order to investigate the mechanism of stabilization of the M_1 phase of VO_2
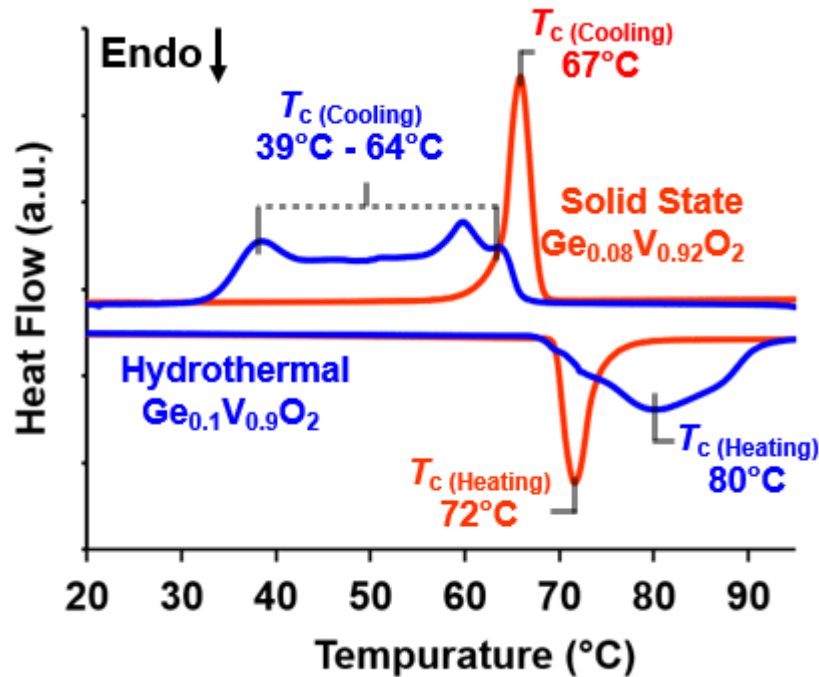
Figure 1.4. DSC Traces for hydrothermally synthesized (blue) and solid-state-synthesized (orange) Ge-doped VO₂.

7

upon germanium incorporation, doped VO_2 particles were synthesized via two synthetic methods, hydrothermal synthesis and solid-state synthesis.

Figure 1.4 plots the differential scanning calorimetry (DSC) traces of the outcome of the individual synthetic methods. There is a stark contrast in the phase transformation between the two synthetic methodologies with the solid-state synthesis displaying sharp phase transition peaks with a hysteresis similar to undoped VO_2 and T_c shift in accordance with increased stabilization of the M_1 phase.

The hydrothermally prepared sample displays a quite different asymmetric heating and cooling transition with an extremely broad, non-gaussian, cooling transition that shows an exothermic heat flow ranging from 64°C to 39°C. Powder X-ray diffraction (**Figure**
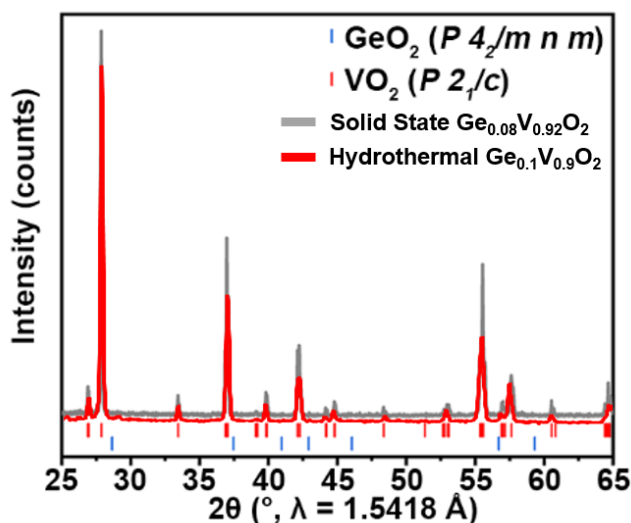
Figure 1.5. Powder XRD patterns for the solid state (gray) and hydrothermally (red) synthesized samples of VO_2 showing a match to the M_1 phase of VO_2. *hkl* positions for GeO_2 are included to for reference.

1.5) confirms both samples are M_1 phase VO_2 at room temperature leading to conclude the observed transition enthalpy is indeed from the MIT transition in VO_2.

The origin of the drastic differences in hysteresis and cooling transition temperature must lie in the synthesis methodology. A main difference between hydrothermal and solid-state methods is the matrix during synthesis. The hydrothermal synthesis reduces and crystallizes an aqueous HVO_3 precursor with isopropanol in the presence of GeO_2. At high temperature (250°C) and pressure, the aqueous environment precipitates doped VO_2 nanocrystals based on the Pourbaix diagram. Conversely the solid-state methodology consists of premade undoped VO_2 sealed in an ampoule under vacuum with GeO_2 and heated in excess of 900°C. The solid-state diffusion of the germanium and the sintering of the VO_2 results in micrometer-sized large alloyed polycrystalline particles. The matrix of the hydrothermal samples can be though to be oxygen rich where the newly forming crystallites have an abundance of oxygen in the matrix around them while the solid-state matrix can be considered oxygen poor due to the only source of oxygen being the VO_2 and GeO_2 precursors.

Oxygen vacancies and point defects are known to be potent nucleation sites for the phase transition in VO_2 that may influence the forward and reverse transitions independently.[20,21] These synthetic environments are thus posited to be affecting the concentration of oxygen vacancies, requiring overcooling to nucleate the monoclinic phase during the cooling transition. **Figure 1.6** shows DFT calculations for the formation energy of charged defects including the substitutional doping of Ge at a vanadium site (Ge_v), the formation of an oxygen vacancy (vac_O), and an oxygen vacancy

9

in the presence of a germanium dopant (Ge_v + vac_O). In an oxygen-poor environment,

the formation of vacancies requires lower energy than in an oxygen-rich environment

with both favorable conditions for substitutional Ge doping. Additionally, in the oxygen-

rich case, vacancies have a higher energetic cost in the presence of substitutional

germanium making it more unfavorable to form vacancies in the system overall.
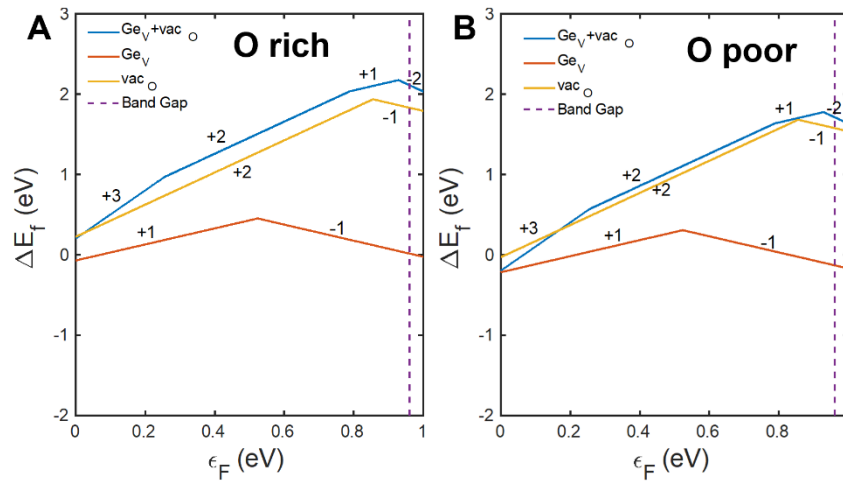
Figure 1.6. A and B show the formation energies for charged defects in oxygen rich and oxygen poor environments respectively. Formation energies were calculated for substitutional doping of Ge at a vanadium site (Ge_V), the formation of an oxygen vacancy (vac_O), and an oxygen vacancy in the presence of a germanium dopant (Ge_V + vac_O).

If nucleation sites such as oxygen vacancies are strongly suppressed in

germanium-doped VO_2 formed in an oxygen-rich environment, the nucleation of the

phase transformation can be severely hindered even if the thermodynamic equilibrium

temperature is increased. As such, considerable super-cooling below the thermodynamic

equilibrium temperature is required to nucleate the monoclinic phase. In contrast, the

concentration of oxygen vacancies is known to have much less of an impact on the heating $M_1 \rightarrow R$ transition where extended defects such as twin planes can instead serve as the nucleation sites. These preliminary results show the complex interplay of synthetic conditions, point defects, and the thermodynamics and kinetics of the VO_2 phase transition illustrating the complexity of this system. By building our understanding of the role of defects and dopants in VO_2, we continue to get closer to the fine control over the design of this material and its phase transition necessary for its use in advanced device applications.[8,22]

1.3. Navigating the design space of inorganic materials synthesis using statistical methods and machine learning.

Data-driven approaches have brought about a revolution in manufacturing, enabling levels of customization and control that were unimaginable with traditional mass-manufacturing.[23,24] Advances in digital manufacturing and nanoscale fabrication have further paved the way to the utilization of a much-expanded palette of materials in technological applications. Powerful as they are, digital manufacturing approaches remain constrained in their ability to structure matter at nanoscale dimensions. An important, yet unresolved, challenge lies at the interface of data science and materials synthesis. From the perspective of inorganic materials chemistry, a fundamental obstacle to the precise structuring of matter that remains to be resolved is to control reaction trajectories to stabilize crystalline solids with precise composition, atomic connectivity (crystallization of a specific polymorph), microstructural dimensionality (particle size, shape, layer thickness, or grain size), and surface structure (texture or surface

crystallographic facets). Typically, materials syntheses are developed almost entirely in an empirical manner, based on fragmented knowledge of the underlying sequences of chemical reactions, heterogeneous and homogeneous equilibria, and their coupling with mesoscale mass transport and energy transfer phenomena. Much of current research practice comprises Edisonian trial-and-error methods involving changing a single synthetic variable and observing the response. Such methods are not just inherently inefficient in their exploration of potentially vast design spaces (spanning multiple process variables, reaction sequences, as well as structural parameters and reactivities of precursors and capping ligands) but furthermore do not provide a satisfactory understanding of the underlying chemical and physical principles, ultimately stymying the application of modern process design tools.

The functionality of materials derive from complex convolutions of composition and (atomistic as well as mesoscale) structure, which in turn are determined by their processing history. The design of materials for a specific application requires unraveling the interplay between physical principles that underpin materials function; weighing trade-offs across frontiers of candidate solutions to identify optimal solutions that satisfy multiple constraints; and mapping efficient pathways from starting precursors to arrive at the target material composition and structure. Navigation of synthetic design spaces is challenging because often the structures that are of greatest use are metastable in nature, resident within shallow wells on rugged energy landscapes (**Figure 1.7A**).[25–27] Considerable effort has focused on the application of data science methods to accelerate the investigation of structure—property relationships based on mining of

crystallographic databases and first-principles calculations of known and putative structures in search of specific function.[28–32] For instance, machine learning of experimental and computational data has enabled high-accuracy predictions of bandgap and crystal structure.[33–37] However, explorations of reaction trajectories and mapping of response surfaces of materials synthesis spaces with a view towards learning process–structure and process–property relationships are much less common.[26,38–42]
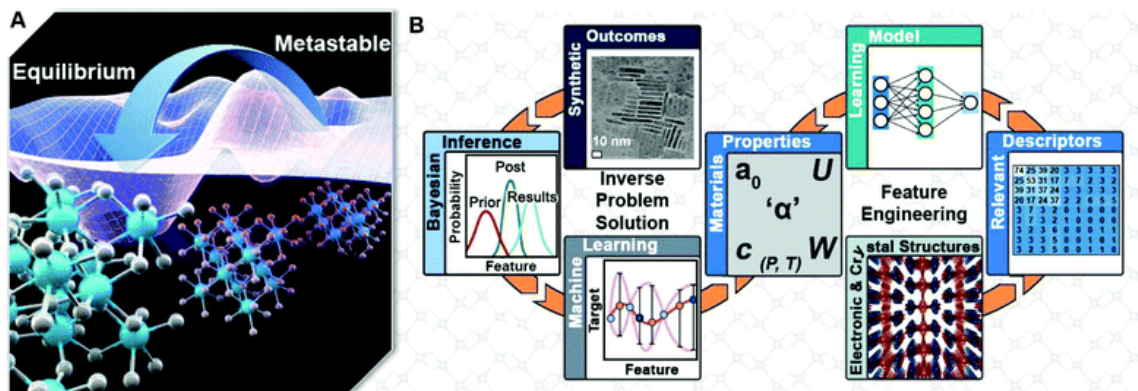
Figure 1.7. (A) Illustration of a rugged energy landscape showing metastable and equilibrium energy wells for polymorphs of HfO_2. (B) Schematic illustration of a data-driven approach to feature engineering and inverse synthesis design.

1.3.1. Towards machine-learning-aided inverse synthesis design

Challenges in the application of data science methods to materials synthesis stem from the high dimensionality of problems where n synthesis variables create an n-dimensional space for exploration, the sparsity and expense of available data, and the non-monotonicity and extreme non-linearity of many thermodynamic functions (evidenced as phase transitions).[43–46] Furthermore, understanding synthesis requires

13

elucidation of process–structure relationships or using processing–function relationships as a proxy. Modeling the former requires the decoding of structure into numerical descriptor(s) or limits the modeling to expressions that accept categorical variables as inputs. The latter, in turn, requires that the entire design space be reasonably represented by a single or small subset of properties. This would typically translate the task of 'learning' a synthesis to the task of optimizing a specific property (*e.g.*, particle size). The strength of coupling between spin, charge, orbital, lattice, and compositional degrees of freedom determine the shape of thermodynamic energy landscapes of periodic solids.[26,46] Strong coupling amongst the degrees of freedom can make it difficult to traverse along pathways to arrive at specific polymorphs.

In conventional high-temperature synthesis, as a system relaxes towards equilibrium, from an initial high-energy state, it scans the landscape for efficient paths to enable dissipation of the available free energy. Conventional metallurgical and ceramic processing provide a large excess of energy, enabling the material to readily find its way towards equilibrium, without being trapped in a metastable state, although there are notable examples, particularly in phase-transforming materials, in which the trapping in metastable states is highly history/processing-dependent.[47] However, given the challenges with ensuring homogeneous energy and mass flows across the system, and the sensitivity of crystallization processes to mesoscale phenomena, such processes can be difficult to control. Solution-phase synthesis, *chimie douce* routes, and templated processes (*e.g.*, molecular beam epitaxy and pulsed laser deposition) can potentially allow for more deterministic navigation of energy landscapes such as to trap the material

in a local minimum (Figure 1.7A). However, the intrinsic path-dependence of these methods increases the dimensionality and complexity of the reaction space.[48–51] Data science methods hold promise for "learning" the design space and enabling the design of synthetic pathways that connect starting precursors and the target structure. In principle, machine learning allows for the possibility of inverse design synthesis (Figure 1.7B); the generation of models which can take a target structure as the input and predict synthetic routes to generate materials with those properties as outputs.[52–55] Increasingly complex problems have been addressed working towards modeling systems with high costs of experimentation, optimization with multiple target objectives, and providing greater understanding of error in systems with relatively limited amounts of data.

Statistical regression and machine learning methods can aid the mapping of pathways between the target material and precursors based on the fusion of disparate types of data. First, data mined from the literature provide access to specific hyperplanes, in that it is typically data collected through consideration of one-variable-at-a-time (OVAT), which is analogous to examining a singular plane of experiments within a high dimensional reaction space wherein each variable adds another dimension to the space. These hyperplanes oftentimes reflect chemical intuition, serendipity, accessibility of specific precursors, or a combination thereof in terms of experimental design, and can provide valuable inputs to algorithms and provide a means of seeding initial experiments (albeit failed experiments typically go unreported and thus vast sections of the design space are underrepresented in the literature). Codified prior knowledge of thermodynamics and chemical concepts allow for the application of

specific constraints (*e.g.*, knowledge of decomposition temperatures or solubility guide precursor selection). Results from first-principles calculations and molecular dynamics simulations, oftentimes coupled with metaheuristic algorithms (simulated annealing or basin hopping),[54,55] algorithms that screen different optimization procedures for their facility with converging at a minimum, can guide exploration of the adjacent phase space to identify potential intermediates that can be exploited as waystations to the target, or conversely, to avoid thermodynamic dead ends. Accurate first-principles descriptions of entire systems and energy landscapes are inaccessible in most cases owing to inadequate energy resolution and high computational costs. The available inputs can then inform the targeted navigation of the synthesis design spaces without having to perform full factorial experiments across multiple dimensions of chemical, process, and temporal variables. Microfluidic platforms,[30] high-throughput robotic arm dispensation systems, entirely mobile robots,[56] and parallelized hydrothermal platforms[57] have emerged as alternatives for rapidly acquiring data to test the validity of data-driven synthesis models.

A major advantage afforded by machine-learning-aided approaches is the ability to progress beyond expensive one-variable-at-a-time (OVAT) sampling methods to more efficiently explore synthetic landscapes, minimization of sampling bias often inherent in human intuition, and a decrease in likelihood of arrival at a local minimum hyperplane. Perhaps more importantly, machine learning algorithms are generalizable and can thus be used as a means of "rule discovery", thereby unraveling hidden correlations and providing fundamental chemical and physical insight of the underlying reactivity.[58] Here, we will outline the use of design of experiments in exploration of

16

synthetic landscapes and discuss how machine learning algorithms can complement these statistical sampling techniques in order to accelerate materials discovery referencing some illustrative examples from the literature.

1.3.2. Beyond guess and check: design-of-experiments and connections to machine learning

Data is at the core of any machine learning model, and for applications in materials science, the lack of data, format of data, and quality of data can frequently represent a bottleneck to progress. For problems in which data is not available elsewhere, starting with the design-of-experiments (DOE) sampling techniques, rather than OVAT methods, can often afford a more richly diverse dataset that is readily amenable to modeling with machine learning algorithms.[59–61] An abiding challenge is to determine the best approaches to represent chemical structure and composition in a manner amenable to the application of statistical regression tools. A major research question is thus to identify the structural and compositional motifs, processing conditions, and reaction sequences that are most strongly associated with the synthetic outcomes. Such "feature engineering" (Figure 1.7B) is pivotal to developing a scored experimental design approach that allows for identification of the key descriptors underpinning a specific synthetic output and enables iterative improvement of the synthesis models.

Predating the use of machine learning methods, DOE methodologies have shown considerable value in materials synthesis.[40,62–66] These methods aim to first broadly sample large design spaces with as few experiments as possible utilizing approaches

such as full and fractional factorial designs, random sampling, or, more recently,

Bayesian optimization in which probability estimates from the model are continuously

updated as new data is acquired. These sampling methods are typically coupled with

response surface modeling to generate a rough model of the system through use of a

simple regressor.[67,68] As a notable example of this approach, Murphy and co-

workers[69] explored the seed-mediated silver-assisted growth of gold nanorods using

fractional factorial DOE along eight independent experimental parameters. In the

synthesis, gold seeds are prepared by combining a solution containing a gold precursor

and capping ligand (*e.g.*, cetyltrimethylammonium bromide (CTAB)) with a solution

containing the reducing agent. The seed solution is then added to a solution containing a

capping ligand, additional gold precursor, a weaker reducing agent, and silver nitrate.

Numerous studies had previously evaluated effects of different reaction parameters using

traditional OVAT methods and had determined that the concentration of gold seeds,

temperature, amount of silver nitrate, and concentration of the ascorbic acid reducing

agent were all of relevance to determining the aspect ratio of nanorods.[70–73] Using DOE

methods, the authors not only demonstrated all of the trends observed previously with

the separate OVAT studies but also determined that the interaction of variables was

significant. They demonstrated that while there is a positive correlation between

concentration of silver nitrate and the nanorod length, it has no primary effect on the

length and instead demonstrates a secondary interaction with the amount of reducing

agent. These results provided valuable insight into the true role of silver nitrate and the

general mechanisms of anisotropic growth. While it was previously postulated that silver

18

or silver bromide absorbed on the gold surface may serve as a blocking layer resulting from underpotential deposition on certain crystallographic faces, the correlation of $AgNO_3$ concentration with the concentration of reducing agent indicates that it more likely shields charge for negatively charged species headed towards the negatively charged (as a result of Br^- adsorption) nanocrystal surface. The authors postulated that surface adsorption of Br^- ions directs anisotropic growth.

In DOE studies, the initial round of sampling is frequently used as a means of down-selecting to variables with the highest influence on synthetic outcomes through feature selection (Figure 1.7B), allowing for the possibility of a second round of more dense sampling of the design space of interest. In the steepest ascent approach this involves iterative sampling in the direction which heads towards an optimum in output. While the data is ascending, a first-order model is used which does not account for curvature in the output data. Once near the apex in data, a second order model which accounts for curvature of the data provides a better fit.[57] Mora-Tamez *et al.*[40] explored the colloidal synthesis of Ni_2P nanoparticles to generate a model predicting particle size. In the first-order design, six possible factors were screened for influence on the size of nanoparticles followed by a second-order design model of the dependence on the strongest influencing factors; triphenylphosphine/nickel ratio and temperature. This model was then corroborated with four additional samples all resulting in particles with excellent agreement to the predicted values well within experimental error. The high monodispersity of nanoparticles and low experimental noise of the chosen synthetic method implemented within a microfluidic platform combined with the lack of complex

variable correlation in this study allowed an accurate response surface model to be built

from a relatively small (9 sample) DOE chosen dataset. This methodology is useful for

analyzing the trends, magnitude of influence, and correlation of a large set of variables.

As it is typically implemented, DOE is best suited for optimization problems.

The interpolation offered with response surfaces can be predictive for small design areas

with linear or quadratic trends but often is constrained in its ability to analyze design

spaces with more complex responses and systems where exploration, rather than

optimization, is the focus. When coupled with the capabilities of machine learning

algorithms and with the incorporation of features representative of chemical structure

and composition, the opportunities for systematic exploration of synthetic landscapes are

greatly expanded. **Figure 1.8** depicts a workflow for machine-learning-aided navigation

of synthetic design space.
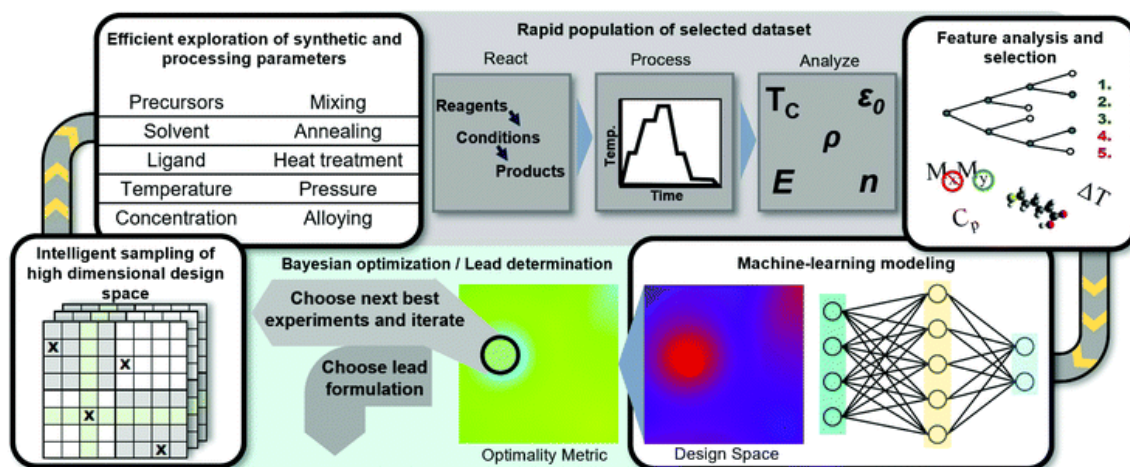
Figure 1.8. Schematic depiction of an example of a machine-learning workflow for the iterative exploration and exploitation of a synthetic design space for inorganic materials.

1.4. References

[1]   F. J. Morin, *Phys. Rev. Lett.* **1959**, *3*, 34.

[2]   M. Imada, A. Fujimori, Y. Tokura, *Rev. Mod. Phys.* **1998**, *70*, 1039.

[3]   Y. Zhou, S. Ramanathan, *Crit. Rev. Solid State Mater. Sci.* **2013**, *38*, 286.

[4]   G. Stefanovich, A. Pergament, D. Stefanovich, *J. Phys. Condens. Matter* **2000**, *12*, 8837.

[5]   G. A. Horrocks, S. Singh, M. F. Likely, G. Sambandamurthy, S. Banerjee, *ACS Appl. Mater. Interfaces* **2014**, *6,* 15726.

[6]   N. A. Fleer, K. E. Pelcher, J. Zou, K. Nieto, L. D. Douglas, D. G. Sellers, S. Banerjee, *ACS Appl. Mater. Interfaces* **2017**, *9*, 38887.

[7]   Y. V. Pershin, M. Di Ventra, *Adv. Phys* **2011**, *60*, 145.

[8]   J. L. Andrews, D. A. Santos, M. Meyyappan, R. S. Williams, S. Banerjee, *Trends Chem.* **2019**, *1*, 711.

[9]   A. Yano, H. Clarke, D. G. Sellers, E. J. Braham, T. E. G. Alivio, S. Banerjee, P. J. Shamberger, *J. Phys. Chem. C* **2020**, *124*, 21223.

[10]   J. B. Goodenough, *J. Solid State Chem.* **1971**, *3*, 490.

[11]   E. J. Braham, J. L. Andrews, T. E. G. Alivio, N. A. Fleer, S. Banerjee, *Phys. Status Solidi A.* **2018**, *215*, 1700884.

[12]   A. Krammer, A. Magrez, W. A. Vitale, P. Mocny, P. Jeanneret, E. Guibert, H. J. Whitlow, A. M. Ionescu, A. Schüler, *J. Appl. Phys.* **2017**, *122*, 45304.

[13]   Y. Wu, L. Fan, Q. Liu, S. Chen, W. Huang, F. Chen, G. Liao, C. Zou, Z. Wu, *Sci. Rep.* **2015**, *5*, 1.

[14]   K. Miyazaki, K. Shibuya, M. Suzuki, K. Sakai, J. Fujita, A. Sawa, *AIP Adv.* **2016**, *6*, 055012.

[15]   N. Wang, M. Duchamp, R. E. Dunin-Borkowski, S. Liu, X. Ting Zeng, X. Cao, Y. Long, *Langmuir* **2016**, *32*, 759.

[16]   T. E. G. Alivio, D. G. Sellers, H. Asayesh-ardakani, E. J. Braham, G. A. Horrocks, K. E. Pelcher, R. Villareal, L. Zuin, J. Patrick, R. Arroyave, R. Shahbazian-yassar, S. Banerjee, *Chem. Mater.* **2017**, *29*, 5401.

[17]   H. Futaki, K. Kobayashi, M. Aoki, T. Shimoda, E. Yamada, K. Narita, **1968**.

[18]   C. J. Patridge, L. Whittaker, B. Ravel, S. Banerjee, **2012**.

[19]   L. Whittaker, T.-L. Wu, C. J. Patridge, G. Sambandamurthy, S. Banerjee, *J. Mater. Chem.* **2011**, *21*, 5580.

[20]   W. Fan, J. Cao, J. Seidel, Y. Gu, J. W. Yim, C. Barrett, K. M. Yu, J. Ji, R. Ramesh, L. Q. Chen, J. Wu, *Phys. Rev. B - Condens. Matter Mater. Phys.* **2011**, *83*, 235102.

[21]   E. J. Braham, D. Sellers, E. Emmons, R. Villarreal, H. Asayesh-Ardakani, N. A. Fleer, K. E. Farley, R. Shahbazian-Yassar, R. Arròyave, P. J. Shamberger, S. Banerjee, *Chem. Mater.* **2018**, *30*, 214.

[22]   W. Yi, K. K. Tsang, S. K. Lam, X. Bai, J. A. Crowell, E. A. Flores, *Nat. Commun.* **2018**, *9*, 4661.

[23]   G. Daehn, G., and Spanos, *Metamorphic Manufacturing: Shaping the Future of On-Demand Components*, Pittsburgh, PA, **2019**.

[24]   A. Bajpayee, M. Farahbakhsh, U. Zakira, A. Pandey, L. A. Ennab, Z. Rybkowski, M. K. Dixit, P. A. Schwab, N. Kalantar, B. Birgisson and S. Banerjee, *Front. Mater.*, **2020**, *7*, 52.

[25]   D. P. Shoemaker, Y.-J. Hu, D. Y. Chung, G. J. Halder, P. J. Chupas, L. Soderholm, J. F. Mitchell and M. G. Kanatzidis, *Proc. Natl. Acad. Sci.*, **2014**, *111*, 10922.

[26]   A. Parija, G. R. Waetzig, J. L. Andrews and S. Banerjee, *J. Phys. Chem. C*, **2018**, *122*, 25709.

[27]   W. Sun, S. T. Dacek, S. P. Ong, G. Hautier, A. Jain, W. D. Richards, A. C. Gamst, K. A. Persson and G. Ceder, *Sci. Adv.*, **2016**, *2*, e1600225.

[28]   J. J. de Pablo, N. E. Jackson, M. A. Webb, L.-Q. Chen, J. E. Moore, D. Morgan, R. Jacobs, T. Pollock, D. G. Schlom, E. S. Toberer, J. Analytis, I. Dabo, D. M.

DeLongchamp, G. A. Fiete, G. M. Grason, G. Hautier, Y. Mo, K. Rajan, E. J. Reed, E. Rodriguez, V. Stevanovic, J. Suntivich, K. Thornton and J.-C. Zhao, *npj Comput. Mater.*, **2019**, *5*, 41.

[29]   A. O. Oliynyk and A. Mar, *Acc. Chem. Res.*, **2018**, *51*, 59–68.

[30]   A. O. Oliynyk, L. A. Adutwum, B. W. Rudyk, H. Pisavadia, S. Lotfi, V. Hlukhyy, J. J. Harynuk, A. Mar and J. Brgoch, *J. Am. Chem. Soc.*, **2017**, *139*, 17870.

[31]   D. L. McDowell and S. R. Kalidindi, *MRS Bull.*, **2016**, *41*, 326.

[32]   D. P. Tabor, L. M. Roch, S. K. Saikin, C. Kreisbeck, D. Sheberla, J. H. Montoya, S. Dwaraknath, M. Aykol, C. Ortiz, H. Tribukait, C. Amador-Bedolla, C. J. Brabec, B. Maruyama, K. A. Persson and A. Aspuru-Guzik, *Nat. Rev. Mater.*, **2018**, *3*, 5.

[33]   Y. Zhuo, A. Mansouri Tehrani and J. Brgoch, *J. Phys. Chem. Lett.*, **2018**, *9*, 1668.

[34]   A. O. Oliynyk, L. A. Adutwum, J. J. Harynuk and A. Mar, *Chem. Mater.*, **2016**, *28*, 6672.

[35]   G. Pilania, A. Mannodi-Kanakkithodi, B. P. Uberuaga, R. Ramprasad, J. E. Gubernatis and T. Lookman, *Sci. Rep.*, **2016**, *6*, 19375.

[36]   J. Hachmann, R. Olivares-Amaya, S. Atahan-Evrenk, C. Amador-Bedolla, R. S. Sánchez-Carrera, A. Gold-Parker, L. Vogt, A. M. Brockway and A. Aspuru-Guzik, *J. Phys. Chem. Lett.*, **2011**, *2*, 2241.

[37]   M. A. F. Afzal, C. Cheng and J. Hachmann, *J. Chem. Phys.*, **2018**, *148*, 241712.

[38]   W. Sun, D. A. Kitchaev, D. Kramer and G. Ceder, *Nat. Commun.*, **2019**, *10*, 573.

[39]   E. J. Braham, J. Cho, K. M. Forlano, D. F. Watson, R. Arròyave and S. Banerjee, *Chem. Mater.*, **2019**, *31*, 3281.

[40]   L. Mora-Tamez, G. Barim, C. Downes, E. M. Williamson, S. E. Habas and R. L. Brutchey, *Chem. Mater.*, **2019**, *31*, 1552.

[41]   N. D. Burrows, S. Harvey, F. A. Idesis and C. J. Murphy, *Langmuir*, **2017**, *33*, 1891.

[42]   J. Kirman, A. Johnston, D. A. Kuntz, M. Askerka, Y. Gao, P. Todorović, D. Ma, G. G. Privé and E. H. Sargent, *Matter*, **2020**, *2*, 938.

[43]   B. Meredig, E. Antono, C. Church, M. Hutchinson, J. Ling, S. Paradiso, B. Blaiszik, I. Foster, B. Gibbons, J. Hattrick-Simpers, A. Mehta and L. Ward, *Mol. Syst. Des. Eng.*, **2018**, *3*, 819.

[44]   P. Raccuglia, K. C. Elbert, P. D. F. Adler, C. Falk, M. B. Wenny, A. Mollo, M. Zeller, S. A. Friedler, J. Schrier and A. J. Norquist, *Nature*, **2016**, *533*, 73.

[45]   E. Kim, K. Huang, A. Saunders, A. McCallum, G. Ceder and E. Olivetti, *Chem. Mater.*, **2017**, *29*, 9436.

[46]   J. L. Andrews, D. A. Santos, M. Meyyappan, R. S. Williams and S. Banerjee, *Trends Chem.*, **2019**, *1*, 711.

[47]   A. Talapatra, R. Arróyave, P. Entel, I. Valencia-Jaime and A. H. Romero, *Phys. Rev. B - Condens. Matter Mater. Phys.*, **2015**, *92*, 054107.

[48]   J. R. Chamorro and T. M. McQueen, *Acc. Chem. Res.*, **2018**, *51*, 2918.

[49]   J. Gopalakrishnan, *Chem. Mater.*, **1995**, *7*, 1265.

[50]   N. T. K. Thanh, N. Maclean and S. Mahiddine, *Chem. Rev.*, **2014**, *114*, 7610.

[51]   J. Livage, M. Henry and C. Sanchez, *Prog. Solid State Chem.*, **1988**, *18*, 259.

[52]   A. Jain, J. A. Bollinger and T. M. Truskett, *AIChE J.*, **2014**, *60*, 2732.

[53]   A. Talapatra, S. Boluki, T. Duong, X. Qian, E. Dougherty and R. Arróyave, *Phys. Rev. Mater.*, **2018**, *2*, 113803.

[54]   D. C. Lonie and E. Zurek, *Comput. Phys. Commun.*, **2011**, *182*, 372.

[55]   A. Shamp, T. Terpstra, T. Bi, Z. Falls, P. Avery and E. Zurek, *J. Am. Chem. Soc.*, **2016**, *138*, 1884.

[56]   B. Burger, P. M. Maffettone, V. V. Gusev, C. M. Aitchison, Y. Bai, X. Wang, X. Li, B. M. Alston, B. Li, R. Clowes, N. Rankin, B. Harris, R. S. Sprick and A. I. Cooper, *Nature*, **2020**, *583*, 237.

[57]   D. Y. Shahriari, A. Barnabè, T. O. Mason and K. R. Poeppelmeier, *Inorg. Chem.*, **2001**, *40*, 5734.

[58]   S. M. Moosavi, A. Chidambaram, L. Talirz, M. Haranczyk, K. C. Stylianou and B. Smit, *Nat. Commun.*, **2019**, *10*, 539.

[59]   B. Cao, L. A. Adutwum, A. O. Oliynyk, E. J. Luber, B. C. Olsen, A. Mar and J. M. Buriak, *ACS Nano*, **2018**, *12*, 34.

[60]   T. Lundstedt, E. Seifert, L. Abramo, B. Thelin, Å. Nyström, J. Pettersen and R. Bergman, *Chemom. Intell. Lab. Syst.*, **1998**, *42*, 3–40.

[61]   R. G. Brereton, *Applied Chemometrics for Scientists*, John Wiley & Sons, Ltd, Chichester, UK, **2007**.

[62]   A. J. Rondinone, A. C. S. Samia and Z. J. Zhang, *J. Phys. Chem. B*, **2000**, *104*, 7919.

[63]   T. Taghvaee, S. Donthula, P. M. Rewatkar, H. Majedi Far, C. Sotiriou-Leventis and N. Leventis, *ACS Nano*, **2019**, *13*, 3677.

[64]   H. Maleki, L. Durães and A. Portugal, *J. Phys. Chem. C*, **2015**, *119*, 7689.

[65]   M. A. B. Meador, L. A. Capadona, L. McCorkle, D. S. Papadopoulos and N. Leventis, *Chem. Mater.*, **2007**, *19*, 2247.

[66]   C. Barglik-Chory, C. Remenyi, H. Strohm and G. Müller, *J. Phys. Chem. B*, **2004**, *108*, 7637.

[67]   J. J. Sheng, in *Modern Chemical Enhanced Oil Recovery*, Elsevier, 4th edn., **2011**, pp. 1–11.

[68]   M. A. Bezerra, R. E. Santelli, E. P. Oliveira, L. S. Villar and L. A. Escaleira, *Talanta*, **2008**, *76*, 965.

[69]   S. E. Lohse, N. D. Burrows, L. Scarabelli, L. M. Liz-Marza and C. J. Murphy, *Chem. Mater*, **2014**, *26*, 24.

[70]   N. R. Jana, *Small*, **2005**, *1*, 875.

[71]   F. Hubert, F. Testard, G. Rizza and O. Spalla, *Langmuir*, **2010**, *26*, 6887.

[72]   T. K. Sau and C. J. Murphy, *Langmuir*, **2004**, *20*, 6414.

[73]   F. Hubert, F. Testard and O. Spalla, *Langmuir*, **2008**, *24*, 9219.

2. MODULATING THE HYSTERESIS OF AN ELECTRONIC TRANSITION: LAUNCHING ALTERNATIVE TRANSFORMATION PATHWAYS IN THE METAL—INSULATOR TRANSITION OF VANADIUM(IV) OXIDE*

2.1. Overview

Materials exhibiting pronounced metal—insulator transitions such as VO_2 have acquired great importance as potential computing vectors and electromagnetic cloaking elements given the large accompanying reversible modulation of properties such as electrical conductance and optical transmittance. As a first-order phase transition, considerable phase coexistence and hysteresis is typically observed between the heating insulator→metal and cooling metal→insulator transformations of VO_2. Here, we illustrate that substitutional incorporation of tungsten greatly modifies the hysteresis of VO_2; both increasing the hysteresis as well as introducing a distinctive kinetic asymmetry wherein the heating symmetry-raising transition is observed to happen much faster as compared to the cooling symmetry-lowering transition, which shows a pronounced rate dependence of the transition temperature. This observed kinetic asymmetry upon tungsten doping is attributed to the introduction of phase boundaries resulting from stabilization of nanoscopic M_2 domains at the interface of the monoclinic M_1 and tetragonal phases. In contrast, the reverse cooling transition is mediated by point defects, giving rise to a pronounced size dependence of the hysteresis. Mechanistic elucidation of the influence of dopant incorporation on hysteresis provides a means to

rationally modulate the hysteretic width and kinetic asymmetry, suggesting a remarkable programmable means of altering hysteretic widths of an electronic phase transition.

2.2. Introduction

Reversible solid—solid phase transformations bring about a pronounced modulation of properties such as electrical conductance, dielectric permittivity, optical transmittance, and magnetic remanence underpinned often by only a slight distortion of structure induced as a function of a state variable such as temperature, strain, or pressure.[1–6] First-order solid—solid phase transformations in early transition metal oxides such as HfO_2, ZrO_2, VO_2, and likely NbO_2, are thought to follow a diffusionless martensitic pathway involving a lowering of symmetry upon cooling.[5,7–10] The first-order nature of these transitions implies a pronounced discontinuity of lattice enthalpy at the transition temperature; the relative phase stabilities of the martensite and austenite determine the transition temperature. Systems manifesting first-order phase transitions characteristically exhibit hysteresis between the symmetry lowering and symmetry raising transitions with the hysteretic width posited to be a function of the mismatch in structure between the low- and high-symmetry phases.[11] Considering temperature-induced transitions, supercooling of the high-temperature phase, super-heating of the low-temperature phase, and the resulting thermal hysteresis depend on a number of parameters including the composition-dependent free energy landscape, microstructure, dopants, and dimensionality;[12] hysteresis effects can furthermore have a dynamical origin as a result of sluggish nucleation and growth kinetics often manifested at finite particle sizes.[13]

29

The hysteresis thus manifested in martensitic transitions is tremendously consequential for practical applications; mitigating hysteresis can extend the lifetime and diminish degradation of materials subjected to prolonged thermal cycling such as demonstrated in the case of a $Zn_{45}Au_{30}Cu_{25}$ alloy by engineering close geometric compatibility of the austenite and martensite.[14] Alternatively, a large hysteretic width in a thermal or voltage-driven phase transition reflects greater non-volatility of the individual states and is potentially useful for the fabrication of memristive device architectures.[15–17] Mechanistic understanding of hysteretic phenomena is thus vital in order to engineer precise tunability of the distinctive structural and electronic instabilities of transition metal oxides as required for practical applications.

Of the abovementioned binary oxides, vanadium(IV) oxide (VO_2) is a material of great interest as a result of its large metal—insulator transition at ca. 67°C. A pronounced modulation of many physical properties of VO_2, some by orders-of-magnitude, is manifested at this temperature including its electrical conductivity, optical transmittance, thermal emissivity, specific heat, Seebeck coefficient, and magnetic susceptibility.[2,18–20] The modulation of these properties underpins potential applications in device constructs spanning the range from Mott field-effect transistors and thermal emissivity coatings to optical limiters, infrared modulators, and reconfigurable RF devices.[15,19] In order to fully realize the potential of this material, the properties of the electronic transition including the critical transition temperature (T_c) and hysteresis width need to be predictively tunable. For Mott memory applications utilizing memristive and memcapacitive properties, a small hysteresis will enable rapid switching,

30

whereas a large hysteresis is expected to facilitate stable and non-volatile on/off states resistant to spontaneous resetting with minimal energy dissipation.[15]

The origin of the metal—insulator transition in VO_2 has been extensively debated in the past since the transition exhibits characteristics of both a Mott—Hubbard transition underpinned by a change in electron correlation and a Peierls' transition with electron—phonon coupling as the primary driving force.[5,21–23] Additionally the phase nucleation of metallic and insulating phases has been examined to elucidate the influence of conditions such as strain, doping, pressure, defects, and scaling to nanometer-sized dimensions.[24–28] It is worth noting that as a result of electron correlation and the manifestation of a complex phase diagram with multiple accessible metastable states, hysteretic effects remain to be conclusively elucidated for this system.[11,14,29,30] The underlying structural transition takes the material from a low-temperature monoclinic M_1 insulating phase (space group: *P2₁/c*) or alternatively a monoclinic M_2 insulating phase (space group *C2/m*) stabilized under strain to a high-symmetry rutile metallic phase R with space group *P₄/2mnm* (**Figure 2.1**).[31–33] Figures 2.1a—c illustrate that the three structures differ primarily in terms of the V—V separation and the degree of canting of VO_6 octahedra along the rutile *c* axis. Figure 2.1a shows that the M_1 polymorph is characterized by two distinct V—V separations of 2.65 and 3.13 Å; this distortion is furthermore preserved in the M_2 phase, which has sequential chains of evenly spaced and alternating short and long V—V distances. The rutile structure with higher symmetry has a consistent V—V separation of 2.87 Å along the *c* direction.

31
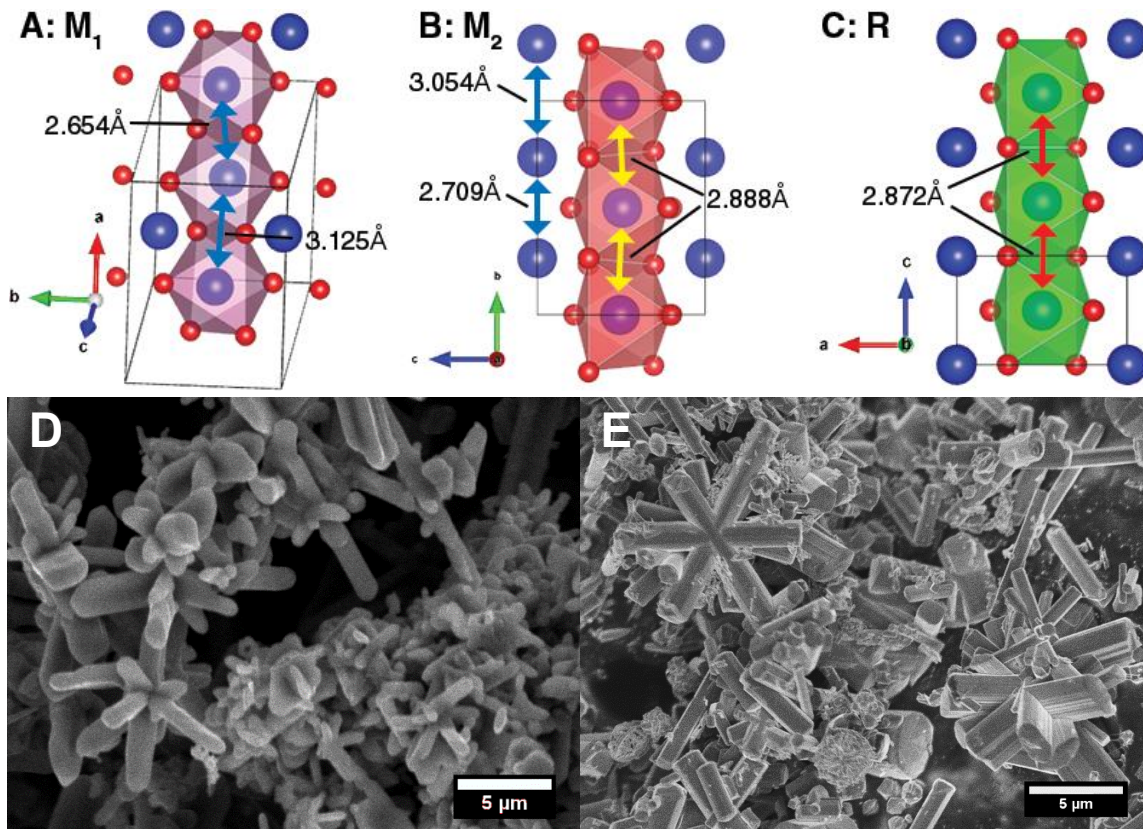
Figure 2.1. Atomistic structure renditions of (A) M_1; (B) M_2; and (C) R polymorphs of VO_2. Scanning electron microscopy (SEM) images of (D) undoped and (E) W-doped VO_2 particles prepared by the oxalic acid reduction of V_2O_5 under hydrothermal conditions ((E) depicts VO_2 particles with a W concentration of ca. 0.23 at.%).

Much work has focused on the modulation of the critical transition temperature (T_c) of VO_2 by substitutional and interstitial doping with different cations and anions, introduction of defects such as oxygen vacancies, and by the addition of strain to the system.[34–42] Fan *et al.* have examined hysteretic effects within a single nanobeam and observe a symmetrical decrease in hysteresis with increasing defect concentration for unstrained nanobeams.[27] Since defects can serve as nucleation sites, increasing defect density is correlated with a higher nucleation probability. In contrast, an asymmetric

32

response has been observed for strained clamped nanobeams wherein the cooling (R→M$_1$) transition temperature increases, signifying a decrease in the amount of supercooling, with increased defect concentration, whereas the heating transition remains unmodified. These authors suggest that in the latter clamped systems that are under anisotropic strain, the heating M$_1$→R transition is more likely to nucleate at extended defects such as twin planes, which reflect higher energy domains on the free energy surface as compared to point defects.[13,27] Consequently, the introduction of localized point defects does not modify the heating M$_1$→R transition but has a disproportionate effect on the cooling R→M$_1$ transition. Recent work by Miyazaki and co-workers suggest that co-doping with appropriate amounts of Cr and Nb can almost entirely suppress the thermal hysteresis in the metal—insulator transition of VO$_2$ although the underlying mechanism for the suppressed hysteresis remains to be elucidated.[30] In contrast other studies have suggested that doping with atoms such as tungsten and molybdenum increases the hysteretic width;[34,43] however, a clear correlation between dopant incorporation and hysteresis has not been established and a reliable mechanistic description remains elusive. Here, we examine the influence of substitutionally doping tungsten atoms within the vanadium sublattice of VO$_2$ on the hysteresis between the heating insulator→metal and cooling metal→insulator transitions. The availability of detailed atomistic understanding of the local structure of tungsten dopant sites and their influence on the surrounding VO$_2$ lattice make W-doped VO$_2$ an ideal system for elucidating structure—hysteresis correlations.[43–46] In previous work, z-contrast high angle annular dark field scanning transmission electron

33

microscopy (HAADF STEM) measurements have enabled us to establish that W atoms substitutionally occupy vanadium sites in VO_2 wherein they induce anisotropic strain.[44] No evidence for occupation of interstitial sites or multi-atom dopant clusters was observed. Modeling of radial distribution functions measured from extended X-ray absorption fine structure (EXAFS) spectroscopy also suggest the stabilization of WO_6 octahedra that induces a local "tetragonal-like" distortion as also predicted by density functional theory calculations.[43,47] We demonstrate here that W-doping acts much in the same way as tensile strain in terms of inducing asymmetric broadening of hysteresis and further illustrate that the extent of W doping greatly modifies the extent of asymmetry of the hysteresis. Dopant control of hysteresis achieved within single-crystalline free-standing nanostructures provides an unprecedented means to control an important aspect of the electronic instability of these materials and is imperative for integration of such materials within memristive device architectures.

2.3. Results and Discussion

The M_1 monoclinic polymorph is the thermodynamically stable phase of VO_2 at room temperature in the absence of strain. Under compressive strain or upon substitutional doping with elements such as Cr or Al, the M_2 phase can be stabilized.[48,49] It is now clear that the M_1 and M_2 phases (Figures 2.1a and b) represent two discrete free-energy valleys that represent alternative structural modifications accessible upon reducing the symmetry of the tetragonal rutile phase (Figure 2.1c). Indeed, Ginzburg—Landau mapping of symmetry relationships across the tetragonal—monoclinic phase transition suggests that neither of the two phases can be considered an

intermediate for transformation of the other polymorph to the higher symmetry

tetragonal structure.[50,48] However, the two monoclinic distortions can coexist within

strained systems due to inhomogeneous strain gradients established within strained

nanobeams of VO_2.[51] The monoclinic phases can each further stabilize multiple ferroic

variants, which are typically separated by twin boundaries;[52,53] however, twin planes are

symmetry forbidden in the high-symmetry rutile phase.[52–54] Figures 2.1d and e depict

SEM images of undoped and W-doped VO_2 nanostructures stabilized by hydrothermal

synthesis, respectively. The structures depicted are a mixture of nanostars comprising

multiple single-crystalline nanowires attached at a center junction as well as unattached

single-crystalline wires. These specific morphologies result from the oxalic acid

structure directing agent used in synthesis. The "asterisk-like" assemblies are fragmented

into single-crystalline wires upon grinding and such samples have been analyzed in the

measurements noted below. The confined dimensions of these single-crystalline

nanostructures make these structures particularly useful as model systems for examining

the influence of doping on phase stabilities and hysteresis without confounding factors

such large scale grain boundaries and dopant segregation.

The phase transition of undoped and W-doped VO_2 has been examined by

temperature-dependent powder XRD in order to ascertain the influence of doping on the

M_1 and R phase stabilities. **Figure 2.2** depicts *in situ* temperature-dependent powder

XRD patterns (acquired in the 2θ range from 27.2° to 28.4° (Figures 2.2a,b,e,f) and 63°

to 67° (Figures 2.2c,d,g,h) showing the most pronounced changes) for undoped VO_2 and

VO_2 with 0.51 at.% substitutional incorporation of tungsten (as determined from

inductively coupled plasma mass spectrometry analysis).[43] Extended diffraction patterns acquired in the 2θ range from 25—70° are depicted in **Figure A.1** (Appendix A). The sample has been heated from 30 to 100°C then cooled back to 30°C with spectra acquired at 5°C intervals. All reflections are indexed to either the M_1 (Joint Committee on Powder Diffraction Standards (JCPDS) 43-1051) or R (JCPDS 79-1655) phases of VO_2 with the relative proportion varying as a function of temperature. The intensity modulation maps in Figure 2.2 highlight the 2θ range from 27.2—28.4° and 64—66°, which correspond to reflections that exhibit the most pronounced changes across the M_1 to R transition. Upon heating of the undoped sample, Figure 2.2A shows a strong reflection at 2Θ=27.8° corresponding to the separation between M_1 [011] planes; this reflection is greatly diminished in intensity at 65°C; at which temperature, a pronounced reflection appears at $2\theta = 27.7°$, which is attributed to the separation between the [110] planes of the R-phase. Upon cooling, Figure 2.2B indicates that the M_1 [011] reflection is recovered but only at a temperature of 55°C, illustrating a clear hysteresis between heating and cooling transitions. Figure 2.2C depicts a pronounced splitting of the reflection indexed to the [013] planes of the M_1 polymorph at $2\theta = 65°$ to reflections that can be indexed to the [310] and [002] planes of the R phase at 64.7° and 65.3° upon heating. The splitting characteristic of the R phase is most clearly discernible starting at 65°C at which point the sample is predominantly in the R phase. Upon cooling, the two reflections collapse to a single reflection corresponding to the [011] reflections of the M_1 polymorph at a temperature of 55 °C.
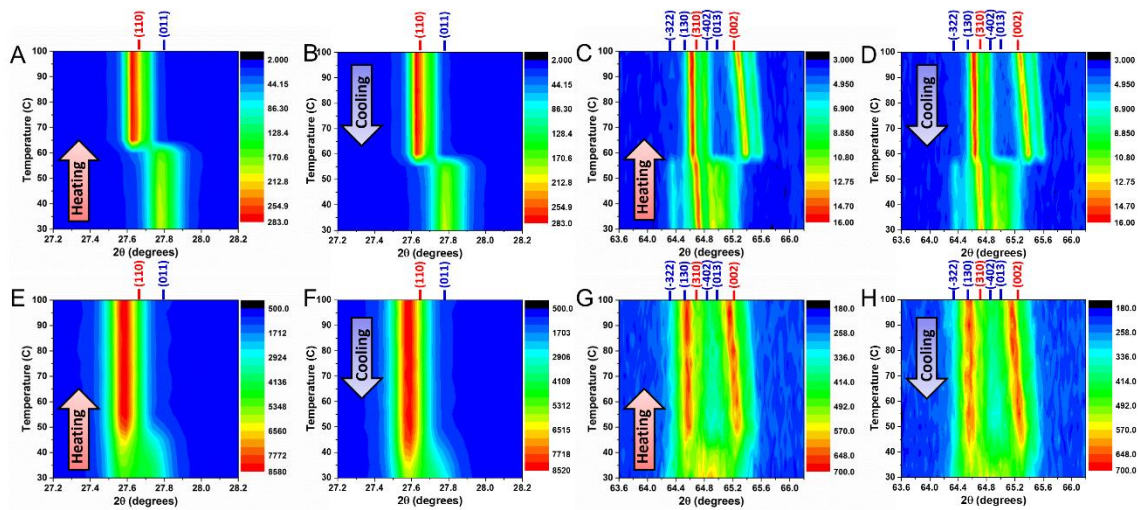
Figure 2.2. Temperature-dependent XRD patterns plotted as intensity modulation maps. Maps acquired for (A—D) undoped and (E—H) W-doped VO$_2$ (with ca. 0.51 at.% W doping) nanostructures. The red and blue indices depict reflections for R and monoclinic M$_1$ phases of VO$_2$, respectively. The regions of the diffraction patterns delineated here are characterized by the most pronounced changes resulting from the thermally driven structural transformation. The extended diffraction patterns are shown in Figure A.1.

Similar structural distortions are observed for the 0.51 at.% W-doped VO$_2$ sample with a couple of notable exceptions. The first most notable difference is that at room temperature, reflections attributed to both M$_1$ and R phases are observed (specifically, the M$_1$ [011] and R [110] reflections) suggesting a much more extended phase coexistence regime for these two polymorphs. The second difference is that the transformation upon heating to a fully R phase occurs at a much lower temperature (ca. 45°C) as compared to undoped VO$_2$ (Figs. 2.2E and G). Upon cooling to room temperature, the R phase is found to persist (Figs. 2.2F and H as well as Figure A.1) suggesting that W-doping not only induces a pronounced diminution of the transition temperature as is well known but also induces significant supercooling of the high-

symmetry phase.[43–46,55] **Figure 2.3A and 2.3B** depict a direct comparison between

XRD patterns acquired for W-doped ($W_xV_{1-x}O_2$ with x of ca. 0.051) and undoped VO_2 at

30 °C (A) and 100 °C (B). At low temperatures, we note both a broadening of the

reflections and a shift to lower 2θ values when W is substitutionally doped. The

broadening is a result of multiple X-ray coherent domains within a single-crystalline

nanowire as well as the presence of anisotropic strain.[44,46] The increased lattice spacing

is the result of lattice expansion induced by incorporation of larger W atoms in V sites as

per Vegard's law. Interestingly, the increased lattice spacing is discernible only for

specific planes, for instance, the separation between [011] planes is increased from 3.209

Å to 3.278 Å, whereas the separation between the [$\bar{2}$11] planes is unchanged. In other

words, Figure 2.3 suggests an anisotropic influence of W-doping on the VO_2 lattice,

which creates inhomogeneous strain gradients in the M_1 phase (*vide infra*).[44,46]

Comparing the XRD patterns at 100°C, Figure 2.3B indicates stabilization of the R

phase with and without doping. Interestingly, upon W doping, the reflections are

uniformly shifted to lower 2θ values, suggesting homogenous lattice expansion of the

rutile phase as a result of dopant incorporation. The observation of inhomogeneous strain

generated in the M_1 phase as a result of substitutional W incorporation being alleviated

upon transitioning to the rutile phase has further been evidenced by strain analysis of

high HAADF STEM and it was posited that the depression of the transition temperature

upon dopant incorporation results in large measure from a greater driving force for

resolving atomic instabilities in proximity of the dopant atoms.[44]
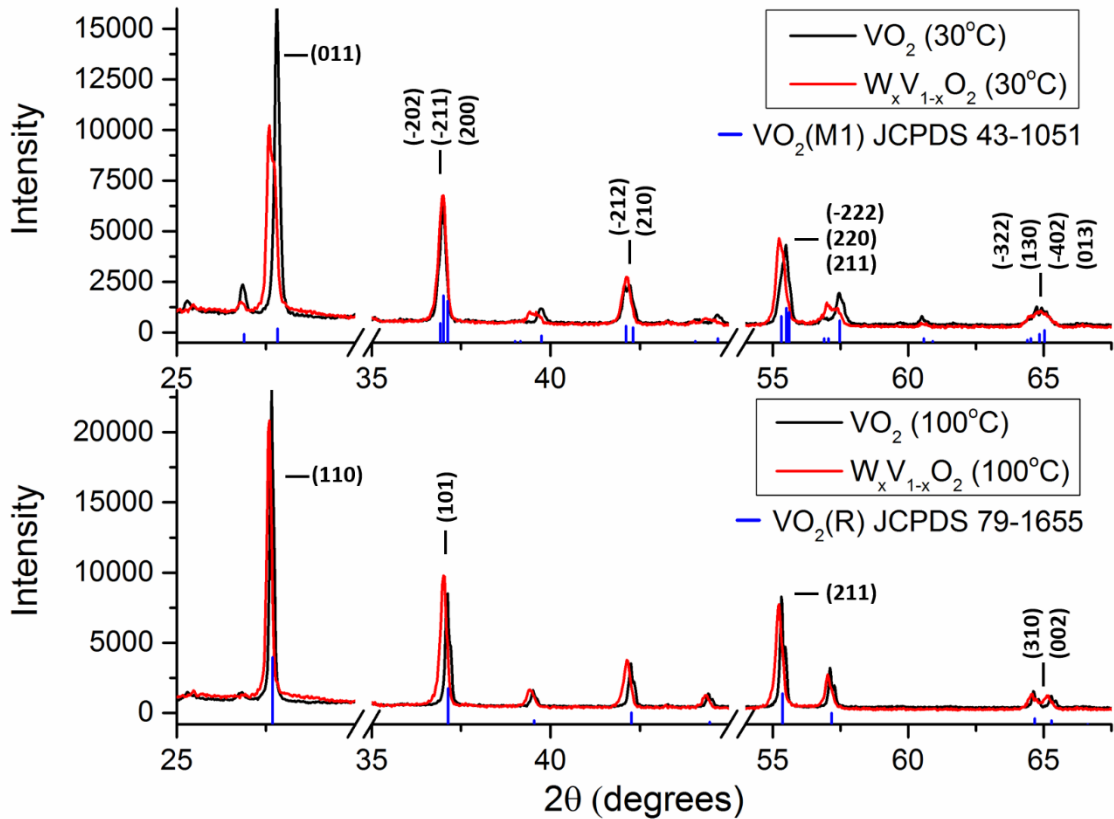
Figure 2.3. A) Room-temperature (30°C) and B) high-temperature (100°C) XRD patterns acquired for undoped and W-doped VO$_2$ (W$_x$V$_{1-x}$O$_2$ with x of ca. 0.051). Breaks in the horizontal-axes are included to highlight the part of the scale with the most pronounced differences.

Another key observation from XRD studies of doped and undoped VO$_2$ depicted in Figure 2.2 and Figure A.1 is the clear manifestation of hysteresis between the heating M$_1$→R and cooling R→M$_1$ transitions. Considering undoped VO$_2$, the transition temperature from M$_1$ to R is 65°C (Figures 2.2A and C). When the sample is cooled, the reverse R→M$_1$ transition occurs between 60—55 °C (Figures 2.2B and D). The 5—10°C temperature differences between the M$_1$ to R and the R to M$_1$ phase transformations illustrates a pronounced hysteresis.[56] For the 0.51 at.% W-doped sample, the M$_1$ to R

phase transition temperature is depressed to 45°C.[43] However, the R phase is retained

down to room temperature suggesting a greatly expanded phase coexistence regime and

substantially greater hysteresis.

Given that it is a first-order transition, the metal—insulator transition of VO_2 is

accompanied by a considerable consumption ($M_1{\rightarrow}R$) or release ($R{\rightarrow}M_1$) of latent heat.

The latent heat comprises a lattice enthalpy component resulting from the structural

distortions accompanying the phase transition, which is compensated in part by a

modulation of the phonon entropy as well as the conduction entropy of the

electrons.[57,58] In order to examine dynamical evolution of the thermal hysteresis upon

doping, differential scanning calorimetry (DSC) measurements have been performed for

both doped and undoped VO_2 at various scan rates as depicted in **Figure 2.4**. Two

parameters are defined to aid the interpretation of the thermal analysis data; T_{max}, which

represents the temperature at the maximum height of the transition peak and is indicative

of the maximum transformation rate, and T_{onset}, which represents the onset temperature

of the transition measured as the intersection of the baseline with the steepest slope of

the peak. Figure 2.4A depicts DSC traces acquired at various scan rates for undoped

VO_2 indicating a symmetrical evolution of T_{max} towards a temperature of ca. 66°C with

decreasing scan rate upon both heating and cooling. The consistent narrowing of the

hysteresis with decreasing scan rate implies manifestation of a significant kinetic

dependence on the timescales accessible within these measurements (from 0.1 to 20°C

min^{-1}). The total hysteresis width, ΔT_{hyst}, can be interpreted as a combination of rate-

dependent kinetic and rate-invariant components, which are denoted as $\Delta T_{hyst}^{kinetic}$ and

$\Delta T_{\text{hyst}}^{\text{intrinsic}}$, respectively, as illustrated in Figure 2.4c. The intrinsic hysteresis width for undoped VO_2 is only ca. 1.1 °C, representing the difference between a temperature of 66.0 ± 0.1°C for heating and 64.9 ± 0.1°C for cooling across the measured scan rates.
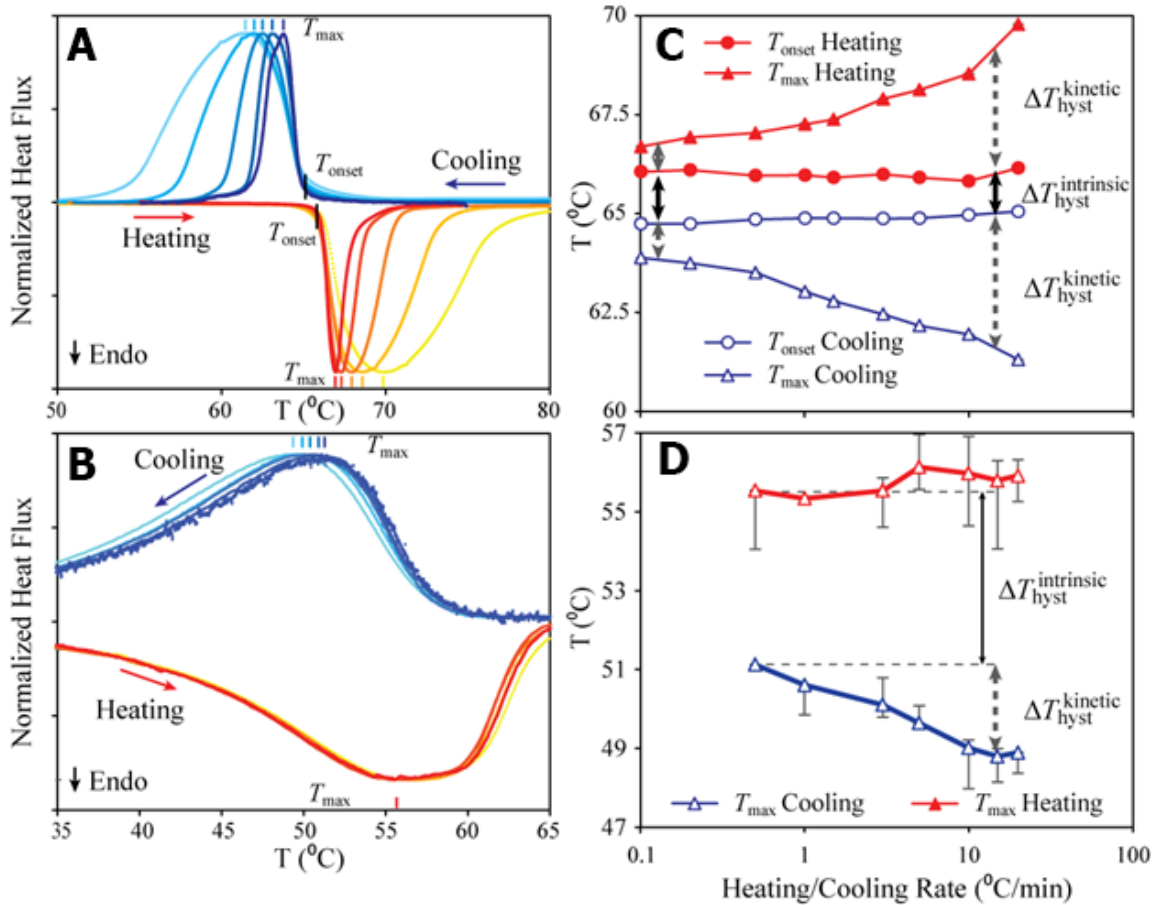
Figure 2.4. Scan-rate dependent DSC results for A) undoped VO_2, and B) W-doped VO_2 (ca. 0.23 at.% W doping)[59]. The gradient from lighter to darker colors corresponds to a decrease of the scan rate with light blue and yellow representing 15°C/min decreasing through the rates 10, 5, 3, 1°C/min to dark blue and red for cooling and heating, respectively. T_{onset} and T_{max} have been deduced from the observed traces. Evolution of T_{onset} and T_{max} for C) undoped VO_2, and D) W-doped VO_2 (ca. 0.23 at.% W doping), as a function of the heating/cooling rate. ΔT_{hyst} is decomposed into a kinetic contribution, $\Delta T_{\text{hyst}}^{\text{kinetic}}$, which decays as the temperature ramp rate is decreased; intrinsic (thermodynamic) contributions that remain independent of ramp rate are denoted as $\Delta T_{\text{hyst}}^{\text{intrinsic}}$.

Figure 2.4b shows the DSC traces for W-doped VO_2 with notably broader peaks due to inhomogeneity in transition temperature either between particles or across domains within individual particles. Figure 2.4d suggests that hysteresis behavior in W-doped VO_2 is considerably altered. The temperature of the heating transition is essentially scan-rate-invariant, whereas the temperature of the cooling transition monotonically increases with decreasing scan rate bringing about a pronounced asymmetry; the hysteretic width for this system is thus determined greatly by the cooling transition. Indeed, this asymmetry is consistently observed upon increasing the concentration of incorporated W dopants and in particular corresponds to a pronounced modification of the phase transformation pathway for the heating $M_1 \rightarrow R$ transition, which facilitates a much more rapid transformation.

As previously established in the literature, substitutional incorporation of tungsten decreases the T_c as a function of dopant concentration by making the R phase more thermodynamically stable at lower temperatures.[43,44] **Figure 2.5** plots the maximum transition temperature measured for W-doped VO_2 during heating and cooling cycles for two different scan rates (10 and 1°C min^{-1}) as a function of the transition temperature. The approximate W doping concentration is determined based a ca. 52°C/at.% W correlation between the transition temperature and tungsten concentration previously established for these materials by inductively coupled plasma mass spectrometry, which has been confirmed as an accurate measurement of homogenous doping based on atomic resolution electron microscopy studies.[43,44,59] Considering the 1°C min^{-1} scan to most closely approximate thermodynamic conditions, the hysteresis is

increased from 1.1°C min^{-1} for undoped VO$_2$ to ca. 6.6—7.2 °C min^{-1} for the W-doped samples. The extended phase stability of the R phase gives rise to an extended phase coexistence regime and thus increased hysteresis. However, the hysteresis ($\Delta T_{hyst}^{intrinsic}$) remains essentially invariant as a function of dopant concentration. Intriguingly, a pronounced kinetic asymmetry is observed between the heating and cooling transitions across all the doped samples. The cooling transitions are conspicuously far more rate-
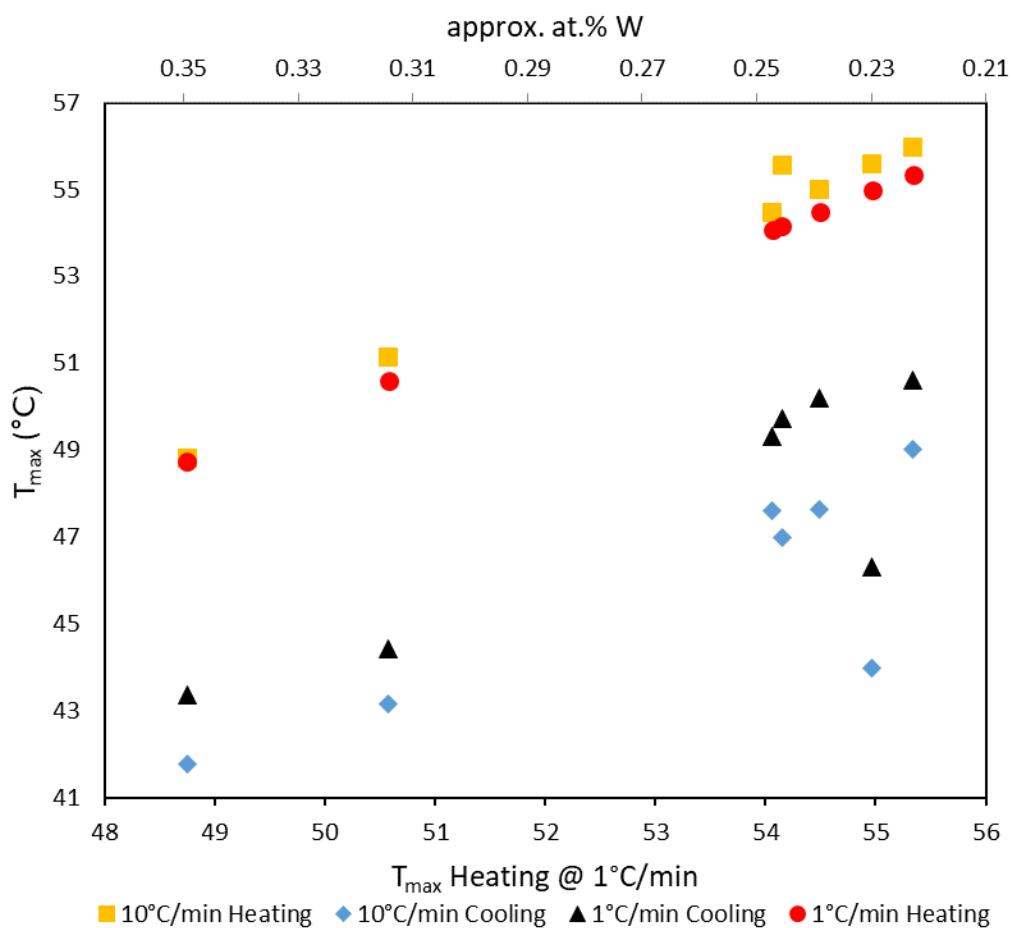
Figure 2.5. T_{max} for heating and cooling (as measured by DSC) at 10 and 1°C min^{-1} scan rates as a function of tungsten concentration (the active dopant concentration is calculated using the T_{max} heating at 1°C min^{-1} using a correlation of -52°C decrease of transition temperature per at.% W as noted previously for these materials.[59])

dependent as compared to the heating transitions. The magnitude of the kinetic

hysteresis appears to remain essentially invariant with increasing tungsten concentration.

In order to elucidate the origins of the increased thermal hysteresis and

unprecedented kinetic asymmetry noted upon W-doping, it is important to consider the

distinctive origins of the $M_1 \rightarrow R$ and $R \rightarrow M_1$ transitions. At the atomistic scale, the

structural transformations follow a diffusionless (and reversible) Martensitic pathway

that nevertheless must be first nucleated at a discrete site and then propagated across the

particle volume in the form of a transformation dislocation.[13] For undoped and

unstrained VO_2, it has been posited that both the $M_1 \rightarrow R$ and $\rightarrow M_1$ transitions are

nucleated at point defects. Indeed, the extent of supercooling of the high-temperature

phase and superheating of the low-temperature phase are decreased with increasing

concentration of point defects since the nucleation probability is increased with

increasing defect density.[27] In contrast, in strained VO_2 nanobeams, the introduction of

nanotwinned M_1 domains derived from anisotropic strain gradients gives rise to twin

boundaries that represent higher energy segments of the free energy landscape; these

twin boundaries serve as more favorable nucleation sites for initiation of the phase

transformation, thereby facilitating a distinctive transformation pathway exclusively

available for the $M_1 \rightarrow R$ transition (in contrast, the symmetry of the R phase does not

permit stabilization of twinned domains in the high-temperature phase).[27] Indeed, recent

atomistic high-angular annular dark field imaging of a similar $M_1 \rightarrow R$ transition in HfO_2

has for the first time provided direct evidence for twin boundaries serving as preferential

nucleation sites for initiation of the symmetry-raising phase transition. In contrast, the

cooling R→M$_1$ transition is still mediated by point defects in the absence of such ferroelastic domain formation.[13] The hysteretic behavior of undoped VO$_2$ depicted in Figure 2.4 is consistent with the idea of point-defect-mediated pathways for both M$_1$→R and R→M$_1$ transformations. In this picture, rapid scan rates require a greater driving force to initiate nucleation, whereas slower scan rates allow for a greater proportion of local higher energy segments in the free energy landscape (a broader range of imperfections) to serve as nucleation sites. In contrast, the hysteretic behavior of W-doped VO$_2$ nanowires is reminiscent of clamped or strained nanobeams that are conducive to domain formation and thereby have an alternative set of sites that allow for more facile nucleation of the M$_1$→R transition.

In order to examine domain formation, atomic-resolution high-angle annular dark field (HAADF) images and selected area electron diffraction (SAED) patterns have been acquired for a W-doped VO$_2$ sample (W$_x$V$_{1-x}$O$_2$ with x of ca. 0.008) at 25°C after first quenching the sample to -180 °C where the entire particle was confirmed to be in the M$_1$ phase. The sample examined here has a metal—insulator transition temperature of ca. 28°C, which thus allows for imaging of phase heterogeneity.[59] Remarkably, **Figure 2.6** shows the unambiguous formation of phase domains and considerable phase coexistence across a single particle upon warming to 25°C. The SAED patterns indicate diffraction spots derived from nanoscale M$_2$ domains in addition to M$_1$ and R-phases. Distinctive electron diffraction spots attributed to [100] R, [0$\bar{1}$0]M$_1$, and [00$\bar{1}$]M$_2$ are highlighted in blue, green, and red, respectively. These diffraction spots have been used to construct a composite phase map as described in the previous work by Asayesh-Ardakani *et al.*[46]

The phase map shown in Figure 2.6B depicts red M_2 domains interspersed between green M_1 and blue R-domains. Figure A.2 depicts another example of the stabilization of M_1, M_2, and R domains. The anisotropic strain induced by W-doping, as also observed in the XRD data of Figure 2.3, is observed here to stabilize nanoscopic M_2 domains at the interface with incipient R-phase nuclei;[44,46] the stabilization of M_1/M_2/R phase boundaries is likely energetically more favorable as compared to a direct M_1/R phase boundary. The doped system thus mimics a three-phase-regime observed for compressively strained nanowires albeit induced here as a result of chemical strain.[51,33]
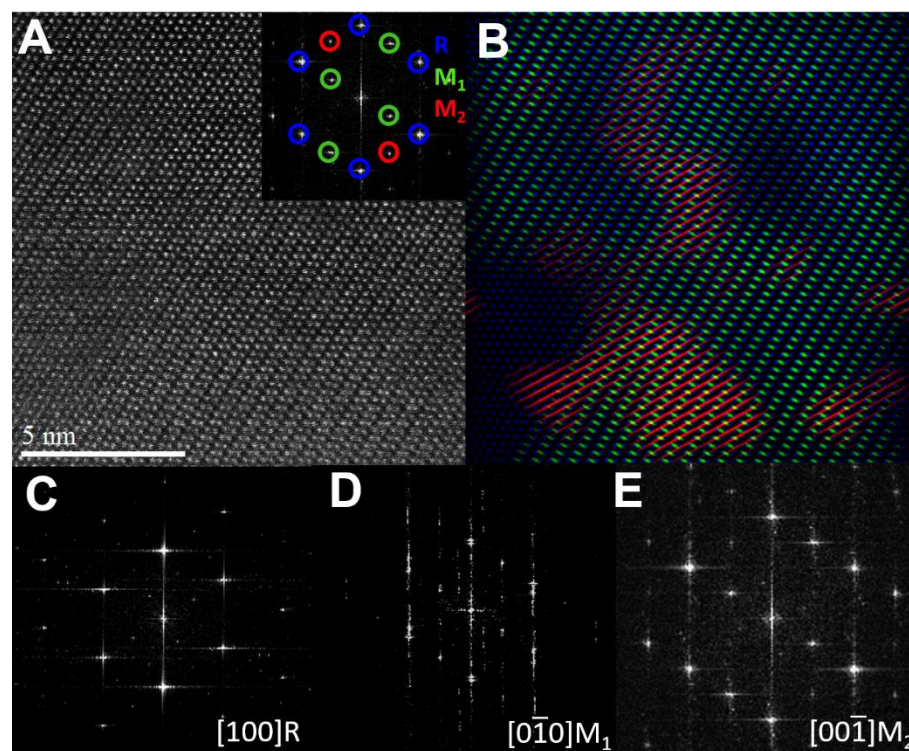
Figure 2.6. Atomic-resolution HAADF TEM image of a $W_xV_{1-x}O_2$ particle (with x of ca. 0.008) acquired at 25°C after warming from -180°C. A) TEM image and diffraction patterns with distinct diffraction spots indexed to R (blue), M_1 (green), and M_2 (blue) polymorphs. B) Composite map depicting the spatial distribution of the three phases. C-E) SAED patterns for R, M_1, and M_2 polymorphs.

It is important to note that unlike the quasi 2D ordering found in epitaxially strained nanowires,[27] the formation of M_2 domains in this system appears to show little by way of periodic ordering leading to the conclusion that the stochastically doped W atoms create complex inhomogenous strain gradients resulting in aperiodic M_2 domains stabilized to minimize energy.[44] A phase field modeling approach will likely be necessary to model the spatiotemporal propagation of these domains. The absence of reflections characteristic of the M_2 phase in the powder XRD patterns of Figures 2.2 and 2.3 is not surprising considering the few-unit-cell-thickness spans of the stabilized domains, which given their low X-ray coherence contributes primarily to broadening of the closely spaced M_1 reflections. Figure A.3 shows a corresponding TEM image and selected area electron diffraction pattern acquired for an undoped VO_2 nanowire. Solely M_1 domains are observed. While TEM examination of undoped VO_2 cannot entirely rule out phase coexistence occurring over a much narrower temperature range, distinctive multiphasic domains corresponding to M_1, M_2, and R phases have not been observed in the absence of W-doping for these unconstrained nanowires.

It is worth noting that extensive scanning tunneling microscopy studies of undoped VO_2 nanowires have allowed for visualization of discrete nucleation events giving rise to R-phase domains but have not provided any evidence for stabilization of the M_2 phase.[60,61] These studies suggested the nucleation and growth of distinctive low-resistance sites with metallic character; no semiconducting or insulating domains were seen to be stabilized at the interface between the incipient metallic domains and the insulating (M_1) matrix.[61] The appearance of the M_2 phase and the inevitable

stabilization of M_1/M_2 phase boundaries can thus be directly attributed to the anisotropic strain generated as a result of tungsten doping.[44] The phase boundaries provide a wealth of relatively higher free energy sites within the particle that can serve to nucleate the phase transformation. Indeed, much like clamped nanobeams, the localized anisotropic strain gradients generated by dopant incorporation greatly modify the $M_1 \rightarrow R$ transformation pathway; the extended defects (M_1/M_2 phase boundaries, M_1/M_1 twin boundaries) stabilized by doping are far more effective as compared to point defects at facilitating the $M_1 \rightarrow R$ transformation, thereby reducing superheating and giving rise to the mostly scan-rate-invariant heating transformation observed in Figures 2.4 and 2.5. The resulting R phase does not form twin walls and thus point defects are thought to remain the primary means for nucleating the reverse $R \rightarrow M_1$ transition.[50,54]

Experimental evidence supporting the role of point defects in determining the dynamical thermal hysteresis effects comes from evaluation of VO_2 nanocrystals of varying dimensions using variable rate DSC. Smaller particles have fewer point defects in general as a result of self-purification effects wherein defects can readily migrate to surfaces and be eliminated.[13,62,63] The reduced density of defects is thus expected to decrease the nucleation probability, thereby requiring a greater driving force to induce the transformation and resulting in increased hysteresis.[6,64] For this analysis, four undoped samples of different dimensions have been examined:[39,43] the particles have been prepared by reduction of V_2O_5 using different reducing agents, oxalic acid (average length of 7.0 ± 2.0 μm, average width of 500 ± 100 nm); 2-propanol (average length of 4.3 ± 3.0 μm, average width of 210 ± 70 nm); 2-propanol followed by ball milling (average

length of 215±196 nm, average width of 110±90 nm); and acetone (average length of

1.6±1.0 μm, average width of 180±70 nm); and ultrasmall VO_2 (quasi-spherical particles

with a diameter of 44±31 nm prepared as described in the Materials and Methods

section).[39] Size distributions for particles prepared by these methods are depicted in

Figure A.4. Figure 2.7 plots the hysteresis width (ΔT_{hyst}) at both 1°C min^{-1} and 10 °C

min[-1] as a function of the approximate particle volume deduced from the size distribution
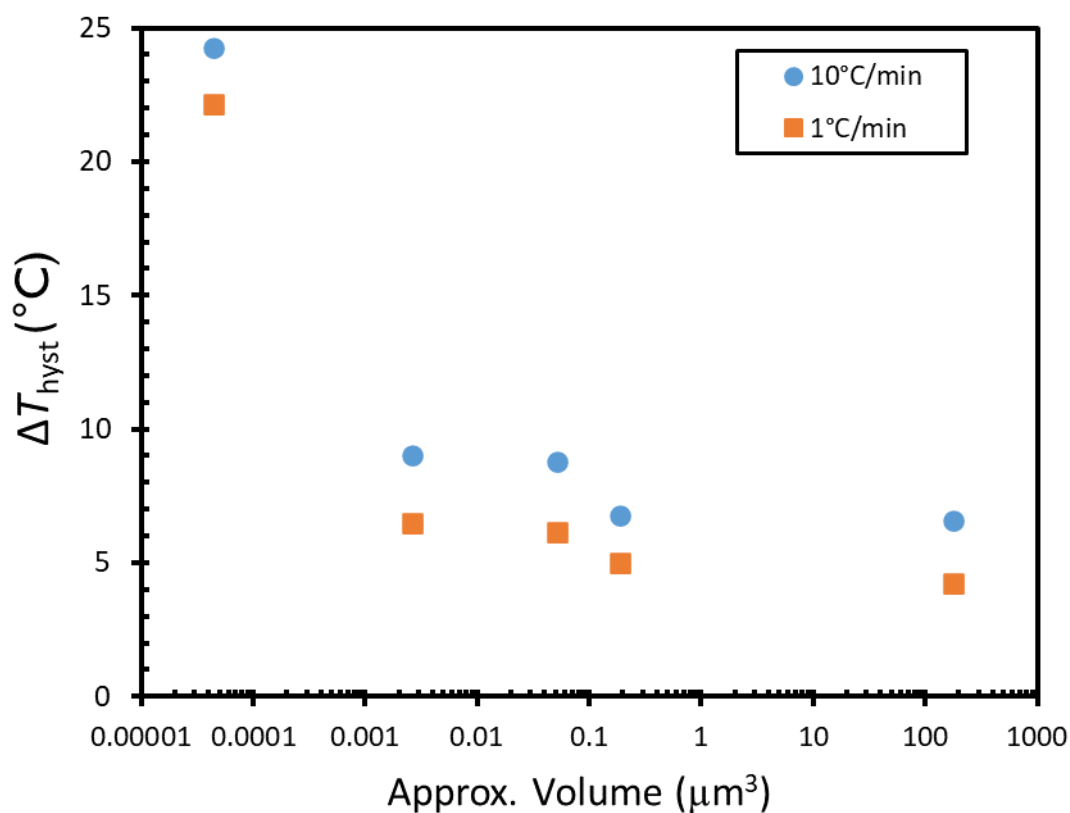
Figure 2.7. Plot depicting the evolution of hysteresis width measured during heating and
cooling cycles at scan rates of 1 and 10°C min^{-1} for undoped VO_2 nanocrystals as a
function of particle volume. Size distributions used to derive particle volumes are
provided in Figure A.4.

histograms (the relevant values are listed in **Table 2.1**). The overall hysteresis is seen to initially scale inversely with volume, from 22.1°C measured for the ultra-small VO_2 nanocrystals with a diameter of 44±31 nm to 4.2°C for the large micron-sized particles prepared by oxalic acid reduction of V_2O_5; however, the size scaling is greatly diminished at larger particle sizes, which show only a relatively small difference in their hysteretic widths. The scaling with volume can be rationalized based on a diminished defect density and thus reduced density of nucleation sites for smaller particles as well as the influence of a restricted nucleation volume; beyond a certain volume, the particle size is much larger than the nucleation volume and the defect density is high enough such that a change in volume has a negligible effect on the availability of nucleation sites. Consequently, the two larger samples prepared by reduction of V_2O_5 using oxalic acid and 2-propanol show little difference in the hysteretic widths (4.2 and 5.0 °C, respectively) or rate dependence. The hysteresis of the undoped samples of varying particle sizes contain distinctive kinetic and intrinsic components for both heating and cooling transitions with the one exception being the heating transition for the ultra-small VO_2 nanocrystals where the kinetic component appears to have been eliminated. Given the exceedingly low defect density for these particles, which give rise to the large observed hysteresis of 22.1°C, the most likely explanation is that the measured span of scan rates (from 1—20°C min^{-1}) does not substantially modify the distribution of defect sites that can serve to nucleate the phase transformation. The volume scaling of thermal hysteretic widths thus provides compelling evidence for the influence of point defects and their effect on nucleation probability in mediating the structural transformations.

50

Table 2.1. Transition temperatures measured during heating and cooling transitions for VO$_2$ nanocrystals with varying dimensions at scan rates of 1 and 10°C/min

Method of Preparation	Length (nm)	Width (nm)	10°C min^{-1} Heating (°C)	10°C min^{-1} Cooling (°C)	1°C min^{-1} Heating (°C)	1°C min^{-1} Cooling (°C)
Oxalic acid reduction	n/a	7000 ± 400	68.5	61.9	67.3	63.0
2-propanol reduction	4300 ± 3000	210 ± 70	68.7	61.9	68.0	63.0
Acetone reduction	1600 ± 1000	180 ± 70	68.7	59.9	67.4	61.3
2-propanol reduction (milled)	215 ± 196	110 ± 90	69.9	60.8	68.8	61.7
Ultrasmall	n/a	44 ± 31	59.0	34.7	58.9	36.7

The data above suggests that substitutional incorporation of tungsten atoms on the vanadium sublattice of VO$_2$ modifies the heating M$_1$→R transition by introducing phase boundaries that serve as nucleation sites, thereby eliminating the kinetic hysteresis derived from point-defect nucleation. The cooling R→M$_1$ transition is still mediated by point defects resulting in a pronounced asymmetry. The overall thermal hysteretic width is thus determined in large part by this latter transition. Figure 2.4 indicates that incorporation of W nevertheless greatly increases the intrinsic hysteresis, suggesting that substantially greater undercooling is required to drive the R→M$_1$ transition.

In order to examine the influence of tungsten doping of VO$_2$ on the point defect concentration, density functional theory (DFT) has been used to contrast the energy of formation for an oxygen vacancy within a tungsten-doped VO$_2$ lattice versus an undoped lattice in both the M$_1$ and R phases. A supercell with composition of V$_{32}$O$_{64}$ is used as the model system and formation energy for oxygen vacancy formation, ΔF, is computed

as described in the Methods section. This supercell with a tungsten atom substitutionally doped in a vanadium site ($V_{31}O_{64}W_1$) represents a doping amount of ca. 3 at.%. A major caveat with the use of DFT arises from its inadequacies with the treatment of electron correlation. Contrasting band theory and dynamical mean field theory approaches for treating the dynamically evolving electron—phonon coupling and electron correlation across the metal-insulator transition of VO_2 have been developed.[21,65] Electron correlation is furthermore sensitive to strain as recently shown by Mukherjee and co-workers and is furthermore likely to be considerably modified in the M_2 polymorph as compared to the M_1 polymorph.[33,66,67] While a precise treatment of electron correlation and particularly the extent to which it is affected by strain, doping, and defect dynamics is not currently accessible, the calculations presented herein nevertheless allow for an evaluation of the influence of W doping on the stabilization of oxygen vacancies. **Figure A.5** depicts $V_{31}O_{64}W_1$ supercells in the M_1 and R phases with a single oxygen vacancy. The numerical value of ΔF represents the energy cost of a vacancy being introduced within the VO_2 lattice. **Table 2.2** lists formation energies and ΔF values for creation of an oxygen vacancy in doped and undoped VO_2 in both R and M_1 phases. A comparison of ΔF values for doped and undoped VO_2 illustrates that oxygen vacancy formation is relatively less favored for the doped sample in both R and M_1 phases by about 730 and 1410 meV, respectively. The destabilization of oxygen vacancies upon W-doping can be rationalized based on the formal valence of the doped atoms being W^{6+}, which renders the loss of oxygen atoms more difficult.[43] The relatively large magnitude of the energy differentials illustrate the influence of tungsten on defect stability again with the caveat

Table 2.2. Total energies and energy of oxygen vacancy formation computed for undoped and W-doped VO_2 in M1 and R phases.

Phase	Cell	F (eV/cell)	ΔF
R	$V_{32}O_{64}$	-238.92	--
	$V_{31}O_{64}W_1$	-238.66	--
	$V_{32}O_{63}$ *(O vacancy)*	-236.27	2.65
	$V_{31}O_{63}W_1$ *(O vacancy)*	-235.28	3.38
M_1	$V_{32}O_{64}$	-235.93	--
	$V_{31}O_{64}W_1$	-235.26	--
	$V_{32}O_{63}$ *(O vacancy)*	-236.29	-0.36
	$V_{31}O_{63}W_1$ *(O vacancy)*	-234.22	1.05

that it has not been possible to fully treat correlation effects given the complexity of this system.[66] Relating back to the observations of Figures 2.4 and 2.5, a reduced point defect concentration resulting from an increased formation energy upon tungsten doping implies the need for greater undercooling to engender the R→M_1 phase transition (as also illustrated by Figure 2.7). Indeed, one influence of tungsten doping appears to be to decrease the oxygen vacancy concentration, thereby increasing the hysteretic width. Furthermore, the F values in Table 2.2 suggest that introduction of an oxygen vacancy stabilizes the M_1 phase over the R-phase for undoped VO_2 but stabilizes the R-phase over the M_1 phase for W-doped VO_2, which further leads to an extended phase coexistence regime.

Figure 2.8 schematically illustrates the distinctive mechanisms of the structural

transformations in doped and undoped VO_2 determined based on the experimental data

and results of DFT calculations noted above. The left scheme shows the mechanism for

undoped VO_2 particles where both the $M_1{\rightarrow}R$ (white to red) and $R{\rightarrow}M_1$ (red to white)

transitions are nucleated at point defects (blue dots) in a symmetrical manner as

observed for VO_2 nanobeams,[27] and consistent with the symmetric kinetic hysteresis

observed in Figure 2.4A. The pronounced inverse modulation of the thermal hysteresis

width with particle volume for undoped VO_2 observed in Figure 2.7 further corroborates

the central role of point defects as nucleation sites. In contrast, the right scheme in

Figure 2.8 illustrates that upon the substitutional incorporation of W-dopants within the

VO_2 lattice, the $R{\rightarrow}M_1$ transition is still nucleated at point defects but the $M_1{\rightarrow}R$

transition is instead nucleated at newly introduced extended defects (grey), specifically

heterophasic interphases of M_1 and M_2 as directly observed in Figure 2.6 or at M_1/M_1

twin domains. The presence of these extended defects greatly facilitates the $M_1{\rightarrow}R$

transformation and almost entirely eliminates the kinetic hysteresis component measured

for this transformation. The phase boundaries and stabilization of the M_2 phase is

analogous to the behavior of clamped VO_2 beams and is thought to result from

anisotropic strain gradients induced upon W-doping of the monoclinic VO_2 lattice.[27,44] In
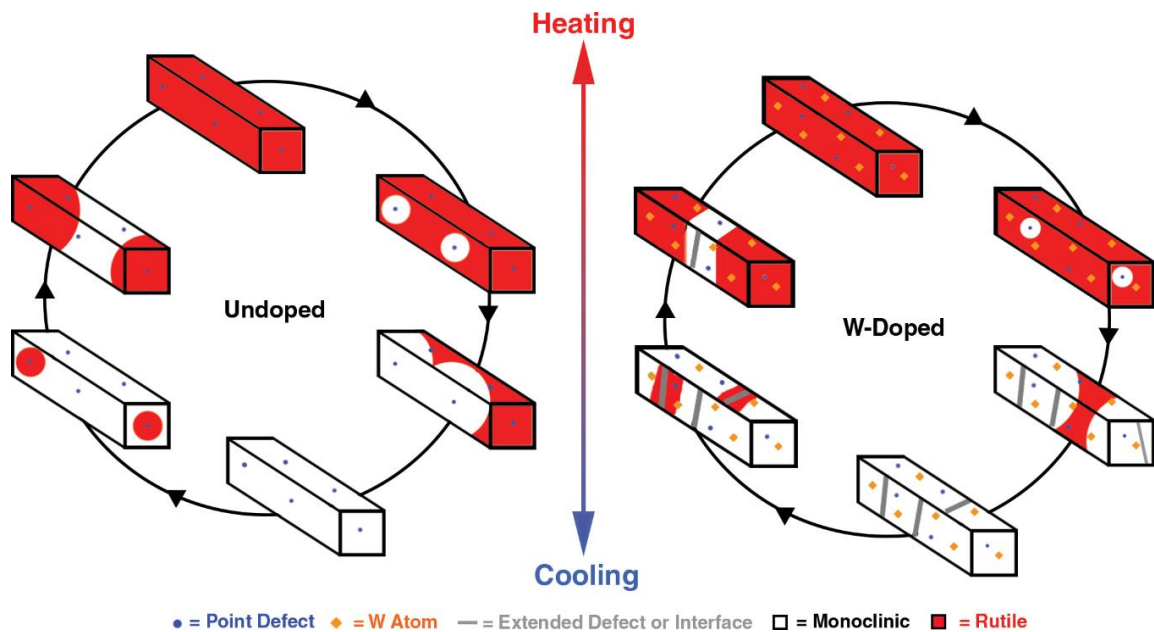
Figure 2.8. Schematic depiction of the mechanisms of $M_1 \rightarrow R$ and $R \rightarrow M_1$ transformations for undoped (left) and W-doped (right) VO_2

contrast, the formation of twins is symmetry forbidden in the R-phase and thus a continued kinetic hysteresis is observed for the $R \rightarrow M_1$ transformation. The incorporation of W-dopants further increases the energy of formation of an oxygen vacancy in the VO_2 lattice as per Table 2.2, and the resulting decrease in point defect density results in greater supercooling and a wider hysteresis. The distinct mechanisms for the $M_1 \rightarrow R$ and $R \rightarrow M_1$ transitions creates a pronounced asymmetry of the kinetic hysteresis as observed in Figures 2.4B and 2.5.

2.4. Conclusions

Tungsten-doped VO_2 presents a pronounced kinetic asymmetry during the metal—insulator phase transition that stems from the operation of disparate nucleation mechanisms for the heating $M_1 \rightarrow R$ (mediated at twin boundaries and extended phase

boundaries) and cooling R→M$_1$ (mediated by point defects) transitions. These effects can be explained by tungsten dopants inducing anisotropic strain within the system, thereby increasing the likelihood of extended defects and stabilizing the formation of nanoscale M$_2$ domains as observed for mechanically strained VO$_2$ systems. The ease of nucleating the transformation controls the apparent hysteresis at a given temperature ramp rate and tungsten concentration. Insight into this effect allows for better understanding of the underlying mechanisms of the hysteresis in doped VO$_2$ systems and suggests a means for rational modulation of thermal hysteresis widths as required for applications within memrsitive and memcapacitative elements.

2.5. Experimental

2.5.1. Synthesis

W-doped and undoped VO$_2$ nanostructures were synthesized hydrothermally based on the hydrothermal reduction of V$_2$O$_5$ powder (primarily micron-sized particles, Beantown Chemicals) using either anhydrous oxalic acid (Sigma-Aldrich), acetone (Sigma-Aldrich), or 2-propanol (Sigma-Aldrich) as the reducing agent, as reported in previous work.[43] Tungstic acid (H$_2$WO$_4$, Sigma Aldrich) was used as the dopant precursor. In a typical reaction for the preparation of W-doped VO$_2$, 300 mg V$_2$O$_5$, 450 mg of oxalic acid, and the appropriate amount of the dopant precursor were mixed with 15 mL of deionized water (ρ = 18.2 MΩ cm^{-1}, purified using a Barnstead International NANOpure Diamond system). Particle dimensions were varied by mixing 300 mg V$_2$O$_5$ with either 5 mL 2-propanol and 11 mL of deionized water or 9 mL of acetone and 7 mL of deionized water.[43,68] In each case, the mixtures were placed within 23 mL

polytetrafluoroethylene cups and heated within a high-pressure autoclave reactor for 72 h. A reaction temperature of 250 °C was used with oxalic acid as the reducing agent, whereas a reaction temperature of 210 °C was used with 2-propanol or acetone as the reducing agents. Upon completion of the hydrothermal reaction, the samples were recovered by vacuum filtration and washed with copious amounts of deionized water and acetone. Subsequently, samples were annealed under a flow of argon (150 mL·min^{-1}) at 550 °C for 3 h within a tube furnace in order to relieve strain. A 2-propanol reduced sample was also further processed to a smaller size though ball milling (SPEX Sampleprep 5100) under ambient conditions with beads of yttrium stabilized zirconia (Inframat Advanced Materials – 3.0mm).

In order to elucidate the influence of particle size on hysteresis, ultra-small VO_2 nanocrystals were synthesized based on adapting a previously reported procedure.[69,70] Briefly, amorphous VO_x was prepared by dissolving 0.5 g NH_4VO_3 in 15 mL deionized water at 100°C. After dissolution of the metavanadate precursor, 0.75 mL of 5% hydrazine (N_2H_4) was added dropwise and allowed to stir for 30 min while maintaining the reaction mixture at 100°C. After 30 min, the total volume was adjusted back to 15 mL and subject to bath sonication (Branson 5510) for 5 min to obtain a homogeneous dispersion. The amorphous dispersion of VO_2 was then transferred to a 23 mL polytetrafluoroethylene cup and heated within a sealed high-pressure autoclave reactor (Parr Instruments) at 250°C for 24 h. After cooling, the obtained nanocrystals were washed with water using three successive cycles of dispersion by ultrasonication and precipitation by centrifugation (8000 rpm, 10 min).

2.5.2. Characterization

Powder X-ray diffraction (XRD) patterns were acquired using a Bruker D8-Vario X-ray powder diffractometer equipped with a Cu Kα (λ = 1.5418Å) source and operated at 40 kV accelerating voltage and 40 mA current with a MTC oven attachment for heating experiments. Variable temperature measurements were acquired at 5°C intervals in the temperature range from 30 to 100°C.

Differential scanning calorimetry (DSC) analysis was performed using a TA instruments Q2000 instrument. The temperature was scanned from 0 to 100°C and back again to 0°C at ramp rates ranging from 0.1 to 20°C min^{-1}. Aluminum T-Zero pans were used for DSC experiments under a purge flow of Ar gas.

The size and morphology of the prepared materials were investigated using scanning electron microscopy (SEM) and transmission electron microscopy (TEM). SEM images of the nanocrystals were collected on a JEOL JSM-7500F instrument operated at an accelerating voltage of 5.0 kV. TEM images were acquired using a JEOL JEM-2010 instrument operated at a 200 kV accelerating voltage. Particle size distributions were deduced based on analysis of 100—200 individual particles using ImageJ software. High-angle annular dark field TEM (HAADF-TEM) imaging was performed using a probe-corrected JEOL JEM-ARM200CF instrument with a cold field-emission gun operated at a 200 kV bias. The convergence angle was 22 mrad, whereas the inner angle of the HAADF detector was 90 mrad. Modeling of diffraction data was performed using SingleCrystal software (CrystalMaker Software Ltd., Oxford, England, 2017); structural

information of VO$_2$ phases was obtained from Pearson's Crystal data (ASM International, Materials Park, Ohio, USA, 2013).

2.5.3. Density Functional Theory Modeling

Supercell total energies were calculated based on DFT as implemented in the Vienna *ab-initio* Simulation Package (VASP).[71] The generalized gradient approximation (GGA) under the Perdew-Burke-Ernzerhof (PBE) formalism was used to describe exchange correlation terms. Pseudopotentials were generated by the projector augmented wave (PAW) method and a cut-off energy of 533 eV for the plane wave basis was set. Structures were considered to be relaxed when the change in total energy between successive steps was reduced below 10^{-6} eV. Supercells of 96 atoms were created for undoped and W-doped VO$_2$ rutile and monoclinic M$_1$ structures. The formation energy of an oxygen vacancy in these structures was calculated with a vacancy concentration of 1:95 total atoms.

The formation energy F (per cell) is calculated as follows:

$$F = E_{cell} - \sum_i n_i E_i^0 \qquad\qquad 2.1$$

and ΔF for stabilization of an oxygen vacancy in VO$_2$:[72]

$$\Delta F = \left(E_{cell}^{Vac} - \sum_i n_i E_i^0\right) - \left(E_{cell} - \sum_j n_j E_j^0\right) \qquad\qquad 2.2$$

where E_{cell} is the bulk cell energy, E_i^0 is the energy of the ith atom reference state, and n_i is the cell count of the ith atom.

2.6. References

[1]   P. Monceau, *Adv. Phys.* **2012**, *61*, 325.

[2]   Z. Yang, C. Ko, S. Ramanathan, *Annu. Rev. Mater. Res.* **2011**, *41*, 337.

[3]   J. Wang, H. P. Li, R. Stevens, *J. Mater. Sci.* **1992**, *27*, 5397.

[4]   P. M. Marley, G. A. Horrocks, K. E. Pelcher, S. Banerjee, *Chem. Commun.* **2015**, *51*, 5181.

[5]   L. Whittaker, C. J. Patridge, S. Banerjee, *J. Phys. Chem. Lett.* **2011**, *2*, 745.

[6]   A. Navrotsky, *ChemPhysChem* **2011**, *12*, 2207.

[7]   V. L. Solozhenko, O. O. Kurakevych, P. S. Sokolov, A. N. Baranov, *J. Phys. Chem. A* **2011**, *115*, 4354.

[8]   J. Tang, F. Zhang, P. Zoogman, J. Fabbri, S.-W. Chan, Y. Zhu, L. E. Brus, M. L. Steigerwald, *Adv. Funct. Mater.* **2005**, *15*, 1595.

[9]   S. H. Guan, X. J. Zhang, Z. P. Liu, *J. Am. Chem. Soc.* **2015**, *137*, 8010.

[10]   J. Chevalier, L. Gremillard, A. V. Virkar, D. R. Clarke, *J. Am. Ceram. Soc.* **2009**, *92*, 1901.

[11]   J. Cui, Y. S. Chu, O. O. Famodu, Y. Furuya, J. Hattrick-Simpers, R. D. James, A. Ludwig, S. Thienhaus, M. Wuttig, Z. Zhang, I. Takeuchi, *Nat. Mater.* **2006**, *5*, 286.

[12]   G. M. Wolten, *J. Am. Ceram. Soc.* **1963**, *46*, 418.

[13]   B. M. Hudak, S. W. Depner, G. R. Waetzig, A. Talapatra, R. Arroyave, S. Banerjee, B. S. Guiton, *Nat. Commun.* **2017**, *8*, 15316.

[14]   Y. Song, X. Chen, V. Dabade, T. W. Shield, R. D. James, *Nature* **2013**, *502*, 85.

[15]   Y. V. Pershin, M. Di Ventra, *Adv. Phys. B* **2011**, *60*, 145.

[16]   D. B. Strukov, G. S. Snider, D. R. Stewart, R. S. Williams, *Nature* **2008**, *459*, 80.

[17]   M. D. Pickett, G. Medeiros-Ribeiro, R. S. Williams, *Nat. Mater.* **2012**, *12*, 114.

[18]   M. Imada, A. Fujimori, Y. Tokura, *Rev. Mod. Phys.* **1998**, *70*, 1039.

[19]   Y. Zhou, S. Ramanathan, *Crit. Rev. Solid State Mater. Sci.* **2013**, *38*, 286.

[20]   A. L. Pergament, G. B. Stefanovich, A. A. Velichko, *J. Sel. Top. Nano Electron. Comput.* **2013**, *1*, 24.

[21]   W. H. Brito, M. C. O. Aguiar, K. Haule, G. Kotliar, *Phys. Rev. Lett.* **2016**, *117*, 1.

[22]   D.-S. Yang, P. Baum, A. H. Zewail, *Struct. Dyn.* **2016**, *3*, 034304.

[23]   G. Stefanovich, A. Pergament, D. Stefanovich, *J. Phys. Condens. Matter* **2000**, *12*, 8837.

[24]   T. H. Yang, C. Jin, H. Zhou, R. J. Narayan, J. Narayan, *Appl. Phys. Lett.* **2010**, *97*, 1.

[25]   R. Lopez, L. C. Feldman, R. F. Haglund, *Phys. Rev. Lett.* **2004**, *93*, 20.

[26]   J. Wei, Z. Wang, W. Chen, D. H. Cobden, *Nat. Nanotechnol.* **2009**, *4*, 420.

[27]   W. Fan, J. Cao, J. Seidel, Y. Gu, J. W. Yim, C. Barrett, K. M. Yu, J. Ji, R. Ramesh, L. Q. Chen, J. Wu, *Phys. Rev. B - Condens. Matter Mater. Phys.* **2011**, *83*, 235102.

[28]   T. Driscoll, H.-T. Kim, B.-G. Chae, B.-J. Kim, Y.-W. Lee, N. M. Jokerst, S. Palit, D. R. Smith, M. Di Ventra, D. N. Basov, *Science.* **2009**, *325*, 1518.

[29]   S. Chen, J. Liu, L. Wang, H. Luo, Y. Gao, *J. Phys. Chem. C* **2014**, *118*, 18938.

[30]   K. Miyazaki, K. Shibuya, M. Suzuki, K. Sakai, J. Fujita, A. Sawa, *AIP Adv.* **2016**, *6*, 55012.

[31]   J. Galy, G. Miehe, *Solid State Sci.* **1999**, *1*, 433.

[32]   J. B. Goodenough, *J. Solid State Chem.* **1971**, *3*, 490.

[33]   N. F. Quackenbush, H. Paik, M. J. Wahila, S. Sallis, M. E. Holtz, X. Huang, A. Ganose, B. J. Morgan, D. O. Scanlon, Y. Gu, F. Xue, L. Q. Chen, G. E. Sterbinsky, C. Schlueter, T. L. Lee, J. C. Woicik, J. H. Guo, J. D. Brock, D. A. Muller, D. A. Arena, D. G. Schlom, L. F. J. Piper, *Phys. Rev. B* **2016**, *94*, 1.

[34]   C. J. Patridge, L. Whittaker, B. Ravel, S. Banerjee, *J. Phys. Chem. C* **2012**, *116*, 3728.

[35]   N. Wang, M. Duchamp, C. Xue, R. E. Dunin-Borkowski, G. Liu, Y. Long, *Adv. Mater. Interfaces* **2016**, *3*, 1.

[36]   J. Zhou, Y. Gao, X. Liu, Z. Chen, L. Dai, C. Cao, H. Luo, M. Kanahira, C. Sun, L. Yan, *Phys. Chem. Chem. Phys.* **2013**, *15*, 7505.

[37]   S. Lee, C. Cheng, H. Guo, K. Hippalgaonkar, K. Wang, J. Suh, K. Liu, J. Wu, *J. Am. Chem. Soc.* **2013**, *135*, 4850.

[38]   T. D. Manning, I. P. Parkin, C. Blackman, U. Qureshi, *J. Mater. Chem.* **2005**, *15*, 4560.

[39]   T. E. G. Alivio, D. G. Sellers, H. Asayesh-ardakani, E. J. Braham, G. A. Horrocks, K. E. Pelcher, R. Villareal, L. Zuin, J. Patrick, R. Arroyave, R. Shahbazian-yassar, S. Banerjee, *Chem. Mater.* **2017**, *29*, 5401.

[40]   Y. Filinchuk, N. A. Tumanov, V. Ban, H. Ji, J. Wei, M. W. Swift, A. H. Nevidomskyy, D. Natelson, *J. Am. Chem. Soc.* **2014**, *136*, 8100.

[41]   H. Yoon, M. Choi, T.-W. Lim, H. Kwon, K. Ihm, J. K. Kim, S.-Y. Choi, J. Son, *Nat. Mater.* **2016**, *15*, 1113.

[42] J. Wei, H. Ji, W. Guo, A. H. Nevidomskyy, D. Natelson, *Nat. Nanotechnol.* **2012**, *7*, 357.

[43] L. Whittaker, T.-L. Wu, C. J. Patridge, G. Sambandamurthy, S. Banerjee, *J. Mater. Chem.* **2011**, *21*, 5580.

[44] H. Asayesh-Ardakani, A. Nie, P. M. Marley, Y. Zhu, P. J. Phillips, S. Singh, F. Mashayek, G. Sambandamurthy, K. Bin Low, R. F. Klie, S. Banerjee, G. M. Odegard, R. Shahbazian-Yassar, *Nano Lett.* **2015**, *15*, 7179.

[45] C. Tang, P. Georgopoulos, M. E. Fine, J. B. Cohen, M. Nygren, G. S. Knapp, A. Aldred, *Phys. Rev. B* **1985**, *31*, 1000.

[46] H. Asayesh-Ardakani, W. Yao, A. Nie, P. M. Marley, E. Braham, R. F. Klie, S. Banerjee, R. Shahbazian-Yassar, *Appl. Phys. Lett.* **2017**, *110*, 53107.

[47] M. Netsianda, P. E. Ngoepe, C. R. A. Catlow, S. M. Woodley, *Chem. Mater.* **2008**, *20*, 1764.

[48] M. Marezio, D. B. McWhan, J. P. Remeika, P. D. Dernier, *Phys. Rev. B* **1972**, *5*, 2541.

[49] A. Zylbersztejn, N. F. Mott, *Phys. Rev. B* **1975**, *11*, 4383.

[50] A. Tselev, I. A. Luk'Yanchuk, I. N. Ivanov, J. D. Budai, J. Z. Tischler, E. Strelcov, A. Kolmakov, S. V. Kalinin, *Nano Lett.* **2010**, *10*, 4409.

[51] J. H. Park, J. M. Coy, T. S. Kasirga, C. Huang, Z. Fei, S. Hunter, D. H. Cobden, *Nature* **2013**, *500*, 431.

[52] A. Tselev, E. Strelcov, I. A. Luk'yanchuk, J. D. Budai, J. Z. Tischler, I. N. Ivanov, K. Jones, R. Proksch, S. V. Kalinin, A. Kolmakov, *Nano Lett.* **2010**, *10*, 2003.

[53]   A. Tselev, V. Meunier, E. Strelcov, W. A. Shelton, I. A. Luk, K. Jones, R. Proksch, A. Kolmakov, S. V Kalinin, *ACS Nano* **2010**, *4*, 4412.

[54]   G. Van Tendeloo, S. Amelinckx, *Acta Crystallogr. Sect. A* **1974**, *30*, 431.

[55]   J. M. Booth, P. S. Casey, *Phys. Rev. Lett.* **2009**, *103*, 1.

[56]   F. J. Morin, *Phys. Rev. Lett.* **1959**, *3*, 34.

[57]   A. V. Salker, K. Seshan, H. V. Keer, *Phys. Status Solidi* **1983**, *75*, K37.

[58]   J. D. Budai, J. Hong, M. E. Manley, E. D. Specht, C. W. Li, J. Z. Tischler, D. L. Abernathy, A. H. Said, B. M. Leu, L. A. Boatner, R. J. McQueeney, O. Delaire, *Nature* **2014**, *515*, 535.

[59]   T. L. Wu, L. Whittaker, S. Banerjee, G. Sambandamurthy, *Phys. Rev. B - Condens. Matter Mater. Phys.* **2011**, *83*, 2.

[60]   A. C. Jones, S. Berweger, J. Wei, D. Cobden, M. B. Raschke, *Nano Lett.* **2010**, *10*, 1574.

[61]   J. B. Hatch, L. Whittaker-Brooks, T.-L. Wu, G. Long, H. Zeng, G. Sambandamurthy, S. Banerjee, H. Luo, *Phys. Chem. Chem. Phys.* **2014**, *16*, 14183.

[62]   G. M. Dalpian, J. R. Chelikowsky, *Phys. Rev. Lett.* **2006**, *96*, 1.

[63]   S. C. Erwin, L. Zu, M. I. Haftel, A. L. Efros, T. a Kennedy, D. J. Norris, *Nature* **2005**, *436*, 91.

[64]   T. Waitz, K. Tsuchiya, T. Antretter, F. D. Fischer, *Mrs Bull.* **2009**, *34*, 814.

[65]   V. Eyert, *Phys. Rev. Lett.* **2011**, *107*, 2.

[66]   S. Mukherjee, N. F. Quackenbush, H. Paik, C. Schlueter, T. L. Lee, D. G. Schlom, L. F. J. Piper, W. C. Lee, *Phys. Rev. B* **2016**, *93*, 1.

[67]   N. F. Quackenbush, J. W. Tashman, J. A. Mundy, S. Sallis, H. Paik, R. Misra, J.

A. Moyer, J. H. Guo, D. A. Fischer, J. C. Woicik, D. A. Muller, D. G. Schlom, L. F. J.

Piper, *Nano Lett.* **2013**, *13*, 4857.

[68]   G. A. Horrocks, S. Singh, M. F. Likely, G. Sambandamurthy, S. Banerjee, *ACS*

Appl. Mater. Interfaces **2014**, *6,* 15726.

[69]   W. Li, S. Ji, K. Qian, P. Jin, *Ceram. Int.* **2015**, *41*, 5049.

[70]   J. Zhu, Y. Zhou, B. Wang, J. Zheng, S. Ji, H. Yao, H. Luo, P. Jin, *ACS Appl.*

Mater. Interfaces **2015**, *7*, 27796.

[71]   G. Kresse, J. Furthmüller, *Phys. Rev. B* **1996**, *54*, 11169.

[72]   C. Freysoldt, B. Grabowski, T. Hickel, J. Neugebauer, G. Kresse, A. Janotti, &

C. G. Van de Walle, *Rev. Mod. Phys.* **2014**, *86*, 253.

3. ATOMIC HOURGLASS AND THERMOMETER BASED ON DIFFUSION OF A MOBILE DOPANT IN VO$_2$*

3.1. Overview

Transformations between different atomic configurations of a material oftentimes bring about dramatic changes in functional properties as a result of the simultaneous alteration of both atomistic and electronic structure. Transformation barriers between polytypes can be tuned through compositional modification, generally in an immutable manner. Continuous, stimulus-driven modulation of phase stabilities remains a significant challenge. Utilizing the metal–insulator transition of VO$_2$, we exemplify that mobile dopants weakly coupled to the crystal lattice provide a means of imbuing a reversible and dynamical modulation of the phase transformation. Remarkably, we observe a time- and temperature-dependent evolution of the relative phase stabilities of the M$_1$ and R phases of VO$_2$ in an "hourglass" fashion through the relaxation of interstitial boron species, corresponding to a 50 °C modulation of the transition temperature achieved within the same compound. The material functions as both a chronometer and a thermometer and is "reset" by the phase transition. Materials possessing memory of thermal history hold promise for applications such as neuromorphic computing, atomic clocks, thermometry, and sensing.

3.2. Introduction

The presence of adjacent minima within free energy landscapes of periodic solids (along axes such as temperature, pressure, strain, or alloying) allows for reversible switching of properties as a result of the structural rearrangement of atoms. A structural transformation along such landscapes often brings about pronounced alterations of electronic structure and accompanying electronic, ferroelectric, optical, and magnetic properties; such modulations of functional properties have been utilized for diverse applications spanning the range from neuromorphic computing to thermochromic windows,[1–3] memory storage,[4] and transformation toughening.[5,6] Martensitic transitions, which are characterized by the reversible and diffusionless motion of atoms upon a spontaneous change in symmetry of the unit cell, are particularly facile and provide numerous examples wherein the hysteresis between forward and reverse transitions can be controlled through compositional modulation and strain.[7,8] Compositional modulation through doping or alloying generally changes the relative phase stabilities of adjacent energy wells and the barrier to the transformation between the wells within a thermodynamic energy landscape in an immutable manner, enabling the trapping of metastable phases under ambient conditions. Much less studied is the role of dopants that are diffusive in nature, that are weakly coupled to the lattice, and whose mobility thereby endows a dynamical aspect to the relative phase stabilities of the adjacent wells. In this article, we utilize a canonical metal–insulator transition material VO_2 to demonstrate a remarkable time-dependent evolution of the relative phase stabilities of insulating monoclinic (M_1) and metallic rutile (R) phases (in an "hourglass"

67

fashion) as a diffusive dopant species relaxes from a high-energy site wherein it is initially positioned upon a thermally induced phase transition. Such an in situ modulation of phase stabilities creates a readable thermal-history-dependent signal with the heating transition temperature serving as a characteristic readout; remarkably, this signature is completely reset upon returning to the low-temperature phase. We determine that the dynamically varying local structure of diffusive B dopant atoms provides a means of accessing this reconfigurable time- and thermal-history-dependent response that derives from intrinsic material properties.

The ability to realize a history-dependent nonlinear response is a key tenet for the creation of neuromorphic architectures, which have attracted considerable interest as a means of energy efficient computing.[1,9] Materials exhibiting pronounced metal–insulator transitions (MIT) underpinned by electron correlation can serve as active elements exhibiting such neuromorphic function provided their temporal response can be rendered programmable. VO_2 is characterized by a change of almost 5 orders of magnitude in its electronic transport properties upon the MIT at ∼67 °C. The extent of coupling of the electronic Mott transition with a structural M_1–R transition has been the subject of much discussion.[10–13] The introduction of dopant atoms alters the phase stabilities of insulating M_1 and metallic R phases and the heights of the barriers between them. In the case of tungsten as a substitutional dopant on the vanadium sublattice, the larger ionic radius of the dopant induces strongly anisotropic strain whereas its hexavalent character endows considerably increased metallicity resulting in an overall destabilization of the low-temperature M_1 phase with respect to the high-temperature

68

metallic phase.[10,14,15] Other dopants induce the stabilization of altogether different polymorphs; for instance, Cr- and Al-doping (or coherent epitaxial strain) stabilizes the M_2 phase,[16–18] interstitial hydrogen doping stabilizes orthorhombic variants,[19] and Ir doping stabilizes a 1D tunnel-structured phase.[20] The introduction of B atoms as interstitial dopants within VO_2 selectively stabilizes the R phase over the M_1 phase.[21,22] The distinctive location of boron dopants within interstitial sites causes the incorporated boron atoms to be weakly coupled to the anion and cation sublattice imbuing a mobility that results in a dynamical response in the monoclinic phase hitherto not observed for conventional static substitutional dopants. Such a mobility of the interstitially incorporated dopant atoms is shown to be coupled to the stability of the monoclinic phase and modulates the MIT in a resettable and history-dependent manner. In this manuscript, we detail the behavior of thermal memory effects in B-doped VO_2 and explore the inherent metastability of B dopants that brings about a kinetically controlled modulation of the MIT temperature across a 45 °C temperature range. Analysis of the B local coordination environment as well as the evaluation, via first-principles calculations, of B dopant site energies, charge, and diffusion pathways allows for the development of a mechanistic picture of the observed dynamical response.

3.3. Results and Discussion

3.3.1. Temporally Evolving Metal–Insulator Transition of B-Incorporated VO_2

VO_2 exhibits a hysteretic martensitic-type first-order transition from a monoclinic M_1 phase to a high-symmetry rutile (R) phase at 67 °C. The transition temperature has been shown to be modified through alloying with various dopants to

69

span the range from 23 to 96 °C for the heating transition and from −19 to 90 °C for the cooling transition.[9,22–24] Options for postsynthetically modulating the transition temperature are limited and include the irreversible creation of defects through high-energy irradiation or subjecting nanobeams to tensile strain, both of which have limited reversibility.[25,26] The dynamical and reversible modulation of the transition temperature of VO_2 has not thus far been achievable using a chemical vector.

Hydrothermally prepared VO_2 nanoparticles have been reacted with a molecular boron-containing precursor through rapid thermal annealing to obtain boron atoms lodged in interstitial sites[22] as described in the methods section and schematically illustrated in **Figure 3.1A**. Figure 3.1B depicts differential scanning calorimetry (DSC) plots measured for undoped VO_2, 1.8 atom % B-incorporated VO_2, and 5.2 atom % B-incorporated VO_2 denoting the critical temperatures (Tc) of the heating and cooling transitions based on the maxima of endothermic and exothermic heat flows accompanying the phase transitions, respectively. Incorporation of B atoms depresses the transition temperature by ∼10 °C/atom % B.[22] Figure 3.1C shows powder X-ray diffraction (XRD) patterns for the same samples acquired at 22 °C; the full diffraction patterns and scanning electron microscopy images of the samples are shown in Figure B.1. The (001) reflection of the monoclinic phase shifts slightly to lower 2θ values upon doping with 1.8 atom % B; Rietveld refinement of the diffraction patterns of B-incorporated VO_2 and VO_2 nanoparticles subjected to rapid thermal annealing without the molecular precursor (Table B.1, Figure B.2) demonstrates that B incorporation brings about a slight lattice expansion along the a and c axes resulting in a 0.4% increase

70

in volume. No evidence is observed for crystalline boron oxides or orthorhombic/M_2 phases of VO_2, which have been reported previously to be associated with interstitial hydrogen incorporation,[27] substitutional doping of trivalent cations,[28] and anisotropic strain.[29] Reflections derived from a minority V_8O_{15} impurity phase (JCPDS no. 71-0041) are observed[22] but do not contribute to the observed MIT behavior.[30]

Indeed, evidence for interstitial instead of substitutional incorporation is derived from (i) B K-edge XANES spectra that will be discussed below, which has been assigned with the help of XCH-XAS calculations delineating spectral fingerprints for trigonal and tetrahedral interstitial sites; (ii) high-angle annular dark-field scanning transmission electron microscopy images indicating no modulation of intensity on vanadium sites and concomitant electron energy loss spectra showing the presence of boron atoms within the VO_2 lattice;[22] (iii) the ability to eliminate B atoms from the lattice by annealing to a temperature of 500 °C, where no comparable removal of substitutional dopants has been observed (Figure B.3A shows that the transition temperature for both heating and cooling transitions are shifted to higher temperatures corresponding to extrusion of boron from the lattice; Figure B.3B shows that rapid thermal annealing temperatures of >960 °C results in complete elimination of interstitial B from the VO_2 lattice); and (iv) density functional theory calculations that will be presented below contrasting the stability of boron incorporation at interstitial and substitutional sites.
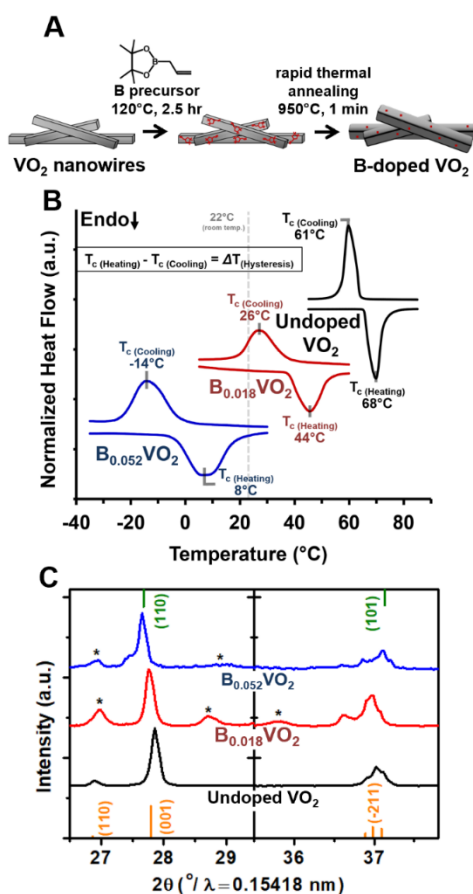
Figure 3.1. A) Schematic illustration of the diffusive doping of B atoms in VO_2 nanobeams. B) DSC traces measured for $B_{0.052}VO_2$, $B_{0.018}VO_2$, and undoped VO_2 acquired at a scan rate of 10°C/min and offset along the vertical axis for clarity. The critical transition temperatures (T_c) are designated as the peaks of the exothermic and endothermic heat flows for the heating and cooling scans, respectively. A monotonic depression of the phase transition is observed as a function of the B concentration. Additionally, the width of hysteresis $\Delta T_{(Hysteresis)}$ between the heating and cooling transitions is increased from 7°C for undoped VO_2 to 18 and 22°C for $B_{0.018}VO_2$ and $B_{0.052}VO_2$, respectively. C) Powder XRD patterns for $B_{0.052}VO_2$, $B_{0.018}VO_2$, and undoped VO_2 in the 2Θ range from 26—29.5° and 35.2—38.2°. Reflections corresponding to the M_1 phase of VO_2 are plotted along the bottom horizontal axis as per Joint Committee on Powder Diffraction Standards (JCPDS) #. 043-1051, whereas reflections corresponding to the R phase of VO_2 are plotted along the top horizontal as per JCPDS# 79-1655. Undoped and $B_{0.018}VO_2$ samples are indexed to the M_1 phase of VO_2, whereas the pattern for the $B_{0.052}VO_2$ sample is indexed to the R polymorph of VO_2. The incorporation of B atoms depresses the $M_1 \rightarrow R$ transition temperature by ca. 10°C/at.% B[22] such that the observed stabilization of R polymorph at room temperature for the $B_{0.052}VO_2$ sample is consistent with a depression of the critical transition temperature for 5.2 at.% B-doping. Reflections derived from a minority V_8O_{15} impurity phase (JCPDS no. 71-0041) are asterisked[22] but do not contribute to the observed MIT behavior.[30]

Figure 3.2 exhibits the results of differential scanning calorimetry (DSC) experiments performed on VO_2 nanoparticles incorporating 5.2 atom % boron that illustrate the dynamical behavior of this material. Figure 3.2A shows the overlaid thermal profiles of 49 experimental heat treatment cycles performed on the same sample systematically varying isothermal hold time (intervals of 15, 30, 45, 60, 90, 120, and 180 min) and the isothermal temperature (from −50 to 10 °C). Figure 3.2B plots the resulting T_c, the temperature corresponding to peak heat flow for the heating transition,[31] as a function of isothermal hold time and temperature. The measured transition temperatures reflect unique coordinates specific to the thermal and temporal history of the samples, which derive from the dynamical diffusion of B atoms in the M_1 phase as will be elucidated below. Panels C and D of Figure 3.2 show DSC data corresponding to slices of the 2D array in Figure 3.2A illustrating the effects of increasing isothermal temperature (held at a constant 90 min isothermal time) and isothermal time (held at a constant −10 °C isothermal temperature), respectively. All temperature changes throughout this series of experiments, cooling from the R phase to −60 °C, heating to the isothermal hold temperature, and heating from the isothermal hold temperature back to the R phase, were performed at a rate of 10 °C/min. Intriguingly, the corresponding cooling $R \rightarrow M_1$ transition was observed to show no analogous dynamical shift of the transition temperature (Figure B.4). Figure B.4 further shows that B incorporation distinctively alters the rate-dependence of the heating transition as

compared to undoped VO$_2$; the transition is shifted to a higher temperature at slower

rates, corresponding to increased residence time in the M$_1$ phase.
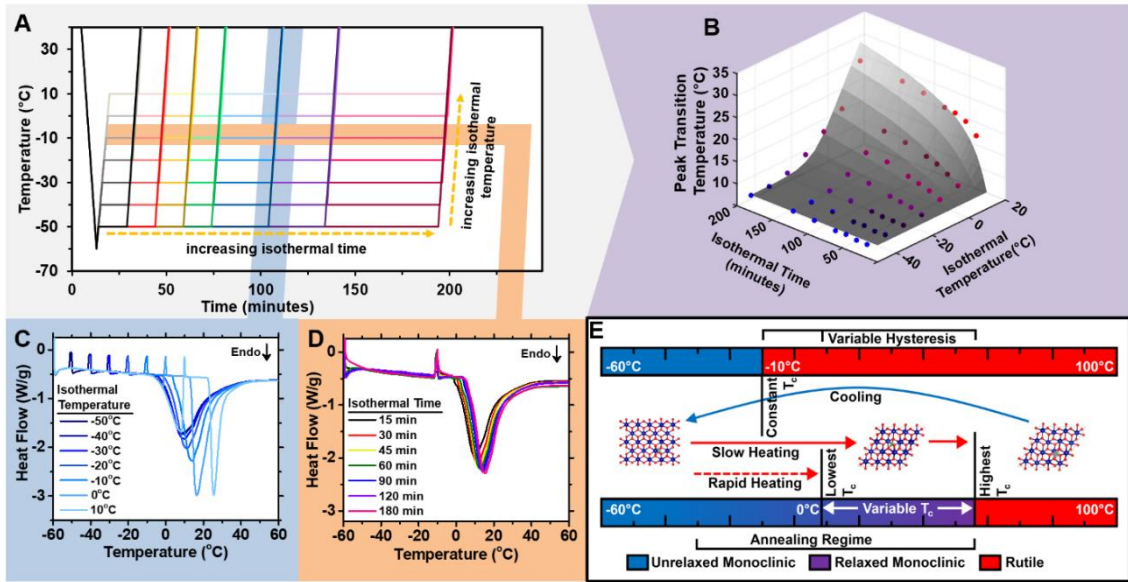
Figure 3.2. Time-dependent evolution of the metal–insulator transition of B-alloyed VO$_2$. (A) Thermal profiles of DSC experiments probing structural relaxation kinetics within the M$_1$ phase of B$_{0.052}$VO$_2$. The series of measurements shown in panels C and D are highlighted with blue vertical and orange horizontal bars, respectively. Vertical series such as the blue highlight correspond to a constant annealing time where the annealing temperature has been varied. Horizontal series such as the orange highlight correspond to a constant annealing temperature where the annealing time has been varied. (B) Three-dimensional representation of T_c as a function of isothermal annealing temperature and time for the thermal profiles shown in (A). An Arrhenius model is overlaid for comparison (see also Figure B.4F,G). (C) DSC traces corresponding to a series of measurements scanned at 10 °C/min from −60 to 100 °C with 90 min isothermal annealing intervals at temperatures ranging from −50 to 10 °C, highlighted as the vertical series in blue. (D) DSC traces of a series of measurements scanned at 10 °C/min from −60 to 100 °C with isothermal annealing at −10 °C for time intervals ranging from 15 to 180 min, highlighted as the horizontal series in orange. For panels A–D the cycles where the material was held at 0 and 10 °C contain a population of particles that have transitioned to the R phase before annealing. The observed shift is recorded for the fraction that had remained M$_1$ as seen in panel C as the lightest blue/furthest shifted peak. (E) Schematic illustrating the time-dependent variation of transformation temperature of VO$_2$ as derived from the DSC measurements.

Figure 3.2B illustrates a pronounced increase in the heating transition temperature as a function of both isothermal residence time and temperature. At the lowest isothermal temperature of −50 °C, a residence time of 180 min does not substantially alter the transition temperature as compared to not having an isothermal period. In contrast, holding the sample at 10 °C for an interval of 180 min shifts the transition temperature upward by greater than 15 °C. A window between −30 °C up to the transition temperature is observed wherein the time spent alters the transition temperature of the heating $M_1 \rightarrow R$ transition and is hereafter denoted as the "annealing" regime. Within this regime, the elapsed time is directly correlated with an increase of the $M_1 \rightarrow R$ transition temperature; the latter experimental observable provides a precise "clock"-like measure of the time elapsed after cooling. In other words, the results suggest that a thermally activated process is operational below the $M_1 \rightarrow R$ transition temperature, which governs the state of the system from which the subsequent $M_1 \rightarrow R$ phase transition is initiated. The quenched system appears to remain in a higher energy state (and can be transitioned back to the R phase at a lower temperature), whereas the relaxed or annealed system appears to be at lower energy and corresponding transitions to the R phase at a higher temperature.

The gray surface in Figure 3.2B denotes an Arrhenius kinetic fit indicating a thermally activated process. A single population model was built using a single activation energy (E_a) of 0.96 eV which provided the fewest residuals in a first order fit assuming a 1×10^{13} attempt frequency (A) based on the typical bond vibrational frequencies in oxides.[32] A single activation energy model proved a poor fit for the

experimental data (as sketched in Figure B.4F). A series of five activation energies

centered around 0.98 eV (in increments of ±0.04 eV) was examined to model a

continuum of activated processes contributing to the observed dynamic relaxation of this

material (Figure B.4G), corresponding to a simplified distributed activation energy

model.[32] This model assumes fractions of B-doped VO_2 in the sample such that the total

observed relaxation is a summation of their effects with φ_i representing the fraction of

the whole population with a given E_a such that the sum of i fractions equals 1. Assuming

five equal fractions such that $\varphi_i = 1/5$ of $E_a{}^i = [0.90, 0.94, 0.98, 1.02, 1.04]$ and an

attempt frequency (A) of 1×10^{13}, the relaxation of each fraction from metastable

$[B]_{ms}$ to relaxed $[B]_{rel}$ is calculated as a first-order rate:

$$[B]^i_{ms} = \phi_i [B]_{ms} \qquad \textbf{3.1}$$

$$\frac{\partial [B]^i_{rel}}{\partial t} = \frac{-\partial [B]^i_{ms}}{\partial t} = k^i [B]^i_{ms} \qquad \textbf{3.2}$$

$$k^i = A e \left(\frac{-Ea^i}{kT} \right) \qquad \textbf{3.3}$$

Such a model provides a substantially improved fit to the observed

phenomenology and is the function plotted as the gray surface in Figure 3.2B. The

improved fit is thought to arise from variations in dopant concentrations, inhomogeneous

strain, or defects, across ensembles of particles, which alter diffusion pathways of boron

atoms, altering the barrier height of this activated process around the central barrier of

0.98 eV as discussed in greater detail below. A phenomenological sketch of the dynamic

activated process is summarized in Figure 3.2E and illustrates the remarkable

resettability of the process. In every case, regardless of the thermal profile adopted to

probe the sample and irrespective of the extent of relaxation, the effect is reset when transitioning back from the R phase.

Additional experimentation contrasted the effects of heating and cooling rates on the transitions of two differently doped samples (Figure B.4) with that of undoped VO_2. Also, the effects of varying transition rates independently and the effects of additional cooling in the M_1 phase (Figure B.5) were examined. Figure B.4 shows a smaller rate dependence of the cooling transition for the B-incorporated samples as compared to undoped VO_2 suggesting easier nucleation of the M_1 phase in the doped samples, which is ascribed to the presence of more potent nucleation sites.[10,33] The heating transition shifts to higher temperature with slower rates which is concordant with the conclusion from Figure 3.2 that the thermal history in the M_1 phase enables modulation of the M_1 to R transition temperature as a function of time and temperature. The extent of cooling was found to have negligible effect. In summary, the data show (1) that applying sufficient thermal energy to the system while maintaining in the M_1 phase relaxes the system from a quenched to a relaxed state and (2) that the extent of transformation between the unrelaxed (quenched) and relaxed states follows an Arrhenius exponential dependence on the annealing temperature. Both observations denote the operation of a thermally activated process for B-doped VO_2 in the M_1 phase that does not have parallels in undoped VO_2.

The *in situ* DSC annealing experiments plotted in Figure 3.2 provide insight into the dynamics of the relaxation process on relatively short time scales. In an attempt to explore the maximal limit of the relaxed state, a more gradual thermal ramp spanning the

course of 7 days has been performed using a programmable water bath. The utilization of a slow ramp rate allows for the annealing temperature to slowly increase as the $M_1 \rightarrow$ R transition increases (due to the relaxation process) allowing for the highest annealing temperature possible. The temperature has been increased following the sequence plotted in Figure 3.3A for two samples to access intermediate and fully relaxed states. The upper portion of Figure 3.3A displays the first cycle of the DSC trace following removal from the water bath. The black curve represents the second cycle where the $B_{0.052}VO_2$ sample once again reflects the 8.5 °C T_c of the quenched state indicating that the sample has been reset after transitioning from $M_1 \rightarrow$ R. The DSC trace of the first relaxation experiment (labeled "intermediate") has been subjected to a stepwise decrease in ramp rate, shown in blue, and exhibits two endothermic features, one sharp feature at 39.3 °C and another smaller and broader transition at 56.3 °C, representing two different populations within the sample. The DSC trace of a second water-bath-aided relaxation experiment (labeled "relaxed") has been subjected to a still slower exponential decrease in ramp rate, shown in red, and exhibits a primary endothermic transition at 53.2 °C and a smaller shoulder at 55.8 °C. All subsequent water bath/DSC relaxation experiments for this sample exhibit transitions at ~56 °C (or lower) indicating that this value corresponds to a quasi-equilibrium limit for this B-doped VO_2 sample. Figure 3.3A illustrates that the magnitude of the T_c shift spans a remarkable 45 °C from a quenched sample (transitioning at 8.5 °C) to a fully relaxed state (transitioning at 53.2 °C). The $M_1 \rightarrow$ R transformation peak is further greatly sharpened upon relaxation suggestive of a convergence or funneling of the population distributions within this sample to a quasi-

78

equilibrium state. Figure B.6A shows analogous data for $B_{0.018}VO_2$, which has been simply allowed to relax at room temperature for 40 and 323 days, evolving from a T_c of 44.1 °C for the quenched sample to an intermediate state of 53.5 °C after 40 days and a T_c of 58.1 °C corresponding to the fully relaxed state after 323 days. Notably, the relaxation process does not correspond to the expulsion of B from the lattice. The
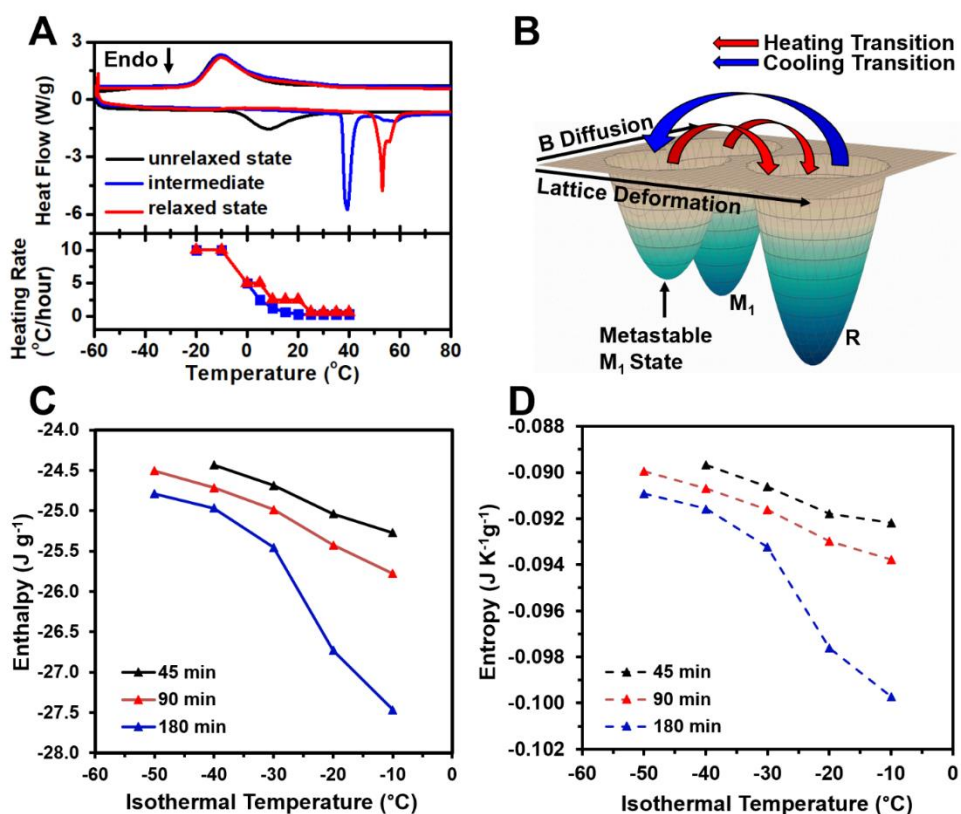
Figure 3.3. Evidencing a thermally activated process below the phase transition. (A) DSC traces of $B_{0.052}VO_2$ immediately upon cooling (quenched or "unrelaxed" state) and for the same sample upon relaxation from −20 °C to 40 °C within an external water bath at different temperature ramp rates (corresponding rates are shown in the lower plot) yielding intermediate and fully relaxed structures. (B) Illustration of energy landscape of the MIT transition as a function of temperature of the system and diffusion of B atoms between interstitial sites. (C, D) Evolution of ΔH and ΔS, respectively, as a function of isothermal temperature for isothermal times of 45, 90, and 180 min, as outlined in Figure 3.2A for the $B_{0.052}VO_2$ sample.

79

observed behavior is completely reversible upon further thermal cycling as demonstrated in Figure B.6B, which shows that the cycle directly after transitioning from a relaxed state mirrors the scan taken before relaxation occurred.

In terms of energy landscapes of structural transformations, the data (Figure B.6B) suggest that following the R $\rightarrow$ M$_1$ phase transition (akin to resetting of the "hourglass"), the M$_1$ lattice is positioned in a higher-energy metastable state that is only slightly lower in energy as compared to the R state and can thereby be readily transitioned back to the latter state at low temperatures. However, given sufficient time and thermal energy, the metastable state can relax through a thermally activated process to the lowest-energy quasi-equilibrium state of the M$_1$ phase. This is substantially lower in energy compared to the metastable state and thereby transitions at a higher temperature (Figure 3.3B). According to this hypothesis, the phase transformation temperature indicates the extent of relaxation from the quenched metastable to the relaxed quasi-equilibrium structure (akin to time-variant flow within an hourglass) and, as such, reflects the thermal history and elapsed time since the last "reset".

In order to further examine the thermodynamics of the phase transformation and better understand the dynamical modulation of the transition temperature upon boron incorporation, we have evaluated the latent heat (M) of the M$_1$ $\rightarrow$ R transition with respect to enthalpic (H) and entropic (S) contributions. Latent heat (M) has been calculated by integration of the exothermic DSC trace for a series of isothermal annealing experiments from the combinations of isothermal time and temperature variations depicted in Figure 3.2A. Around a first-order phase transition, one can express

the Gibbs free energy of transformation as $\Delta G = \Delta H - T\Delta S$. At the thermodynamic

transition temperature, T_c, the Gibbs free energies of the M1 and R phases are equal and

it follows that $\Delta H = T_c\Delta S$. Using this relationship and assuming the temperature

independence of the latent heat and the entropy of the transformation, one can estimate

the latter, provided we have a good estimate for the thermodynamic transition

temperature, T_c. Because of hysteresis, this quantity is unobservable but it can be

estimated as bounded by the measured transformation temperatures during heating and

cooling. Estimating T_c at the midpoint of the transformation range, we have estimated

ΔS. Panels C and D of Figure 3.3 show ΔH (A) and ΔS (B) as a function of isothermal

temperature for annealing times of 45, 90, and 180 min. A correlated change in both

entropy and enthalpy is observed when the metastable quenched state is annealed to the

relaxed state. The correlation of entropy and enthalpy shows that the change in the

thermodynamic stability of the M_1 and R phases, as illustrated in Figure 3.3B, is driven

by both a change in the relative phase enthalpy and electronic entropy (doping changes

not just the lattice enthalpy but also conduction entropy differential). This behavior is

consistently observed across all of the samples.

   The presence of multiple transformation peaks in the intermediate relaxed state

(Figure 3.3A) suggests a hierarchy of metastable states within the landscape. The broad

range of transition temperatures in the quenched sample (Figure 3.3A) suggests that

immediately following the R $\rightarrow$ M_1 transition, the VO$_2$ lattice relaxes into an array of

shallow-energy metastable states such that a relatively broad distribution of thermal

energies can bring about a transformation back to the R phase (but there is only a

relatively small differential separating the metastable M_1 states and the R state). Annealing at temperatures below the T_c allows the lattice to overcome the activation energy barrier associated with transitioning to quasi-equilibrium states; multiple metastable states relax into a narrow distribution of quasi-equilibrium states, thereby narrowing the observed endotherm for the $M_1 \to R$ transition from such states (Figure 3.3A). Nucleation to the R phase from these lower-energy relaxed states requires overcoming a greater energy differential, which is manifested in higher transition temperatures. Beyond the "hourglass" idea of relaxation into the quasi-equilibrium state, an important finding from the perspective of functional applications is the ability to tune the heating transition (and therefore hysteresis) for the same exact sample across a range of 45 °C adjacent to room temperature simply based on thermal history without any alteration of composition.

3.3.2. Unraveling the Atomistic Origins of the Hourglass

We now turn our attention to delineating the atomistic origins of this dynamically evolving low-temperature transformation, which constitutes the second axis in Figure 3.3B. Since such a phenomenon has not been observed in undoped or other previously reported strained or substitutionally doped VO_2 systems,[10,13,14,20] it is reasonable to infer that the B dopant plays a distinctive role in the dynamics of the $M_1 \to$ R transition. It is worth noting that unlike the vast majority of dopants examined for VO_2, B is able to diffuse across the VO_2 lattice owing to its small atomic radius (0.88 Å for four-coordinate B atoms)[34] and high diffusivity.[21,22] One possible origin of differences between the quenched and relaxed state is a change in the strain profile

across the system as a result of B diffusion.[10,14] However, powder XRD measurements acquired at −163 °C for relaxed and quenched states of the $B_{0.052}VO_2$ sample are shown in Figure B.6C and are superimposable with no discernible shifts that would indicate a transition dominated by alleviation of strain effects (thermal relaxation profiles used are shown in Figure B.6D,E).

Given the absence of significant changes in the average structure of the VO_2 lattice and in light of the relatively long relaxation time scales between metastable and quenched states, the specific sites occupied by B atoms warrant further attention and have been evaluated with the help of density functional theory (DFT) calculations at the generalized gradient approximation (GGA) + Hubbard U theory level. While DFT is severely constrained in its treatment of electron correlated materials owing to bandgap and delocalization errors, the large supercells required to model the low dopant concentrations render the materials here intractable by dynamical mean field theory and many body GW approaches.[11,35,36] We have converged on a U parameter ($U = 3.4$ eV) that captures the electronic structure of the two polymorphs (Figure B.7A and B.7B). The use of a large unit cell and a U parameter that accounts for electron correlation enables us to use the DFT calculations to guide spectral interpretation and to develop a physically intuitive albeit inevitably reductionist (in the absence of accurate determination of energetics) model of the phenomena under consideration.

Within their respective unit cells, six M_1 and three R unique interstitial sites have been identified by applying symmetry operations (defined by the respective space groups) on the 68 geometrically determined sites located using the AFLOW software

package.[37] The formation energies (E_f) of each unique interstitial site has been calculated using DFT such that E_f is defined as:

$$E_f = E(BVO_2) - E(VO_2) - E(B) \qquad\qquad \textbf{3.4}$$

where $E(BVO_2)$ is the total energy of a VO_2 supercell containing one B atom ($BV_{32}O_{64}$, corresponding to 3.1 atom % B incorporation in VO_2), $E(VO_2)$ is the energy of an undoped VO_2 supercell, and $E(B)$ is the energy of a single B atom based on a 36 atom unit cell (space group $R\bar{3}m$). This supercell size is in the range of experimentally observed B concentrations while still being computationally tractable in DFT+U calculations. Coordinates and E_f values for each interstitial location within the M_1 and R unit cell are listed in Table B.2. Upon transition from a rutile state, the doped supercell adopts a metastable distortion around the boron atom that does not occur when substituting boron into a monoclinic M_1 lattice as a starting point. To simulate the generation of possible metastable states caused by the boron defect across the R → M_1 phase transition, a rutile-like configuration was used as a starting point for the relaxation. This structure was generated by shifting the vanadium atoms of a monoclinic supercell by linear interpolation toward the R structure, which increases uniform spacing along the c-axis and reduces twisting of the vanadium pairs. From this starting configuration, the ions were relaxed back to a monoclinic configuration resulting in the metastable M_1 configuration. This metastable state has a different lowest energy configuration for the boron position than is found in the relaxed monoclinic M_1 phase or the R phase (Video S1 illustrates the distortion of this quenched metastable state in
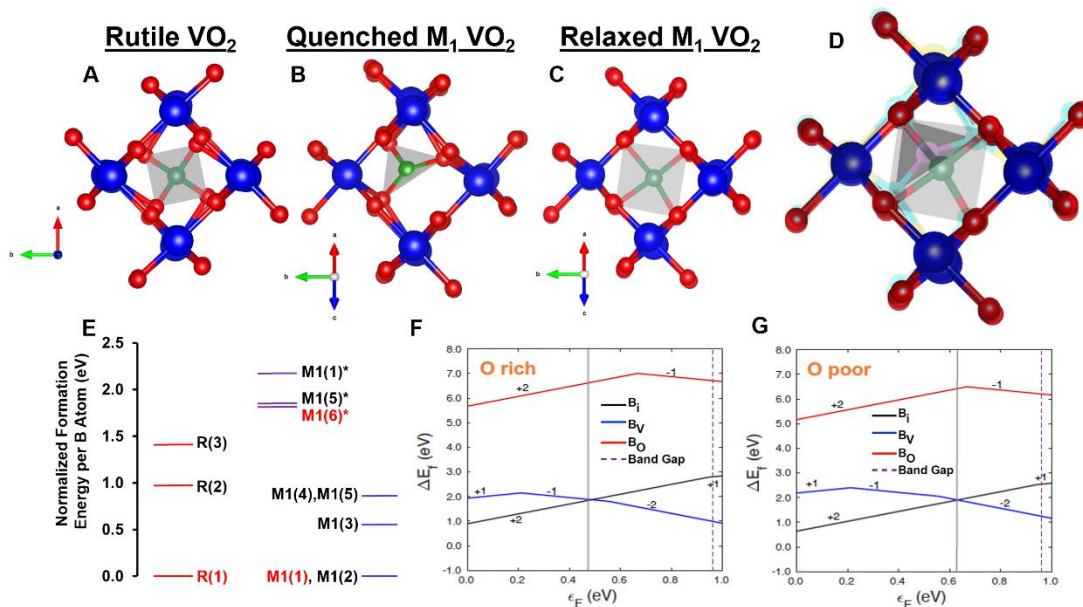
Figure 3.4. Energetics of boron interstitial sites in VO_2 and delineation of spectroscopic signatures. (A–C) DFT calculated coordination environments for B-doped VO_2, illustrating the most thermodynamically favorable interstitial sites for B incorporation for R (A, R(1)), quenched M_1 (B, M1(6)), and relaxed M_1 (C, M1(1)). Vanadium atoms are depicted as blue spheres, oxygen atoms as red spheres, and B atoms as green spheres. Lattice parameters for the doped M_1 structure with different concentrations of boron can be found in Table B.2. Full calculated supercells are shown in Figure B.8. (D) Overlay of quenched (inverted) and relaxed (blue/red/green) states to illustrate distortion (see also Video S1). (E) Normalized formation energies of B incorporation into different interstitial location within the R (red), metastable M_1 (violet), and relaxed M_1 (blue) supercells. Table B.2 catalogs the specific sites and their energetics. Panels F and G display the formation energies of charged defects for oxygen rich and oxygen poor conditions, respectively. The energies were calculated for substitutional boron defects at the oxygen sites (B_o), substitutional boron defects at the vanadium sites (B_v), and interstitial boron defects (B_i). For both oxygen-rich and oxygen-poor environments, the most stable defect at the calculated Fermi level (Figure B.7) of $\epsilon_F = 0.48$ and 0.62 is a 2+ interstitial boron defect B_i.

comparison to the monoclinic M1 phase). Figure 3.4A–C depict the lowest energy

interstitial sites for B atoms in the R phase, metastable M_1 phase, and relaxed M_1 phase,

respectively. Figure 3.4E shows normalized E_f values for the interstitial locations of B

sites in the R and metastable M_1, and M_1 supercells where M1(1) and M1(1)* as well as

M1(5) and M1(5)* are the symmetrically equivalent sites with the asterisk denoting the

metastable M_1 distortion. All stable sites have a tetrahedral coordination with

neighboring oxygen atoms except the trigonally coordinated M1(6)*, which is the lowest

energy boron position of the distorted metastable M_1 state shown in Figure 3.4C. The

three lowest energy sites highlighted in red in Figure 3.4E are posited to correspond to

the path traversed by boron atoms from the transition from rutile to unrelaxed

monoclinic to relaxed monoclinic. Notably, a small thermal population of boron atoms

may occupy higher energy sites, but given the relative energetics, the most stable sites

are expected to be strongly favored.

To better understand the nature of the interstitial boron atoms, the formation

energies have been evaluated for different charged states of boron and contrasted to the

stability of substitutional defects on the cation and anion sublattice. Calculation

methodologies are detailed in the methods section. Panels F and G of Figure 3.4 show

the defect diagrams of boron-associated interstitial and substitutional defects under O-

rich and O-poor conditions, respectively. To determine the equilibrium Fermi level at the

synthesis temperature, the formation energy of native defects has been calculated

assuming that the native point defects play a dominant role (Figure B.7C and B.7D). The

equilibrium Fermi level under O-rich and O-poor conditions is pinned in the range 0.48

and 0.62 eV, respectively, at the synthesis temperature. In both regimes, the most stable

defect is a boron interstitial (B_i) with a 2+ state. Moreover, a substitutional boron on the

vanadium site (B_V) may be occupied as a minority defect type. Density of states plots for

the monoclinic and rutile phases are shown in Figure B.7A and B.7B, confirming that the calculations capture the insulating nature of the monoclinic phase and the metallic nature of the rutile phase.

We note in Figure B.7C and B.7D that (+1/–1) transition levels of B_V are located ~0.2 eV above the valence band maximum, which is potentially indicative of negative U behavior. A similar behavior is observed for substitutional boron atoms in lattice oxygen sites (B_O). As such, further analysis is warranted to determine the origins of this unusual form. Conventional negative U behavior is often associated with localized charges created around defects and the significant local relaxation of the lattice in proximity of the defect. In our case, we find neither localized charge states nor large lattice relaxations near the B atom. Figure B.7E and B.7F plots the charge density of the top valence band states for various charged B_V defects (+2, +1, 0, −1, and −2). The valence electrons are not localized around the boron defect but are instead seen to be delocalized across the lattice, as expected in the case of shallow defects. Indeed, this is consistent with the orbital-resolved density of states (DOS) plot in Figure B.7G–J, which reveals that the electronic states associated with the B atom are localized deep within the valence band and are thus unlikely to contribute to the valence/conduction states near the Fermi level. Hence, the charged defects do not have a charged state localized on the defect atom as often observed in the case of deep defects of large bandgap insulators. In light of the absence of localized electronic states on the B atom, no strong B-related lattice relaxation is expected. Hence, the "negative U" like behavior observed in the defect formation energy diagram is not a result of Anderson's lattice relaxation. In other

87

words, although DFT+U captures the essentials of the band gap of the M1 and R phases

of VO_2, it is still challenging to predict the total energy of such strongly correlated

system accurately, which is beyond the scope of this work. The large size of the unit cell

renders this system intractable to more accurate dynamical mean field theory

approaches.

Experimental evidence for alteration of the B local structure during

transformation from the quenched to relaxed state is derived from B K-edge X-ray

absorption near-edge structure (XANES) spectroscopy measurements. XANES involves

the excitation of core-level electrons to partially occupied and/or unoccupied states and

thus serves as a sensitive element-specific probe of electronic structure.[38,39] Figure 3.5B

plots B K-edge XANES spectra, corresponding to excitation of B 1s electrons to B 2p

hybrid states, acquired at room temperature for quenched M1 $B_{0.004}VO_2$ (red line),

relaxed M1 $B_{0.052}VO_2$ (black line), and R $B_{0.052}VO_2$ (blue line). The low B concentration

of the $B_{0.004}VO_2$ sample is imperative to obtain a quenched sample that is still in the

M_1 phase, since the R $\rightarrow$ M_1 transition for $B_{0.052}VO_2$ is below room temperature

(Figure 3.1B). The low concentration required to stabilize quenched M1 provided far

less signal intensity but delineates stark spectral differences from the unrelaxed sample.

Spectral signatures in B K-edge XANES spectra can be assigned to specific bonding

modes and local coordination environments (a) based on comparison to data acquired for

known periodic solids with varying coordination and local symmetry of B sites and (b)

first-principles excited state core hole X-ray absorption spectroscopy (XCH-XAS)

calculations.[22,39–45] A list of B standards and the corresponding spectral signatures,

assignments, and references used in this study are compiled in Table B.3. Trigonally

coordinated B atoms bonded to oxygen atoms are characterized by absorption features at

194 and 203 eV, corresponding to 1s → π* and 1s → σ* transitions, respectively, to sp^2-

hybrid B–O final states. Tetrahedrally coordinated B is defined by an absorption feature

at 198 eV, which corresponds to a 1s → σ* transition populating sp^3-hybrid B–O final

states. Also associated with tetrahedrally coordinated B is a feature at 200 eV, which is

thought to be a multiple-scattering resonance.[40] When the sample is in the R phase

state, the XANES spectrum shows features associated with both trigonal and tetrahedral

B–O coordination geometries. However, the spectra measured for relaxed M1 and

quenched M1 samples show significant differences. Absorption features in the B K-edge

spectrum acquired for relaxed M1 $B_{0.052}VO_2$ are primarily associated with tetrahedral

coordination (197–200 eV), with only a small absorption at 194 eV associated with

trigonal coordination. In contrast, for the quenched M1 $B_{0.004}VO_2$ sample the opposite is

true; absorption features characteristic of tetrahedral coordination are absent, and the

predominant feature observed is the 1s → π* transition at 194 eV associated with

trigonal coordination. The corresponding 203 eV 1s → σ* transitions are below the

detection limit given the low B concentration in the sample and are further confounded

by multiple scattering resonances that give rise to the baseline, which are not captured in

the DFT simulations. The stark change in local electronic structure and coordination

between the quenched and relaxed M1 samples indicates a change is coordination

geometry from trigonal to tetrahedral geometry during the relaxation, consistent with the
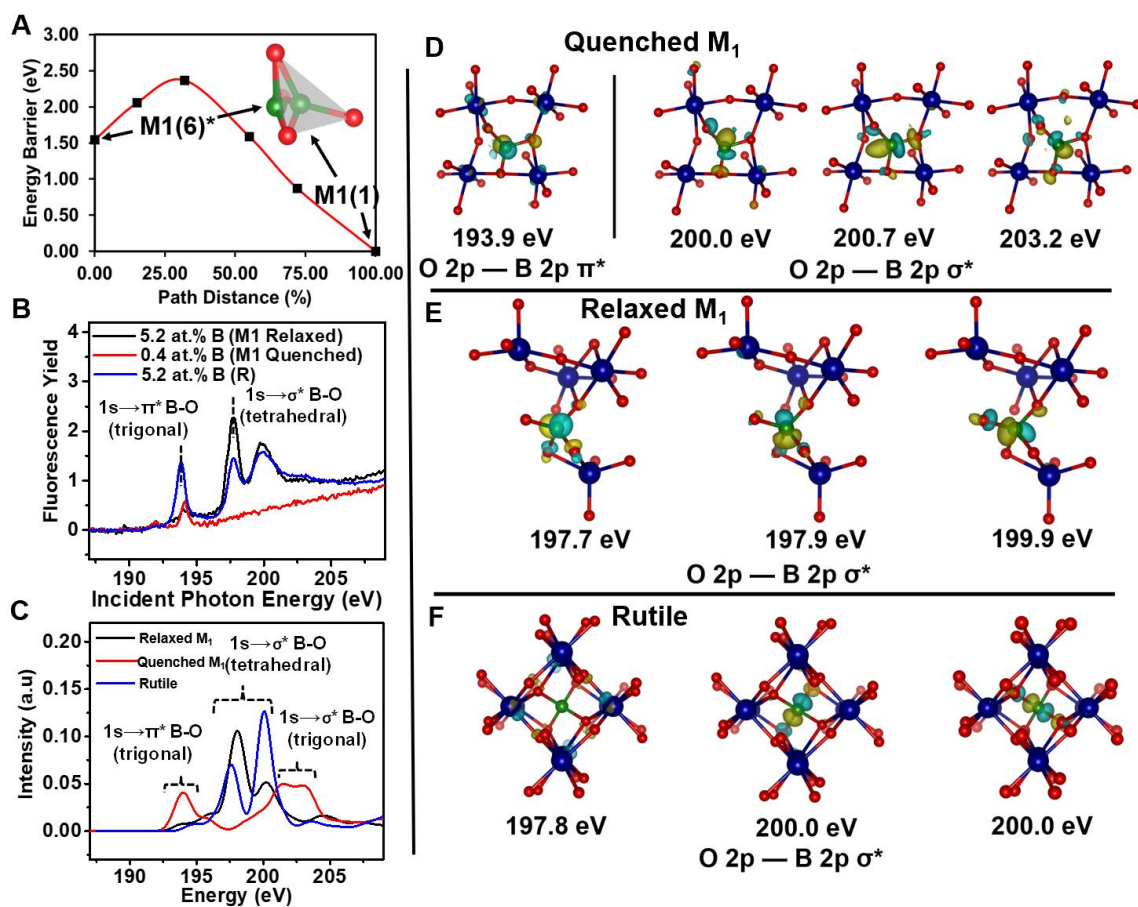
Figure 3.5. Boron diffusion pathways and energetics of diffusion. (A) Energy profile of the minimum energy pathway between the metastable trigonal M1(6)* site and the lowest-energy tetrahedral interstitial site M1(1) as calculated using NEB. Red spheres represent oxygen atoms; green spheres represent B atoms. (B) B K-edge XANES spectra of B-doped VO_2 samples measured at room temperature. The relaxed M_1 $B_{0.052}VO_2$ sample was relaxed *in situ* as described in Figure B.9E,F, and the corresponding DSC scan is shown in Figure B.9G. The quenched M_1 $B_{0.004}VO_2$ and R $B_{0.052}VO_2$ samples were heated to 100 °C and rapidly quenched to 0 °C and brought to room temperature immediately prior to the measurement. (C) Calculated B K-edge XANES spectra of B-doped VO_2. Calculated spectra correspond to a low energy relaxed tetrahedral site and an analogous metastable trigonal site. Final state assignments of the spectral features are assigned based on the symmetries of the states observed in the isosurface plots shown in panels D–F. Features are labeled with their character as assigned from isosurface plots of the final states. Isosurfaces are furthermore labeled with the energy of the transition feature.

most stable B interstitial geometries in metastable M_1 and relaxed M_1 polymorphs

inferred from the DFT+U calculations in Figure 3.4.

The change in local boron coordination environment is more directly corroborated by modeling the B K-edge XANES spectra using DFT for different B interstitial sites. Figure 3.5C shows the B K-edge spectrum calculated using the XAS-XCH[44] approach. The lowest energy tetrahedral sites in the R and M_1 phases as well as an analogous metastable trigonal site to represent the quenched M_1 phase have been calculated. This method provides an orbital-specific description of the origin of the XANES features. The simulated spectra show good agreement with the experimental spectra (with the exception of rutile polymorph, wherein multiple coordination geometries are found to coexist in the experimental spectrum). Observed transitions in the simulated XANES spectra correspond to the final states depicted in the isosurfaces of Figure 3.5D–F. Chemically meaningful assignments of the spectral features can be obtained by visualizing these isosurfaces and analyzing their orbital character. The absorption features between 197 and 200 eV for relaxed M_1 and R structures are assigned to the excitation of a core B 1s electron to a σ* state corresponding to hybridization between B 2p and O 2p states. An analogous transition for the quenched M_1 structure with trigonal coordination of B atoms is observed between 200 and 205 eV. The absorption feature for the quenched M_1 at 193.9 eV is assigned to the excitation of a core B 1s electron to a B 2p–O 2p hybrid π* state. The B 1s → π* transition is observed for approximately trigonal planar geometries and is a distinctive spectral signature of interstitial sites occupied by B atoms in quenched M_1 phase. The isosurface assignments are in excellent agreement with the assignments based on B standards (Table B.3).

Additional simulated XANES spectra for substitutionally doped B in O and V sites

within the M_1 structure are shown along with the associated isosurface assignments

in Figure B.9. The simulated spectra for B substitutionally doped in vanadium and

oxygen sites show substantial differences in terms of the spectral shapes and manifolds

from the experimental results as compared to the interstitial simulations. When

considered with the lower stability of these defects shown in Figure 3.4F,G and in light

of the experimental results summarized above, including the extrusion of B atoms upon

annealing above 500 °C (Figure B.3), the stabilization of interstitial boron dopants

appears to be more favored as compared to substitutional boron incorporation on the

cation or anion sublattice. Taken together, the experimental XANES spectra and XCH-

XAS simulations provide definitive experimental evidence for the diffusion of B atoms

from trigonal planar to tetrahedral local coordination environments and establish a

distinctive spectral signature of B atoms trapped in a metastable site.

The nudged elastic band (NEB) method has been used to examine potential

diffusion pathways and energy barriers for B atoms within M_1 VO_2.[46,47] The initial and

final interstitial B sites have been selected as the lowest energy boron position in the

metastable quenched state upon transformation from R $\rightarrow$ M_1 transitioning to the lowest

energy B site in the undistorted relaxed M_1 state. The XANES spectra of the quenched

VO_2 sample suggest an initially trigonal B coordination environment immediately

following the R $\rightarrow$ M_1 transition. Our initial starting point is the trigonal M1(6)* as the

most stable state in the quenched distorted M_1 state and while the final state is selected

as tetrahedral M1(1), the lowest-energy equilibrium site; these selections are fully

92

consistent with the experimental XANES data and its assignments (Figure 3.5C–F).

While many possible diffusion pathways exist for B atoms positioned in some of the

higher energy sites shown in Figure 3.4E, we have plotted the pathway of the M1(6)*

state to the M1(1) state in Figure 3.5A for a cell with a 2+ global charge (pathways for

other charges are shown in Figure B.9A) as the most likely illustrative pathway

connecting the lowest lattice energy configurations. The energy barrier for diffusion

between the sites is ~0.9 eV, which is consistent with barriers deduced from the

Arrhenius kinetic modeling of the experimental data shown in Figure 3.2B and Figure

B.4G. The minimal alteration of the energy barrier for different global charges in Figure

B.9A is consistent with the delocalization of charges evidenced in Figure B.7 and the

absence of charge localization around the boron atom.

The cooling transition from $R \rightarrow M_1$ may bring B atoms into several metastable

states with the M1(6)* and M1(5)* close in energy, contributing to the broadness of the

$M_1 \rightarrow R$ transition from the incipient quenched state. The $M_1 \rightarrow R$ transformation from

B situated within the most energetically preferred site requires considerably greater

energy given its relative stability with respect to the initial metastable quenched state (as

also sketched in Figure 3.3B). Figure 3.5A illustrates the change in local coordination of

the boron atom upon relaxation from the trigonal M1(6)* site to the tetrahedral M1(1)

site as labeled. The diffusion of B atoms on the time scales observed in this experiment

can be attributed to a coupled distortion of the lattice that takes the system out of its

metastable quenched state and into its thermodynamic minimum. In summary the B

atom finds itself in a metastable state upon transition from R → M_1 structural transition and relaxes toward the most stable configuration through a thermally activated process.

To the best of our knowledge, there are few parallels to the observed dynamic modulation of the phase transition stemming from intrinsic lattice degrees of freedom (and not just domain switching derived from microstructural properties). There are some parallels to the phenomenon of martensite aging observed in shape memory alloys such as Au–Cu–Zn (L21-M18R)(48) and In–Tl (FCC-FCT; disordered),[49,50] wherein a degree of intrinsic modulation of the symmetry raising transition temperatures and critical stress is observed as a function of kinetic relaxation of the martensitic state. Such phenomena have been attributed to defect migration and the evolution of symmetry conforming defect states.[51]

3.4. Conclusions

In summary, we demonstrate that incorporation of a mobile interstitial dopant species imbues a means of dynamically modulating the insulator–metal transition temperature of VO_2. Without engineering any change in composition, the critical transition temperature of a singular sample can be varied across a temperature range of 45 °C (in close proximity of room temperature) by controlling the thermal history and the time elapsed since the material was cooled from the R to the M_1 phase. The dynamic modulation of the transition temperature is explicable considering that the most energetically favored sites for B atoms vary throughout the transition between the M_1 and R polymorphs with an intermediate metastable trigonal state. Consequently, raising the system to the R phase and then cooling it down to the M_1 phase stations the B

atom in an energetically disfavored trigonal site and leaves the system in a metastable

initial state that is energetically only slightly more stable than the R phase (and can be

transitioned to the latter at a lower temperature). Over a period of time, the B atoms

diffuse in real space to energetically more favorable tetrahedral configurations through a

thermally activated process, bringing the system to a quasi-equilibrium arrangement that

represents a deeper valley in the free energy landscape. Transformation to the R phase is

more hindered from this configuration, resulting in a pronounced increase of the

transition temperature. Consistent with the idea of an activated atomic diffusion process,

the relaxation time exhibits an Arrhenius dependence on temperature. B K-edge XANES

and DFT calculations suggest a short hop from an initially trigonal coordinated site to a

tetrahedrally coordinated site as the system relaxes from a quenched metastable structure

to the stable monoclinic polymorph. Heating past the $M_1 \rightarrow R$ transition temperature

results in the B atoms being situated in higher symmetry sites and serves as a means of

resetting the relative populations of metastable and quasi-equilibrium states upon

cooling.

The incorporation of B as a mobile dopant thereby endows a temporal history to

the phase transition that depends on the atomistic diffusion barriers encountered by B

atoms and that can be determined using the heating transition temperature. In addition to

the "hourglass" time and thermal history dependence of the experimentally measured

transition temperature, B-doped VO_2 is seen to exhibit a programmable time-variant

modulation of conductance, which has potential for utilization in neuromorphic circuits

and memory devices. Future work will examine the influence of other diffusive dopant atoms in VO_2 and of B in analogous correlated systems such as NbO_2.

3.5. Experimental

3.5.1. Synthesis of VO_2 Nanowires

VO_2 nanowires with lateral dimensions of 210 ± 70 nm and lengths in the range of 4.0 ± 3.0 μm were prepared as reported in our previous work based on the hydrothermal reduction of V_2O_5 by 2-propanol. Briefly, 1.600 g of V_2O_5 (Sigma-Aldrich, St. Louis, MO) was reduced to VO_2 with 10 mL of 2-propanol (Fisher, Fair Lawn, NJ) dissolved in 65 mL of deionized water (prepared with a Barnstead International NANOpure Diamond ultrapure water system $\rho = 18.2$ MΩ cm^{-1}). The hydrothermal reaction was performed at 210 °C for 72 h in a 125 mL autoclave. The supernatant was discarded, and the precipitate was rinsed with acetone (Macron Fine Chemicals, Center Valley, PA). The samples were then placed within a quartz tube, which was annealed using a tube furnace to a temperature of 550 °C (ramping at a rate of ~45 °C/min) for 3 h under flowing Ar gas at a rate of 800 mL/min.

3.5.2. Incorporation of B by Diffusive Doping

2-Allyl-4,4,5,5-tetramethyl-1,3,2-dioxaborolane (97%) was purchased from Sigma-Aldrich (St. Louis, MO). In a typical reaction, an amount of 20 mg of VO_2 nanowires was dispersed in 1.00 mL of mesitylene by ultrasonication, and 200 μL of 2-allyl-4,4,5,5-tetramethyl-1,3,2-dioxaborolane was added to the reaction mixture. The reactants were allowed to stir for 2.5 h at 120 °C under an Ar ambient in a Schlenk flask. The VO_2 nanowires were recovered by centrifugation, rinsed with toluene, and

annealed using a 2 mL porcelain combustion boat (VWR, Sugar Land, TX) to a temperature of 900–950 °C for 1 min under an Ar ambient in a quartz tube furnace as reported in our previous work.[22] No formation of carbon interstitials or carbides is detectable based on HAADF STEM imaging, XPS, and Raman spectroscopy measurements.[22] Performing the annealing step using VO_2 nanowires without adsorption of the molecular precursor likewise induces sintering of the nanowires; however, in the absence of B atoms, the relative phase stabilities of the monoclinic and rutile phases are essentially unchanged.

3.5.3. Differential Scanning Calorimetry

Differential scanning calorimetry (DSC) analysis was performed using a TA Instruments Q2000 instrument. Aluminum T-Zero pans were used for DSC experiments under a purge flow of Ar gas. Scan rates were varied from 1 °C/min to 15 °C/min.

3.5.4. Powder X-ray Diffraction

Powder X-ray diffraction (XRD) patterns were acquired using a Bruker D8-Focus Bragg–Brentano X-ray powder diffractometer equipped with a Cu Kα ($\lambda = 1.5418$ Å) source and operated at an accelerating voltage of 40 kV. Low-temperature powder XRD patterns were acquired using a Bruker-AXS Venture X-ray (κ geometry) diffractometer with Cu Iμs X-ray tube (Kα = 1.5418 Å) with an Oxford Cyrosystem low temperature attachment (RT to 110 K). Measurements were acquired at a temperature of −163 °C.

3.5.5. XANES Spectroscopy

B K-edge XANES spectra were acquired in the energy range of 185–210 eV at the variable line spacing-plane grating monochromator (VLS-PGM) beamline ($E/\Delta E >$ 10 000) of the Canadian Light Source at the University of Saskatchewan in Saskatoon, SK. The samples were mounted in a UHV chamber at a pressure of 1×10^{-8} Torr. The XANES spectra were measured using the high-energy grating of the beamline yielding a spectral resolution of ~0.1 eV with entrance and exit slit widths of 100 μm. A microchannel plate detector was used to collect the fluorescence yield (FLY) signal. All spectra recorded were normalized to the intensity of the photon beam as measured by the drain current of a Ni mesh (transmission 90%) situated upstream of the sample. Three B-doped VO_2 samples were analyzed: relaxed-monoclinic (M_1) $B_{0.052}VO_2$, unrelaxed-M_1 $B_{0.004}VO_2$, and rutile (R) $B_{0.052}VO_2$. The relaxed-M_1 $B_{0.05}VO_2$ sample was relaxed to room temperature in the DSC using the thermal profile given in Figure B.9E and S9F. To assess the extent of thermal relaxation, DSC scans of a small aliquot of the relaxed-M_1 $B_{0.052}VO_2$ sample (shown in Figure B.9G were run in parallel to the XANES measurements. The R $B_{0.052}VO_2$ sample was an additional $B_{0.052}VO_2$ sample that was reset immediately prior to the XANES measurement by heating to 100 °C (ensuring that the sample was not in the relaxed-M_1 state) and cooling to room temperature. XANES analysis of unrelaxed B-doped VO_2 was done using $B_{0.004}VO_2$ because the MIT temperature of unrelaxed-M_1 $B_{0.052}VO_2$ sample is well below the room temperature measurement making the structure in the R phase. The MIT for $B_{0.004}VO_2$ is 58 °C. The $B_{0.004}VO_2$ sample was reset immediately prior to the XANES measurement by heating to

100 °C (ensuring that the sample was not in the relaxed-M_1 state) and cooling to room temperature.

3.5.6. Scanning Electron Microscopy

SEM images of the nanowires were collected on a Tescan MIRA3 FE-SEM (Figure B.1A) and a Tescan FERA3 FIB-SEM (Figure B.1B) operated at an accelerating voltage of 20 kV for both instruments.

3.5.7. First-Principles DFT Calculations

Prior to first-principles calculations, interstitial sites in the monoclinic ($P2_1/c$) and tetragonal ($P4/2_{mnm}$) phases were located using the cages function implemented in the AFLOW software.[37] The topological search algorithm selects for unique sites within a unit cell by analyzing the site symmetries within the respective space group. Boron-doped structures were generated from the list of irreducible sites and subsequently relaxed according to the specified DFT parameters.

The atomistic, electronic structures and total energies were calculated using first-principles DFT,[52,53] as implemented in the Vienna ab initio simulation package (VASP). The projector augmented wave (PAW)[54] method was used to describe the electronic configurations of the relevant elements, and the exchange–correlation energy functional was modeled using the GGA with the Perdew–Burke–Ernzerhof (PBE) form.[55] A plane wave basis set with an energy cutoff of 533 eV was employed. Considering the strongly correlated d electrons for vanadium, a Hubbard parameter U is applied to the PBE functional in the approach proposed by Dudarev et al.,[56] with $U_{eff} =$ 3.4 eV. As illustrated in Figure B.7A and B.7B, this value of U captures the insulating

nature of the monoclinic polymorph and the metallic nature of the tetragonal polymorph. The doped 97-atom supercells were generated by replicating the monoclinic and rutile unit cells by $2 \times 2 \times 2$ and $2 \times 2 \times 4$, respectively. The pristine $V_{32}O_{64}$ supercells were fully relaxed. For the boron doped structures generated from the supercells, all the V, O, and B atoms were subsequently relaxed. Potential diffusion pathways and the corresponding energy barriers for B atom within M_1 VO_2 were examined using the nudged elastic band (NEB) method,[46,47] where a total of three images were interpolated and subsequently relaxed between the initial and final configurations. The convergence tolerance for electronic relaxation was set to 10^{-7} eV, and the maximum residual force for ionic relaxation was set to <0.01 eV Å^{-1}. A Monkhorst–Pack mesh with at least 5000 k-points per reciprocal atom was used for the Brillouin zone integration.

3.5.8. DFT Calculations of the Formation Energies of Charged Defects

To mimic the dilute limit, the unit cell structure is enlarged to $2 \times 2 \times 2$ supercell, and due to the high computational cost, the k-point sampling is reduced to $2 \times 2 \times 2$ accordingly. Spin polarization is included for all the defect calculations. The defect formation energy is defined by $\Delta E_\text{f}(D,q) = E(D,q) - E(\text{bulk}) - \sum n_i \mu_i + q(\epsilon_f + \epsilon_\text{VBM}) + E_\text{corr}$,(57) where $E(D,\text{q})$ and $E(\text{bulk})$ refer to the total energy of the pristine host cell and the supercell with defect D in charge state q, respectively. μ_i is the chemical potential of species i involved in the defect, and n_i is the number of the atoms added ($n_i > 0$) or removed ($n_i < 1$). In this work, we consider three types of defects: B-on-V substitutional defect, B-on-O substitutional defect, and B interstitial defect. $q\epsilon_\text{F}$ represents the electron reservoir, and ϵ_F is the Fermi level with respect to the valence band maximum ϵ_VBM in

the perfect cell. The range of the chemical potential for each species is determined by the stability of VO_2 relative to the elemental phases and other competing compounds. The last term E_{corr} in the above equation is the correction to the formation energy caused by the interaction between the defect charge and its images and the potential alignment between the defect and host cells under the periodic boundary condition employed in the DFT calculations.[58] To determine the equilibrium Fermi level, we conducted native defect calculations assuming the point defects play a dominating role and solved self-consistent equations under conditions of charge neutrality.[59]

3.5.9. XANES Simulation Calculations

Simulation of X-ray absorption spectra and calculation of orbital density plots was performed using the PWscf code in the Quantum ESPRESSO package. The sampling of the Brillouin zone was achieved using the Shirley optimal basis set.[60,61] A constant value of 192.0 eV is added to all the theoretical spectra in order to align with the experimental spectra. For the simulation of the B K-edge XANES spectra, a uniform k-point sampling grid of $2 \times 2 \times 2$ was used. The B K-edge simulation uses The XCH-CAS approach, in which an electron is removed from the 1s inner shell of the excited B atom within the VO_2 unit cell to account for the excited state core–hole interactions.[44,45] The inclusion of the core–hole perturbation is not explicit but is instead accounted for using a modified boron pseudopotential with one less electron in the 1s orbital for the B K-edge. The excited electron is included in the occupied electronic structure, and the entire electronic system is relaxed to its ground state within DFT. In

order to reproduce the instrumental broadening observed in experimental spectra, a broadening of 0.2 eV was used for the simulated spectra.

3.5.10. Native Defect Calculations

In order to determine the Fermi level, native defect calculations have been performed, as shown in Fig. B.6C and B.6D. The equilibrium Fermi level is computed by solving self-consistent equations under the charge neutrality conditions given by [58]

$$-n_e(E_F, T) + n_h(E_F, T) + \sum_D \sum_q q_D \cdot c_{D,q}(E_F, T) = 0 \qquad \textbf{3.5}$$

where $c_{D,q}(E_F, T)$, n_e and n_h are defect, free electron and hole concentrations, respectively. They can be calculated as the following:

$$c_{D,q}(E_F, T) = N_{site} e^{-\frac{E_f^{D,q}(E_F)}{k_B T}} \qquad \textbf{3.6}$$

$$n_e(E_F, T) = \int_{CBM}^{+\infty} g_e(E) f(E - E_F, T) dE \qquad \textbf{3.7}$$

$$n_h(E_F, T) = \int_{-\infty}^{VBM} g_h(E)(1 - f(E - E_F, T)) dE \qquad \textbf{3.8}$$

$f(E - E_F, T)$ is the Fermi-Dirac distribution. $g_e(E)$ and $g_h(E)$ are the density of states (DOS) of electrons and holes, respectively. Based on the calculated formation energies, the equilibrium Fermi levels are 0.5 eV and 0.55 eV for O-rich and O-poor conditions, respectively. The corresponding electron densities are $\sim 10^{19}$ cm^{-3} and $\sim 10^{20}$ cm^{-3}, and the hole densities are 10^{14} cm^{-3} and 10^{13} cm^{-3}, respectively.

3.5.11. *In Situ* **DSC and Water Bath Relaxation Experiments**

In situ DSC annealing experiments were conducted using the instrument defined above. For all experiments described in Figure 3.3A, the sample was scanned at 10 °C/min from −60 to 100 °C at least once before continuing along a given temperature outlined in the bottom section of Figure 3.3A. This protocol ensured that the sample was fully "reset" into the unrelaxed state before annealing.

Water bath relaxation experiments were preformed using a PolyScience (AP07R) circulating bath with a working temperature range of −40 °C to 200 °C. Samples were sealed in a water-tight glass vial in an inert Ar environment. Immediately prior to the experiment, the samples were heated to 100 °C for 20 min to convert to the R phase before being rapidly cooled to −78 °C with dry ice.

3.6. References

[1]   S. Kumar, J. P. Strachan, R. S. Williams, *Nature* **2017**, *548*, 318.

[2]   J. Shi, S. D. Ha, Y. Zhou, F. Schoofs, S. Ramanathan, *Nat. Commun.* **2013**, *4*, 2676.

[3]   P. M. Marley, G. a Horrocks, K. E. Pelcher, S. Banerjee, *Chem. Commun.* **2015**, *51*, 5181.

[4]   M. Bibes, A. Barthélémy, *Nat. Mater.* **2008**, *7*, 425.

[5]   R. H. J. Hannink, P. M. Kelly, B. C. Muddle, *J. Am. Ceram. Soc.* **2000**, *83*, 461.

[6]   B. M. Hudak, S. W. Depner, G. R. Waetzig, A. Talapatra, R. Arroyave, S. Banerjee, B. S. Guiton, *Nat. Commun.* **2017**, *8*, 15316.

[7]   R. D. James, K. F. Hane, *Acta Mater.* **2000**, *48*, 197.

[8]   Y. Song, X. Chen, V. Dabade, T. W. Shield, R. D. James, *Nature* **2013**, *502*, 85.

[9]   J. L. Andrews, D. A. Santos, M. Meyyappan, R. S. Williams, S. Banerjee, *Trends Chem.* **2019**, *1*, 711.

[10]   E. J. Braham, D. Sellers, E. Emmons, R. Villarreal, H. Asayesh-Ardakani, N. A. Fleer, K. E. Farley, R. Shahbazian-Yassar, R. Arròyave, P. J. Shamberger, S. Banerjee, *Chem. Mater.* **2018**, *30*, 214.

[11]   W. H. Brito, M. C. O. Aguiar, K. Haule, G. Kotliar, *Phys. Rev. B* **2017**, *96*, 195102.

[12]   X. Yuan, Y. Zhang, T. A. Abtew, P. Zhang, W. Zhang, *Phys. Rev. B* **2012**, *86*, 235103.

[13]   L. Whittaker, C. J. Patridge, S. Banerjee, *J. Phys. Chem. Lett.* **2011**, *2*, 745.

[14]   H. Asayesh-Ardakani, A. Nie, P. M. Marley, Y. Zhu, P. J. Phillips, S. Singh, F. Mashayek, G. Sambandamurthy, K. Bin Low, R. F. Klie, S. Banerjee, G. M. Odegard, R. Shahbazian-Yassar, *Nano Lett.* **2015**, *15*, 7179.

[15]   J. Booth, P. Casey, *Phys. Rev. Lett.* **2009**. *103,* 86402.

[16]   J. P. Pouget, H. Launois, T. M. Rice, P. Dernier, A. Gossard, G. Villeneuve, P. Hagenmuller, *Phys. Rev. B* **1974**, *10*, 1801.

[17]   M. Ghedira, H. Vincent, M. Marezio, J. C. Launay, *J. Solid State Chem.* **1977**, *22*, 423.

[18]   N. F. Quackenbush, H. Paik, M. J. Wahila, S. Sallis, M. E. Holtz, X. Huang, A. Ganose, B. J. Morgan, D. O. Scanlon, Y. Gu, F. Xue, L. Q. Chen, G. E. Sterbinsky, C.

Schlueter, T. L. Lee, J. C. Woicik, J. H. Guo, J. D. Brock, D. A. Muller, D. A. Arena, D. G. Schlom, L. F. J. Piper, *Phys. Rev. B* **2016**, *94*, 085105.

[19]   Y. Filinchuk, N. A. Tumanov, V. Ban, H. Ji, J. Wei, M. W. Swift, A. H. Nevidomskyy, D. Natelson, *J. Am. Chem. Soc.* **2014**, *136*, 8100.

[20]   E. J. Braham, J. L. Andrews, T. E. G. Alivio, N. A. Fleer, S. Banerjee, *Phys. status solidi A* **2018**, *215,* 1700884.

[21]   J. J. Zhang, H. Y. He, Y. Xie, B. C. Pan, *J. Chem. Phys.* **2014**, *141*, 194707.

[22]   T. E. G. Alivio, D. G. Sellers, H. Asayesh-ardakani, E. J. Braham, G. A. Horrocks, K. E. Pelcher, R. Villareal, L. Zuin, J. Patrick, R. Arroyave, R. Shahbazian-yassar, S. Banerjee, *Chem. Mater.* **2017**, *29*, 5401.

[23]   L. Whittaker, T.-L. Wu, C. J. Patridge, G. Sambandamurthy, S. Banerjee, *J. Mater. Chem.* **2011**, *21*, 5580.

[24]   A. Krammer, A. Magrez, W. A. Vitale, P. Mocny, P. Jeanneret, E. Guibert, H. J. Whitlow, A. M. Ionescu, A. Schüler, *J. Appl. Phys.* **2017**, *122*, 45304.

[25]   W. Fan, J. Cao, J. Seidel, Y. Gu, J. W. Yim, C. Barrett, K. M. Yu, J. Ji, R. Ramesh, L. Q. Chen, J. Wu, *Phys. Rev. B - Condens. Matter Mater. Phys.* **2011**, *83*, 235102.

[26]   J. Wu, Q. Gu, B. S. Guiton, N. P. De Leon, L. Ouyang, H. Park, *Nano Lett.* **2006**, *6*, 2313.

[27]   J. Wei, H. Ji, W. Guo, A. H. Nevidomskyy, D. Natelson, *Nat. Nanotechnol.* **2012**, *7*, 357.

[28] E. Strelcov, A. Tselev, I. Ivanov, J. D. Budai, J. Zhang, J. Z. Tischler, I. Kravchenko, S. V. Kalinin, A. Kolmakov, *Nano Lett.* **2012**, *12*, 6198.

[29] S. Zhang, J. Y. Chou, L. J. Lauhon, *Nano Lett.* **2009**, *9*, 4527.

[30] S. Kachi, K. Kosuge, H. Okinaka, *J. Solid State Chem.* **1973**, *6*, 258.

[31] J. D. Budai, J. Hong, M. E. Manley, E. D. Specht, C. W. Li, J. Z. Tischler, D. L. Abernathy, A. H. Said, B. M. Leu, L. A. Boatner, R. J. McQueeney, O. Delaire, *Nature* **2014**, *515*, 535.

[32] F. Gervais, W. Kress, *Phys. Rev. B* **1985**, *31*, 4809.

[33] H. Clarke, B. D. Carraway, D. G. Sellers, E. J. Braham, S. Banerjee, R. Arróyave, P. J. Shamberger, *Phys. Rev. Mater.* **2018**, *2*, 103402.

[34] L. Pauling, *J. Am. Chem. Soc.* **1947**, *69*, 542.

[35] V. Eyert, *Phys. Rev. Lett.* **2011**, *107*, 016401.

[36] S. Mukherjee, N. F. Quackenbush, H. Paik, C. Schlueter, T. L. Lee, D. G. Schlom, L. F. J. Piper, W. C. Lee, *Phys. Rev. B* **2016**, *93*, 241110.

[37] S. Curtarolo, W. Setyawan, G. Hart, M. Jahnatek, R. Chepulskii, R. Taylor, S. Wang, J. Xue, K. Yang, O. Levy, M. J. Mehl, H. T. Stokes, D. O. Demchenko, D. Morgan, *Comput. Mater. Sci.* **2012,** *58,* 218.

[38] J. G. Chen, *Surf. Sci. Rep.* **1997**, *30*, 1.

[39] T. Hemraj-Benny, S. Banerjee, S. Sambasivan, D. A. Fischer, W. Han, J. a Misewich, S. S. Wong, *Phys. Chem. Chem. Phys.* **2005**, *7*, 1103.

[40] M. E. Fleet, X. Liu, *Phys. Chem. Miner.* **2001**, *28*, 421.

106

[41]   D. Li, G. M. Bancroft, M. E. Fleet, *J. Electron Spectros. Relat. Phenomena* **1996**, *79*, 71.

[42]   M. E. Fleet, S. Muthupari, *J. Non. Cryst. Solids* **1999**, *255*, 233.

[43]   S. K. Lee, P. J. Eng, H. Mao, Y. Meng, M. Newville, M. Y. Hu, J. Shu, *Nat. Mater.* **2005**, *4*, 851.

[44]   D. Prendergast, G. Galli, *Phys. Rev. Lett.* **2006**, *96*, 215502.

[45]   A. Parija, Y.-H. Choi, Z. Liu, J. L. Andrews, L. R. De Jesus, S. C. Fakra, M. Al-Hashimi, J. D. Batteas, D. Prendergast, S. Banerjee, *ACS Cent. Sci.* **2018**, *4*, 493.

[46]   Y. Meng, M. Arroyo-de Dompablo, *Energy Environ. Sci.* **2009**. *2*, 589.

[47]   Z. Rong, R. Malik, P. Canepa, G. Sai Gautam, M. Liu, A. Jain, K. Persson, G. Ceder, *Chem. Mater.* **2015**, *27*, 6016.

[48]   S. Miura, S. Maeda, N. Nakanishi, *Philos. Mag. A J. Theor. Exp. Appl. Phys.* **1974**, *30*, 565.

[49]   M. W. Burkart, T. A. Read, *J. Met.* **1953**, *5*, 1516.

[50]   Z. S. Basinski, J. W. Christian, *Acta Metall.* **1954**, *2*, 101.

[51]   K. Otsuka, X. Ren, *Scr. Mater.* **2004**, *50*, 207.

[52]   P. Hohenberg, W. Kohn, *Phys. Rev.* **1964**, *136*, B864.

[53]   W. Kohn, L. J. Sham, *Phys. Rev.* **1965**, *140*, A1133.

[54]   G. Kresse, D. Joubert, *Phys. Rev. B* **1999**, *59*, 1758.

[55]   K. Burke, J. P. Perdew, Y. Wang, in *Electronic Density Functional Theory: Recent Progress and New Directions* (Eds.: J.F. Dobson, G. Vignale, M.P. Das), Springer US, Boston, MA, **1998**, pp. 81–111.

[56]   S. Dudarev, G. Botton, *Phys. Rev. B - Condens. Matter Mater. Phys.* **1998**, *57*, 1505.

[57]   C. Freysoldt, B. Grabowski, T. Hickel, J. Neugebauer, G. Kresse, A. Janotti, C. G. Van De Walle, *Rev. Mod. Phys.* **2014**, *86*, 253.

[58]   Y. Kumagai, F. Oba, *Phys. Rev. B - Condens. Matter Mater. Phys.* **2014**, *89*, 195205.

[59]   R. Sun, M. K. Y. Chan, S. Kang, G. Ceder, *Phys. Rev. B - Condens. Matter Mater. Phys.* **2011**, *84*, 035212.

[60]   D. Prendergast, S. G. Louie, *Phys. Rev. B* **2009**, *80*, 235126.

[61]   E. L. Shirley, *Phys. Rev. B* **1996**, *54*, 16464.

4. STABILIZATION OF A METASTABLE TUNNEL-STRUCTURED ORTHORHOMBIC PHASE OF VO$_2$ UPON IRIDIUM DOPING*

4.1. Overview

Metastable compounds accessible through kinetic stabilization or under conditions of constrained equilibrium represent a richly varied landscape of structures, properties, and function that are oftentimes entirely inaccessible in thermodynamic minima. The multiple redox states of vanadium and the ability to modulate the connectivity of vanadium and oxygen atoms yields a rich diversity of structures for binary vanadium oxides. Here we demonstrate that an orthorhombic quasi-1D polymorph of VO$_2$, characterized by extended tunnels with a rectangular cross-section, can be stabilized through the substitutional doping of iridium on the vanadium sublattice. The obtained structure is considerably distorted from a previously reported paramontroseite mineral phase. The metastable phase is obtained in nanoplatelet form and is stable with respect to the energetically proximate monoclinic/rutile thermodynamic minima up to a temperature of 350°C. The open framework structure and the accessibility of multiple redox states at the vanadium center suggests that the polymorph could potentially serve as an intercalation host. Beyond the solubility limit of iridium on the vanadium sublattice (1.28—3.15 at.% depending on the precursor concentration), metallic Ir nanocrystals are found to be homogeneously dispersed on the surfaces of the

_____

nanoplatelets indicating a strong interaction between the metal nanocrystals and oxide lattice.

4.2. Introduction

Kinetically trapped metastable compounds oftentimes exhibit radical departures from equilibrium behavior and thereby provide a much more richly varied landscape of structures, properties, and functions as compared to those accessible within thermodynamic minima.[1,2] Such structures are commonly characterized by unusual framework connectivity and atypical coordination environments, thereby providing access to electronic structure features that can diverge substantially from comparable features in the thermodynamically stable polymorph. For instance, while the hexagonal 2H phase of $MoTe_2$ with trigonal prismatic coordination of Mo atoms is a semiconductor, the monoclinic 1T'-phase is a semi-metal, whereas the orthorhombic T_d phase has recently been discovered to be a Weyl semi-metal with characteristic topologically protected Fermi arcs and is believed to have potential to exhibit novel quantum phenomena such as chiral anomalies.[3] In the binary HfO_2 system, the monoclinic phase is thermodynamically stable, whereas the high-temperature tetragonal phase is predicted to exhibit a dielectric constant value that is substantially higher as a result of its longer Hf—O bonds, softer low-energy phonon modes, and higher bandgap.[4] One approach to stabilization of a metastable compound is to access a regime on a multidimensional energy landscape wherein that compound represents the energetically most favored polymorph and then preventing quenching to the thermodynamically stable polymorph when the relevant constraints are removed.

110

Pressure, strain, surface confinement, and chemical potential are some examples of additional dimensions that can be utilized to access metastable phase space.[1,5,6] In this work, we demonstrate stabilization of an open-framework VO_2 polymorph with rectangular tunnels upon substitutional Ir doping on the cation lattice. The structure is stable towards the energetically proximate rutile/monoclinic thermodynamic polymorphs up to a temperature of 350°C.

The binary Hf—O phase diagram has several variants other than the monoclinic and tetragonal polymorphs noted above; for instance, a cubic polymorph is stable above 2700°C and an orthorhombic polymorph, stabilized by substitutional Y or Al doping on the cation lattice, shows a pronounced ferroelectric distortion with an experimentally demonstrated saturation polarization approaching 16 $\mu C/cm^2$.[7–9] However, the binary Hf—O energy landscape appears to be much more sparsely populated as compared to the energy landscapes of binary vanadium oxides VO_2 and V_2O_5, which are characterized by a multitude of energetically proximate polymorphs.[10–15] Considering the d^0 compound V_2O_5, several polymorphs with widely varying lengths of V—O bonds, connectivity of vanadium-centered polyhedra, and stacking of (V_2O_5) sheets are experimentally accessible.[10,12,15,16] Such compounds allow for a broad range of bandgaps and energy dispersion of V 3d-derived bands as well as define starkly different ion conduction pathways with activation barriers that can differ by an order of magnitude.[10,16,17] The close energetic proximity of insulating monoclinic and metallic tetragonal phases of vanadium(IV) oxide or VO_2 make this material a canonical system for investigation of metal—insulator transitions; the monoclinic M_1 phase undergoes a

pronounced metal—insulator transition (MIT) to the high temperature (R) phase at 65°C.[18] In addition, several other polymorphs are known such as the M_2 polymorph, which is stabilized by strain or chemical pressure, the M_3 phase, metastable $VO_2(A)$ and $VO_2(B)$ phases often accessible from hydrothermal synthesis, and a mineral phase paramontroseite or $VO_2(P)$.[19–22] The ability to access a rich palette of structural motifs with varying connectivity of V—O bonds, tunable linkages of vanadium-centered polyhedra, and reconfigurable stacking of extended sheets has profound implications for the relative extent of ionicity or covalency and allows for broad tunability of transport properties from insulating to semiconducting and metallic regimes.[15]

The paramontroseite (P) phase of VO_2 is a naturally occurring mineral with an open framework structure wherein VO_6 tetrahedra define a rectangular tunnel; it is distinctive for stabilizing vanadium in a low oxidation state and was first noted by Mores and Evans in 1954.[22] In 2008, Wu et al. reported a hydrothermal synthesis that yielded "walnut-like" microstructures of $VO_2(P)$ based on the reaction of sodium orthovanadate and thioacetamide.[23] However, a structure solution was not reported and the presence of potential S incorporation within the anion sublattice, commonly observed upon hydrothermal thioacetamide reduction, does not appear to have been examined. Nevertheless, the rigid tunnel structure and the accessibility of the V^{4+}/V^{3+} redox couple lends itself to Li-ion intercalation and this material has been examined as a potential cathode material for battery applications.[23] Additionally, $VO_2(P)$ has been shown to have an interesting effect on the induction of cell autophagy.[24] Herein, we demonstrate that Ir doping on the cation lattice allows for stabilization of a distorted variant of the

112

VO$_2$(P) phase, which is prepared in nanoplatelet form. We report a refined crystal structure characterized by quasi-1D tunnels that have rectangular cross-sections, map the synthetic regime wherein this polymorph is accessible, and furthermore examine its conversion to the thermodynamically stable M$_1$/R polymorphs upon annealing at 350°C. The atomic concentration of substitutional Ir incorporated on the V sublattice depends on the Ir precursor concentration and a solubility limit of 1.28—3.15 at.% is deduced; close to the solubility limit, metallic Ir nanocrystals are found to be stabilized and homogeneously dispersed on the surfaces of the nanoplatelets indicating a strong interaction between the metal nanocrystals and oxide lattice.

4.3. Results and Discussion

The introduction of dopants within extended periodic solids can stabilize subtle structural distortions and modify relative phase stabilities, thereby giving rise to a substantially altered phase diagram.[11] Such effects can be especially acute for "rugged" energy landscapes characterized by a series of closely related polymorphs. For instance, the introduction of Al and Cr on the vanadium sublattice of VO$_2$ stabilizes the M$_2$ polymorph,[25,26] whereas substitutional W- and Mo-doping on the vanadium sublattice preferentially stabilizes the R polymorph over the M$_1$ polymorph even rendering the former metallic phase accessible at room temperature.[27–29] Interstitial B-doping of VO$_2$ similarly stabilizes the R polymorph over the M$_1$ polymorph,[30] thereby strongly depressing the characteristic metal—insulator transition temperature, whereas in contrast, interstitial H incorporation stabilizes two distinct orthorhombic phases, O$_1$ and O$_2$.[31] In this work, we demonstrate the stabilization of a metastable orthorhombic

113

VO$_2$(P) phase with rectangular tunnels upon substitutional Ir doping on the cation

sublattice of VO$_2$.
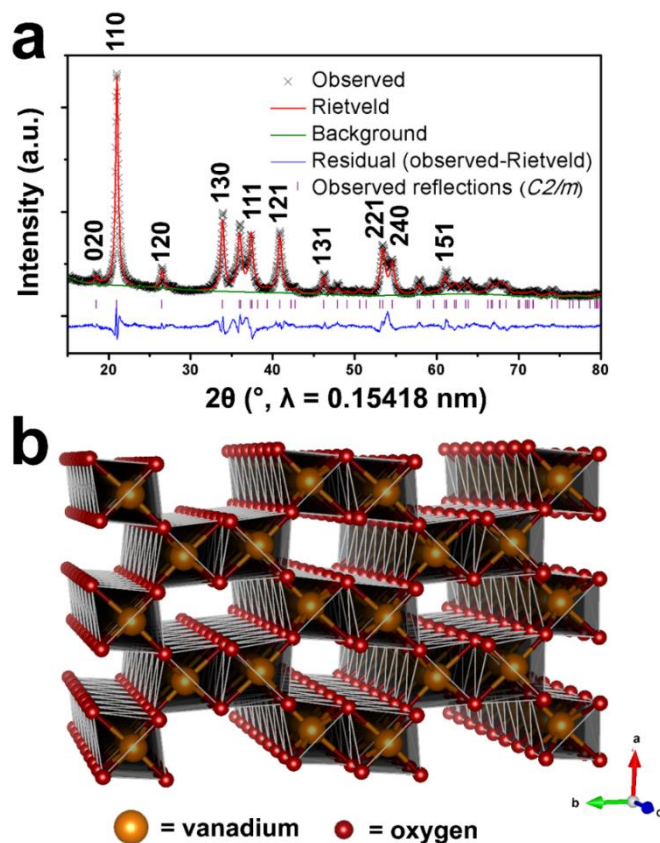
Figure 4.1 Refinement of the Crystal Structure of the VO$_2$(P) Phase. (a) Powder XRD pattern acquired for orthorhombic VO$_2$ (space group: *Pnma*); the experimental diffraction pattern is plotted as black crosses, the green trace represents the background function, the red trace is the Rietveld fit, and the blue trace represents the residuals (Rietveld fit subtracted from the experimental pattern). The obtained unit cell parameters for the refined structure are: a = 4.7014(5) Å, b = 9.567(1) Å, and c = 2.9196(4) Å. Refinement statistics are provided in Table C.1. (b) Representation of the refined structure as a 2×2×2 supercell viewed along the crystallographic *c*-axis; the quasi-1D tunnels of the structure are projected perpendicular to the *a-b* plane. Detailed views of the structure along each crystallographic axis are depicted in Figure C.1; atomic positions, bond distances, and bond angles are presented in Table C.2, C.3, and C.4, respectively

114

4.3.1. Structural and Morphological Characterization

The prepared phase is related to the naturally occurring mineral, paramontroseite, which in turn is crystallographically related to the minerals, montroseite (VOOH), diaspore (α-AlOOH), and ramsdellite (MnO_2).[22,32,33] A synthetic analog of paramontroseite, $VO_2(P)$, has since been synthesized under hydrothermal conditions although a full structure solution was not provided.[23] In previous literature reports, the hydrated montroseite ($VO(OH)_2$) phase has been transformed to $VO_2(P)$ upon annealing at 120°C providing a means to access this metastable phase, representing a local minima on the free-energy landscape, without reversion to the thermodynamic minimum (the M_1 phase of VO_2).[33] It is worth noting that there are stark differences between the naturally occurring paramontroseite phase and the Ir-stabilized $VO_2(P)$ structure reported in this work despite the retention of the quasi-1D tunnel framework.[22,23]

The novel tunnel-structured orthorhombic polymorph has been stabilized by the hydrothermal reduction of V_2O_5 by oxalic acid in the presence of IrO_2 as a dopant precursor. The Ir:V molar ratio has been varied from 0.0068:1 to 0.68:1 in the reaction mixture although the solubility of Ir in the V lattice is substantially lower than the amount of the added precursor and only a fraction of the added Ir is incorporated within the VO_2 lattice as discussed below. **Figure 4.1a** shows the powder XRD pattern acquired for powders obtained at a Ir:V ratio of 0.0068:1 (the actual Ir content is estimated to be 1.28±0.40 at.% Ir at V sites based on XPS analysis, *vide infra*). A Rietveld refinement of the powder XRD pattern has been performed and the refined pattern as well as the residuals are also plotted in Figure 4.1a. Figure 4.1b depicts the refined structure, which

is characterized by quasi-1D tunnels extending along the crystallographic c axis. **Figure C.1** (Appendix C) depicts other views of the crystal structure; Tables C.1, C.2, and C.3 list the refined unit cell parameters, atom positions, and bond distances, respectively.

It is worth noting that the Ir-doped $VO_2(P)$ phase is substantially distorted from the mineral paramontroseite as discernible from comparison of the XRD patterns of the two materials (**Figure 4.2**). Figure 4.2a contrasts the powder XRD patterns for the Ir-doped VO_2 synthesized in this work with that of a pattern simulated from a previously reported structure solution for the mineral phase;[22] the right panel clearly illustrates the relative shifts of the reflections, corresponding to a pronounced distortions of the rectangular tunnel in the Ir-doped phase with respect to the mineral phase. In particular, in the Ir-doped phase stabilized in this work, the lattice is expanded along the b axis, whereas a clear contraction of the lattice is evinced along the a axis (evidenced by the shift of the {110} reflection to higher 2θ values). Comparing the two structures, in the Ir-doped phase, the tunnel is expanded by ca. 1.86%, whereas a 3.86% contraction is observed along the a axis with respect to the mineral phase; the overall unit cell volume is decreased by ca. 2.4% with respect to the mineral phase (Tables C.5 and C.6).

Figures 4.2b and c contrast the tunnels defined by distorted VO_6 octahedra in the Ir-doped VO_2 and mineral phases, respectively. Figure 4.2d and 4.2e depict the local coordination geometry of vanadium atoms in VO_6 octahedra, in the Ir-doped VO_2 and mineral phases, respectively; the octahedra serve as the fundamental building blocks for
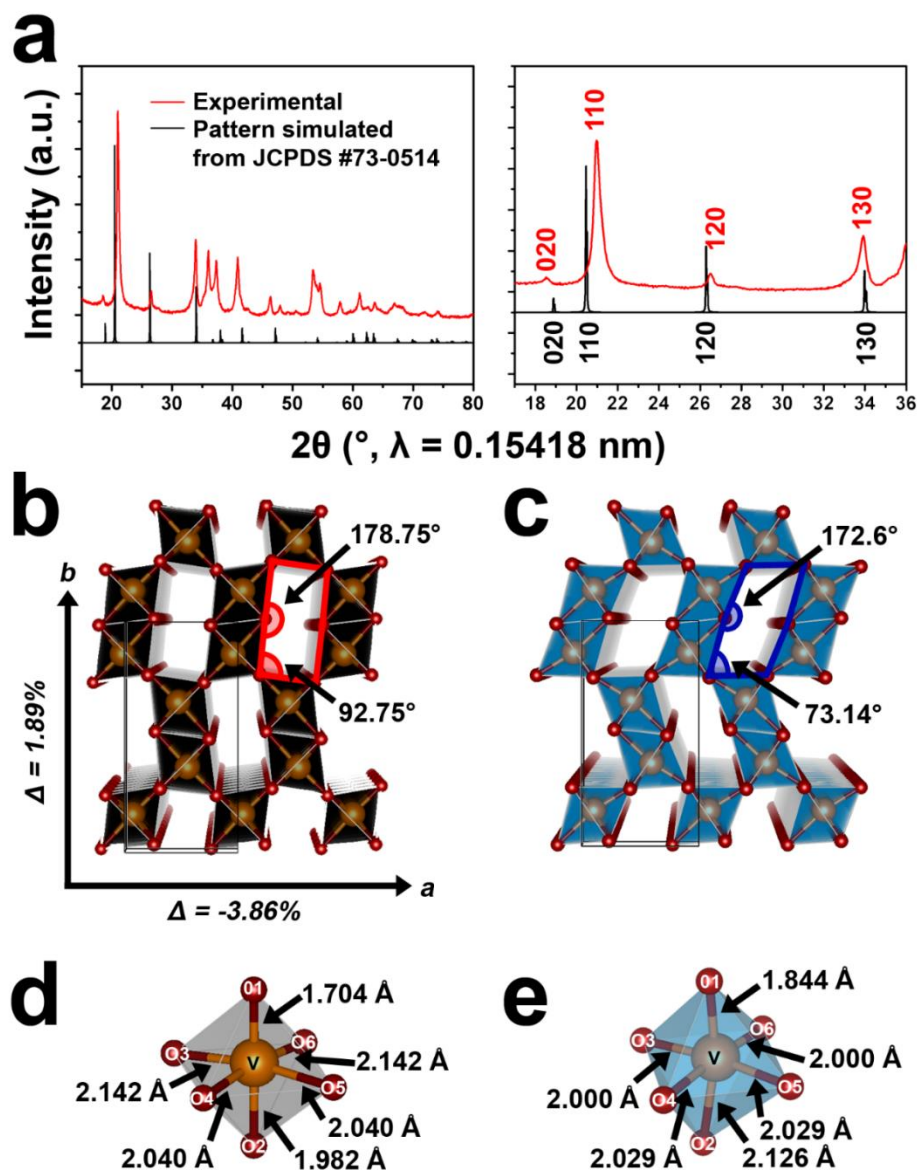
Figure 4.2. Structural Comparison of Ir-Doped $VO_2(P)$ to the Paramontroseite Mineral Phase. (a) A comparison of powder XRD patterns for the Ir-doped VO_2 phase prepared in this work (with a nominal Ir concentration of 1.28±0.40 at.%, depicted in red) to that of the paramontroseite mineral phase simulated from the unit cell reported by Evans *et al.* (shown in black).[22] The right panel shows a magnified view of the powder XRD patterns in the 2θ range between 18—26°, illustrating both the expansion of the lattice along the *b* axis and contraction of the lattice along the *a* axis in Ir-doped VO_2 relative to the naturally occurring mineral. The quasi-1D tunnels defined within (b) Ir-doped VO_2 and (c) the paramontroseite mineral phase are contrasted; the Ir-doped phase shows a considerable distortion with respect to the mineral phase. The local coordination geometries for VO_6 octahedra in (d) Ir-doped VO_2 and (e) the paramontroseite mineral phase show subtle distortions of V—O connectivity.

117

the tunnels. Tables C.5 and Table C.6 contrast the alteration of the lattice constants with respect to previously synthesized $VO_2(P)$[23] and mineral paramontroseite[22] phases. The distortions induced upon Ir-doping relative to both the naturally occurring mineral and synthetic paramontroseite have a profound effect on the shape, orientation and width of the 1D tunnels of the structure. In Figure 4.2c corresponding to the mineral paramontroseite phase, the tunnels closely resemble a trapezoid (highlighted in blue) with an internal angle of 73.14°; the long side of the trapezoid is slightly distorted with a bend of 7.4° from the straight edge. In contrast, the Ir-doped $VO_2(P)$ phase depicted in Figure 4.2b has tunnels with more rectangular cross-sections (highlighted in red); the tunnels are characterized by only a 1.25° deviation from the straight edge and exhibit an internal angle of ca. 90°. The anisotropic distortion can best be understood as a "straightening" of the tunnel shape to a more symmetric four-sided polygon. The increased symmetry of the tunnels furthermore leads to more symmetric quasi-octahedral coordination environments with average bond distances of 2.25 Å for the Ir-doped $VO_2(P)$ phase. The VO_6 octahedra of Ir-doped $VO_2(P)$ (Fig. 4.2d) have bond angles closer to 90° as compared to the wider spread of bond angles observed in the VO_6 polyhedra (Fig. 4.2e) of the mineral paramontroseite (a quantitative comparison of bond angles and bond lengths is presented in in Table C.4).

Notably, the V—V distances in this structure are rather close to the critical distance empirically defined by Goodenough to be the threshold below which increased orbital overlap brings about an electronic transition from semiconducting to metallic transport. [34] While the distortion induced by Ir doping is rather small along the

118

crystallographic c axis, the change in orbital overlap as a function of Ir doping may potentially bring about a pronounced modulation of electronic conductivity and will be the focus of future work.

In order to determine the limits of doping for Ir in VO_2 progressively larger amounts of IrO_2 have been added to the reaction mixture and the products have been analyzed by powder XRD. **Figure 4.3** shows powder XRD patterns acquired for samples prepared with added concentrations of Ir:V ranging from 0.0068:1 to 0.676:1. As will be discussed below, the actual Ir content incorporated within the VO_2 lattice is substantially lower and appears to depend on the precursor concentration (up to a maximum limit estimated to be 1.28—3.15 at.% Ir in VO_2); the competing nucleation of metallic Ir islands is initiated close to the solubility limit. At an added Ir:V precursor concentration of 0.0676:1, two broad reflections at $2\Theta = 40.5$ and $47.3°$, which can be indexed to metallic Ir crystallized in the cubic phase, become discernible. The considerable Debye—Scherrer broadening evidenced for these reflections indicates that Ir atoms that do not form a solid solution on the cation sublattice of VO_2 instead coalesce to form metallic Ir nanocrystals. Above an Ir:V concentration of ca. 0.541:1, the $VO_2(P)$ phase is no longer stabilized and instead the products are a mixture of VO_2 crystallized in the M_1 phase along with metallic Ir nanocrystals. An additional phase does appear in the samples of V:Ir concentrations of 0.135:1 and 0.270:1 as suggested by the asterisked reflections in Figure 4.3. These reflections are attributed to the $\{10\bar{2}\}$, $\{104\}$, and $\{2\bar{1}6\}$

reflections of karelianite V_2O_3 (JCPDS # 85-1403), likely resulting from increased

reduction of V_2O_5 by oxalic acid under these conditions.
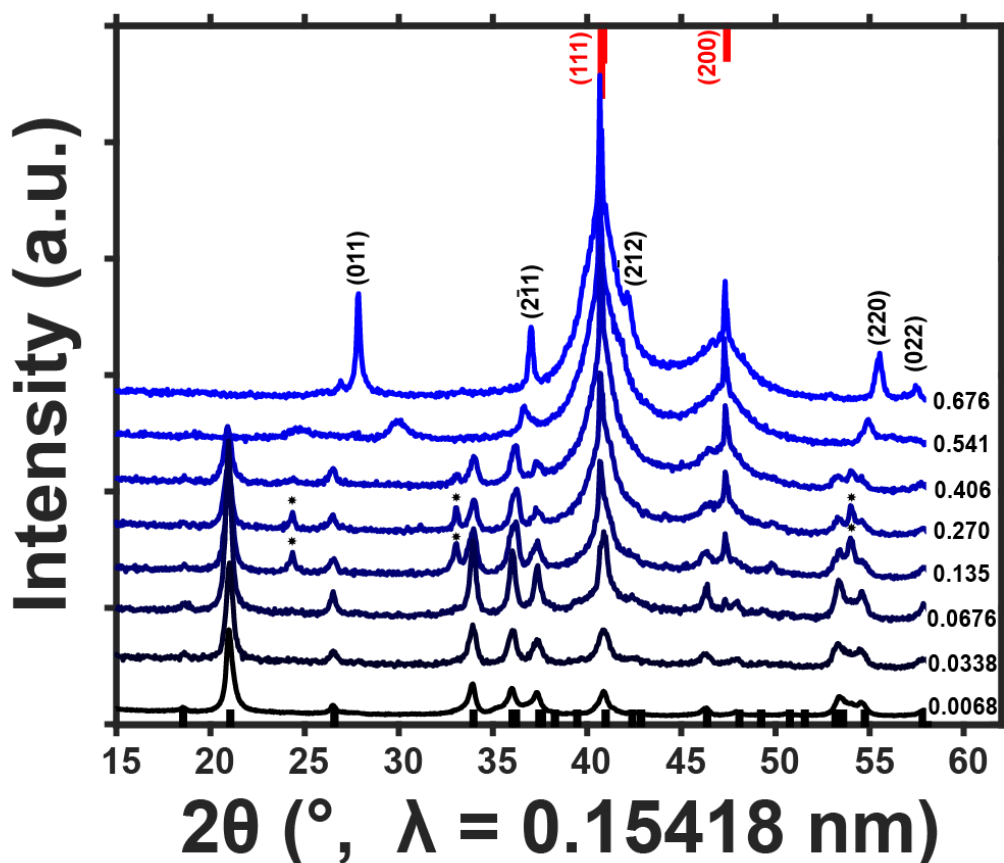
Figure 4.3. Evolution of Products as a Function of Increasing IrO_2 Added to Reaction Mixture. XRD patterns for samples prepared with increasing amounts of added Ir precursor from bottom to top. The relative ratio of Ir to V added to the reaction mixture is labeled on the right. Patterns for $VO_2(P)$ (black, as refined and indexed in Fig. 4.1a) and cubic iridium metal[44] (red, top) are included for reference. Reflections corresponding to the M_1 phase of VO_2 are indexed in black as per JCPDS/PDF card no. 043-1051. The asterisked reflections (*) denote the presence of karelianite V_2O_3 (JCPDS/PDF # 85-1403) contaminants in samples prepared from 0.135:1 and 0.270:1 ratios of Ir:V precursors.

Electron microscopy has been performed to analyze both the morphology of the stabilized $VO_2(P)$ materials as well as to examine the Ir nanocrystals stabilized when the Ir precursor concentration surpasses the solubility of Ir in the VO_2 lattice (**Fig. 4.4**). **Figure 4.4a** depicts TEM images of $VO_2(P)$ nanocrystals corresponding to an added Ir:V concentration of 0.0068:1 (XPS suggests that the concentration of incorporated Ir atoms is 1.28±0.40 at.%, **Fig. 4.5a**). Figure 4.4a shows multiple overlapping particles suggesting that $VO_2(P)$ phase is crystallized as thin nanoplatelets with approximately hexagonal lateral cross-sections. The nanoplatelet morphology is further corroborated by the SEM image shown in **Figure 4.4b**. The lateral dimensions of the nanoplatelets have been determined to be 47.5 ± 21.1 nm. **Figures 4.4c** and **4.4d** show low-magnification and high-resolution TEM images acquired for products obtained with a 0.0338:1 Ir:V ratio of precursors in the reaction mixture. In Figure 4.4c, a similar agglomeration of VO_2 nanoparticles is seen as observed in Figure 4.4a but with the addition of several sparsely distributed high-electron-contrast clusters of <5 nm diameter particles on the surface of the platelets. Lattice-resolved images such as depicted in Figure 4.4d indicate that these particles are metallic Ir nanocrystals with diameters ranging from 2.0—4.0 nm. Given the small size of X-ray coherent metallic Ir domains and their low concentration, it is not surprising that reflections corresponding to metallic Ir are not discernible in XRD patterns acquired for this sample (Fig. 4.3) even though nanoscopic islands are discernible in HRTEM imaging. Consequently, as will be further discussed below, even at this concentration, the Ir precursor content exceeds the solubility of Ir in the VO_2 sublattice and insoluble Ir atoms coalesce in the form of metallic Ir particles

121
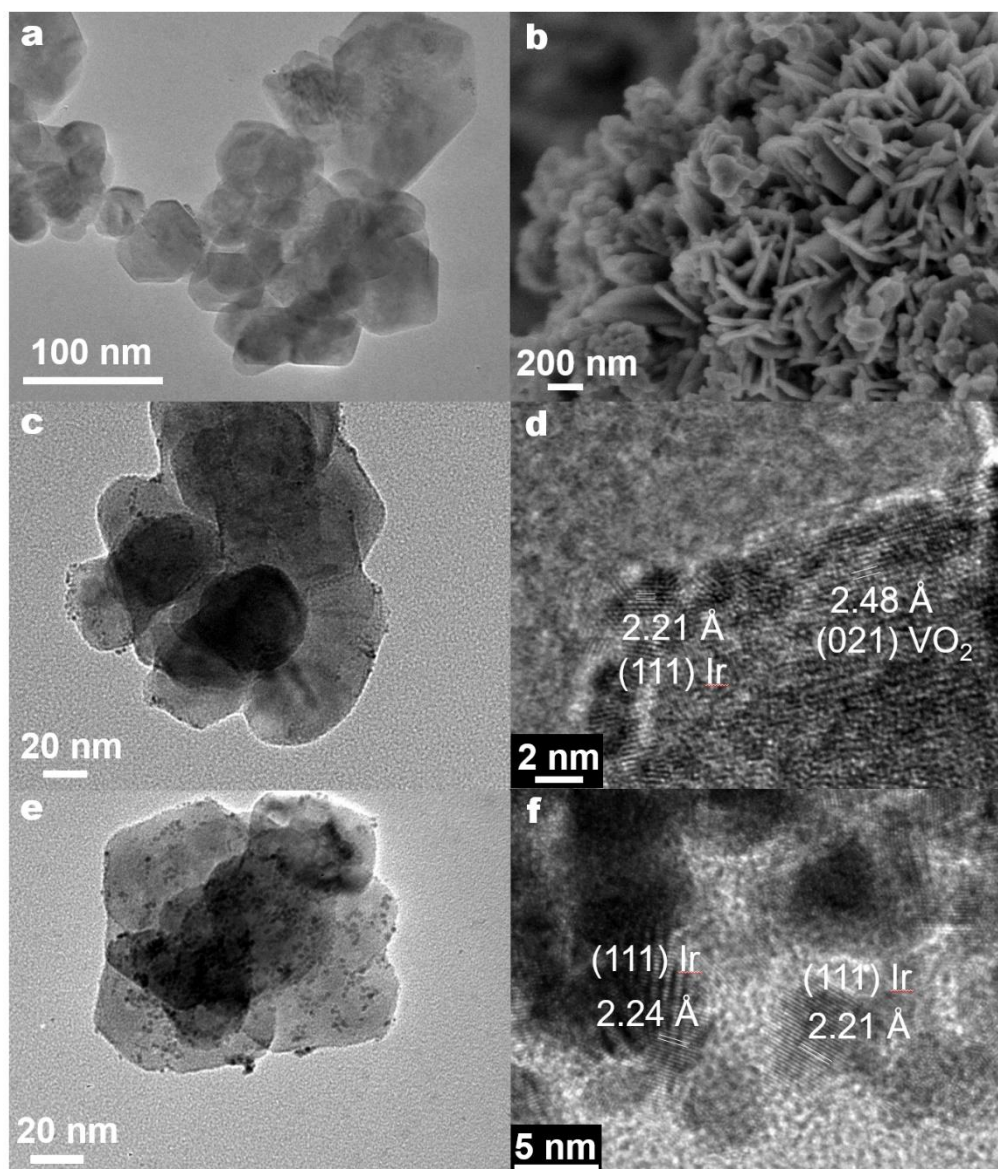
Figure 4.4. Electron Microscopy Characterization of $VO_2(P)$ and $VO_2(P)/Ir$ Heterostructures. (a) Low-magnification TEM and (b) SEM image of Ir-doped $VO_2(P)$ nanoplatelets. The intended Ir-dopant concentration is 0.0068 Ir/V, whereas XPS suggests incorporation of 1.28±0.40 at.% Ir on the V sites. (c) Low-magnification TEM and (d) high-resolution TEM image of an Ir-doped $VO_2(P)$ nanoplatelet with Ir:V precursor ratios of 0.0338:1. (e) Low-magnification TEM of Ir-doped $VO_2(P)$ nanoplatelet with Ir:V precursor ratios of 0.0676:1. (f) An individual Ir-doped $VO_2(M_1)$ nanoplatelet with Ir:V precursor ratios of 0.676:1. Ir nanocrystals with dimensions of ca. 2.0—4.00 nm are observed to be dispersed on the VO_2 nanoplatelets in the 0.0338:1, 0.0676 and 0.676:1 Ir:V samples but are much more abundant in the latter.

crystallized in the cubic phase. In contrast, **Figure 4.4e** shows that upon increasing the

Ir:V precursor ratio to 0.0676:1, the concentration of metallic Ir islands is furthermore

increased albeit XPS measurements suggest a higher amount of tetravalent Ir atoms as

well (estimated to be 3.15±0.82 at.%). At a Ir:V ratio of 0.676:1 in the reaction mixture,

a high density of well-defined metallic Ir particles with dimensions of ca. 5 nm are

observed almost entirely coating the VO_2 nanocrystals (which at this concentration are

crystallized in the M_1 phase) as depicted in **Figure 4.4f**. The dispersion of

nanocrystalline Ir metal on the VO_2 surfaces is suggestive of strong interfacial

interactions and likely derives from d-acid/base interactions as originally suggested by

Brewer wherein early (V) and late (Ir) transition metals undergo strong orbital mixing of

d-states yielding homogeneously dispersed clusters on the oxide surface.[35,36]

4.3.2. Dopant Structure

In order to elucidate the role of the Ir precursor in stabilizing the $VO_2(P)$ phase,

XPS analysis has been performed on samples prepared with increasing amounts of the

IrO_2 precursor. **Figure 4.5a** shows that the sample with the lowest amount of added IrO_2

precursor (0.0068 Ir/V) exhibits features at 61.3 and 64.2 eV, which can be assigned to

emission from Ir $4f_{7/2}$ and $4f_{5/2}$ states, respectively. In contrast, the precursor IrO_2 is

characterized by Ir $4f_{7/2}$ and $4f_{5/2}$ features at 61.8 and 64.8 eV, respectively. The shift of

the features to lower binding energies while still being in the 61.1—62.9 eV range

characteristic of $4f_{7/2}$ features of tetravalent Ir atoms[37–39] suggests the substitutional

incorporation of formally tetravalent Ir within the VO_2 lattice. Based on the survey XPS

scan, the concentration of Ir within this sample is estimated to be 1.28±0.40 at.%, which
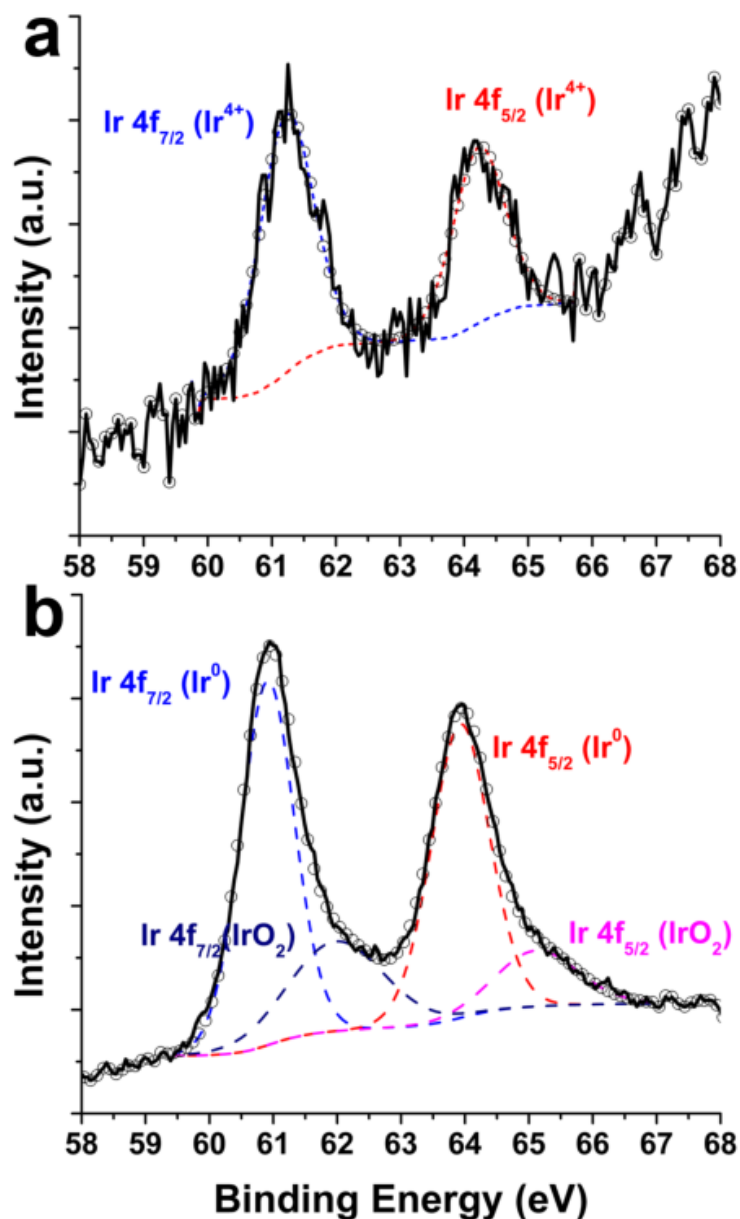
Figure 4.5. XPS Analysis of Dopant Oxidation State. High-resolution XPS spectra in the binding energy range of 58—68 eV corresponding to photoemission from Ir $4f_{7/2}$ and $4f_{5/2}$ for (a) $VO_2(P)$ prepared using a 0.0068:1 Ir:V ratio of precursors (an Ir content of 1.28±0.40 at.% is deduced from integration of the survey XPS span) and (b) $VO_2(P)$ sample prepared using a 0.406:1 Ir:V ratio of precursors (an Ir content of 33.88±7.18 at.% is deduced from integration of the survey XPS span). Fits for Ir^{4+} in (a) and Ir^0 and IrO_2 (b) are included as a measure of the formal valence of Ir within the prepared materials.

124

attests to the low solubility of Ir within the VO$_2$ lattice and is consistent with our observation that a good structure refinement can be obtained without accounting for Ir fractional occupancies on V sites. No metallic Ir is observed for this sample by XRD, XPS, or HRTEM. Increasing the added concentration of the Ir:V precursors to 0.0338:1 results in the appearance of sparsely distributed metallic islands (Fig. 4.4c) although the Ir content is too low to be detectable by XRD. At a Ir:V precursor ratio of 0.0676:1, the concentration of tetravalent doped Ir in the VO$_2$ lattice is estimated to be 3.15±0.82 at.% by XPS, which represents an upper bound of Ir solubility. The concentration metallic Ir nanocrystals is also increased under these conditions as suggested by both TEM and XRD analysis (Fig. 4.4e and Fig. 4.3, respectively). Further increase of the IrO$_2$ precursor concentration in the reaction mixture does not increase the amount of doped Ir and instead metallic Ir nanocrystals and remnant IrO$_2$ are observed, as also discernible from Fig. 4.3. Signatures of these two species are clearly discernible in **Figure 4.5b** corresponding to a sample prepared using a 0.406:1 ratio of the V and Ir precursors (the survey scan indicates an Ir content of 33.88±7.92 at.%). In other words, higher Ir concentrations facilitate increased dopant incorporation within the VO$_2$ lattice, as is typical of kinetically stabilized growth regimes up to a limit in the range of 1.28—3.15 at.%. A competing process for nucleation of metallic Ir is observed at the higher end of the solubility range and dominates at higher IrO$_2$ precursor concentrations. Interestingly, while tetravalent Ir is only sparingly soluble in VO$_2$ perhaps as a result of the estimated 6.25% differential in ionic radii and substantially different extent of covalency, the

125

limited amount of incorporated Ir is sufficient to stabilize the open-framework tunnel structure.

4.3.3. Metastability of the VO₂(P) Polymorph

The stability of the VO_2(P) polymorph with respect to the thermodynamically stable M_1/R polymorphs has been examined using DSC and *in situ* powder XRD measurements. **Figure 4.6a** shows a DSC trace acquired upon heating and cooling a VO_2(P) sample (with a substitutional Ir content of 1.28±0.40 at.%) in the range of -20 to 500°C. Two broad irreversible endothermic features are observed upon heating centered at 140 and 300°C with no corresponding features in the cooling trace. Instead, a small exothermic peak is observed at ca. 60°C upon cooling; **Figure 4.6b** indicates that this peak is reversible in subsequent cycles with an endothermic feature observed at ca. 68°C upon heating and an exothermic feature observed at ca. 58°C upon cooling. These transitions can be ascribed to the latent heat absorbed and released to mediate the $M_1{\rightarrow}$R and R${\rightarrow}M_1$ transitions of VO_2, respectively. The latent heat includes a lattice enthalpy contribution derived from the structural transformation accompanying the phase transition, which is partially offset by change of the phonon entropy as well as alteration of the conduction entropy of the electrons.[40,41]

Figure 4.6c shows the results of *in situ* powder XRD measurements acquired as a function of temperature. Consistent with the broad endothermic peak observed in Figure 4.6a, at a temperature of 200°C, the characteristic (110) reflection of the VO_2(P) phase is greatly diminished in intensity, whereas reflections at higher 2Θ values are retained, suggesting the loss of long-range order. At a temperature of 300°C, the (110)
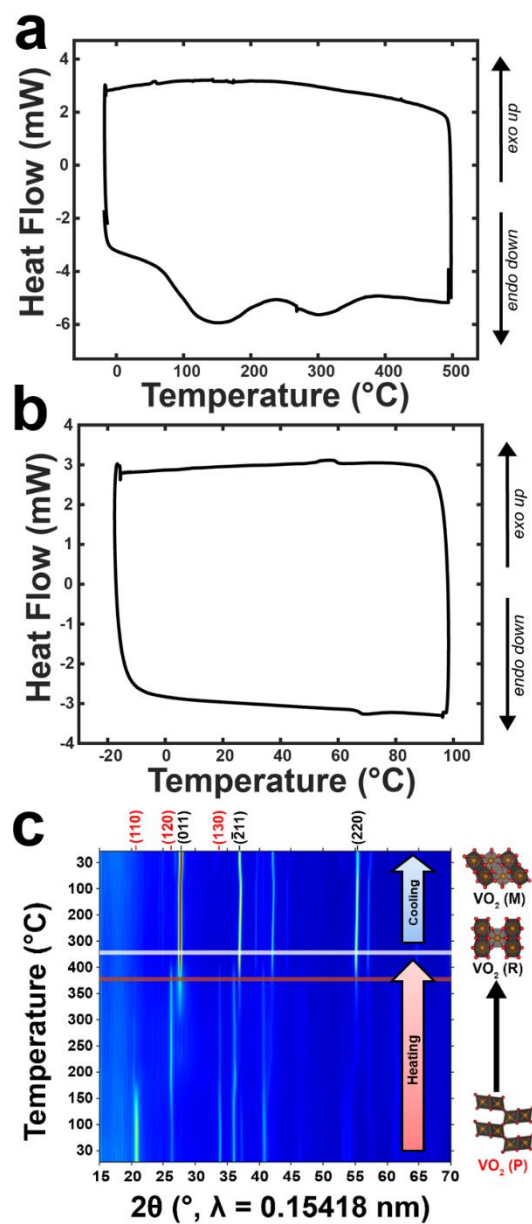
Figure 4.6. Evaluation of the Thermal Stability of $VO_2(P)$. (a) DSC plot corresponding to the heating (bottom) and cooling (top) of $VO_2(P)$ (with an Ir content of 1.28±0.40 at.%) from -20 to 500°C and back down to -20°C. (b) DSC trace for a second cycle wherein the material is heated from -20 to 100°C and then back down to -20°C. The endothermic and exothermic peaks at 68 and 58°C, respectively, can be assigned to the $M_1 \rightarrow R$ and $R \rightarrow M_1$ transitions of VO_2. (c) Intensity modulation maps reflecting the modulation of powder X-ray diffraction intensities upon *in situ* heating and cooling of $VO_2(P)$ to a temperature of 400°C and back down to 30°C. The red and blue indices depict reflections for $VO_2(P)$ and VO_2 (M_1), respectively. The red line denotes the complete structural transformation of $VO_2(P)$ to $VO_2(R)$. The white line represents a change from heating to cooling as also delineated by the arrows.

127

reflection of the R phase becomes discernible; the second endothermic feature in Figure 4.6a thus corresponds to crystallization of the R phase. Next, a phase coexistence regime is observed with a mixture of $VO_2(P)$ and the R phase until complete conversion to the R phase occurs between 350 and 400°C as delineated by the red line in Figure 4.6c. Upon cooling to 30°C, the monoclinic M_1 phase is stabilized, as also suggested by the characteristic exothermic feature in Figure 4.6b. The thermally induced conversion of $VO_2(P)$ to the thermodynamically stable M_1 phase upon heating confirms that the tunnel-structured phase is in fact a metastable structure.

4.4. Conclusions

While Ir has a low solubility in VO_2 (1.28—3.15 at.% on the cation sublattice depending on the precursor concentration), substitutional incorporation of tetravalent Ir in VO_2, achieved under hydrothermal conditions, results in stabilization of an open-framework metastable structure characterized by quasi-1D tunnels defined by corner- and edge-sharing distorted VO_6 octahedra. The incorporation of Ir appears to define tunnels with a rectangular cross-section as compared to trapezoid tunnels characteristic of a related paramontroseite mineral phase. The materials are obtained in the form of ultra-thin nanoplatelets. The metastable tunnel-structured phase is irreversibly transformed to the R phase upon thermal annealing to a temperature of ca. 350°C. The open quasi-1D tunnel framework and the facile accessibility of oxidative and reductive redox couples at the metal center suggest that the prepared frameworks are potential intercalation hosts.

The stabilization of metallic Ir nanocrystals competes with Ir incorporation in VO_2; such nanocrystals are found to nucleate at the surfaces of the nanoplatelets and are observed to be homogeneously dispersed. The homogeneous dispersion and small crystallite size suggests strong interfacial interactions with implications for the design of supported catalysts.

4.5. Experimental

4.5.1. Synthesis

Nanoplatelets of $VO_2(P)$ were synthesized hydrothermally by adding 300 mg of V_2O_5 (Sigma-Aldrich), 450 mg of oxalic acid (Fisher Scientific), and varying amounts of IrO_2 dopant (Strem Chemical, ranging from 5 to 500 mg) to 16 mL of deionized water (ρ = 18.2 MΩ cm^{-1}, purified using a Barnstead International NANOpure Diamond system) in a 23 mL polytetrafluoroethylene cup; the reaction mixture was heated within an autoclave (Parr Instrument Company) to 250°C for 72 h. A matte-black powder was recovered by vacuum filtration and washed with copious amounts of water and acetone.

4.5.2. Characterization

Powder X-ray diffraction (XRD) data were collected in Bragg—Brentano geometry on a Bruker D8-focus short-arm diffractometer equipped with a Lynxeye detector. Variable-temperature XRD data were collected using a Bruker D8-Vario X-ray powder diffractometer with a MTC oven attachment using Cu Kα radiation (λ= 1.5418Å) in an ambient atmosphere of argon. Rietveld analysis of the powder XRD data was performed using the EXPGUI interface in the GSAS software suite; all crystal structure renditions were generated using the VESTA software suite.[42,43]

X-ray photoelectron (XPS) spectra were collected using an Omicron system equipped with an Argus detector using a Mg Kα X-ray source with a source energy of 1253.6 eV. Sample charge neutralization was accomplished using a CN10 electron flood source. All high-resolution spectra were measured with an energy step size of -0.05 eV and a pass energy of 20 eV in constant analyzer energy (CAE) mode. The energy resolution of the XPS measurements was ca. 0.8 eV. Calibration of all high-resolution spectra was performed against the C 1s line of adventitious carbon at ca. 284.8 eV. Relative atomic concentrations of V, O, and Ir were determined using the CasaXPS 2.3.16 software based on application of the Marquardt-Levenberg optimization algorithm.

Low-magnification transmission electron microscopy (TEM) images were collected on a JEOL 2010 electron microscope at an operating voltage of 200 kV. High-resolution TEM images were acquired on a Tecnai G2 F20 ST instrument at an operating voltage of 200 kV. Scanning electron microscopy (SEM) images were acquired on a JEOL JSM-7500F field-emission SEM equipped with a high-brightness conical FE gun and a low-aberration conical objective lens. A cold cathode UHV field-emission conical anode gun was used as the source and imaging was performed at an accelerating voltage of 3 kV.

Differential scanning calorimetry (DSC) measurements were performed on a Thermal Advantage Q2000 instrument under a flowing Ar ambient. Scans were performed by scanning the temperature at a rate of 15°C/min from -20 to 500 °C in Tzero aluminum pans crimped sealed with Tzero lids.

4.6. References

[1]   W. Sun, S. T. Dacek, S. P. Ong, G. Hautier, A. Jain, W. D. Richards, A. C.

Gamst, K. A. Persson, G. Ceder, *Sci. Adv.* **2016**, *2*, e1600225.

[2]   J. Reed, G. Ceder, *Chem. Rev.* **2004**, *104*, 4513.

[3]   K. Deng, G. Wan, P. Deng, K. Zhang, S. Ding, E. Wang, M. Yan, H. Huang, H. Zhang, Z. Xu, J. Denlinger, A. Fedorov, H. Yang, W. Duan, H. Yao, Y. Wu, S. Fan, H. Zhang, X. Chen, S. Zhou, *Nat. Phys.* **2016**, *12*, DOI 10.1038/nphys3871.

[4]   B. M. Hudak, S. W. Depner, G. R. Waetzig, A. Talapatra, R. Arroyave, S. Banerjee, B. S. Guiton, *Nat. Commun.* **2017**, *8*, 15316.

[5]   A. Navrotsky, *ChemPhysChem* **2011**, *12*, 2207.

[6]   A. Ambrosi, Z. Sofer, M. Pumera, *Chem. Commun.* **2015**, *51*, 8450.

[7]   G. R. Waetzig, S. W. Depner, H. Asayesh-Ardakani, N. D. Cultrara, R. Shahbazian-Yassar, S. Banerjee, *Chem. Sci.* **2016**, *7*, 4930.

[8]   S. Mueller, J. Mueller, A. Singh, S. Riedel, J. Sundqvist, U. Schroeder, T. Mikolajick, *Adv. Funct. Mater.* **2012**, *22*, 2412.

[9]   T. Shimizu, K. Katayama, T. Kiguchi, A. Akama, T. J. Konno, O. Sakata, H. Funakubo, *Sci. Rep.* **2016**, *6*, 32931.

[10]   A. Parija, Y. Liang, J. L. Andrews, L. R. De Jesus, D. Prendergast, S. Banerjee, *Chem. Mater.* **2016**, *28*, 5611.

[11]   L. Whittaker, C. J. Patridge, S. Banerjee, *J. Phys. Chem. Lett.* **2011**, *2*, 745.

[12]   N. A. Chernova, M. Roppolo, A. C. Dillon, M. S. Whittingham, *J. Mater. Chem.* **2009**, *19*, 2526.

[13]   T. Chirayil, P. Y. Zavalij, M. S. Whittingham, *Chem. Mater.* **1998**, *10*, 2629.

[14]   J. B. Goodenough, *J. Solid State Chem.* **1970**, *1*, 349.

[15] P. M. Marley, G. A. Horrocks, K. E. Pelcher, S. Banerjee, *Chem. Commun.* **2015**, *51*, 5181.

[16] A. Parija, D. Prendergast, S. Banerjee, *ACS Appl. Mater. Interfaces* **2017**, *9*, 23756.

[17] T. M. Tolhurst, B. Leedahl, J. L. Andrews, P. M. Marley, S. Banerjee, A. Moewes, *Phys. Chem. Chem. Phys.* **2016**, *18*, 15798.

[18] J. H. Park, J. M. Coy, T. S. Kasirga, C. Huang, Z. Fei, S. Hunter, D. H. Cobden, *Nature* **2013**, *500*, 431.

[19] J. Galy, G. Miehe, *Solid State Sci.* **1999**, *1*, 433.

[20] C. Leroux, G. Nihoul, G. Van Tendeloo, *Phys. Rev. B* **1998**, *57*, 5111.

[21] F. J. Morin, *Phys. Rev. Lett.* **1959**, *3*, 34.

[22] H. T. Evans, M. E. Mrose, *U.S. Geol. Surv.* **1954**, 861.

[23] C. Wu, Z. Hu, W. Wang, M. Zhang, J. Yang, Y. Xie, *Chem. Commun. (Camb).* **2008**, 3891.

[24] Z. Wei, M. Yanyan, Z. Yunjiao, L. Liang, L. Jun, Y. Y. James, X. Yi, W. Longping, *Nanotechnology* **2013**, *24*, 165102.

[25] J. P. Pouget, H. Launois, T. M. Rice, P. Dernier, A. Gossard, G. Villeneuve, P. Hagenmuller, *Phys. Rev. B* **1974**, *10*, 1801.

[26] M. Ghedira, H. Vincent, M. Marezio, J. C. Launay, *J. Solid State Chem.* **1977**, *22*, 423.

[27] L. Whittaker, T.-L. Wu, C. J. Patridge, G. Sambandamurthy, S. Banerjee, *J. Mater. Chem.* **2011**, *21*, 5580.

[28]   C. J. Patridge, L. Whittaker, B. Ravel, S. Banerjee, *J. Phys. Chem. C* **2012**, *116*, 3728.

[29]   J. M. Booth, P. S. Casey, *Phys. Rev. Lett.* **2009**, *103*, 086402.

[30]   T. E. G. Alivio, D. G. Sellers, H. Asayesh-ardakani, E. J. Braham, G. A. Horrocks, K. E. Pelcher, R. Villareal, L. Zuin, J. Patrick, R. Arroyave, R. Shahbazian-yassar, S. Banerjee, *Chem. Mater.* **2017**, *29*, 5401.

[31]   Y. Filinchuk, N. A. Tumanov, V. Ban, H. Ji, J. Wei, M. W. Swift, A. H. Nevidomskyy, D. Natelson, *J. Am. Chem. Soc.* **2014**, *136*, 8100.

[32]   L. Lo, W. Mader, **2003**, *40*, 534.

[33]   C. Wu, F. Feng, J. Feng, J. Dai, J. Yang, Y. Xie, *J. Phys. Chem. C* **2011**, *115*, 791.

[34]   J. B. Goodenough, *Ann. Rev. Mater. Sci.* **1971**, *1*, 101.

[35]   M. E. Strayer, T. P. Senftle, J. P. Winterstein, N. M. Vargas-Barbosa, R. Sharma, R. M. Rioux, M. J. Janik, T. E. Mallouk, *J. Am. Chem. Soc.* **2015**, *137*, 16216.

[36]   L. Brewer, *Acta Metall.* **1967**, *15*, 553.

[37]   A. Minguzzi, C. Locatelli, O. Lugaresi, E. Achilli, G. Cappelletti, M. Scavini, M. Coduri, P. Masala, B. Sacchi, A. Vertova, P. Ghigna, S. Rondinini, *ACS Catal.* **2015**, *5*, 5104.

[38]   C. Wang, R. B. Moghaddam, S. H. Bergens, *J. Phys. Chem. C* **2017**, *121*, 5480.

[39]   L. Atanasoska, R. Atanasoski, S. Trasatti, *Vacuum* **1990**, *40*, 91.

[40]   A. V. Salker, K. Seshan, H. V. Keer, *Phys. Status Solidi* **1983**, *75*, K37.

[41]   J. D. Budai, J. Hong, M. E. Manley, E. D. Specht, C. W. Li, J. Z. Tischler, D. L. Abernathy, A. H. Said, B. M. Leu, L. A. Boatner, R. J. McQueeney, O. Delaire,

Nature **2014**, *515*, 535.

[42] B. H. Toby, *J. Appl. Crystallogr.* **2001**, *34*, 210.

[43] K. Momma, F. Izumi, *J. Appl. Crystallogr.* **2011**, *44*, 1272.

[44]   E. A. Owen, E. L. Yates, *London, Edinburgh, Dublin Philos. Mag. J. Sci.* **1933**,
15, 472.

5. MACHINE LEARNING-DIRECTED NAVIGATION OF SYNTHETIC DESIGN SPACE: A STATISTICAL LEARNING APPROACH TO CONTROLLING THE SYNTHESIS OF PEROVSKITE HALIDE NANOPLATELETS IN THE QUANTUM-CONFINED REGIME*

5.1. Overview

The design of a chemical synthesis often relies on a combination of chemical intuition and Edisonian trial-and-error methods. Such methods are not just inefficient but inherently limited in their ability to quantitatively predict synthetic outcomes, easily defeated by complex interplays between variables, and oftentimes based on suppositions that are limited in validity. The synthesis of nanomaterials has been especially prone to empiricism given the combination of complex chemical reactivity as well as mesoscopic nucleation and growth phenomena spanning multiple temporal and spatial dimensions. Here, utilizing the synthesis of 2D $CsPbBr_3$ nanoplatelets as a model system, we demonstrate an efficient machine learning navigation of reaction space that allows for predictive control of layer thickness down to sub-monolayer dimensions. Support vector machine (SVM) classification and regression models are used to initially separate regions of the design space that yield quantum confined nanoplatelets from regions yielding bulk particles and subsequently to predict the thickness of quantum confined $CsPbBr_3$ nanoplatelets that can be accessed under specific reaction conditions. The SVM models are not just predictive and efficient in sampling the available design space but

also provide fundamental insight into the influence of molecular ligands in constraining the dimensions of nanocrystals. The results illustrate a quantitative approach for efficient navigation of reaction design space and pave the way to navigation of more elaborate landscapes beyond dimensional control spanning polymorphs, compositional variants, and surface chemistry.

5.2. Introduction

Scaling periodic solids to nanometer-sized dimensions gives rise to distinctive quantum confinement effects, an increased proportion of atoms residing at surfaces, and the elimination of extended defects. Such phenomena have spurred intense interest in the programmable growth and assembly of nanomaterials with potential applications in optoelectronics, medical diagnostics, catalysis, and energy harvesting. Colloidal nanocrystal synthesis represents an important tool in the arsenal of synthetic materials chemists and provides access to well-defined monodisperse nanocrystals with surfaces passivated by coordinating ligands or electrostatically bound surfactants.[1–4] The synthesis of nanocrystals from molecular precursors is generally understood according to variations of nucleation and growth theory with the added ligands enabling the temporal separation of the two steps, stabilizing specific crystallographic facets through preferential binding, and providing control over monomer supersaturation.[5–9] Achieving precise synthetic control over the shape and size distributions of these ensembles of nanocrystals is imperative for the effective utilization of such materials. Recent efforts have sought to expand mechanistic understanding and establish correlations between precursor reactivity and the eventual crystal structure, dimensionality, shape, and surface

136

chemistry of nanocrystals; nevertheless, much of synthetic nanochemistry remains strongly reliant on the development of empirical synthetic strategies.[10–14] Edisonian trial-and-error methods involving changing a single synthetic variable and observing the response are standard practice but represent a rather inefficient means of exploring potentially vast design spaces. Such methods are furthermore limited in their ability to quantitatively predict synthetic outcomes and do not provide a satisfactory understanding of variable correlations, factors underpinning challenges with reproducibility, and parameters necessary to facilitate the application of modern process design tools. Some initial attempts at bringing statistical learning to nanocrystal synthesis have invoked design of experiments (DOE) methods such as full and fractional factorial sampling coupled with ridge regression to establish correlations between synthetic variables and nanocrystal dimensions.[15,16] These methods provide a means of rapidly exploring synthetic correlations but impose specific sampling constraints on creation of the model and often interpolate large areas of the design space. In contrast, machine learning approaches are more versatile in enabling the use of incomplete (and sparse) datasets not acquired according to specific constraints allowing for the creation of robust models for the prediction of quantitative or qualitative synthetic outcomes. In this article, we demonstrate the application of a non-linear data-driven machine learning model to predictively control the layer thickness of perovskite halide nanoplatelets.

The intersection of machine learning and chemistry has provided new opportunities spanning the range from atomistic design of solid-state compounds to elucidation of ligand parameters underpinning molecular catalysis[17–19] and mapping of

compositional gradients in hyperspectral maps of discharged cathode materials.[20] Nonlinear modeling, such as using support vector machines for classification or regression, has proven to be successful at predicting a wide range of materials properties based on elemental parameters and atomic interactions ranging from crystal structure to band gap.[21–25] However, such methods have rarely been applied to a singular chemical synthesis due to the cost of creating a viable dataset large enough to both provide new chemical insights and avoid overfitting. By utilizing existing synthetic results as initial datasets, input data can be efficiently acquired to allow for the meaningful use of robust nonlinear modeling techniques. Size control in nanocrystal synthesis provides an excellent output for evaluating quantitative predictive models developed based on existing data. The synthesis of 2D $CsPbBr_3$ perovskite nanoplatelets is used here as a model system given the clear layer-thickness-dependent photoluminescence spectral signatures that allow for rapid evaluation of size distributions within samples.[26–28]

Lead halide perovskites have attracted extensive interest as a result of their remarkable properties including tunable exciton binding energies, high oscillator strengths of bandgap transitions, narrow emission bands, and high photoluminescence quantum yields.[29–34] $CsPbBr_3$ is a stable all-inorganic perovskite accessible from solution-phase synthesis; dimensional confinement below the characteristic Bohr radius of 3.5 nm brings this material to the quantum confined regime and allows for tunability of the bandgap as a function of the layer thickness.[35] Discrete photoluminescence emission bands characteristic of each layer thickness indicate a pronounced modulation of the bandgap from 2.36—3.20 eV upon scaling from the bulk material down to

138

monolayer platelets.[36,37] Control of the layer thickness is generally accomplished

through ligand-assisted synthesis.[35,38,39] In this work, utilizing photoluminescence

spectroscopy as the primary probe, we demonstrate a predictive, statistically informed

model for synthetic control of particle thickness developed using a sparse dataset. A

machine learning approach for exploration of multivariate design space further provides

mechanistic insight into the role of the ligand shell in inducing dimensional confinement.

5.3. Results and Discussion

5.3.1. Mapping Multivariate Reaction Space

Figure 5.1A represents an initial data set for the synthesis of $CsPbBr_3$

nanoplatelets prepared using a hot colloidal method where multivariate reaction

parameters have been explored by independently varying the reaction temperature (50,

100, and 150°C at a fixed Pb:alkylamine ratio of 1:20), ligand concentration (in the 1:x

range spanning $x = 5$—40 (wherein x is concentration of alkylamine) at a constant

temperature of 100°C), and chain-lengths of n-alkylamine ligands (C4, C8, C12, and

C18). The addition of coordinating amine ligands brings about pronounced dimensional

confinement as schematically illustrated in Figure 5.1B.[38,45]

Colloidal $CsPbBr_3$ nanoplatelets adopts a distorted orthorhombic crystal structure upon

dimensional confinement, which stands in contrast to the cubic phase stabilized at high

temperature (>130°C) and tetragonal phase at intermediate temperatures (88-130°C) of

bulk $CsPbBr_3$.[46] The powder X-ray diffraction patterns (XRD) in Figure 5.1C for

$CsPbBr_3$ nanoplatelets grown using alkylamines with different chain lengths can be

indexed to the orthorhombic phase.[38,46,47] The average layer thickness ($n_{avg.}$) of 2D

CsPbBr$_3$ nanoplatelets is expressed in terms of the number of [PbBr$_6$]$^{4-}$ octahedral layers.

Values
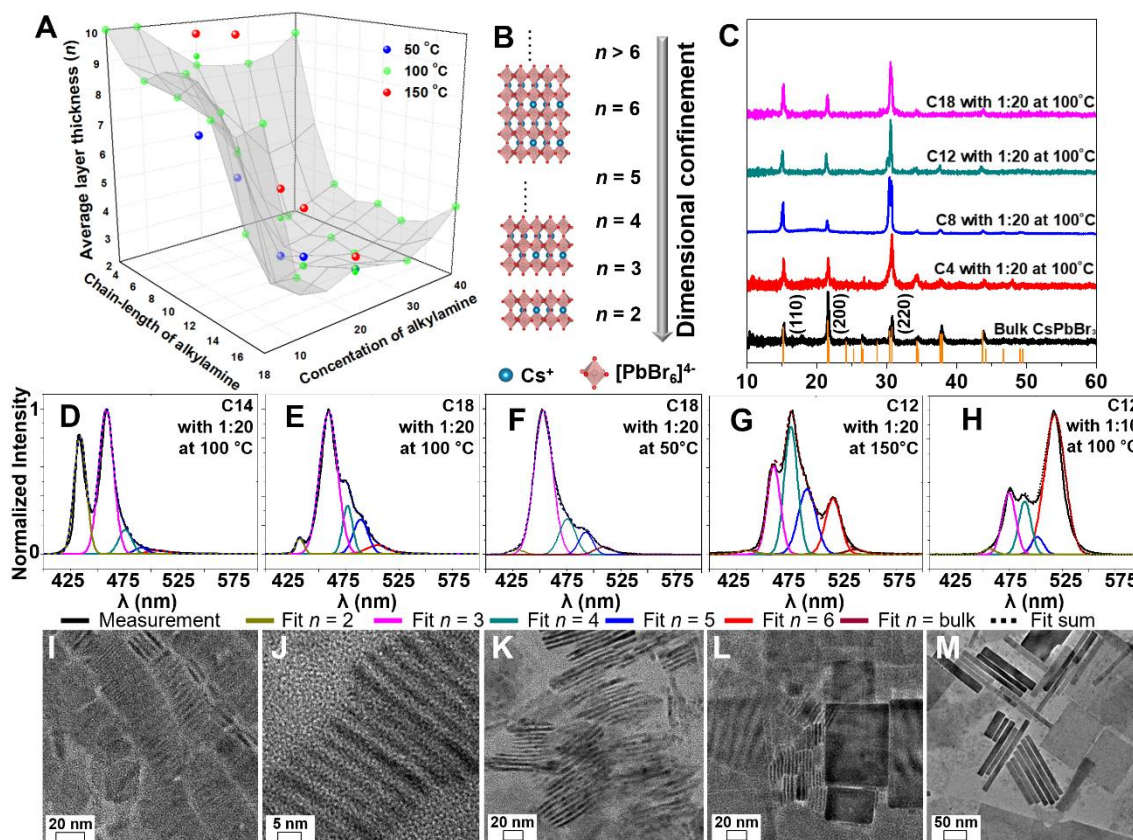
Figure 5.1. Sampling of the multivariate design space for the synthesis of CsPbBr$_3$ nanoplatelets. (A) 3D visualization of the average layer thickness as a function of the ligand chain-length and concentration at different reaction temperatures with added contrast on overlapping data points; (B) schematic illustration of ligand-induced dimensional confinement; (C) XRD patterns of CsPbBr$_3$ nanoplatelets as a function of the alkylamine chain length; the orange ticks on the horizontal axis correspond to the reflections of orthorhombic CsPbBr$_3$ with PDF# 01−072−7929. (D)-(H) PL emission spectra of CsPbBr$_3$ nanoplatelets grown under different reaction conditions and (I)-(M) corresponding TEM images obtained for these samples. The photoluminescence emission spectra have been obtained at an excitation wavelength of 360 nm and are fitted to multi-peak Gaussian lineshapes representing the characteristic emission bands of different layer thicknesses.

of $n_{avg.}$ plotted in Figure 5.1A been determined from the photoluminescence (PL) emission spectra as described in the experimental section and have been further verified by electron microscopy.[38] The photoluminescence emission spectra have been fit to multiple Gaussian distributions centered on the wavelengths of the discrete emission bands to deconvolute the fractional contribution of individual emission bands. The correlation between $n_{avg.}$ and the thickness determined by TEM (t_m) is illustrated for five representative samples in Figures 5.1D—M. Figures 5.1D—H exhibit the photoluminescence spectra and Figures 5.1I—M show the corresponding TEM images.

Unlike II-VI quantum dots, the size distribution of CsPbBr$_3$ 2D nanoplatelets is not continuous but instead discretized based on the layer thicknesses. Emission spectra acquired at each set of reaction conditions are characterized by multiple PL emission bands quantized to populations of different layer thicknesses and manually assigned to peak positions as previously determined in single-particle PL emission spectra measurements.[28,36,38] **Figure D.1** plots the PL emission wavelength of 2D CsPbBr$_3$ nanoplatelets measured from single-particle measurements *versus* the vertical dimension of nanoplatelets.[38] In the strongly quantum confined regime (below $n = 10$ and 6 nm), the energy bandgap (and consequently the photoluminescence resulting from bandgap emission) varies strongly as a function of layer thickness. As the vertical dimension of CsPbBr$_3$ nanoplatelets increases to greater than the exciton Bohr diameter, the PL emission converges to a maximum wavelength of approximately 525 nm (which reflects the 2.36 eV bandgap of bulk CsPbBr$_3$) and no longer varies with thickness. Emission bands at 525 nm are assigned to $n = 10$ layers when computing n_{avg}; the validity of this

assignment is further examined below. It is worth noting that the type of alkylamine ligand induces subtle shifts of PL emission maxima owing to (i) variations in types and concentrations of trap states, (ii) differences in dielectric constants and surface dipoles of the ligand shell, (iii) extent of electronic coupling between nanoplatelets.[38,48,49] Instead of fitting to the same peak maximum across all conditions, each spectrum has been manually fitted to account for these shifts of the PL emission maxima. **Figure D.2** shows the fitting residual obtained from subtracting the multi-Gaussian fit sum from the experimental PL emission spectrum for the $CsPbBr_3$ nanoplatelets synthesized using C12 with 1:40 at 100 °C demonstrating that the residuals are negligible and distributed randomly around zero. This procedure (in contrast to unconstrained automated fitting protocols) yields discrete bands correspondent with the single-particle emission spectra.

The oscillator strength of 2D $CsPbBr_3$ nanoplatelets can vary somewhat as a function of layer thickness depending on the specific synthetic route. However, there is considerable literature precedent of the PL quantum yield (QY) of $CsPbBr_3$ perovskite nanocrystals in the quantum confined regime being within the same order of magnitude (33 % for $n = 3$, 44.7 % for $n = 4$, 31 % for $n = 5$) since these nanocrystals are not as prone to surface traps as II-VI semiconductors. Indeed, the elimination of trap states and the resulting defect-tolerant band structure is pivotal to the utilization of the relative intensities of discrete PL bands as a reliable proxy for the fractional contributions of different layer thicknesses.[28,37,40,50,51] **Figure D.3** exhibits additional TEM images acquired for the five samples noted in Figure 5.1. The average layer thicknesses from left to right are $n_{avg.} = 2.8$ ($t_m = 1.9\pm0.4$ nm), $n_{avg.} = 3.5$ ($t_m = 2.3\pm0.4$ nm), $n_{avg.} = 3.5$ (t_m

= 2.5±0.3 nm), $n_{avg.}$ = 5.1 (t_m = 3.0±0.3 nm), and $n_{avg.}$ = 7.9 (t_m = 10.3±0.7 nm) ordered

from thinner to thicker nanoplatelets. A strong correlation is observed between the

spectroscopic measurements and TEM imaging of layer thicknesses when the dimension

of 2D nanoplatelets is below the exciton Bohr diameter in the strongly quantum confined

regime, which corroborates the validity of the former method in providing a quantitative

metric of layer thickness in the quantum confined regime.

Table D.1 summarizes the results of the syntheses, shown in Figure 5.1A, and

the estimated populations corresponding to the different layer thicknesses. Figure 5.1

illustrates the clear influence that the choice of the ligand exerts on the extent of

dimensional confinement of 2D $CsPbBr_3$ nanoplatelets. In general, higher ligand

concentrations, longer alkyl chain lengths, and lower reaction temperatures are observed

to result in the stabilization of few-layered nanoplatelets in the strongly quantum

confined regime. In contrast, lower ligand concentrations, shorter chain lengths, and

higher reaction temperatures bring about rapid growth of thicker nanoplatelets

approaching the bulk limit. The extent of dimensional confinement is generally

understood to depend on the crystalline order of the self-assembled monolayer of ligand

molecules and their dynamic equilibrium with free ligand molecules in solution.[45] The

structure of the ligand shell, the extent of monomer supersaturation, and the rate of

monomer addition are in turn determined by the length of the alkyl chains, their

branching, the reaction temperature, and concentrations. In this article, we have sought

to develop a predictive machine learning model that captures the complex interplay

between these reaction parameters.

In addition to the vectoral exploration shown in Figure 5.1A, 34 additional samples were synthesized randomly expanding the dataset to areas of design space that do not fall along the initial exploration vectors and are summarized in **Table D.2**. These selections were not selected for design space optimization but in the hope that a more random dataset would allow for better sampling of the design space and improve the robustness of the machine learning modeling methods.

5.3.2. Classification, Curation, and Feature Set Development

The initial dataset of 74 samples has been used to build two models of the reaction design space: (*a*) a classifier to define a boundary between bulk and quantum confined particles and (*b*) a regressor to predict the thickness of particles in the quantum confined regime. **Figure 5.2** depicts the steps involved in the modeling procedure beginning with curation of the dataset and feature set development, followed by modeling of both the classifier and regressor, and finally, validation of the regressor using samples randomly selected from the quantum confined regime as determined by the classifier.

The first step in most machine learning processes involves identifying the features that best describe the data.[22] In the case of the $CsPbBr_3$ nanocrystal synthesis, the goal of relating synthetic parameters to layer thickness limits the selection of features to the independent variables explored in the experimental dataset spanning ligand choice, ligand concentration, and reaction temperature. In principle, numerous other factors can contribute to determining the product distribution, including ambient pressure, stirring rate, injection rate, precursor reactivity, and concentration of

144

precursors, which would altogether define an even more complex design space than considered here. In this case, in order to constrain the model system and limit the dimensionality of independent variables to three, these variables have been held
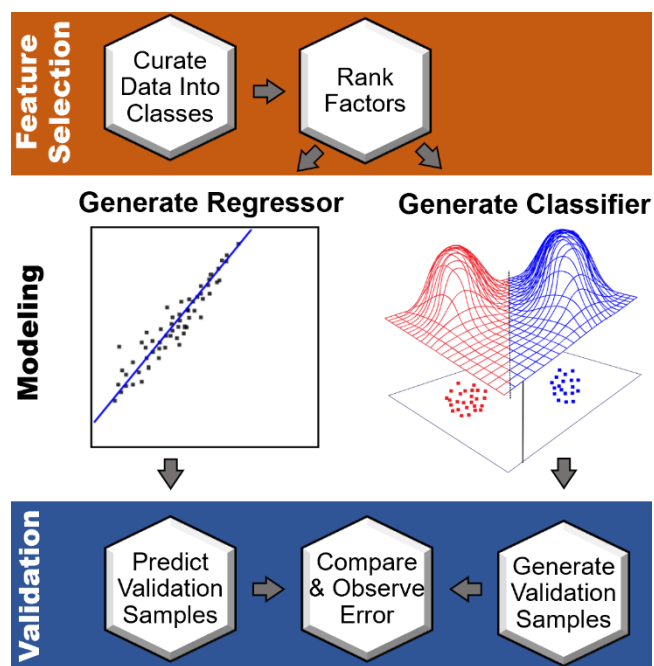
Figure 5.2. Schematic depiction of steps involved in developing a predictive model for the synthesis of $CsPbBr_3$ nanoplatelets.

constant. The effect of these variables that have been held constant on the experimental dataset shown in Tables D.1 and D.2 is within the experimental noise. It is worth noting that characteristics such as precursor concentrations further shift the synthetic landscape to enable entirely different synthetic outcomes within the ternary Cs-Pb-Br system such as stabilization of the 0D Cs_4PbBr_6 phase. Clear trends are discernible in Figure 5.1A for the independent variables, ligand choice, ligand concentration, and temperature, in terms

of their ability to influence the particle size.[38] A metric needs to be defined that best captures the influence of the ligand chemical structure and composition on the kinetics of crystal growth to allow for regression and interpolation to new values. A series of values have been tabulated for the *n*-alkylamine physical and chemical properties (**Table D.3**) and compared using both a t-test, as shown in **Table 5.1,** and by error analysis of a models calculated with each descriptor (a wrapper), the results of which are presented in **Tables D.4 and D.5**. The classes being compared in the t-test have been created by curating the dataset into two sections: a rigorously quantum confined class comprising samples where <5% of photoluminescence intensity arises bulk particles (31 samples, shaded grey in Tables D.1 and D.2) and a bulk class comprising all the samples where over 50% of the photoluminescence intensity can be ascribed to bulk $CsPbBr_3$ particles (17 samples, shaded blue in Tables D.1 and D.2). The heuristic decision to omit samples containing 5—50% bulk photoluminescence intensity allows for mitigation of errors in misclassifying of samples arising from experimental variability in particle thickness. The wrapper, as well as subsequent regressive models, used samples that contained <50% bulk photoluminescence intensity (57 samples).

Table 5.1 computes the t-test scores (equal variance two sample t-test) for different chemical and physical properties of *n*-alkylamines of varying chain lengths from 4—18 carbons used as the capping ligands with regards to their effectiveness; the T statistic, a relative score with an absolute value representative of the separation of the two classes; and the p-values, a normalized value indicating the significant difference between the two classes based on the distributions along the tested variables are

146

Table 5.1. T and P value results for t-testing of various alkylamine descriptors.

Factors	Ref.	T score	p-value
Diffusion coefficient 20°C	45	4.884	1.30×10^{-5}
Boiling point	59	-4.855	1.43×10^{-5}
Enthalpy of vaporization	59	-4.776	1.86×10^{-5}
Density	60	-4.745	2.06×10^{-5}
Melting point	60	-4.719	2.24×10^{-5}
^{1}H-NMR shift (terminal CH_3)	61	4.700	2.39×10^{-5}
Molar mass	60	-4.526	4.23×10^{-5}
Chain length	n/a	-4.526	4.23×10^{-5}
ΔG agglomeration 100°C	62	4.526	4.23×10^{-5}
Polarizability	59	-4.518	4.35×10^{-5}
^{1}H-NMR shift ($-NH_2$)	61	4.246	1.05×10^{-4}
Dipole moment	63	-4.033	2.05×10^{-4}
pKa	60	-0.525	6.02×10^{-1}

delineated for each of tabulated properties. Properties reflective of nonpolar alkyl chains that are governed by additive chain-length-dependent intermolecular London dispersion forces, such as the diffusion coefficient and boiling point, yield T statistics farthest from zero accompanied by the smallest P values. Conversely, properties that in essence are associated with the amine functionality, such as pKa, the electronic shielding of the amine hydrogens, and the dipole moment yield T statistics closest to zero and the largest P values which is indicative of the relative insensitivity of properties determined by the amine functionality on the length of the alkyl chains. These results are furthermore mirrored for the best performing regression method in the wrapper analysis using leave-one-out cross-validation to analyze the predictive error as discussed in the next section.

According to this descriptor analysis, the ligand diffusion coefficient (at constant temperature), computed as:

$$D = \frac{k_b T}{6\pi\eta a} ln\left(\frac{2a}{b}\right) \qquad\qquad \textbf{5.1}$$

where k_b is Boltzmann's constant, T is temperature, η is the solvent viscosity, a is the radius of the long axis of the molecule, and b is the short axis of the molecule, is marginally the best metric for separating the bulk samples from the quantum confined regime in the t-test (as well as the top performing descriptor in the wrapper) and thus will be used as the numerical representation of choice to denote the alkylamine used in synthesis.[45] A singular descriptor representing the amine is most appropriate for the intended modeling owing to bias introduced using colinear variables in a feature set of only three independent variables. However, combinations of descriptors could be particularly useful for multi-objective optimization such as for control over layer thickness and quantum yield. The diffusion coefficient has previously been shown to be a useful measure of capping ligand effects owing to the ability to capture the shape of the molecule and its interaction with the solvent within one numerical parameter.[45] Notably, the T scores for reaction temperature and ligand concentration computed in the same manner are 2.411 and -3.676, respectively, which suggests that it is the choice of ligand rather than these parameters that have the most pronounced impact on the extent of dimensional confinement.

5.3.3. Modeling and Model Validation

Using the same heuristically separated classes as defined for the t-test, a classifier has been generated to separate the bulk samples from the quantum confined regime in design space with the objective of first developing a model that provides a predictive binary output of "bulk" or "quantum confined". A three-dimensional non-linear decision

boundary has been created to separate these classes along the axes of reaction temperature, ligand concentration, and ligand diffusion coefficient. The classes of data are seen not to be linearly separable and thus support vector machine (SVM) classification has been used with a radial basis kernel (**Fig. 5.3**) to define the decision boundary.[42] The SVM classifier shows no apparent test-set error; leave-one-out cross validation (an error metric where a single datum is removed, the model computed, and the left out datum is predicted and compared to the true value and repeated for every data point in the set to get an average error) exhibits a misclassification error of 2.1% indicating that this boundary is both robust and successful at classifying bulk from quantum confined nanocrystals as a function of the synthetic conditions. This classifier has further been used to select samples for a validation set to evaluate the performance of the regressor that will be subsequently described.

Regression is commonly used to create models in datasets where the relationship between the input and output is a known function (*e.g.*, linear, quadratic). However, in complex or higher dimensional systems where functions or variable correlation is unknown, a non-linear data driven regression oftentimes better captures relationships within the data. In order to investigate a model that can predict the average layer thickness of $CsPbBr_3$ from a sparse data set, we will examine four regressors: linear, quadratic, quadratic with cross terms, and support vector machine regression (SVM) using a radial basis kernel, the lead machine learning model. For comparison, several other machine-learning based models were tested including SVM with linear, quadratic, and cubic kernels, KNN regression with k = 3, and linear ridge regression with penalty λ
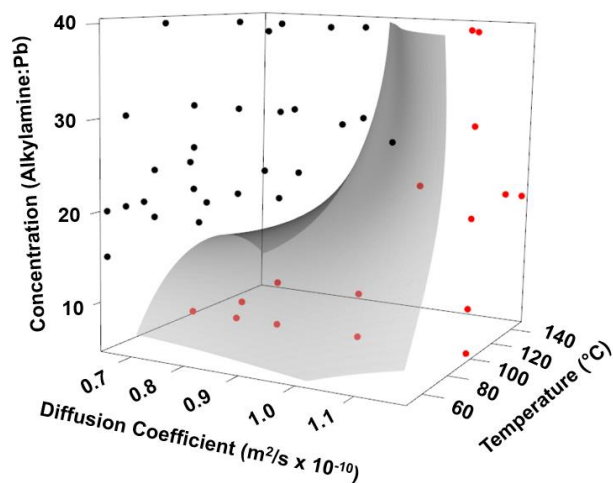
Figure 5.3. 3D scatter plot showing the SVM classifier decision boundary (grey surface) separating quantum confined samples containing <5% bulk photoluminescence intensity (black/left) from bulk samples containing >50% bulk photoluminescence emission (red/right).

values ranging from 50-0.001. The results of these models can be found in Tables D.4 and D.5 where each method was included in the wrapper analysis of the alkylamine descriptors.

A dataset of 53 samples has been used for this analysis including all samples from the original experimental data set that contain a majority of quantum confined particles (<50% of the photoluminescence is derived from bulk particles). The four regressors have been analyzed using leave-one-out cross validation to estimate the error. **Figure 5.4** shows the cross-validation results in the form of a plot of actual average layer thickness plotted *versus* the predicted average layer thickness according to the regressor as well as an evaluation of the root-mean-squared cross-validation errors (RMSE-CV). Linear regression provides the largest error with a RMSE-CV of 1.0266 layers; Figure
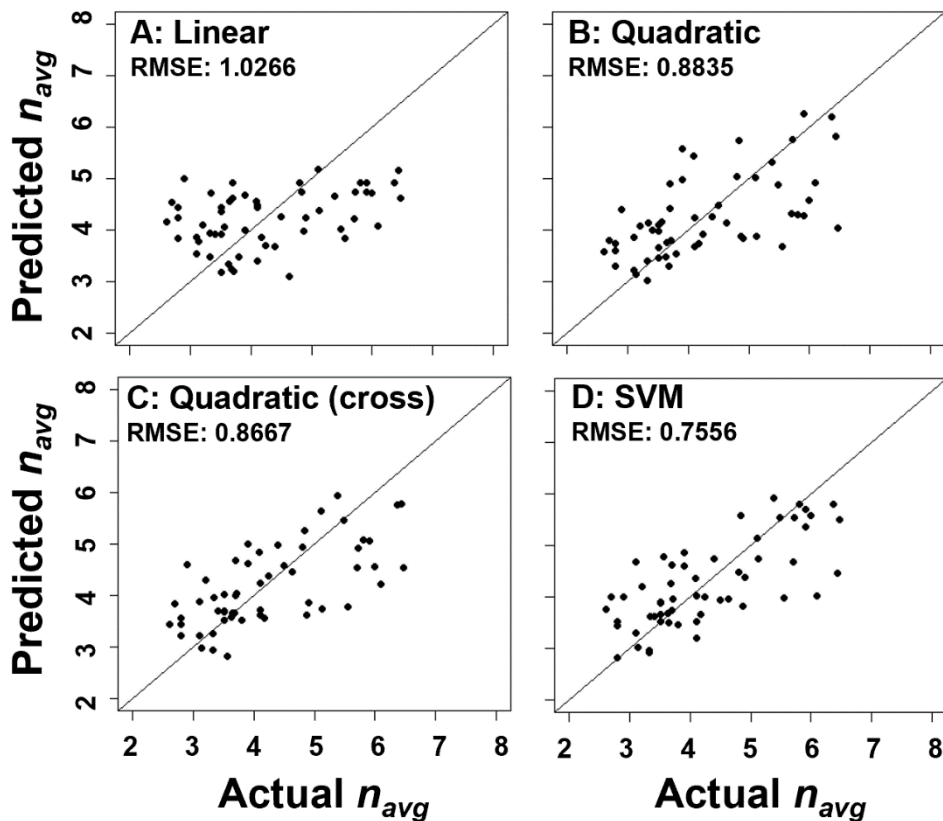
Figure 5.4. Leave-one-out cross validation results for four different regression models predicting the synthesis of CsPbBr$_3$: (A) linear regression ($R^2 = 0.645$), (B) quadratic regression ($R^2 = 0.838$), (C) quadratic regression with cross terms ($R^2 = 0.861$), and (D) support vector machine regression ($R^2 = 0.965$). The $Y = X$ line is delineated as a representation of an ideal prediction. R^2 values are for the model fits to the experimental data with the full 57 data point set.

5.4A shows that such a regression overestimates thinner $n_{avg.} = 2$—3.5 layer samples and

underestimates thicker samples with $n_{avg.} > 5$. The quadratic fit in Figure 5.4B has a

more even error distribution but is prone to large error, particularly for $n_{avg.} > 5$

predictions, which appear to be generally underestimated, resulting in a RMSE-CV of

0.8835 layers. The addition of cross terms to the quadratic regressor, which allows for a

degree of correlation in the variables (Fig. 5.4C), yields a RMSE-CV of 0.8667 layers

and a similar result wherein samples of $n_{avg.} > 5$ have large underestimation errors. The SVM regressor (Fig. 5.4D) performs the best with a RMSE-CV of 0.7556 layers but still shows some underestimation of layer thicknesses for $n_{avg.} > 5$ layers. This regression is the top performer of all the tested machine learning models shown in Tables D.4 and D.5. This lead model has an aforementioned RMSE-CV of 0.7556 layers, a coefficient of determination of 0.895, a gamma of 0.5, a cost of 2.1 and a support vector count of 48.

The difficulties in accurate prediction of thicker layers derives from assumptions made in inclusion of bulk photoluminescence emission as a constant 10 layers, which thereby introduces greater error in samples with proportionately larger bulk contributions. Note that this is essentially a limitation of the spectroscopic method, which allows for clear delineation of layer thicknesses near the quantum confined regime but does not allow for multilayered platelets to be distinguished in the bulk regime. **Figure D.4** plots the RMSE leave-one-out cross validation as a function of the estimated bulk thickness demonstrating that the estimate of 10 layers is the best option for a bulk estimation to avoid skewing the data to higher averages (which would increase the cross-validation error). Despite this underestimation, the RMSE values of the cross-validation analysis indicate that the SVM model has achieved a reasonable level of predictivity for this dataset achieving sub-monolayer accuracy.

Video D.1 exhibits the four-dimensional design space mapped by the SVM model indicating the evolution of the layer thickness as a function of the diffusion coefficient and ligand concentration with increasing temperature. **Figure 5.5** plots contour SVM regressor slices from this model. Examination of the SVM model built

from the 57 quantum confined samples indicates that the model approximation of the response space is influenced by each independent variable. **Figure 5.5A** shows a slice of the regressor output at 50°C with the color map corresponding to the predicted layer thickness for the given synthetic conditions. A minimum of 3.0 average layers can be observed at an approximate ligand concentration of Pb:alkylamine of 1:30 for a ligand diffusion coefficient of 0.85×10^{-10} m^2/s. The location of this minimum indicates that at 50°C, increasing the concentration and the chain length (decreasing diffusion coefficient) yields smaller predicted thicknesses (up until a precursor:ligand ratio of 1:30 and diffusion coefficient of 0.85×10^{-10} m^2/s, respectively). Further increases in ligand concentration and chain length bring about an increase in thickness. The increase observed for 1:x concentrations greater than 1:30 is most likely a result of (i) the rapid formation of the ligand shell at high ligand concentrations, which results in shells with less regular packing that are more pervious to monomer addition, as well as (ii) the high concentration of complexed monomeric species. Both these factors result in more rapid crystal growth yielding thicker nanoplatelets. The increase in thickness with diffusion coefficients lower than 0.85×10^{-10} m^2/s, corresponding to higher chain lengths, is furthermore a reflection of the increased disorder of ligand shells for longer-chain alkylamines at low temperatures. Disordered ligand shells with lower packing densities allow for easier monomer addition, which results in the growth of thicker nanoplatelets (**Fig. 5.6**).[38] Indeed, the self-assembly of *n*-alkylamines on surfaces proceeds through initial adsorption and desorption steps until the system approaches quasi-equilibrium close-packed conditions as sketched in Figure 5.6 wherein dispersive interactions have

153
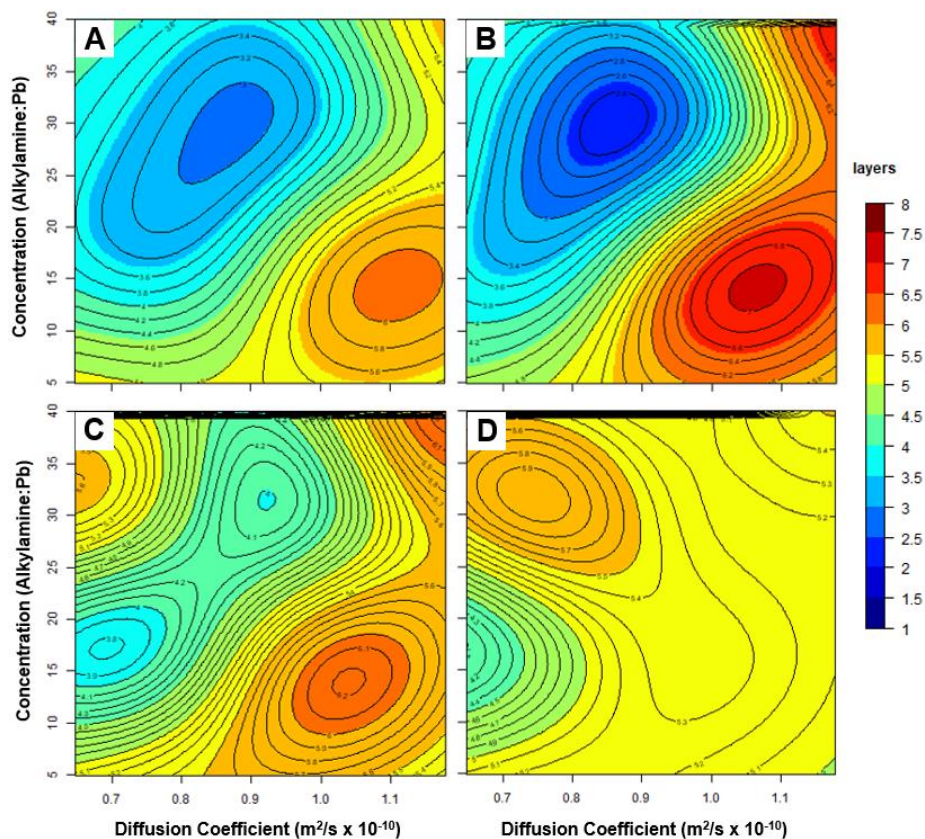
Figure 5.5. Contour plot slices of the SVM regression at temperatures of (A) 50°C, (B) 82°C, (C) 120°C, and (D) 150°C. Video S1 shows the continuous evolution of the contours as a function of temperature.

been maximized along the chain lengths, thereby yielding the most optimal enthalpic stabilization to offset entropic losses from conformational restrictions.[52] For longer chain amines at lower temperatures, thermal desorption is more hindered and thus kinetically trapped imperfectly ordered ligand shells are more likely to be stabilized, allowing for an increased rate of monomer addition and faster crystal growth.[38,52,53] Remarkably, the SVM model accurately captures this complex interplay between enthalpic and entropic factors.

154

The correlation of average layer thickness of $CsPbBr_3$ nanoplatelets to synthetic conditions is not intuitive given the trade-offs between entropic and enthalpic factors, kinetics and thermodynamics of ligand shell assembly (**Fig. 5.6J**), and sensitivity of the stabilized phase to ligand denticity, concentration, and branching.[45] In a similar vein, temperature both accelerates growth kinetics and monomer diffusion while allowing for stabilization of more ordered ligand shells, which retards monomer addition. Naively, the highest concentration and longest chain length of ligands can be anticipated to stabilize the thinnest nanoplatelets by effectively buffering monomer supersaturation, regulating monomer diffusion, and constituting an extended ligand shell. However, the highest ligand concentrations or longest chain ligands do not always yield the thinnest nanoplatelets. **Figure 5.5B** shows model results at 82°C where the global minimum of the model of 2.4 average layers is observed for similar ligand concentrations and diffusion coefficients as in Figure 5.5A indicating that increasing temperature up to 82°C allows for the most effective confinement of crystal growth. **Figures 5.5C** and **D** plot slice contour maps at higher temperatures of 120 and 150°C, respectively; the predicted layer thickness increases with temperature across the entire response space in this range.

The stabilization of relatively thicker layers results from increased diffusion coefficients of monomeric species, which facilitates faster crystal growth. The ligand concentration and chain length are correlated in the temperature range between 76—150°C with the local minima shifting to lower concentrations and longer chain lengths with increasing temperature, which is reflective of the interplay between formation of a well-ordered ligand shell and the mobility of monomeric species. The highest

alkylamine concentration of $x = 40$ induces a phase transformation from $CsPbBr_3$ to an altogether different lead-deficient Cs_4PbBr_6 structure as a result of the amine ligands mediating leaching of surficial $PbBr_2$ layers.[41,54] Additionally, the longest chain length ligands (e.g., C14 or C18) yield thicker nanoplatelets at low reaction temperatures in the range of 50—100°C since at low temperatures, a kinetically trapped disordered ligand shell is stabilized (and cannot be rapidly equilibrated to a thermodynamically stable self-assembled monolayer), which allows for facile diffusion of monomeric species.[38] At higher temperatures, longer-chain alkylamines are able to form ordered ligand shells as a result of thermally facilitated desorption,[52,53] allowing for quasi-equilibrium conditions to be reached. However, monomer diffusion is also greatly enhanced as expected for temperature-variant Fickian diffusion.[55] The local minima reflects the achievable balance between these two competing influences representative of thermodynamic equilibrium and kinetic metastable regimes. In other words, the correlations provided by the regression model allow for qualitative mechanistic understanding to be gleaned from the SVM model in a non-intuitive manner.

To illustrate some of the mechanistic regimes, **Figure 5.6** provides a schematic of the 82°C and 150°C slices of the SVM contour plot also shown in Figures 5.5B and 5.5D respectively. These illustrations show the entropic effects of ligand concentration and chain length at the two different temperatures. Figure 5.6J shows a general schematic of the nucleation and growth process differentiating the stabilization of ordered ligand shells or kinetically trapped disordered states. Figures 5.6A-I
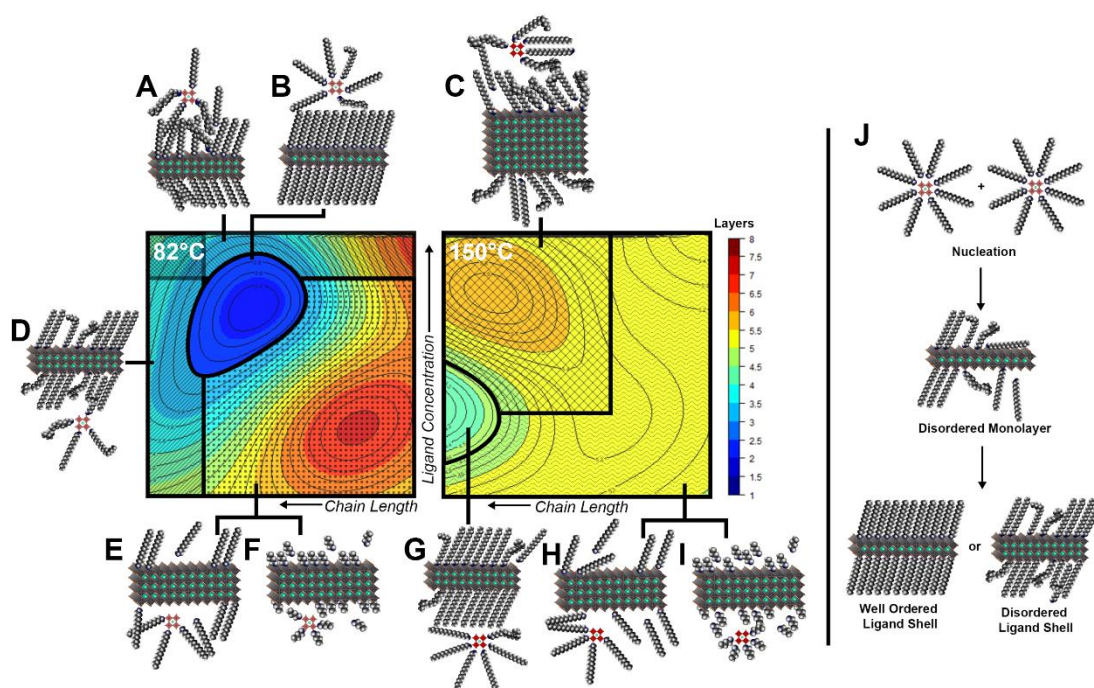
Figure 5.6. Schematic of crystal growth regimes corresponding to the 82 and 150°C slices of the RBF-SVM model. Illustrations of different regimes are shown as follows (darker red monomers imply faster diffusion as a result of higher temperatures): (A) high ligand concentration results in a disordered monolayer; (B) conditions allowing for optimal ligand shell monolayer formation resulting in the global minimum of layer thicknesses accessed in this work; (C) high temperature and concentration as well as longer ligand chain lengths yield disordered layers whilst facilitating relatively rapid monomer diffusion; (D) longer chain length increases packing disorder (corresponding to stabilization of a kinetic product); (E) low ligand concentration enables facile crystal growth at sub-monolayer coverages; (F) short chain length allows desorption and passivation as well as easier monomer transport, thereby favoring crystal growth; (G) at high temperatures, long ligand chain lengths allows for stabilization of somewhat ordered ligand shells thereby limiting crystal growth; (H) low ligand concentration and high temperature favors ligand desorption enabling facile monomer addition and crystal growth; (I) high temperature and short ligand chain length favors facile monomer addition and enables rapid crystal growth; (J) schematic illustration of ligand shell formation alternatively yielding an ordered monolayer maximizing dispersive interactions (thermodynamic product) or becoming trapped within a disordered state representing the kinetic product.

schematically illustrate different ligand shell configurations and their ability to modulate

monomer addition.

In order to test for overfitting and analyze the predictivity of the regressors, a validation test set of six newly synthesized samples that had no influence on the creation of the models has been selected and analyzed. The six samples have been selected to be in the <50% bulk regime by sampling randomly from the design space within the quantum confined classification of the SVM classifier shown in Figure 5.3. All six samples have been synthesized with the alkylamine chain lengths, concentrations, and temperatures listed in **Table 5.2**. All of the samples contain less than 50% contribution of photoluminescence signals from bulk crystals (**Fig. 5.7** and **Table D.6**), verifying the robustness of the classifier. A range of thicknesses between 3.72 to 7.17 layers have been identified, falling within the range of the model. As seen in the cross-validation results of Figure 5.4, the model has some degree of underestimation for all regressors as a result of the limitations of the spectroscopic method delineated above. The average layer thicknesses ($n_{avg.}$) of 2D perovskite nanoplatelets in the validation set as deduced from ensemble PL emission spectra and determined from TEM imaging (t) in Figure 5.7 are listed in Table D.6. **Figure D.5** shows additional TEM images acquired for these validation samples. The RMSE of the validation set for the linear and quadratic regression models was 1.233 and 1.175 layers, respectively. The SVM regression yields the lowest error for the validation set as well as the cross validation, the great improvement of the quadratic model with the addition of cross terms is not mimicked in the leave-one-out cross-validation error estimation leading to the conclusion that the SVM regression is the most consistently high performing model.

As a test of the ability of our model to perform as predictive map to entirely new samples, an attempt was made to synthesize a sample with a specific thickness and use the model to select parameters. The target was to achieve an n_{avg} of 3.0 layers using the parameters selected from the current RBF-SVM model. Three sets of parameters with different chain lengths were selected (**Table D.7**) and yielded experimental n_{avg} values of 2.90, 2.74, and 2.45 layers, (**Figure D.6**) all of which are within the observed error seen in the leave-one-out cross validation and validation set.

Table 5.2. Validation samples and predicted thicknesses from linear, quadratic, quadratic with cross terms, and support vector machine (RBF kernel) regressors.

Chain length	Temp. °C	Pb:RA=1:x	Average (n) when bulk n=10	Linear	Δ%	Quadratic	Δ%	Quadratic (cross)	Δ%	SVM - RBF	Δ%
7	70	30	4.314	4.526	5%	3.987	-8%	3.661	-15%	3.456	-20%
7	90	15	6.413	4.922	-23%	4.693	-27%	5.841	-9%	6.935	8%
16	90	25	3.724	3.864	4%	3.463	-7%	3.304	-11%	3.346	-10%
18	80	25	4.626	3.587	-22%	3.491	-25%	3.472	-25%	3.734	-19%
6	70	15	7.172	4.933	-31%	5.319	-26%	6.759	-6%	7.012	-2%
16	90	40	4.605	3.747	-19%	3.950	-14%	4.355	-5%	4.088	-11%
			RMSE:	1.233		1.175		0.645		0.611	

It is worth noting that given the rapid nucleation and growth within this highly ionic system and the high mobility of the precursors, no Ostwald size focusing has been attempted. Size monodispersity can be experimentally achieved in nanocrystal synthesis through multiple injections or by differentiating nucleation and growth steps through variational temperature ramps.[56,57] Our model has sought to relate nanocrystal
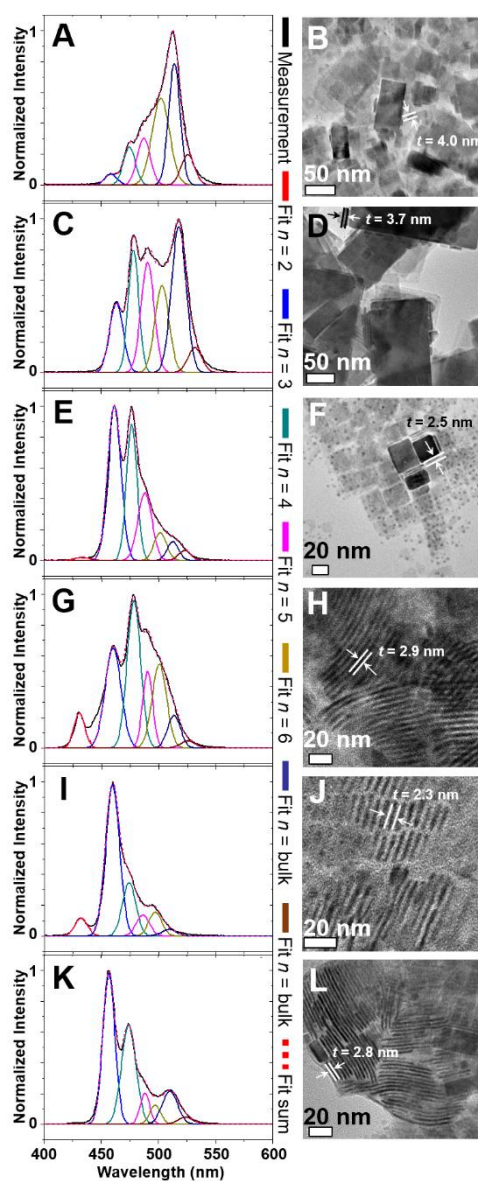
Figure 5.7. PL emission spectra and TEM images acquired for validation set of 2D CsPbBr$_3$ nanoplatelets at different reaction conditions: A,B) C6 with 1:x = 1:15 at 70°C; C,D) C7 with 1:x = 1:15 at 90°C; E,F) C7 with 1:x = 1:30 at 70°C; G,H) C18 with 1:x = 1:25 at 80°C; I,J) C16 with 1:25 at 90°C; and K,L) C16 with 1:x = 1:40 at 90°C.

nucleation and growth of platelets with discrete layer thicknesses (which stands in

contrast to colloidal nanocrystals exhibiting a Gaussian size distribution profile) arising

from the interplay between temperature, concentration, and nature of the amine ligand,

160

and as such captures the fundamental chemical reactivity and crystallization; it does not

account for secondary growth processes and process interventions necessary for

obtaining monodisperse samples, which involve a much more elaborate variable space

and data related to temporal evolution of nanocrystal growth. Elaboration of the model

to include time-variant temperature ramps will be the focus of future work to add

monodispersity as a second synthetic outcome. An additional analysis of the ability of

this modeling method to deal with sparse datasets has been performed by testing the

cross-validation error as a function of folds, the fraction of data removed in each

iteration of validation (*e.g*., 2 fold is half the dataset). At lower folds ($n = 2, 3, 4$, etc.)

the cross-validation error is approximately 50% higher than leave-one-out cross

validation (**Figure D.7**). An average performance is reached around 5 folds, which in

this set leaves out sets of 11 and 12 samples showing that an approximate minimum

viable sample size for this model is around 45-46 samples. The small number of

synthetic data needed to create a viable model emphasizes the non-parametric flexibility

of SVM with a radial basis function kernel allowing for the creation of a robust

predictive model with little overfitting.

The establishment of a well-defined predictive model for control over

dimensional confinement of colloidal $CsPbBr_3$ nanocrystals indeed has significant

implications for device design and performance. For instance, Kamat and co-workers

have performed an extensive investigation of the thickness-dependence of device

performance of $CsPbBR_3$ nanocrystals assembled in thin film form via layer-by-layer

deposition.[58] Analogously, the layer thickness further correlates to color tunability of

the materials with applications in phosphors and optoelectronic devices. The emission of CsPbBr3 nanoplatelets is tunable from deep violet for $n = 1$ to bluish green for $n = 6$ to green for bulk materials.

5.4. Conclusions

The hot colloidal synthesis of nanocrystals involves complex phenomena spanning the range from molecular reactions to nucleation, monomer addition, and crystal growth. The complex reaction variables at play and the multitude of phenomena spanning multiple temporal and spatial dimensions are challenging to model from first principles, and thus not surprisingly synthetic methods have evolved in a primarily empirical manner. We demonstrate here the utilization of a relatively sparse dataset to create a non-linear model for predictive synthesis of CsPbBr$_3$ nanoplatelets with controllable layer thickness. The utilization of SVM classification and regression provides a means of developing robust predictive models from limited datasets. SVM classification is shown to accurately predict the likelihood of a CsPbBr$_3$ synthesis creating a majority population of quantum confined nanoplatelets. SVM regression is further shown to estimate the average thickness outcome of the synthesis of CsPbBr$_3$ nanoplatelets within sub-monolayer accuracy.

The approach demonstrated here is expected to be broadly generalizable to designing the synthesis of nanocrystals and illustrates an efficient means of navigating potentially vast design spaces. Further elaboration of these methods will utilize the spectral data for composite modeling of each individual layer thickness and predict distribution and size while investigating the role of changing the solvent/viscosity and

162

ligand type (*n,* branching, denticity, binding group) as well as the precursor

concentrations (mapping across the ternary Cs-Pb-Br phase diagram).[54] As such, better

numerical descriptors of the ligands will need to be developed as an initial step.

Subsequent models will further be elaborated to multi-objective optimization of multiple

synthetic outcomes such as quantum yield and monodispersity.

A major challenge with this approach to modeling of nanocrystal synthesis is the

bottleneck in rapid characterization of synthetic outcomes; the PL emission

measurements used here are excellent proxies of size but cannot be used for samples

without a distinct size-dependent photoluminescence signature wherein a substantial

statistical analysis of TEM images becomes a necessary probe of average particle size.

Alternatively, probing the X-ray coherent domain size represents a potential means of

sampling ensemble averages of nanocrystals and will further be examined as a

continuous variable. In addition to particle size, such a method can be applied to model

any numerical output of a synthetic process (e.g., the reaction yield, atomic composition,

and absorption maxima).

5.5. Experimental

5.5.1. Materials

All chemicals were used as received without further purification. Cesium

carbonate (Cs_2CO_3, 99.9%, Alfa Aesar), oleic acid (OLAc, 90%, Aldrich), octadecene

(ODE, 90%, Aldrich), lead bromide ($PbBr_2$, 98%, Alfa Aesar), *n*-butylamine (C4, 99%,

TCI America), *n*-pentylamine (C5, 98%, Alfa Aesar), *n*-hexylamine (C6, 99%, Alfa

Aesar), *n*-heptylamine (C7, 98%, Alfa Aesar), *n*-octylamine (C8, 98%, TCI America), *n*-

nonylamine (C9, 98%, TCI America), *n*-undecanylamine (C11, 98%, TCI America), *n*-dodecylamine (DA, 98%, Alfa Aesar), *n*-tetradecylamine (TA, 95%, Aldrich), *n*-octadecylamine (ODA, 97%, Alfa Aesar) were used in the synthesis of $CsPbBr_3$ nanoplatelets.

5.5.2. Preparation of Cs-oleate precursors

Cesium-oleate (Cs-OA) precursors for the synthesis of 2D $CsPbBr_3$ nanoplatelets were prepared following a previously reported method.[38,40] Briefly, Cs_2CO_3 (32 mg) and 10 mL of oleic acid were mixed in a 50 mL three-neck round-bottomed flask, dried under vacuum at 120°C for 30 min, and heated to 150°C under Ar flow in Schlenk apparatus until all of the solids were dissolved, yielding a colorless or light yellow solution.

5.5.3. Synthesis of 2D CsPbBr₃ nanoplatelets

All synthetic processes for the preparation of 2D $CsPbBr_3$ nanoplatelets were performed under standard Schlenk conditions in an ambient of Ar gas. $CsPbBr_3$ nanoplatelets were synthesized based on the hot injection of Cs-OA precursors into a mixture containing $PbBr_2$, a variable amount of the alkylamine, oleic acid, and ODE.[38] In brief, 15 mg of $PbBr_2$, 0.250 mL of OLAc, and 5 mL of ODE were mixed in a 50 mL three-neck round-bottomed flask wherein the desired stoichiometric amount of the alkylamine (with alkyl chain lengths ranging from C4—C18) was added to vary the Pb:RA molar ratio in the range of 1:5—1:40; the mixtures were degassed under vacuum for 30 min at 100°C to form lead oleate. Note that at alkylamine concentrations below $x = 5$, ligand shells cannot be effectively constituted, precluding ligand-induced

dimensional confinement, and resulting in the rapid growth of micron-sized cubes. In contrast, at higher concentrations of ligands, above $x = 40$, the complexation of the alkylamines with $PbBr_2$ results in stabilization of the lead-deficient Cs_4PbBr_6 phase.[41] After complete dissolution of $PbBr_2$, the temperature of the flask was set at the desired reaction temperature under argon flow, which was varied from 50–150°C. Subsequently, 1 mL of the as-prepared Cs-OA solution was swiftly injected into the mixture containing lead oleate. The reaction mixture was maintained for 10 s at the injection temperature and immediately quenched with 15 mL of hexanes to cool the reaction mixture down to 30—40°C. The precipitate was collected by centrifugation at 12,000 rpm for 10 min and then resuspended to form a colloidal dispersion in hexanes. The colloidal dispersion of the nanoplatelets in hexanes was used for further characterization.

5.5.4. Characterization

U UV-Vis absorption spectra were measured using a Hitachi U-4100 UV-Vis-NIR spectrophotometer. Photoluminescence emission spectra were acquired using a Horiba PTI Quanta-Master series spectrofluorometer with a Xenon arc lamp as the light source and a photomultiplier tube (PMT) as the detector. Photoluminescence emission spectra were acquired at 360 nm excitation for all of the samples unless otherwise specified. UV-vis absorption and photoluminescence emission spectra were acquired by diluting the as-prepared colloidal dispersion of nanoplatelets in hexanes. Quartz cuvettes with a path length of 1 cm were used for both sets of measurements.

Powder X-ray diffraction (XRD) measurements were conducted using a Bruker D8-Focus Bragg-Brentano X-ray Powder Diffractometer with a Cu Kα radiation source

(λ = 1.5418 Å) in the 2Θ range of 10—60°. Samples for XRD measurements were prepared by drop-casting a colloidal dispersion in hexanes onto a zero-background XRD holder.

High-resolution transmission electron microscopy (TEM) images were acquired using a FEI Tecnai G2 F20 ST instrument at an accelerating voltage 200 kV. Samples for TEM measurements were prepared by drop-casting dilute hexanes dispersions of the nanoplatelets onto 400 mesh TEM grids coated with formvar carbon films.

5.5.5. Calculation of the average layer thickness (*n*) of 2D CsPbBr₃ nanoplatelets

The The average layer thickness ($n_{avg.}$) of nanoplatelets in terms of octahedral layers is calculated as per the following equations:

$$n_{avg.} = \sum_{i=1}^{\infty}(a_i \times n_i) \cdot \qquad \textbf{5.2}$$

$$a_i = \frac{Integrated\ area\ of\ n_{i}\ in\ PL\ spectra}{Totally\ integrated\ area\ in\ PL\ spectra} \qquad \textbf{5.3}$$

where $n_{avg.}$ is average octahedral layer thickness for a specific sample; a_i (i = 1—6 and bulk) is the weighting factor corresponding to the population of a specific layer thickness; and n_i (i = 1—6 and bulk) is the number of octahedral layers. For nanoplatelets with $n > 6$, corresponding to particles above the quantum confined regime, a layer thickness of $n = 10$ has been approximated. Assignments of layer thicknesses (n_i) have been made based on previously reported single-particle photoluminescence maximum emission wavelengths.[38] The integrated area of the photoluminescence emission band corresponding to a specific layer thickness (n_i) is divided by the total

166

integrated area of the photoluminescence spectrum to yield the relative proportion of each layer (n_i) within the sample. Tables D.1 and D.2 list the deconvoluted areal intensities for the different syntheses examined in this work. Gaussian lineshapes have been used to fit emission bands in each case.

All statistical models were computed using R 3.4.1 with linear (eq. 4) and quadratic (eqs. 5-6) regressions of the following form computed using a linear modeling function to determine the coefficients of the regressions:

$$y = b_1 + b_2 x_1 + b_3 x_2 + b_4 x_3 \qquad \textbf{5.4}$$

$$y = b_1 + b_2 x_1 + b_3 x_1^2 + b_4 x_2 + b_5 x_2^2 + b_6 x_3 + b_7 x_3^2 \qquad \textbf{5.5}$$

$$y = b_1 + b_2 x_1 + b_3 x_1^2 + b_4 x_2 + b_5 x_2^2 + b_6 x_3 + b_7 x_3^2 + b_8 x_1 x_2 + b_9 x_1 x_3 + b_{10} x_2 x_3 \quad \textbf{5.6}$$

The variables x_n represent the three input variables and b_n represent the coefficients of the regression. Eq. 5 includes calculation of coefficients b_{8-10} allowing for the inclusion of variable correlation. The T-test was performed assuming equal variance as a standard two sample t-test (eqs. 7-8).

$$T = \frac{\bar{X}_1 - \bar{X}_2}{s_p\sqrt{\frac{1}{n_1} + \frac{1}{n_2}}} \qquad \textbf{5.7}$$

$$s_p = \sqrt{\frac{(n_1-1)s_{X_1}^2 + (n_2-1)s_{X_2}^2}{n_1+n_2-2}} \qquad \textbf{5.8}$$

The variable $\bar{X}$ represents the sample means, n the sample sizes and s the sample standard deviations with s_p the pooled variance. The e1071 R package version 1.6-8 was utilized to compute the support vector machine classifier and regressors.[42] All SVM calculations were algorithmically tuned to pick the best performing cost terms (all kernels) and gamma terms (radial basis function kernel) using "leave-one-out" cross validation as a performance metric. Nearest neighbors regression was calculated using the FNN R package (version 1.1.2.1) with a k value of 3.[43] Ridge regression was performed with the glmnet R package (version 2.0-16) for penalty constants (λ) of 0.001 to 50.[44]

5.6. References

[1]   C. B. Murray, C. R. Kagan, M. G. Bawendi, *Annu. Rev. Mater. Sci.* **2000**, *30*, 545.

[2]   N. R. Jana, L. Gearheart,, C. J. Murphy, *Adv. Mater.* **2001**, *13*, 1389.

[3]   Y. Yin, A. P. Alivisatos, *Nature* **2005**, *437*, 664.

[4]   C. A. Stowell, B. A. Korgel, *Nano Lett.* **2005**, *5*, 1203.

[5]   K. R. Kort, S. Banerjee, *Small* **2015**, *11*, 329.

[6]   W. W. Yu, Y. A. Wang, X. Peng, *Chem. Mater.* **2003**, *15*, 4300.

[7]   J. Y. Rempel, M. G. Bawendi, K. F. Jensen, *J. Am. Chem. Soc.* **2009**, *131*, 4479.

[8]   L. S. Hamachi, I. Jen-La Plante, A. C. Coryell, J. De Roo, J. S. Owen, *Chem. Mater.* **2017**, *29*, 8711.

[9]   H. Huang, J. Raith, S. V. Kershaw, S. Kalytchuk, O. Tomanec, L. Jing, A. S. Susha, R. Zboril, A. L. Rogach, *Nat. Commun.* **2017**, *8*, 996.

[10]   H. P. Andaraarachchi, M. J. Thompson, M. A. White, H. J. Fan, J. Vela, *Chem. Mater.* **2015**, *27*, 8021.

[11]   J. Owen, *Science.* **2015**, *347*, 615.

[12]   M. B. Braun, L. Korala, J. M. Kephart, A. L. Prieto, *ACS Appl. Energy Mater.* **2018**, *1*, 1053.

[13]   H. Lu, Z. Zhou, O. V. Prezhdo, R. L. Brutchey, *J. Am. Chem. Soc.* **2016**, *138*, 14844.

[14]   S. W. Depner, N. D. Cultrara, K. E. Farley, Y. Qin, S. Banerjee, *ACS Nano* **2014**, *8*, 4678.

[15]   A. J. Rondinone, A. C. S. Samia, Z. J. Zhang, *J. Phys. Chem. B* **2000**, *104*, 7919.

[16]   N. D. Burrows, S. Harvey, F. A. Idesis, C. J. Murphy, *Langmuir* **2017**, *33*, 1891.

[17]   A. O. Oliynyk, A. Mar, *Acc. Chem. Res.* **2018**, *51*, 59.

[18]   A. O. Oliynyk, L. A. Adutwum, B. W. Rudyk, H. Pisavadia, S. Lotfi, V. Hlukhyy, J. J. Harynuk, A. Mar, J. Brgoch, *J. Am. Chem. Soc.* **2017**, *139*, 17870.

[19]   Z. L. Niemeyer, A. Milo, D. P. Hickey, M. S. Sigman, *Nat. Chem.* **2016**, *8*, 610.

[20]   L. R. De Jesus, P. Stein, J. L. Andrews, Y. Luo, B. X. Xu, S. Banerjee, *Mater. Horizons* **2018**, *5*, 486.

[21]   Y. Zhuo, A. Mansouri Tehrani, J. Brgoch, *J. Phys. Chem. Lett.* **2018**, *9,* 1668.

[22]   A. O. Oliynyk, L. A. Adutwum, J. J. Harynuk, A. Mar, *Chem. Mater.* **2016**, *28,* 6672.

[23]   G. Pilania, A. Mannodi-Kanakkithodi, B. P. Uberuaga, R. Ramprasad, J. E. Gubernatis, T. Lookman, *Sci. Rep.* **2016**, *6,* 19375.

[24]   J. Hachmann, R. Olivares-amaya, S. Atahan-evrenk, C. Amador-bedolla, A. Gold-parker, L. Vogt, A. M. Brockway, *J. Phys. Chem. Lett.* **2011**, *2,* 2241.

[25]   M. Atif, F. Afzal, C. Cheng, J. Hachmann, *J. Chem. Phys.* **2018**, *148,* 241712.

[26]   Y. Dong, T. Qiao, D. Kim, D. Parobek, D. Rossi, D. H. Son, *Nano Lett.* **2018**, *18,* 3716.

[27]   G. Almeida, L. Goldoni, Q. Akkerman, Z. Dang, A. H. Khan, S. Marras, I. Moreels, L. Manna, *ACS Nano* **2018**, *12,* 1704.

[28]   Y. Bekenstein, B. A. Koscher, S. W. Eaton, P. Yang, A. P. Alivisatos, *J. Am. Chem. Soc.* **2015**, *137,* 16008.

[29]   P. Tyagi, S. M. Arveson, W. A. Tisdale, *J. Phys. Chem. Lett.* **2015**, *6,* 1911.

[30]   H. Wang, L. Whittaker-Brooks, G. R. Fleming, *J. Phys. Chem. C* **2015**, *119,* 19590.

[31]   D. Di, K. P. Musselman, G. Li, A. Sadhanala, Y. Ievskaya, Q. Song, Z. K. Tan, M. L. Lai, J. L. MacManus-Driscoll, N. C. Greenham, R. H. Friend, *J. Phys. Chem. Lett.* **2015**, *6,* 446.

[32]   Q. Dong, Y. Fang, Y. Shao, P. Mulligan, J. Qiu, L. Cao, J. Huang, *Science.* **2015**, *347,* 967.

[33]   D. Shi, V. Adinolfi, R. Comin, M. Yuan, E. Alarousu, A. Buin, Y. Chen, S. Hoogland, A. Rothenberger, K. Katsiev, Y. Losovyj, X. Zhang, P. A. Dowben, O. F. Mohammed, E. H. Sargent, O. M. Bakr, *Science.* **2015**, *347*, 519.

[34]   A. Swarnkar, R. Chulliyil, V. K. Ravi, M. Irfanullah, A. Chowdhury, A. Nag, *Angew. Chemie* **2015**, *127*, 15644.

[35]   L. Protesescu, S. Yakunin, M. I. Bodnarchuk, F. Krieg, R. Caputo, C. H. Hendon, R. X. Yang, A. Walsh, M. V. Kovalenko, *Nano Lett.* **2015**, *15*, 3692.

[36]   H. Huang, L. Polavarapu, J. A. Sichert, A. S. Susha, A. S. Urban, A. L. Rogach, *NPG Asia Mater.* **2016**, *8*, e328.

[37]   Q. A. Akkerman, S. G. Motti, A. R. Srimath Kandada, E. Mosconi, V. D'Innocenzo, G. Bertoni, S. Marras, B. A. Kamino, L. Miranda, F. De Angelis, A. Petrozza, M. Prato, L. Manna, *J. Am. Chem. Soc.* **2016**, *138*, 1010.

[38]   J. Cho, H. Jin, D. Sellers, D. F. Watson, D. H. Son, S. Banerjee, *J. Mater. Chem. C* **2017**, *5*, 8810.

[39]   I. Lignos, S. Stavrakis, G. Nedelcu, L. Protesescu, A. J. Demello, M. V. Kovalenko, *Nano Lett.* **2016**, *16*, 1869.

[40]   J. Shamsi, Z. Dang, P. Bianchini, C. Canale, F. Di Stasio, R. Brescia, M. Prato, L. Manna, *J. Am. Chem. Soc.* **2016**, *138*, 7240.

[41]   Z. Liu, Y. Bekenstein, X. Ye, S. C. Nguyen, J. Swabeck, D. Zhang, S. T. Lee, P. Yang, W. Ma, A. P. Alivisatos, *J. Am. Chem. Soc.* **2017**, *139*, 5309.

[42]   D. Meyer, E. Dimitriadou, K. Hornik, A. Weingessel, F. Leisch, *E1071: Misc Functions of the Department of Statistics, Probability Theory Group (Formerly: E1071);* TU Wien, **2017**.

[43]   B. Alina, K. Sham, L. John, A. Sunil, M. David, L. Shengqiao, *FNN: Fast Nearest Neighbor Search Algorithms and Applications.* R package version **2018**.

[44]   J. Friedman, T. Hastie, R. Tibshirani, *J. Stat. Softw.* **2010**, *33*. 1.

[45]   J. Cho, Y. H. Choi, T. E. O'Loughlin, L. De Jesus, S. Banerjee, *Chem. Mater.* **2016**, *28*, 6909.

[46]   P. Cottingham, R. L. Brutchey, *Chem. Commun.* **2016**, *52*, 5246.

[47]   P. Cottingham, R. L. Brutchey, *Chem. Mater.* **2016**, *28*, 7574.

[48]   S. G. Cloutier, *Materials* **2015**, *8*, 1858.

[49]   J. J. Choi, J. Luria, B. R. Hyun, A. C. Bartnik, L. Sun, Y. F. Lim, J. A. Marohn, F. W. Wise, T. Hanrath, *Nano Lett.* **2010**, *10*, 1805.

[50]   Z. Liang, S. Zhao, Z. Xu, B. Qiao, P. Song, D. Gao, X. Xu, *ACS Appl. Mater. Interfaces* **2016**, *8*, 28824.

[51]   X. Du, G. Wu, J. Cheng, H. Dang, K. Ma, Y. W. Zhang, P. F. Tan, S. Chen, *RSC Adv.* **2017**, *7*, 10391.

[52]   A. Ulman, *Chem. Rev.* **1996**, *96*, 1533.

[53]   P. Silberzan, L. Léger, D. Ausserré, J. J. Benattar, *Langmuir* **1991**, *7*, 1647.

[54]   J. Cho, S. Banerjee, *Chem. Mater.* **2018**, *30*, 6144.

[55]   A. Mistry, D. Juarez-Robles, M. Stein, K. Smith, P. P. Mukherjee, *J. Electrochem. Energy Convers. Storage* **2016**, *13*, 031006.

[56]   R. Viswanatha, P. K. Santra, C. Dasgupta, D. D. Sarma, *Phys. Rev. Lett.* **2007**, *98*, 255501.

[57]   N. J. J. Johnson, A. Korinek, C. Dong, F. C. J. M. Van Veggel, *J. Am. Chem. Soc.* **2012**, *134*, 11068.

[58]   J. B. Hoffman, G. Zaiats, I. Wappes, P. V. Kamat, *Chem. Mater.* **2017**, *29*, 9767.

[59]   *ACD/Percepta*; Advanced Chemistry Development Inc. Toronto. **2017**

[60]   W. M. Haynes, D. R. Lide, J. B. Thomas, *CRC Handbook of Chemistry and Physics : A Ready-Reference Book of Chemical and Physical Data*, 97th ed. CRC Press **2017**.

[61]   National Institute of Advanced Industrial Science and Technology, Spectral Database for Organic Compounds. http://sdbs.db.aist.go.jp (accessed July 25, 2017)

[62]   D. Matulis, V. A. Bloomfield, *Biophys. Chem.* **2001**, *93*, 53.

[63]   M. D. Hanwell, D. E. Curtis, D. C. Lonie, T. Vandermeerschd, E. Zurek, G. R. Hutchison, *J. Cheminform.* **2012**, *4*, 17.

6. CONCLUSIONS AND FUTURE OUTLOOK*

Mechanistic investigations into the influence of dopants in VO_2 have allowed us to see further into the complex design landscape of this metal insulator material. The role of defects as nucleation sites for the MIT of VO_2 is incredibly impactful. Defect nucleation contributing directly to the broadening of the kinetic hysteresis observed in tungsten and germanium doped VO_2 allows for the shifting of the thermodynamic transition temperature up or down while maintaining a vector to control the hysteresis.[1] Boron doping, in addition to lowering the thermodynamic equilibrium temperature of VO_2 also imparts a dynamic variable hysteresis.[2] The discovery of a relaxation mechanism in VO_2 doped interstitially with boron presents a fully readable and resettable atomic hourglass and thermometer effect. By modulating the stability of the insulating M_1 phase of VO_2 through the kinetic relaxation of the boron dopant, we demonstrate a switchable material with built in resettable sensing. The complex energy landscape of VO_2 is influenced in drastically different ways by the incorporation of these various dopants. The phase stabilities are greatly influenced by dopant incorporation, a fact that is undeniable in our demonstration in the stabilization of the metastable VO_2 (P) phase upon iridium doping.[3]

Process design of the synthesis of $CsPbBr_3$ as a model system to achieve control over the particle thickness and resultant quantum confinement was successful due to the utilization of machine learning modeling.[4] Using support vector machine regression, we

_____

demonstrated that even with sparse and uneven data predictive utility can be derived to build an interpretable model of the synthetic design space. The visualization and interpretation of a machine learning model allows for insight into the mechanisms that influence a synthetic outcome. This inference and utility can be improved greatly with the introduction of designed experimentation and Bayesian iteration leading to future work future work modeling synthetic processes in the most efficient manner.

6.1. Outlook for Predictive Synthesis

6.1.1. Efficient Routes to Complex Predictivity

Canonical machine learning techniques are particularly well suited to large amounts of data with complex prediction or optimization-based goals.[5,6] While the goals of prediction and optimization remain the same for materials synthesis, the cost of data is much higher. While response-surface DOE provides a distinct edge over OVAT sampling and allows for reliable inferences from a small amount of data, it is often unable to handle data that has a more complex response. Machine learning methods have the ability to provide valuable insight and to develop useful models that can be further iteratively improved. However, the sparsity of datasets and the substantial costs of experiments have limited its application in the exploration of synthesis design spaces. In recent work, we have performed a study using existing OVAT data supplemented with random sampling to build a predictive model of a nanocrystal synthesis.[4] The study used only 74 samples to create a model that was able to predict both the conditions that will lead to quantum confined $CsPbBr_3$ nanoplatelets and their average thickness for a given sample. This relation of three experimental parameters (temperature, ligand

choice, and ligand concentration) generated a highly nonlinear response that was mapped within one unit cell layer of accuracy using support vector machine regression (SVM, **Figure 6.1**). This supervised learning model chooses the fit that minimizes the length of vectors perpendicular to the fit that connect the model to the data. The model was physically interpretable in terms of the competition between enthalpic and entropic considerations and in distinguishing thermodynamic and kinetic regimes under different synthetic conditions. The observed resolution of mapping, ability to handle imperfect data, and insight into a nonlinear reaction space was made possible by using machine learning. Despite the positive use case shown in this work, the number of experiments was high, and parts of the design space may have been under sampled. To increase efficiency and lower variability of the response space, more targeted sampling and iterative design methods are desirable. Cao *et al.* have described and demonstrated this synergistic relationship between DOE and ML in a perspective article examining the optimization of the power conversion efficiency for a bulk heterojunction photovoltaic device created *via* spin casting a mixture of a low-band-gap donor polymer and fullerene as an acceptor with the addition of diiodooctane, which is thought to decrease donor– acceptor phase segregation.[7] These authors specifically considered the influence of the weight percentage of the low-band-gap polymer, total solution concentration, spin-casting speed, and the volume percent of the diiodooctane additive. They sampled the reaction space using a fractional factorial, analyzed variance in the data using ANOVA analysis to understand feature correlations, and fitted the data using an SVM with a radial basis function kernel. The SVM was then used to generate a visual map of the

176
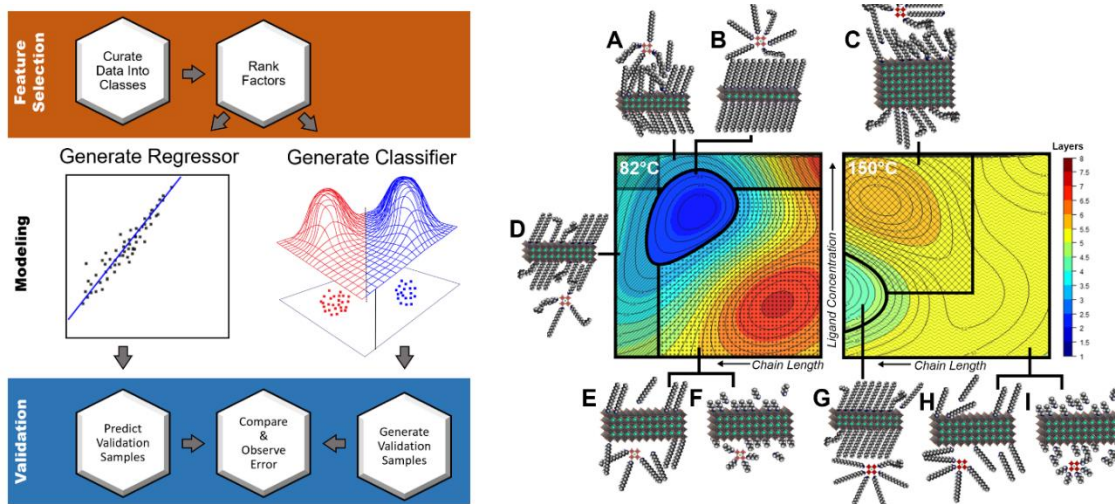
Figure 6.1. Machine learning flowchart (left) and interpretation of the SVM regression results (right) from the study of CsPbBr$_3$ perovskite nanocrystal growth by Braham et al.[4] Regression heatmaps of the particle thicknesses along the modeled axes of ligand chain length and ligand concentration is shown at two temperatures of 82 and 150°C. Interpretation and illustration of 9 selected growth regimes are depicted in A-I showing findings of chemical significance with a global minimum thickness regime with a close packed monolayer (B), entropy-driven monolayer misalignments for high chain lengths or concentration (A,C,D), incomplete monolayer formation owing to low ligand concentrations or weak intermolecular interactions (E,F,H,I,) and a local minimum at high temperature illustrating the shift in ideal monolayer packing conditions as a function of temperature (G). Reprinted with permission from ref. 15; Copyright 2019, the American Chemical Society.[4]

space, which informed the design of a second round of fractional factorial sampling,

eliminating the addition of diiodooctane as a variable and narrowing the range of the

other factors to target the area of the space demonstrating the highest power conversion

efficiency values. While this second round of sampling narrowed in on the optima, a

purely exploitative approach can potentially converge on local rather than global optima.

However, this study exemplifies the promise of using a combination of DOE and ML to

sample, model, and explore a synthesis space. While ML algorithms can oftentimes

uncover hidden correlations among variables and provide some predictivity, a 'one-shot'

fitting of a model to a space often lacks predictive capability beyond that of interpolation.

Active learning, sometimes referred to as sequential learning, is an iterative process where a utility or acquisition function is applied to the output of an initial surrogate model (typically a ML model) to strategically select a new area of the design space to sample.[8-10] Such an approach, illustrated in Fig. 1.8, allows for rapid updating of the model and enables efficient exploration of the synthetic design space. Active learning approaches often leverage exploration strategies from global optimization methods with a Bayesian-optimization-based approach being most popular.[11] In this particular iterative approach, the acquisition functions are based on Bayes Theorem and leverage information previously observed to find a posterior distribution using scores from the surrogate model. The acquisition function then chooses the most valuable experiment to perform next, balancing a preference towards choosing samples that would either be the most helpful to improve the extent to which the model captures the dataset (exploration) or move towards a predicted maximum or minimum of the surrogate function (exploitation). This typically limits use of the Bayesian optimization strategy to problems using regression-based models. Just as no single ML model works well to fit every dataset, various active learning workflows are better suited for different problems.[10] Utility or acquisition functions vary in the degree to which they favor exploration or exploitation of the data, allowing for users to focus more on creating either the most accurate design space model or finding an optimal solution. Xue *et al.* demonstrated the efficacy of this approach in the systematic exploration of the

synthesis of a Ti_{50} ($Ni_{50-x-y-z}Cu_xFe_yPd_z$) shape memory alloy.[12] In order to optimize the transformation temperature, the authors synthesized an initial set of 53 alloys, and applied a polynomial model to serve as the surrogate model coupled with iterative sampling using expected improvement as the acquisition function. The model effectively identified samples with increased transformation temperatures and captured the influence of atomic size on local strain and influence of bond strength on the transformation temperature. While this process can in principle be used to explore a wide variety of synthetic landscapes, examples involving active learning of experimental synthesis spaces are still limited. The iterative framework adds another layer of constraints on the framing of the problem, as the data must be suitably modeled by a regressor in order to reasonably predict the subsequent samples to be measured. Strategies for Bayesian sequential learning are currently being developed to overcome challenges.[8,13-16] For example, Wang *et al.* developed a Bayesian optimization approach to enable nested-batch sampling.[13] In this method the algorithm predicts the most beneficial batch of samples to run next, rather than a ranked list of single experiments. It additionally allows for the user to rank variables to avoid variance within a given batch of variables that would not be feasible within a batchwise process. This addresses two problems which are unique to synthesis; some variables are more expensive to vary than others and sampling two drastically different samples may be much more expensive than sampling two similar samples. For example, it is often simple to vary concentration, as a single stock solution can be made and then diluted to different extents. However, varying the reaction temperature may be limited by the number of independent thermal profiles

179

accessible within a single autoclave, or varying the solvent may negate the opportunity

to work with a stock solution. To consider this constraint, the acquisition function

estimates the value of information for each batch of samples that could be generated.

Most Bayesian optimization efforts have focused on single-objective optimization.

However, in materials chemistry, multiple objectives (along a Pareto frontier) must be

optimized at once. For instance, minimizing defect density and positioning dopant atoms

within a particle while controlling particle size. This problem can be framed as

identifying the optimal sequence of observations (*via* experiments or simulations) that is

most efficient at identifying the Pareto frontier of candidate solutions, which is a

graphical representation of the tradeoffs between two output parameters. In common

Bayesian optimization methodologies, it is assumed that the search for the global

optimum of the descriptive function is sequential, evaluating the function one step at a

time, regardless of the number of objectives to optimize. This means that even in multi-

objective Bayesian optimization it is necessary to quantify the utility of a potential

experiment as a scalar quantity. A powerful scalar utility metric used in multi-objective

optimization is the so-called Expected Hyper-Volume Improvement (EHVI).[17] Similar

to the utility functions used in single-objective Bayesian optimization, EHVI is

constructed by balancing the exploration and exploitation of the design space in order to

efficiently locate the Pareto frontier. Recently, we have developed a multi-objective (up

to three objectives) optimal materials discovery framework[18] and demonstrated its

efficacy by identifying regions in the microstructural space that yielded optimal

performance in a precipitation-strengthened NiTi-based shape memory alloy. The alloy

composition as well as microstructural features (specifically, the precipitate volume fraction) of precipitation-hardened nickel—titanium alloys have been optimized within a pre-defined budget of experimental steps.[18] This approach demonstrates the promise of multi-objective Bayesian optimization methods to develop optimal sequence of experiments allowing for simultaneous control of different synthetic outcomes.

An alternative approach to overcome the constraints of a Bayesian-based active learning approach was demonstrated by Moosavi and co-workers, who decoupled the tasks of learning and exploring the space by using a ML algorithm to understand correlations among variables and gain insight into the reaction mechanisms, while using a metaheuristic global optimization strategy to iteratively explore the space in their search for a metal–organic framework (HKUST-1) with the highest surface area.[19] In doing so, they relax the need for a good initial fit to a surrogate model and gain greater flexibility in choice of ML model, as the model does not need to work well within an optimization workflow. Looking broadly for opportunities to leverage tools in adjacent areas of work will likely be key in increasing the use and diversity of spaces explored experimentally using iterative methods.

The consistency of microstructure in an alloy is an excellent case study in not only synthetic optimization but building fundamental scientific understanding of process—structure relationships though statistical learning. The influence of microstructure on key materials properties such as tensile strength and cycling fatigue creates a crucial need for a clear understanding of processing–structure–property relationship that go beyond empirical constructs. Recent studies by Elwany and co-

workers have applied statistical learning methods to reveal processing—

microstructure/mesostructure relationships in additive manufacturing techniques,

specifically laser powder-bed fusion.[20,21] Using a Ni–Nb alloy as a model system, this

work utilizes machine learning and a set of materials properties/processing features (melt

pool depth, diffusivity of liquid, the Gibbs–Thomson coefficient, and the equilibrium

partition coefficient) to model an experimental "base truth" dataset of microsegregation

in the grain structure of the alloy.[21] The statistical model showed a level of predictivity

to the experimentally compiled dataset but was not able to reach the level of

multiphysics phase-field simulations. The approach demonstrates that with a sufficient

dataset and by investigating alternative machine learning or featurization methods,

design principles underpinning processing–structure relationships can be revealed.

6.1.2. Looking Forward

The salient features of OVAT, DOE, ML, and active learning sampling and

modeling methods are summarized in **Figure 6.2.** OVAT sampling is limited largely by

the sampling bias of the scientist and in its limitations in demonstrating correlation

among variables. While DOE is an excellent and efficient qualitative strategy for

unraveling the impacts of different variables on a synthetic outcome, the standard

response surface methodology falls short in fitting highly non-linear responses. Iterative

processes in DOE are generally exploitative (rather than exploratory) in nature. DOE is

also incompatible with working from found/sparse data. When designing a new

modeling or optimization experiment, DOE sampling methods represent an excellent

choice for building an initial dataset that can be used in conjunction with ML. When

refining and improving a ML model, emerging active learning techniques provide

excellent targeted sampling to achieve a certain goal or for multi-objective optimization,

given that the function most appropriate for the goal(s) and modeling method is used.

The combination of DOE, ML, and active learning would allow for a more robust and

efficient path to navigating the design space of materials synthesis. The sparsity of data

and the relative cost of synthesis and characterization represent significant barriers.

Greater flexibility in automated synthesis platforms, either based on microfluidic

systems or robotic arms performing multiplexed synthesis, hold promise for resolving

these bottlenecks.[22,23] DOE techniques, ML, and automation of synthesis together

represent a promising toolbox for accelerating materials synthesis, providing

foundational understanding of the underlying chemical reactivity, and for extracting

design principles in order to precisely control reaction trajectories.
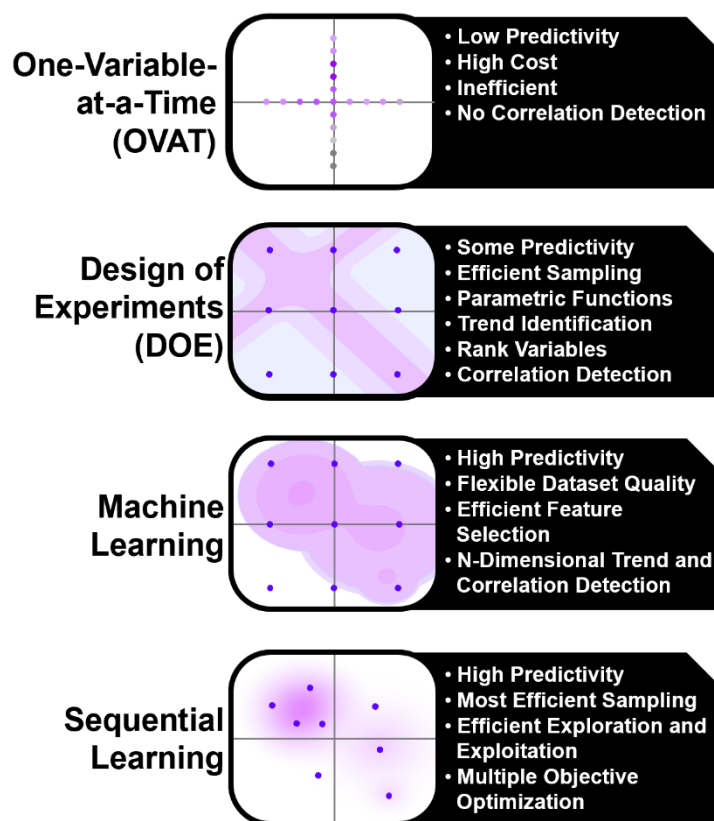
Figure 6.2. Schematic contrasting the sampling and modeling features contained in OVAT, DOE, ML, and sequential/active learning.

6.2. References

[1]   E. J. Braham, D. Sellers, E. Emmons, R. Villarreal, H. Asayesh-Ardakani, N. A.

Fleer, K. E. Farley, R. Shahbazian-Yassar, R. Arròyave, P. J. Shamberger, S. Banerjee,

Chem. Mater. **2018**, *30*, 214.

[2]   D. G. Sellers, E. J. Braham, R. Villarreal, B. Zhang, A. Parija, T. D. Brown, T. E.

G. Alivio, H. Clarke, L. R. De Jesus, L. Zuin, D. Prendergast, X. Qian, R. Arroyave, P.

J. Shamberger, S. Banerjee, *J. Am. Chem. Soc.* **2020**, *142*, 15513-15526.

[3]   E. J. Braham, J. L. Andrews, T. E. G. Alivio, N. A. Fleer, S. Banerjee, *Phys. Status Solidi A.* **2018**, *215*, 1700884.

[4]   E. J. Braham, J. Cho, K. M. Forlano, D. F. Watson, R. Arròyave and S. Banerjee, *Chem. Mater.*, **2019**, *31*, 3281.

[5]   U. S. Shanthamallu, A. Spanias, C. Tepedelenlioglu and M. Stanley, in *2017 8th International Conference on Information, Intelligence, Systems & Applications (IISA),* IEEE, Larnaca, **2017**, pp. 1–8

[6]   K. T. Butler, D. W. Davies, H. Cartwright, O. Isayev and A. Walsh, *Nature*, **2018**, *559*, 547.

[7]   B. Cao, L. A. Adutwum, A. O. Oliynyk, E. J. Luber, B. C. Olsen, A. Mar and J. M. Buriak, *ACS Nano*, **2018**, *12*, 34.

[8]   R. Dehghannasiri, D. Xue, P. V. Balachandran, M. R. Yousefi, L. A. Dalton, T. Lookman and E. R. Dougherty, *Comput. Mater. Sci.*, **2017**, *129*, 311.

[9]   P. V. Balachandran, B. Kowalski, A. Sehirlioglu and T. Lookman, *Nat. Commun.*, **2018**, *9*, 1668.

[10]   B. Settles, *Active Learning Literature Survey*, **2009**.

[11]   T. Lookman, P. V. Balachandran, D. Xue and R. Yuan, *npj Comput. Mater.*, **2019**, *5*, 21.

[12]   D. Xue, D. Xue, R. Yuan, Y. Zhou, P. V. Balachandran, X. Ding, J. Sun and T. Lookman, *Acta Mater.*, **2017**, *125*, 532.

[13]   Y. Wang, K. G. Reyes, K. A. Brown, C. A. Mirkin and W. B. Powell, *SIAM J. Sci. Comput.*, **2015**, *37*, B361.

[14]   R. Aggarwal, M. J. Demkowicz and Y. M. Marzouk, in *Springer Series in Materials Science*, **2016**, *225*, 13.

[15]   T. Ueno, T. D. Rhone, Z. Hou, T. Mizoguchi and K. Tsuda, *Mater. Discov.*, **2016**, *4*, 18–21.

[16]   J. Ling, M. Hutchinson, E. Antono, S. Paradiso and B. Meredig, *Integr. Mater. Manuf. Innov.*, **2017**, *6*, 207–217.

[17]   M. T. M. Emmerich, A. H. Deutz and J. W. Klinkenberg, in *2011 IEEE Congress of Evolutionary Computation, CEC 2011*, **2011**, pp. 2147–2154.

[18]   A. Solomou, G. Zhao, S. Boluki, J. K. Joy, X. Qian, I. Karaman, R. Arróyave and D. C. Lagoudas, *Mater. Des.*, **2018**, *160*, 810.

[19]   S. M. Moosavi, A. Chidambaram, L. Talirz, M. Haranczyk, K. C. Stylianou and B. Smit, *Nat. Commun.*, **2019**, *10*, 539.

[20]   J. Mingear, B. Zhang, D. Hartl and A. Elwany, *Addit. Manuf.*, **2019**, *27*, 565.

[21]   S. Ghosh, R. Seede, J. James, I. Karaman, A. Elwany, D. Allaire and R. Arroyave, *Philos. Mag. Lett.*, **2020**, *100*, 271.

[22]   D. P. Tabor, L. M. Roch, S. K. Saikin, C. Kreisbeck, D. Sheberla, J. H. Montoya, S. Dwaraknath, M. Aykol, C. Ortiz, H. Tribukait, C. Amador-Bedolla, C. J. Brabec, B. Maruyama, K. A. Persson and A. Aspuru-Guzik, *Nat. Rev. Mater.*, **2018**, *3*, 5.

[23]   B. Burger, P. M. Maffettone, V. V. Gusev, C. M. Aitchison, Y. Bai, X. Wang, X. Li, B. M. Alston, B. Li, R. Clowes, N. Rankin, B. Harris, R. S. Sprick and A. I. Cooper, *Nature*, **2020**, *583*, 237.

SUPPLEMENTARY FIGURES AND TABLES
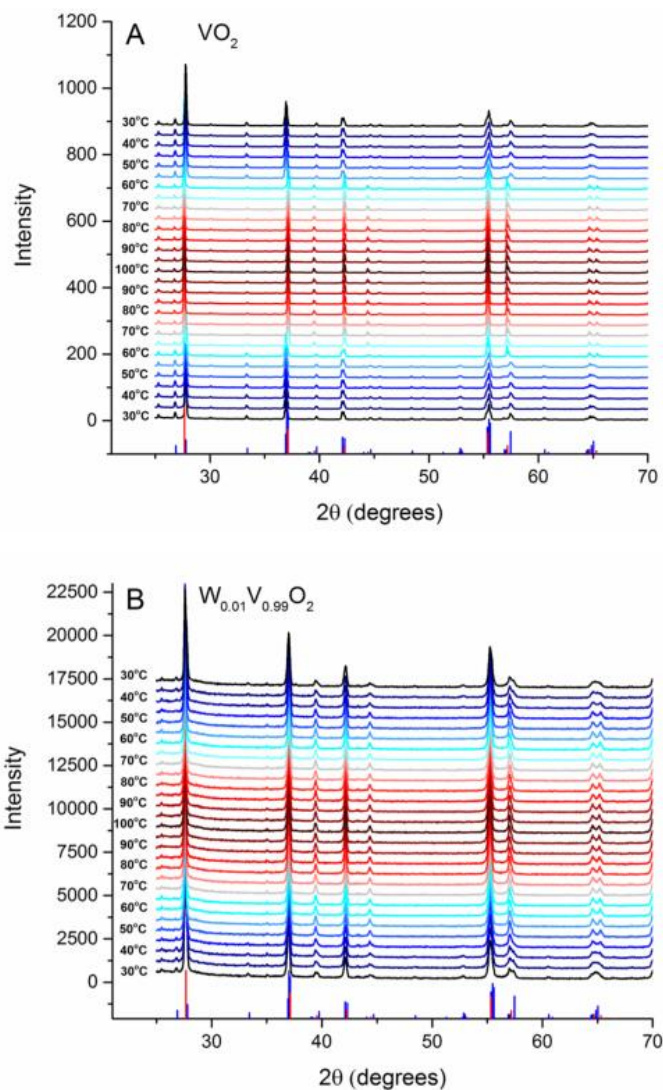
Figure A.1. Extended powder XRD patterns acquired in the 2θ range from 25—70° for (A) undoped and (B) VO_2 incorporating 0.51 at.% W as a substitutional dopant.
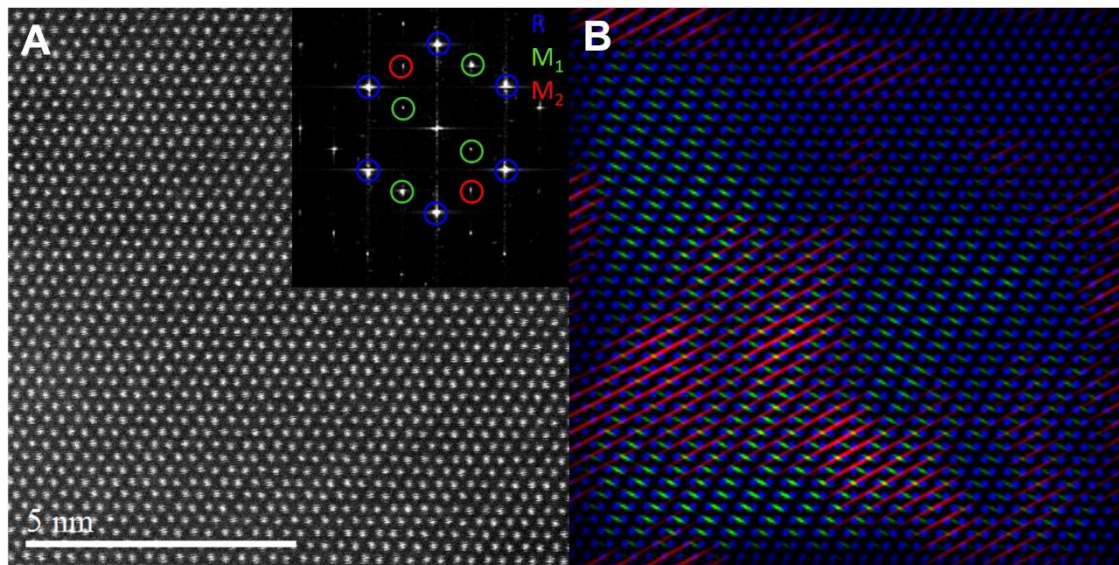
Figure A.2. Atomic-resolution HAADF TEM image of a $W_xV_{1-x}O_2$ particle (with x of ca. 0.008) acquired at 25°C after warming from -180°C. A) TEM image and diffraction patterns with distinct diffraction spots indexed to R (blue), M_1 (green), and M_2 (blue) polymorphs. B) Composite map depicting the spatial distribution of the three phases.

.
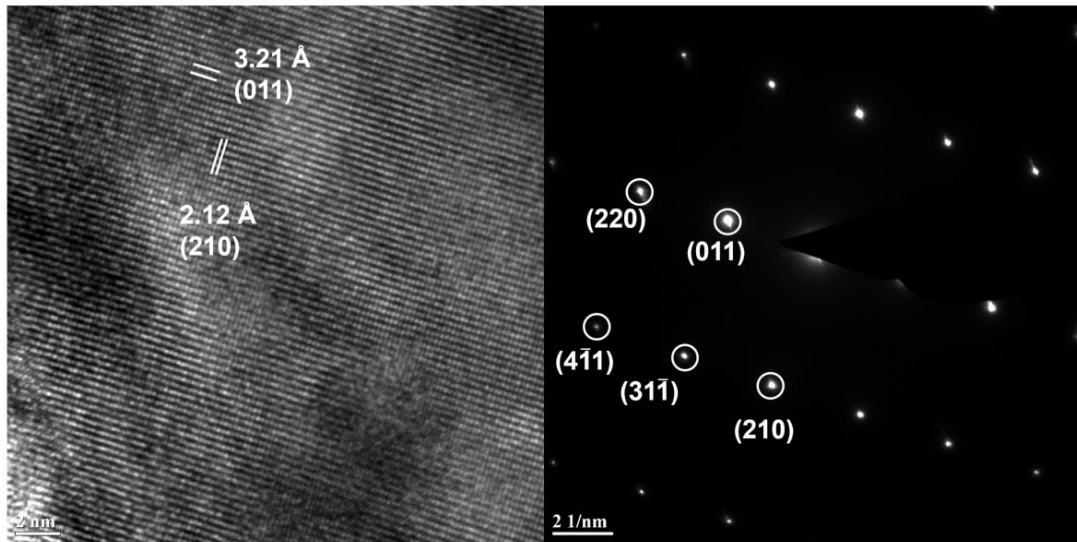
Figure A.3. High-resolution TEM image (left) and selected area electron diffraction pattern (right) acquired for undoped VO_2 prepared by acetone reduction of V_2O_5. The diffraction pattern and interplanar separations correspond solely to the M_1 phase of VO_2
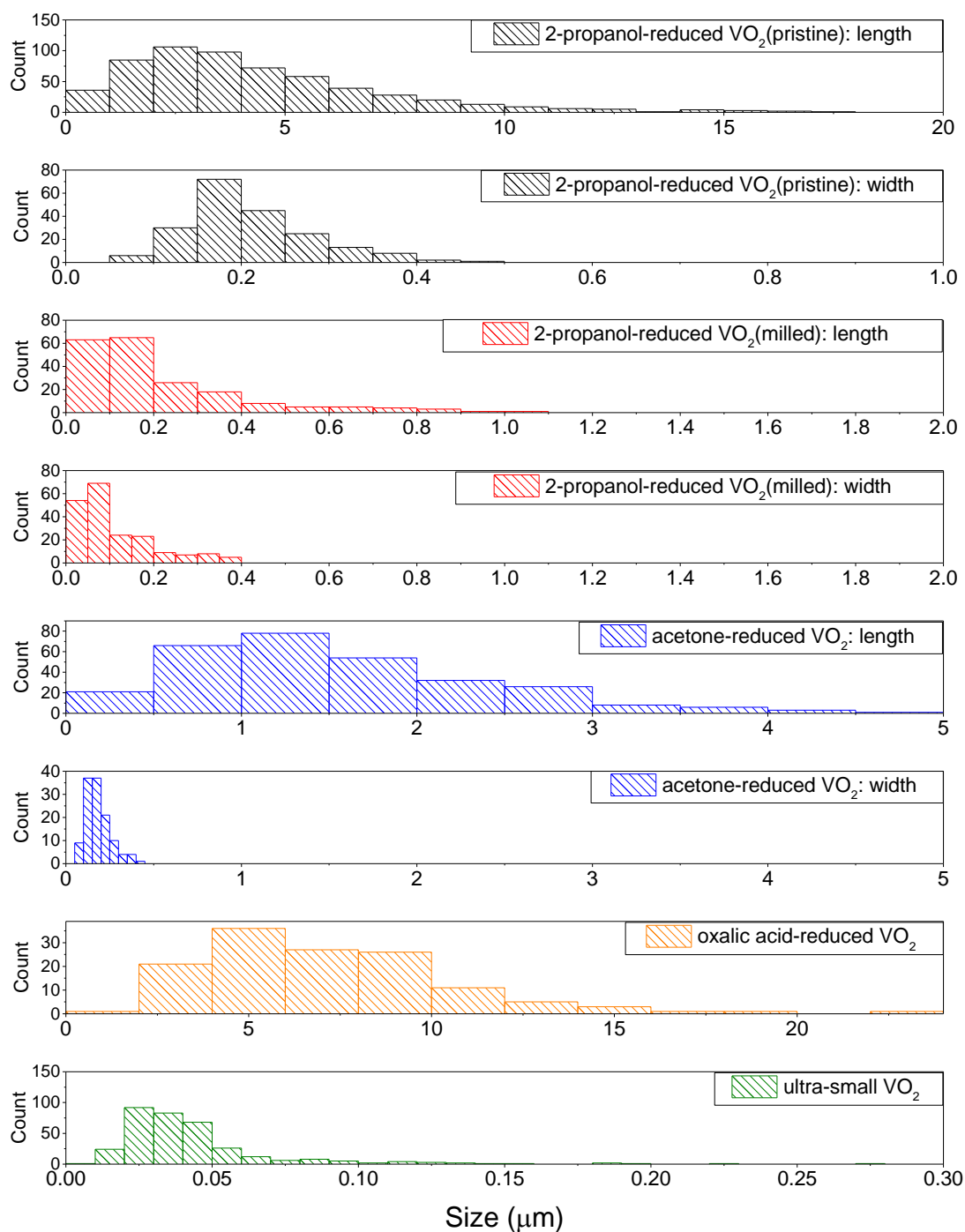
Figure A.4. Size distribution histograms for four different sample preparations yielding different sized particles. Oxalic acid and ultra-small VO₂ yield star shaped and spherical particles respectively and thus a single value, the diameter, is shown as a measure of the size.
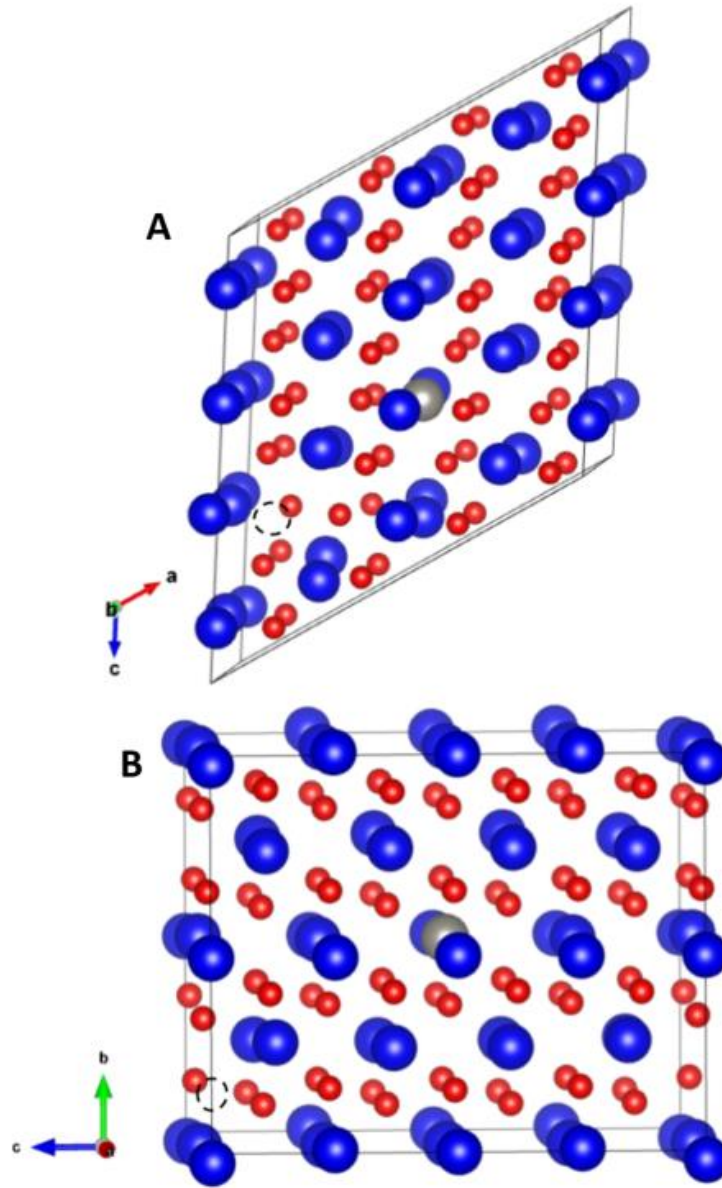
Figure A.5. Structural representation of supercell used in defect calculations of doped A) M_1 and B) R polymorphs of VO_2. The oxygen vacancy is represented by a dashed circle, whereas the tungsten atom is depicted in silver. Vanadium atoms are depicted in blue and oxygen atoms in red. To test for a possible local effect, an oxygen vacancy was created at an adjacent site and far from tungsten as seen in Figure A.3 in both rutile and monoclinic supercells. After introducing a vacancy, supercell structures were fully relaxed. The energy of the rutile cell did not change significantly, less than 6 meV, as a result of proximity of the oxygen vacancy to the tungsten atom.

191

SUPPLEMENTARY FIGURES AND TABLES
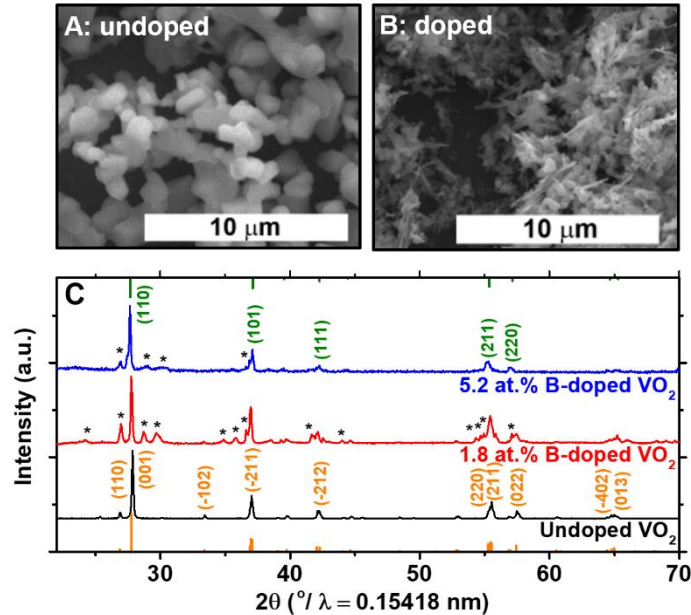
Figure B.1. SEM images show A) undoped and B) $B_{0.018}VO_2$; the annealing step resulted in the incorporation of B atoms within interstitial sites of VO_2 and induces the sintering of VO_2 nanowires into irregular shaped platelets with lateral dimensions extending to 1.9 ± 1.0 μm. C) Powder XRD pattern in the 2Θ range from 22—70° of undoped VO_2, $B_{0.018}VO_2$, and $B_{0.052}VO_2$ acquired at 22°C. Reflections corresponding to the M_1 phase of VO_2 are plotted along the bottom axis as per Joint Committee on Powder Diffraction Standards (JCPDS) # 043-1051, whereas reflections corresponding to the R phase of VO_2 are plotted along the top axis as per JCPDS # 79-1655. Undoped and $B_{0.02}VO_2$ samples are indexed to the M_1 phase of VO_2, whereas the pattern for the $B_{0.05}VO_2$ sample is indexed to the R polymorph of VO_2. The incorporation of B atoms depresses the $M_1 \rightarrow R$ transition temperature by ca. 10°C/at.% B(*22*) such that the observed stabilization of R polymorph at room temperature for the $B_{0.05}VO_2$ sample is consistent with a depression of the critical transition temperature for 5.2 at.% B-doping. Reflections derived from a minority V_8O_{15} phase (JCPDS no. 71-0041) are asterisked and are thought to arise from increased VO_2 reduction(*22*) but do not contribute to the observed MIT behavior.(*30*) No evidence is observed for crystalline boron oxides or orthorhombic/M_2 phases of VO_2, which have been reported previously to be associated with interstitial hydrogen incorporation,(*27*) substitutional doping of trivalent cations,(*28*) and anisotropic strain.(*29*)
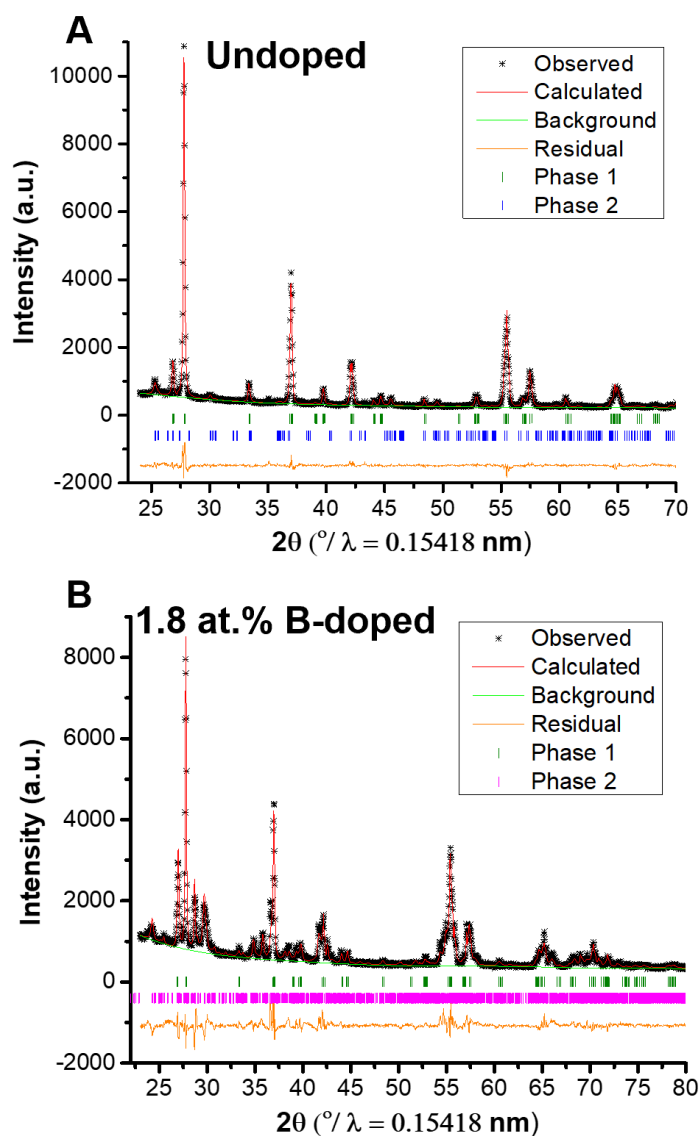
Figure B.2. Rietveld refinement of powder X-ray diffraction pattern of undoped VO_2 and $B_{0.018}VO_2$. A) Undoped VO_2 was subjected to rapid thermal annealing without inclusion of 2-allyl-4,4,5,5-tetramethyl-1,3,2-dioxaborolane; two distinctive phases are identified, monoclinic M_1 VO_2 and phase 2 and trificlinic V_6O_{13}. See also Table B.1. B) Phase 1 is monoclinic M_1 VO_2 and phase 2 is the triclinic V_8O_{15} impurity phase. Two distinctive phases are identified, monoclinic M_1 VO_2 and phase 2 and triclinic V_8O_{15}. See also Table B.1.

Table B.1. Rietveld refinement parameters Tabulated parameters from a Rietveld refinement of powder XRD patterns for undoped VO_2 subjected to rapid thermal annealing without addition of the 2-allyl-4,4,5,5-tetramethyl-1,3,2-dioxaborolane precursor and 1.8 at.% B-doped VO_2. Refinement statistics, including goodness of fit (χ^2), weighted goodness of fit (wRp) and the individual point residuals (Rp) are listed.

Undoped VO_2		
Phase 1: $VO_2(M_1)$ // Space Group: *P1 21/c 1* // Wt. Fraction: 0.8662(5) // Vol: 118.290 (4) Å^3		
$\alpha = 90.000(0)°$	$\beta = 122.597(3)°$	$\gamma = 90.000(0)°$
$a = 5.7561(1)$	$b = 4.529(2)$	$c = 5.385(2)$
$X^2 = 2.282$	wRp = 0.0692	Rp = 0.0538
Phase 2: V_6O_{13}// Space Group: *C 1 2/m 1*// Wt. Fraction: 0.133(3) // Vol: 437.9(2) Å^3		
$\alpha = 90.000(0)°$	$\beta = 101.15 (4)°$	$\gamma = 90.000(0)°$
$a = 11.943(3)$	$b = 3.6818(7)$	$c = 10.149(4)$
$X^2 = 2.282$	wRp = 0.0692	Rp = 0.0538
1.8 at.% B-doped VO_2		
Phase 1: $VO_2(M_1)$ // Space Group: *P1 21/c 1* // Wt. Fraction: 0.389(2) // Vol: 118.77 (2) Å^3		
$\alpha = 90.000(0)°$	$\beta = 122.512(8)°$	$\gamma = 90.000(0)°$
$a = 5.7635(5)$	$b = 4.5291(4)$	$c = 5.3953(8)$
$X^2 = 5.824$	wRp = 0.0907	Rp = 0.0699
Phase 2: V_8O_{15}(triclinic) // *Space Group: P -1* // Wt. Fraction: 0.610(3) // Vol: 916.702 (0) Å^3		
$\alpha = 99.060(8)°$	$\beta = 128.398 (8)°$	$\gamma = 108.925(6)°$
$a = 5.431(7)$	$b = 7.0128(3)$	$c = 37.098(4)$
$X^2 = 5.824$	wRp = 0.0907	Rp = 0.0699
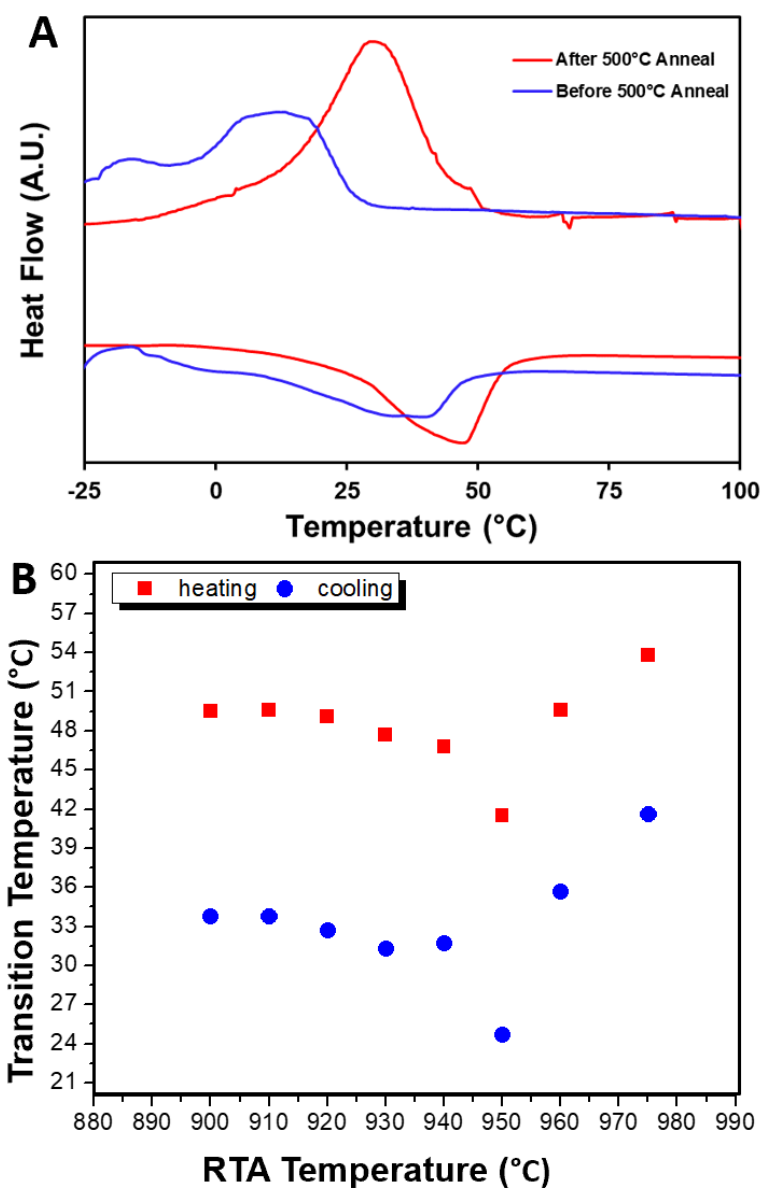
Figure B.3. Boron annealing results A) DSC trace for boron doped VO2 with cycles before (blue) and after (red) an annealing step within the DSC of a 500°C isothermal hold for 2 hours. The shift to higher transition temperature for the heating and cooling transition is indicative of the boron diffusing out of the lattice at high temperature effectively lowering the observed dopant concentration. B) Resulting peak transition temperatures for samples synthesized at various rapid thermal anneal (RTA) temperatures with the boron precursor. The depression leading up to 950°C indicates an optimal temperature for the degradation of the precursor and diffusion of boron in without overshooting to higher temperatures allowing diffusion of boron out of the lattice again.
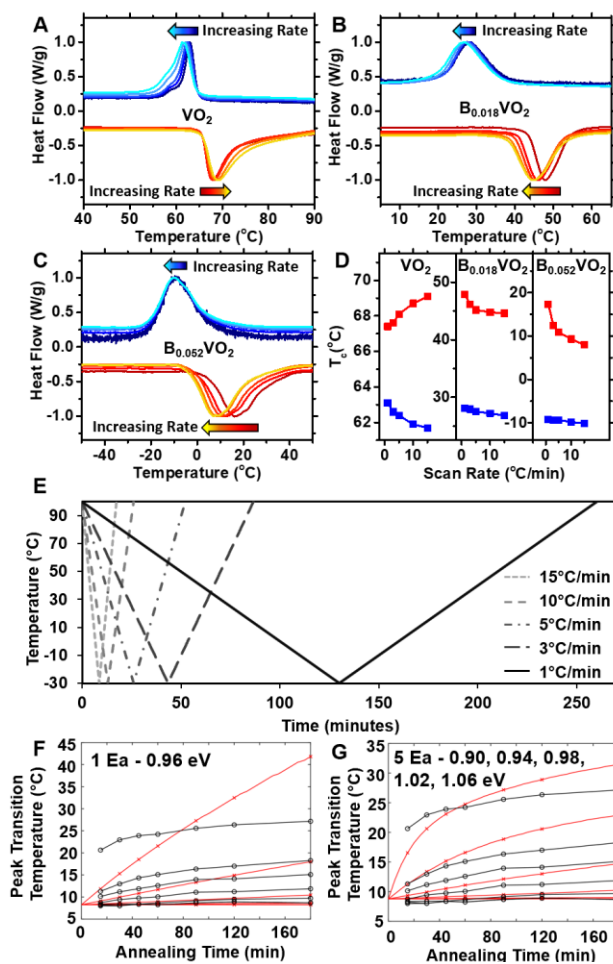
Figure B.4. Additional DSC results – Rate and annealing dependence. Rate-dependent DSC traces for A) VO_2, B) $B_{0.018}VO_2$, and C) $B_{0.052}VO_2$. The red and blue traces depict the evolution of the heating and cooling transitions, respectively, as a function of the scan rate. The shading of the trace represents the scan rate such that the slowest rate (1°C/min) is the darkest and the fastest rate (15°C/min) is the lightest coloration. The resulting T_c values from (A)—(C) are plotted as a function of scan rate in D) with the heating transition in red and cooling transition in blue. E) Thermal profile applied during the rate-dependent DSC experiment for undoped VO_2 and $B_{0.02}VO_2$ samples, the $B_{0.05}VO_2$ sample was cooled to -60°C owing to the lower shifted MIT but followed the same rate pattern. The dash type and shade of the line delineates rate with the most broken/lightest line being the fastest and the unbroken/darkest line as the slowest. F) and G) show arrhenius models for 49 isothermal experiments described in Fig. 3.2 as a function of varying time and temperature at which the sample was held in the monoclinic M_1 phase. Black circles represent the experimental data and red curves and crosses denote the model predictions. Each line represents a different isothermal temperature of -50, -40, -30, -20, -10, 0, and 10°C ascending from the bottom of the plots. F represents a single activation energy of 0.96 eV, whereas G represents a combination of 5 activation energies of 0.90, 0.94, 0.98, 1.02, and 1.06 eV in equal contribution.
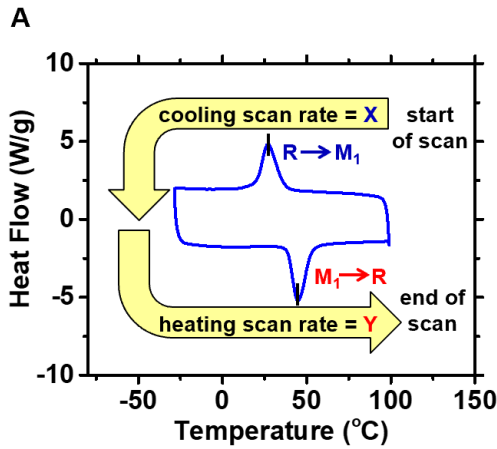
196
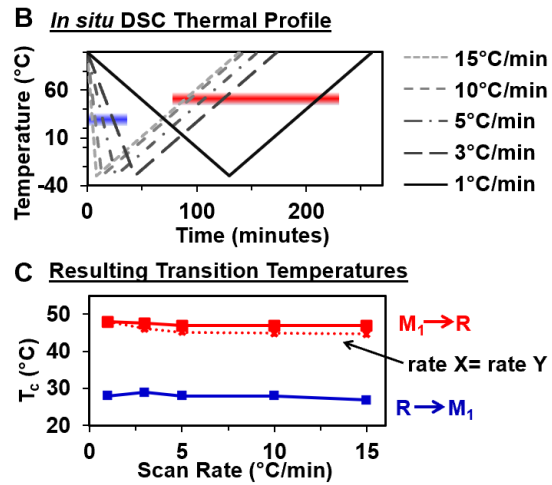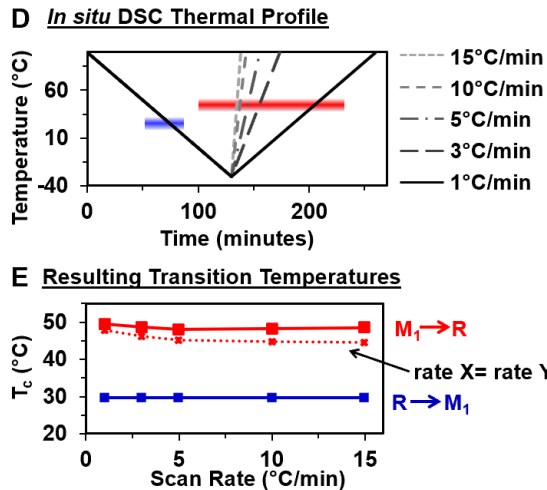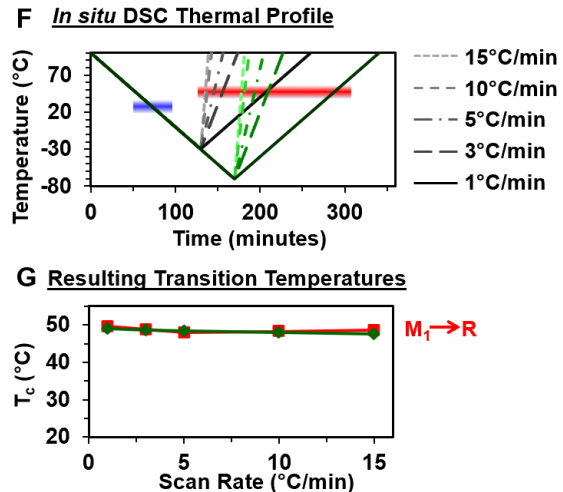
Figure B.5. Additional DSC results – Rate and turnaround dependence. A) Illustration of the procedure employed in DSC Experiments 1—3 for evaluation of a VO_2 sample with 1.8 at.% B in interstitial sites. Experiment 1 involves varying the cooling rate whilst holding the heating rate at 1°C/min (B,C); experiment 2 involves varying the heating rate whilst holding the cooling rate at 1°C/min (D,E); and experiment 3 involves varying the heating rate whilst holding the cooling rate at 1°C/min and comparing turn around temperatures of -30°C and -70°C (F,G). For each experiment, the thermal profiles (B, D, F) and resulting T_c values plotted as a function of scan rate (C, E, G) are given. The T_c values of the heating transition for the full scan rate dependent measurement shown in Fig. B.3D have been added to C and E as a dotted line for comparison. These measurements are aimed at separately evaluating the rate dependence of the R $\rightarrow$ M_1 and

$M_1 \rightarrow R$ transitions and evaluating the influence of time spent within the low-temperature phase. The resulting T_c values for constant heating rate and constant cooling rate measurements are shown in C and E, respectively, and both exhibit T_c of the heating transition ($M_1 \rightarrow R$) to decreases only marginally with increasing scan rate in comparison to the fully rate dependent scans with shifts of less than 1.0°C for both constant heating and constant cooling measurements. Such a result indicates that kinetic asymmetry does not originate in rate-dependent behavior of either of the transitions and suggests that the observed phenomenon derives from the residence time within the M_1 phase. For the experiment in F and G the cooling rate was held constant while the heating rate was varied as in D, but for two different turnaround temperatures, -30°C and -70°C. The difference in T_c between the -30°C and -70°C measurements was negligible indicating that the time the sample spent lower than -30°C does not impact the $M_1 \rightarrow R$ transition temperature for this sample.
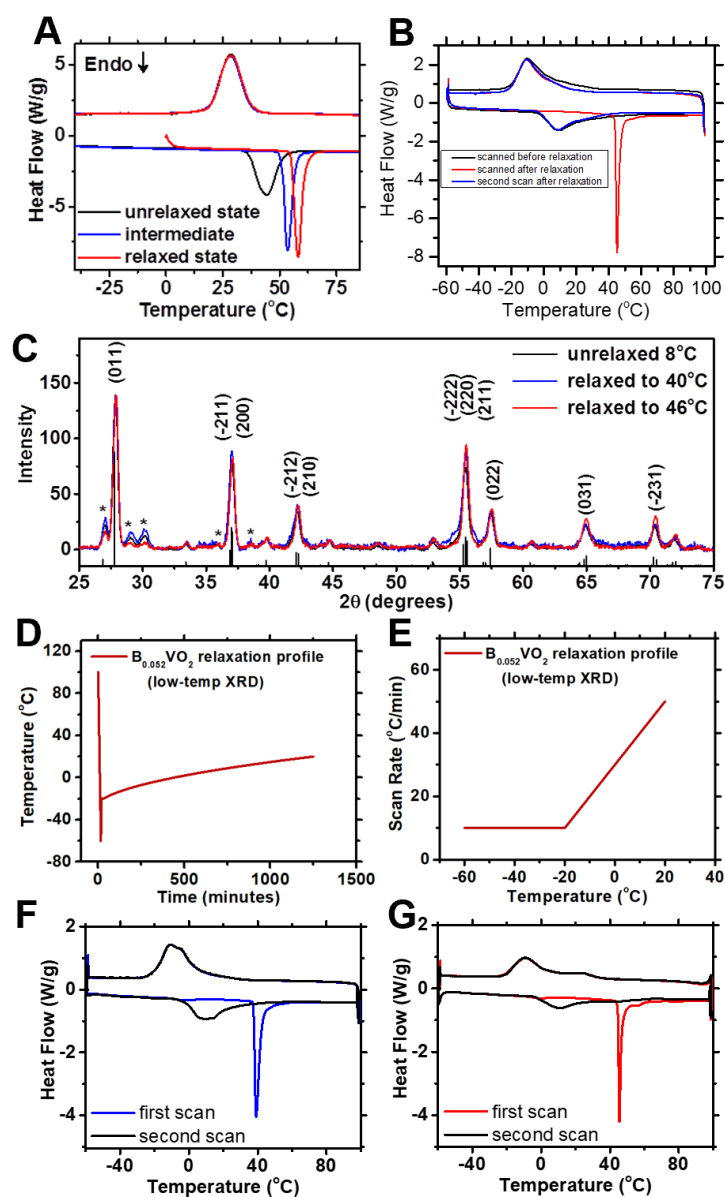
Figure B.6. Probing Quenched and Relaxed States of B-Doped VO$_2$. A) DSC traces of B$_{0.018}$VO$_2$ in the unrelaxed (quenched) state, and states that were thermally-relaxed as a function of time at room temperature amounting to intermediate (40 days) and relaxed (323 days) structures. B) DSC traces of B$_{0.052}$VO$_2$ in the unrelaxed (quenched) state, a thermally-relaxed state after being held at room temperature for 40 days after being relaxed above room temperature in a water bath, and a scan immediately after the cycle that was relaxed showing the resetting nature of this material. C) Powder XRD patterns measured at -163K for a B$_{0.052}$VO$_2$ sample in the relaxed and unrelaxed states of the M1 phase. The unrelaxed sample was heated to 100°C and then rapidly cooled to -163 K. Thermal-relaxation profilesand DSC scans before and after resetting are provided for the 7 (D, F) and 28 (E, G) days before low-temperature XRD.

199

Table B.2. Calculated formation energies and lattice parameters Formation energies and atomic coordinates of all unique interstitial B sites in the M_1 and R unit cells as well as calculated M_1 lattice parameters for different levels of interstitial B doping. Sites denoted with an (*) indicate the sites in a distorted and unrelaxed intermediate M_1 phase calculated as metastable when transitioning from rutile in a doped 97 atom $2\times2\times2$ supercell.

Location	Formation Energy (eV)	Coordinates		
		x	*y*	*Z*
M_1 - $BV_{32}O_{64}$				
M1(1)	-1.465	0.444	0.750	0.446
M1(2)	-1.465	0.564	0.494	0.313
M1(3)	-0.914	0.473	0.527	0.285
M1(4)	-0.604	0.727	0.209	0.279
M1(5)	-0.604	0.524	0.780	0.433
M1(6)*	0.348	0.484	0.770	0.451
M1(5)*	0.384	0.524	0.780	0.473
M1(1)*	0.705	0.440	0.748	0.441
R - $BV_{32}O_{64}$				
R (1)	-3.559	0.500	0.750	0.687
R (2)	-2.154	0.120	0.447	0.295
R (3)	-2.590	0.551	0.710	0.628
Monoclinic lattice change			Δvolume (Å³)	vol. (Å³)
boron (at. %)	Δ*a* (Å)	Δ*b* (Å)	Δ*c* (Å)		
1.03	0.384%	0.322%	0.196%	0.628%	121.8
2.04	0.743%	0.786%	0.354%	1.502%	122.8
4	2.452%	0.484%	1.577%	6.908%	129.4
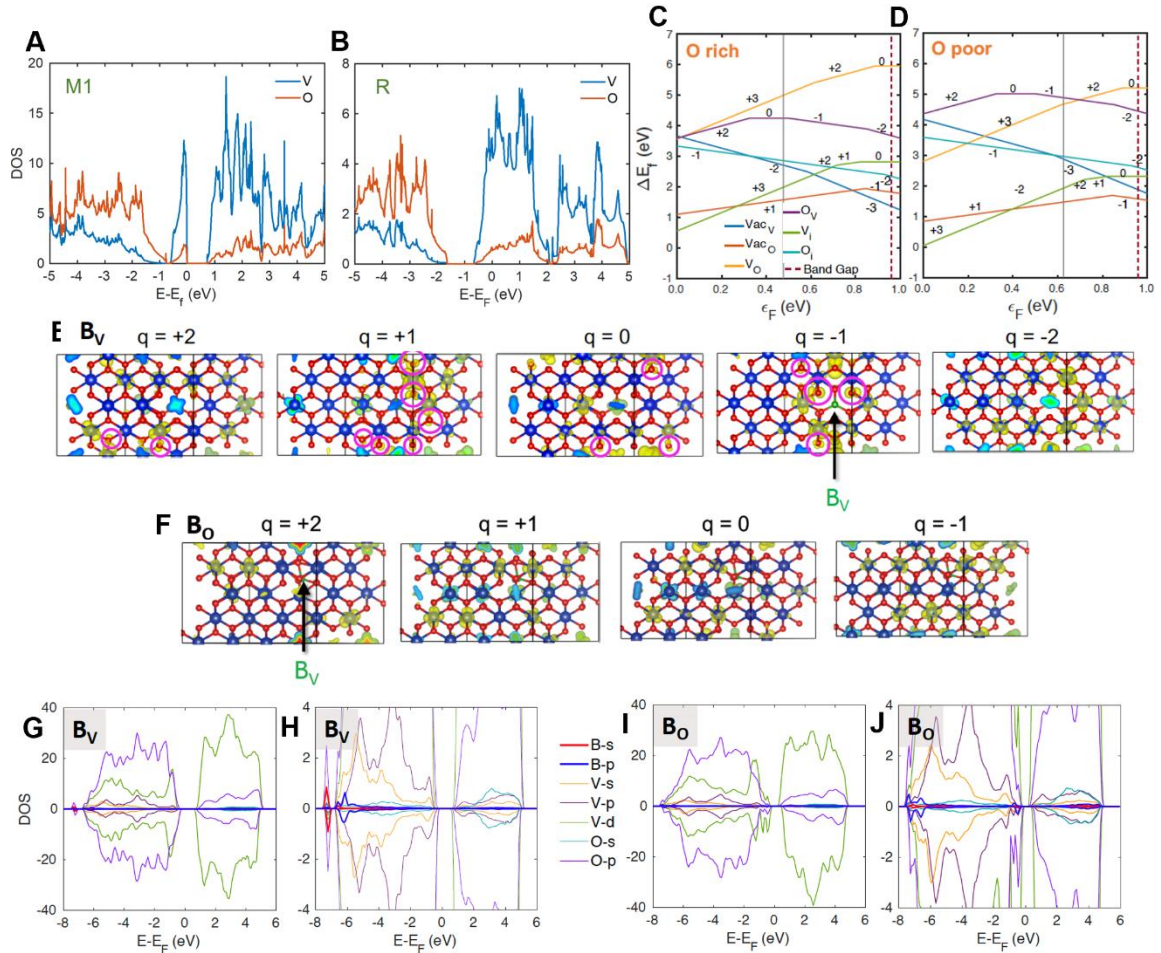
Figure B.7. Defect and band structure calculations. Density of states for (A) M$_1$ and (B) R phases respectively, using a *U* value of 3.4 eV, which captures the insulating nature of the M$_1$ polymorph and the metallic nature of the rutile polymorph. Native defect diagrams under (C) O-rich and (D) O-poor conditions. The vertical grey line indicates where the equilibrium Fermi level is pinned by the native defects. Charge density of the highest energy valence states for (E) B$_V$ and (F)B$_O$ defects with various charge states. In all cases, the charge is delocalized on V and O atoms instead of being localized around the B atom, which is expected from shallow defects. Purple circles indicate the electron density on oxygen atoms in the B$_V$ defect cell. Analogous to the discussion of the B$_v$ defect, the charges associated with B$_O$ defect are delocalized also indicated in the also the 0 charge state orbital-resolved DOS plots for (G,H) B$_V$ and (I,J) B$_O$ defects. Hence, no significant lattice distortion is observed in proximity of the B atom. H and J are respective magnified views of G and I orbital-resolved projected DOS plots. The electronic states associated with the boron atom are mainly located within the deep valence band around -8 to -6 eV below the Fermi level, making it unlikely to induce significant electron density around the B atom near the Fermi level. This is consistent with Fig. B.7C-D where the top valence electrons are mostly delocalized across the V and O atoms instead of the B defect.

201
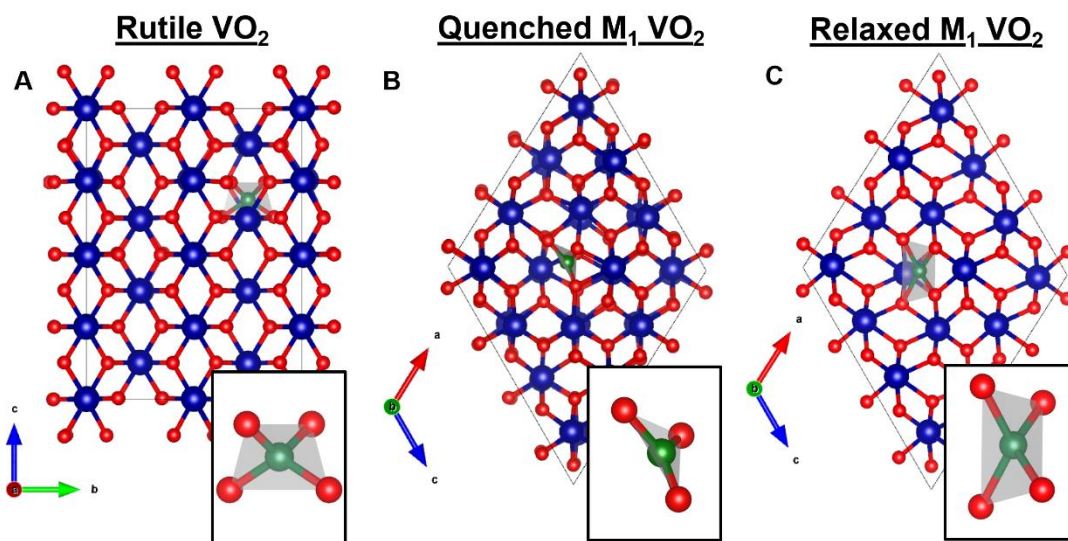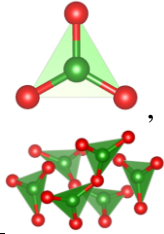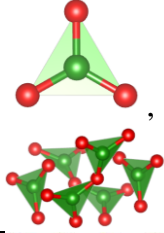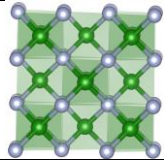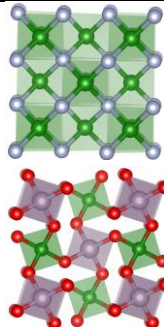
Figure B.8. Calculated suspercells: DFT calculated supercells for B-doped VO_2, illustrating the most thermodynamically favorable interstitial sites for B incorporation for R (A, R(1)), quenched M_1 (B, M1(6)), and relaxed M_1 (C, M1(1)). Vanadium atoms are depicted as blue spheres, oxygen atoms as red spheres, and B atoms as green spheres. Lattice parameters for the doped M_1 structure with different concentrations of boron can be found in Table B.2. Insets show oxygen coordination of boron in each respective state.

.

Table B.3. Boron spectral features reference Assignment of B—O electronic transitions to spectral features in B K-edge XANES spectra using B standards.

Assignment	Incident Photon Energy (eV)	Standard	Structure	References
B 1s → π* B—O (trigonal)	194.4	H_3BO_3, B_2O_3		22,38-41
B 1s → σ* B—O (trigonal)	203.0	H_3BO_3, B_2O_3		22,39-41
B 1s → σ* B—O (tetrahedral)	198.2	cubic-BN		22,39,40
B 1s → σ* B—O (tetrahedral) multiple scattering resonances	~200	cubic-BN, BPO_4		22,38,40
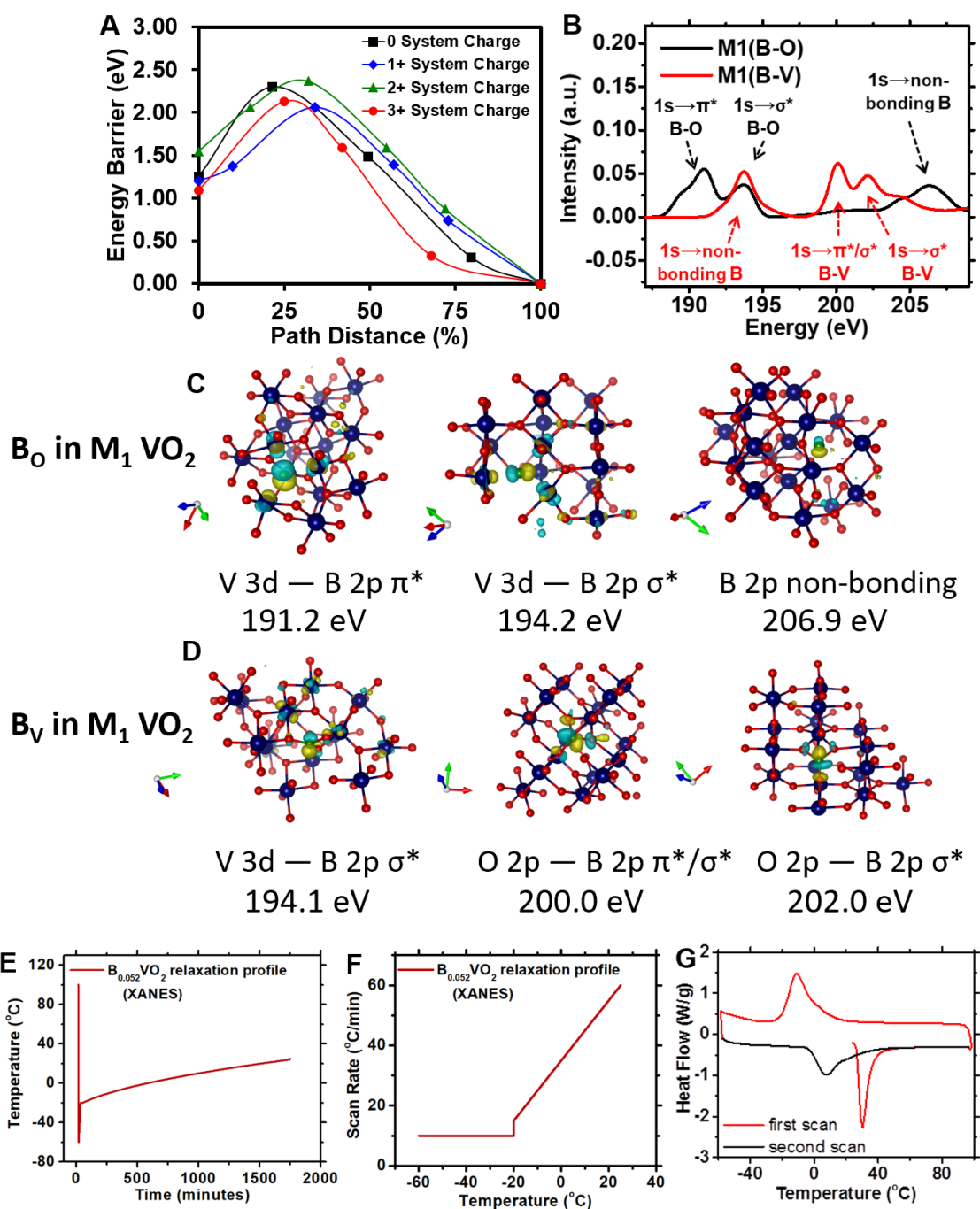
Figure B.9. Additional NEB and XANES details A) Minimum energy pathways obtained from NEB calculations when different charges were added to the supercell. B) Calculated B K-edge XANES spectra of substitutionally B-doped VO_2 when B occupies an O site (black) or a V site (red). Final state assignments of the spectral features are

assigned based on the symmetries of the states observed in the isosurface plots shown in (C) and (D). Features are labeled with their character as assigned from isosurface plots of the final states. Isosurfaces are furthermore labeled with the energy of the transition feature. The absorption features at 191 eV and 194 eV for a B atom in a O site are assigned to the excitation of a core B 1s electron to π^* and σ^* states, respectively, associated with hybridization between V 3d and B 2p states. The absorption feature at 206 eV is assigned to a non-bonding B 2p state. The absorption feature at 194 eV for a B atom in a V site is assigned to a non-bonding B 2p state. The isosurface structure associated with the absorption feature at 200 eV depicts both π^* and σ^* character for the excitation of a core B 1s electron to a hybridized O 2p—B 2p state. The final absorption feature at 202 eV is assigned to the excitation of a core B 1s electron to a O 2p—B 2p hybrid σ^* state. (E,F) Thermal DSC profile expressed as (E) temperature vs. time and (F) scan rate vs. temperature, used to thermally-relax the $B_{0.052}VO_2$ sample to room temperature prior to Boron K-edge XANES spectroscopy measurements (shown in Figure 3.5B). G) DSC cycling measurement scans of the thermally-relaxed $B_{0.05}VO_2$ sample taken immediately following the Boron K-edge XANES analysis shown in Fig. 3.5B.

SUPPLEMENTARY FIGURES AND TABLES
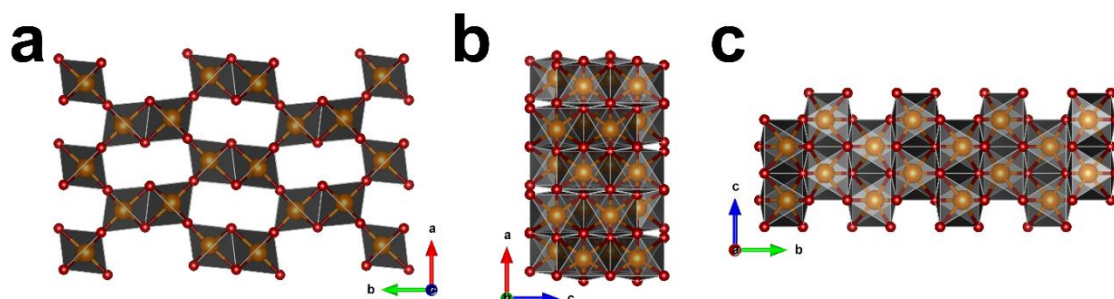
Figure C.1. Crystal structure renditions of a single unit-cell of VO_2 (orthorhombic, alternate setting *Pbnm*) as refined by Rietveld analysis of powder XRD data depicted in Figure 4.1a presented along the crystallographic (a) *c*-, (b) *b*-, and (c) *a*-axes.

Table C.1. Statistics for the Rietveld refinement plotted in Fig. 4.1 (red). Unit cell parameters obtained by Rietveld refinement of powder XRD data.

$\chi^2 = 10.11$, $R_p = 5.15\%$, $wR_p = 6.74\%$	
Lattice parameter	Value (Å)
a	4.7014(5)
b	9.567(1)
c	2.9196(4)
V	131.33(1) (Å^3)

Table C.2. Atom positions of crystallographically distinct vanadium and oxygen atoms. Note that isotropic thermal parameters, with the exception of vanadium, were set to the values tabulated without further refinement.

Atom Label	*x*	*y*	*z*	Uiso*100	Fractional Occupancy
V	0.0452(7)	0.1423(4)	0.2500	2.772	1.00
O1	0.1917(18)	-0.2352(11)	0.2500	1.00	1.00
O2	-0.2411(13)	-0.0097(11)	0.2500	1.00	1.00

Table C.3. Unique bond distances for V—O bonds within distorted VO_6 octahedra as obtained by the Rietveld refinement of the powder XRD data presented in Figure 4.1. The bond distances are the same as displayed in Figure C.1d. Comparable values for the paramontroseite mineral phase as reported by Evans *et al.* are shown for comparison.[1]

Bond distances			
		Distance (Å)	
Polyhedron	Bond (Atom pair)	IrO_2-doped $VO_2(P)$	Mineral Paramontroseite
VO_6	V—O1	1.704(7)	1.844
	V—O1	2.040(5)	2.024
	V—O2	2.040(5)	2.024
	V—O3	1.982(9)	2.000
	V—O4	2.142(7)	2.000
	V—O5	2.142(7)	2.126
Nearest V-V bond	V—V	2.9196	2.93

Table C.4. Unique bond angles for the VO_6 octahedra as obtained by the Rietveld refinement of the powder XRD data presented in Fig. 4.1. Comparable values for the paramontroseite mineral phase as reported by Evans *et al.* are shown for comparison.[1]

Bond angles			
		Angle (°)	
Polyhedron	Atom Pairs	IrO_2-doped $VO_2(P)$	Mineral Paramontroseite
VO_6	O1_V_O2	176.2(6)	168.08
	O1_V_O3	95.46(35)	95.7
	O1_V_O4	95.55(13)	91.75
	O1_V_O5	95.55(13)	91.75
	O1_V_O6	95.46(35)	95.7
	O2_V_O3	81.799	92.41
	O2_V_O4	87.1(4)	80.08
	O2_V_O5	87.1(4)	80.08
	O2_V_O6	81.80(28)	92.41
	O3_V_O4	90.29(22)	86.05
	O3_V_O6	85.92(33)	94.21
	O5_V_O4	91.39(31)	92.72
	O5_V_O6	90.29(22)	86.05

Table C.5. Lattice parameters obtained for the samples reported in this work compared to those reported for the paramontroseite phase in the literature.[1,2]

Comparison of lattice parameters			
Parameter	Ir-Doped $VO_2(P)$ (This work)	Synthetic Paramontroseite	Naturally Occurring Paramontroseite
a (Å)	4.7014	4.956	4.89
b (Å)	9.567	9.332	9.39
c (Å)	2.9196	2.896	2.93
V (Å)^3	131.33	133.9	134.5

Table C.6. Change of lattice parameters and unit cell volume for prepared material as compared to synthetic and mineral phases reported in the literature.[1,2]

Parameter	Strain in Ir-Doped $VO_2(P)$	
	Relative to $VO_2(P)$	Relative to Naturally Occurring Paramontroseite
a (Å)	-5.137%	-3.86%
b (Å)	2.518%	1.885%
c (Å)	0.815%	-0.355%
V (Å)^3	-1.956%	-0.239%

C.1. References

[1]   H. T. Evans, M. E. Mrose, *U.S. Geol. Surv.* **1954**, 861.

[2]   C. Wu, Z. Hu, W. Wang, M. Zhang, J. Yang, Y. Xie, *Chem. Commun. (Camb).*

2008, 3891.

SUPPLEMENTARY FIGURES AND TABLES
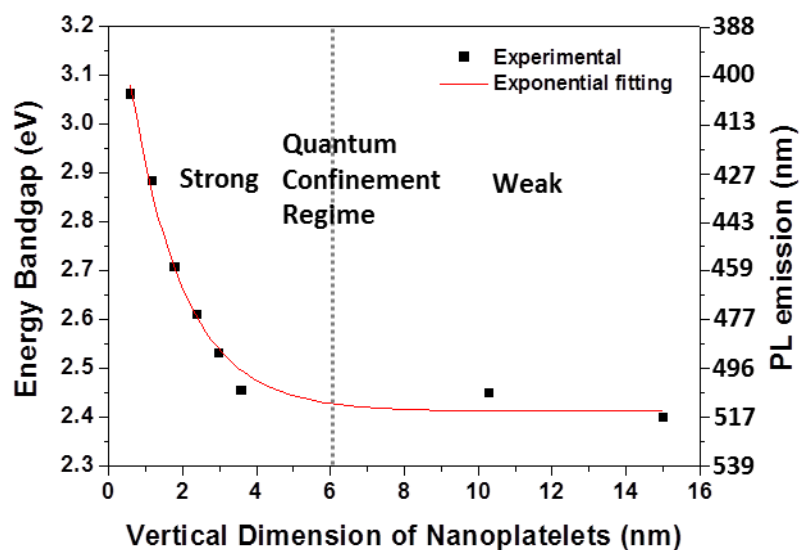
Figure D.1. PL emission wavelength (or energy bandgap) of 2D $CsPbBr_3$ nanoplatelets derived from single-particle measurements plotted as a function of the vertical dimension of the nanoplatelets.
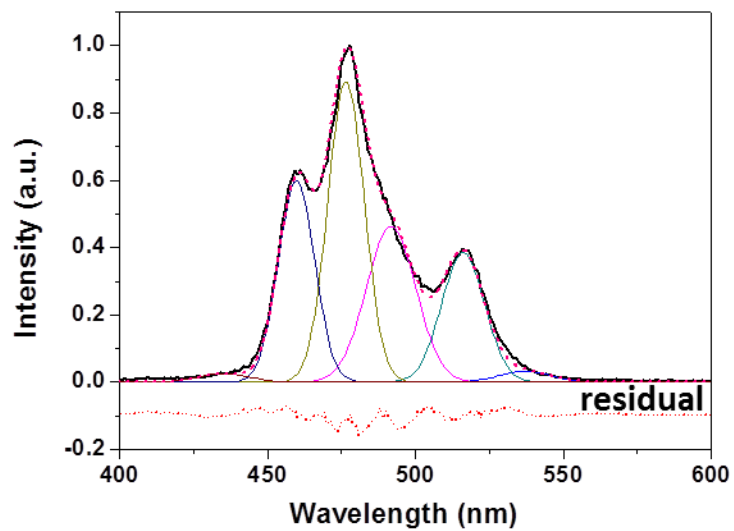
Figure D.2. Deconvolution of PL emission spectra with multiple Gaussian fitting for CsPbBr₃ nanoplatelets obtained at the reaction condition of using C12 with 1:20 at 150 °C. The dotted line at the bottom of the plot represents the residual of the fit.
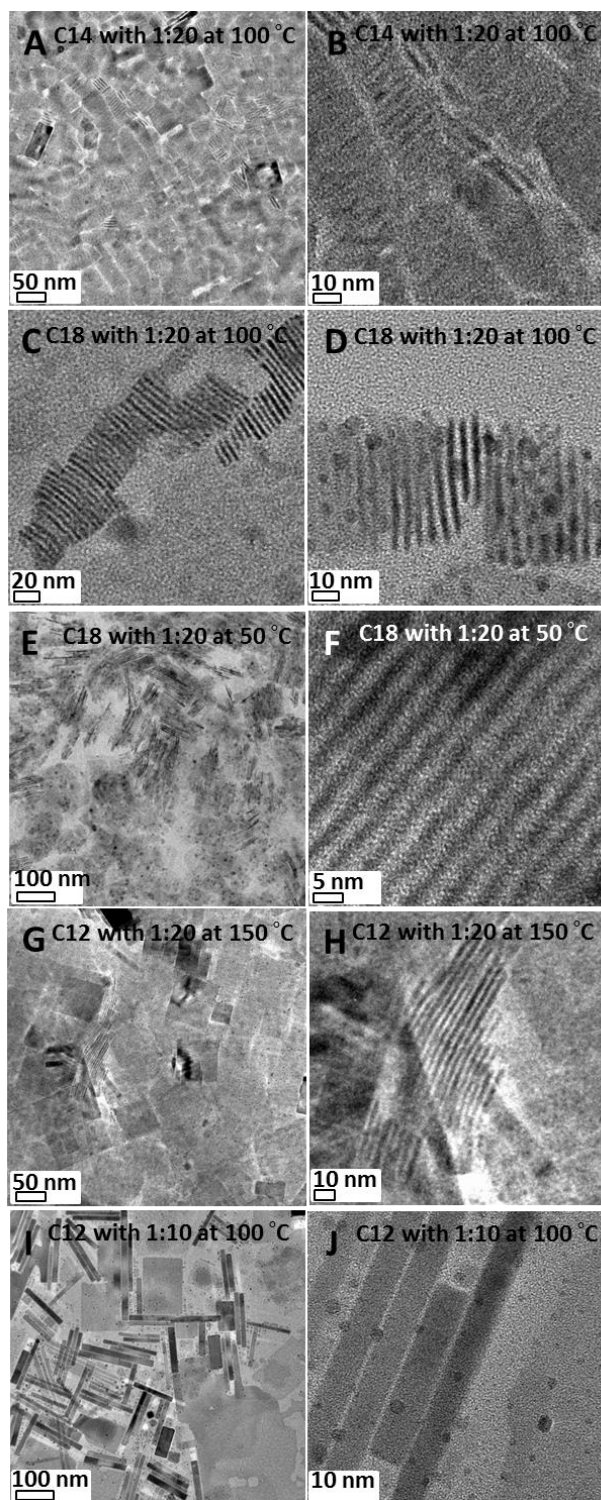
Figure D.3. TEM images of 2D CsPbBr$_3$ nanoplatelets grown under different reaction conditions: A,B) C14 with 1:20 at 100°C; C,D) C18 with 1:20 at 100°C; E,F) C18 with 1:20 at 50°C; G,H) C12 with 1:20 at 150°C; I,J) C12 with 1:10 at 100 °C.

211
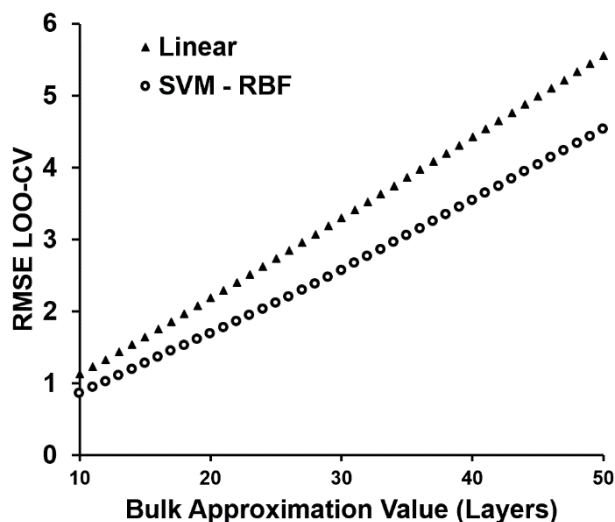
Figure D.4. Plot of leave-one-out cross-validation RMSE-CV as a function of the bulk thickness approximation for linear and SVM with a radial basis function kernel models using diffusion coefficient as the alkylamine descriptor.

Table D.1. Deconvolution of PL emission spectra for an initial sampling of multivariate reaction space (40 samples). Multi-peak Gaussian fitting has been used to determine the fractional populations for different layer thicknesses ($n = 1, 2, 3, 4, 5, 6$, and bulk). Grey shading indicates samples with $< 5\%$ bulk PL emission intensity. Blue shading indicates samples with $> 50\%$ bulk PL emission intensity.

Entry	Alkyl-amine Chain-length (Cn)	T (°C)	Conc. (x)	$n = 2$	$n = 3$	$n = 4$	$n = 5$	$n = 6$	$n =$ bulk	$n_{avg.}$
1	4	50	1:20	-	0.204	0.198	0.289	-	0.309	5.95
2	4	100	1:20	-	-	0.060	0.091	0.094	0.755	8.81
3	4	100	1:5	-	-	-	-	-	1.000	10.0
4	4	100	1:10	-	-	-	-	-	1.000	10.0
5	4	100	1:20	-	-	0.035	0.125	0.170	0.671	8.49
6	4	100	1:30	-	0.045	0.060	0.087	0.146	0.661	8.30
7	4	100	1:40	-	-	-	-	0.191	0.809	9.23
8	4	150	1:20	-	0.023	0.028	0.017	-	0.932	9.59
9	8	50	1:20	0.021	0.508	0.177	0.061	-	0.232	4.84
10	8	100	1:20	0.009	0.297	0.227	0.113	-	0.354	5.92
11	8	100	1:5	-	-	-	0.071	0.243	0.686	8.67

Table D.1. Continued

Entry	Alkyl-amine Chain-length (Cn)	T (°C)	Conc. (x)	$n = 2$	$n = 3$	$n = 4$	$n = 5$	$n = 6$	$n =$ bulk	$n_{avg.}$
12	8	100	1:10	0.011	0.017	0.109	0.225	-	0.638	8.01
13	8	100	1:20	0.015	0.326	0.194	0.080	0.071	0.314	5.75
14	8	100	1:30	0.456	0.383	0.090	0.023	0.017	0.032	2.95
15	8	100	1:40	-	0.514	0.332	0.078	0.076	-	3.71
16	8	150	1:20	-	-	-	-	0.053	0.947	9.77
17	12	50	1:20	0.412	0.527	0.025	0.017	-	0.019	2.78
18	12	100	1:20	0.047	0.493	0.246	0.119	-	0.096	4.11
19	12	100	1:5	0.025	0.015	0.035	0.055	-	0.870	9.21
20	12	100	1:10	-	0.015	0.179	0.141	0.047	0.618	7.92
21	12	100	1:20	0.460	0.443	0.050	0.027	0.008	0.012	2.75
22	12	100	1:30	0.387	0.486	0.081	0.025	0.015	0.006	2.83
23	12	100	1:40	0.030	0.661	0.190	0.070	0.023	0.025	3.56
24	12	150	1:20	0.013	0.221	0.351	0.229	-	0.186	5.10
25	14	50	1:20	0.108	0.746	0.083	0.037	0.026	-	3.10
26	14	100	1:20	0.357	0.524	0.079	0.02	0.019	-	2.81
27	14	100	1:5	0.024	0.052	0.105	0.087	0.073	0.659	8.09
28	14	100	1:10	-	0.253	0.426	0.193	0.055	0.073	4.48
29	14	100	1:20	0.358	0.524	0.079	0.021	0.019	-	2.82
30	14	100	1:30	0.531	0.378	0.054	0.018	0.019	-	2.62
31	14	100	1:40	0.098	0.657	0.184	0.039	0.023	-	3.23
32	14	150	1:20	0.010	0.385	0.312	0.096	0.030	0.168	4.76
33	18	50	1:20	0.012	0.684	0.179	0.107	-	0.017	3.50
34	18	100	1:20	0.063	0.589	0.234	0.076	0.039	-	3.44
35	18	100	1:5	0.019	0.046	0.101	0.096	-	0.738	8.43
36	18	100	1:10	0.017	0.629	0.185	0.078	0.015	0.076	3.91
37	18	100	1:20	0.035	0.656	0.125	0.132	0.053	-	3.52
38	18	100	1:30	0.128	0.692	0.124	0.038	0.018	-	3.12
39	18	100	1:40	-	0.484	0.245	0.151	-	0.121	4.40
40	18	150	1:20	-	0.589	0.221	0.097	0.044	0.044	3.89

Table D.2. Deconvolution of PL emission spectra for additional random sampling of multivariate reaction space (34 samples) performed to expand the dataset to a viable size outside of the original experimental vectors. Multi-peak Gaussian fitting has been used to determine the fractional populations for different layer thicknesses (n = 1, 2, 3, 4, 5, 6, and bulk). Grey shading indicates samples with < 5% bulk PL emission intensity. Blue shading indicates samples with > 50% bulk PL emission intensity.

Entry	Chain length (Cn)	T (°C)	Conc. (x)	n = 2	n = 3	n = 4	n = 5	n = 6	n = bulk	$n_{avg.}$
1	4	70	1:35	-	0.031	0.107	0.169	0.482	0.210	6.36
2	5	50	1:30	-	0.248	0.172	0.221	0.322	0.037	4.84
3	5	60	1:35	-	0.118	0.124	0.404	0.175	0.179	5.71
4	5	110	1:40	-	-	0.019	0.205	0.183	0.594	8.13
5	5	150	1:20	-	-	-	-	0.040	0.961	9.84
6	6	110	1:40	0.012	0.195	0.116	0.211	0.089	0.376	6.43
7	7	80	1:30	0.110	0.700	0.110	0.030	0.030	0.030	3.33
8	7	80	1:20	-	0.146	0.192	0.083	0.234	0.345	6.47
9	9	50	1:40	0.032	0.599	0.249	0.078	0.028	0.014	3.55
10	9	70	1:25	-	0.743	0.123	0.082	0.037	0.015	3.51
11	9	80	1:40	-	0.479	0.288	0.111	0.063	0.059	4.11
12	9	90	1:40	0.035	0.600	0.167	0.131	0.040	0.027	3.70
13	12	110	1:30	0.112	0.564	0.117	0.114	0.060	0.032	3.64
14	14	50	1:25	0.065	0.754	0.093	0.043	0.029	0.016	3.31
15	14	70	1:25	0.136	0.665	0.151	0.027	0.020	-	3.13
16	14	80	1:20	0.020	0.720	0.200	0.030	0.030	-	3.33
17	14	120	1:30	0.030	0.341	0.157	0.135	0.155	0.181	5.13
18	14	120	1:40	-	0.338	0.187	0.069	0.119	0.287	5.69
19	14	150	1:30	0.040	0.224	0.170	0.173	0.059	0.335	6.00
20	14	150	1:40	0.046	0.169	0.276	0.188	0.118	0.203	5.38
21	16	70	1:40	0.052	0.398	0.161	0.274	0.089	0.026	4.10
22	16	90	1:40	0.115	0.527	0.084	0.033	0.121	0.119	4.24
23	16	100	1:35	0.029	0.107	0.089	0.072	0.646	0.057	5.54
24	16	120	1:5	-	-	-	0.05	-	0.949	9.74
25	18	50	1:15	0.016	0.503	0.306	0.133	0.033	0.009	3.72
26	18	50	1:10	0.021	0.217	0.353	0.202	0.136	0.071	4.64
27	18	60	1:30	0.035	0.529	0.270	0.104	0.048	0.014	3.69
28	18	60	1:20	0.052	0.529	0.259	0.113	0.033	0.014	3.63
29	18	70	1:20	0.060	0.512	0.205	0.140	0.054	0.029	3.79
30	18	100	1:25	0.025	0.306	0.339	0.230	0.073	0.026	4.18
31	18	110	1:25	0.021	0.271	0.293	0.143	0.149	0.125	4.87
32	18	120	1:10	-	-	0.05	0.11	0.76	0.08	6.09
33	18	130	1:40	0.036	0.126	0.133	0.247	0.326	0.132	5.49
34	18	140	1:15	0.012	0.480	0.256	0.109	0.092	0.051	4.09

Table D.3. Descriptor values for the alkylamines used for t-test and wrapper evaluation

Chain length	Molar mass (g/mol)[1]	Boiling point (°C)[2]	Enthalpy of vaporization (kJ/mol)[2]	Density (g/mL)[1]	pKa[1]	Diffusion coefficient 20°C (m²/s×10⁻¹⁰)[3]	ΔG agglomeration 100°C (kJ/mol)[4]	Dipole moment (D)[5]	Polarizability (Å³)[2]	Melting point (°C)[1]	¹H-NMR shift (terminal CH₃) (ppm)[6]	¹H-NMR shift (-NH₂) (ppm)[6]
4	73.137	77.3	31.8	0.74	10.60	1.177	6.222	0.742	9.6	224	0.92	1.77
5	87.163	105.5	34.0	0.755	10.63	1.147	1.740	0.723	11.4	218.15	0.91	1.12
6	101.19	131.8	36.5	0.77	10.56	1.080	-2.742	1.029	13.2	249.8	0.9	1.17
7	115.217	156.4	39.3	0.777	10.67	0.991	-7.225	0.837	15.1	250.15	0.89	1.4
8	129.243	179.4	41.6	0.782	10.65	0.979	-11.707	1.125	16.9	272.15	0.881	1.69
9	143.27	201.1	43.7	0.798	10.64	0.941	-16.189	0.97	18.7	272.15	0.881	1.14
12	185.35	258.6	49.6	0.806	10.63	0.822	-29.636	1.384	24.3	300.15	0.89	1.19
14	213.403	291.9	53.1	0.81	10.62	0.739	-38.601	1.535	27.9	313.15	0.888	1.26
16	241.456	321.8	56.4	0.813	10.61	0.690	-47.565	1.693	31.6	319.95	0.88	1.26
18	269.509	348.9	59.3	0.862	10.60	0.648	-56.530	1.86	35.3	326.05	0.88	1.29

Table D.4. CsPbBr$_3$ wrapper R^2 results for a selection of modeling methods using each of the descriptors of the alkylamine ligands for comparison.

	Chain length	Molar mass	Boiling point	Enthalpy of vaporization	Density	pKa	Diffusion coefficient 20°C	ΔG agglomeration 100°C	Dipole moment	Polarizability	Melting point	^{1}H-NMR shift (terminal CH$_3$)	^{1}H-NMR shift (-NH$_2$)
Linear	0.1927	0.1927	0.2362	0.2278	0.1747	0.0669	0.2416	0.1927	0.1771	0.1924	0.2764	0.2066	0.1700
Quadratic	0.4945	0.4945	0.5011	0.5020	0.4870	0.2763	0.4893	0.4945	0.4104	0.4941	0.4598	0.3792	0.3100
Quadratic (Cross)	0.5991	0.5991	0.6002	0.6071	0.5417	0.3902	0.5990	0.5991	0.5439	0.5993	0.5946	0.4169	0.3810
SVM - RBF	0.8574	0.8589	0.8522	0.8560	0.9429	0.7198	0.8263	0.8499	0.8342	0.8599	0.8208	0.4110	0.8918
SVM - Linear	0.1282	0.1282	0.2138	0.2091	0.1526	-0.0021	0.2249	0.1282	0.0994	0.1275	0.2463	0.1999	0.1534
SVM Quadratic	-0.3139	0.3140	0.3581	0.3521	0.1911	0.2960	0.3490	0.3139	0.2692	0.3123	0.3167	0.2081	0.2468
SVM - Cubic	0.3286	0.3284	0.2837	0.3152	0.2888	0.0328	0.3310	0.3286	0.2369	0.3281	0.2853	0.1783	0.2474
KNN - K=3	0.0598	0.1181	0.2244	0.0179	0.0402	-0.0033	0.0614	0.1744	0.0588	0.0153	0.1366	-0.0492	-0.0442
Ridge λ=50	0.1206	0.1919	0.2352	0.1934	0.0601	0.0601	0.0603	0.1896	0.0607	0.1644	0.2740	0.0601	0.0602
Ridge λ=10	0.1753	0.1926	0.2362	0.2243	0.0607	0.0607	0.0615	0.1925	0.0635	0.1896	0.2762	0.0607	0.0613
Ridge λ=5	0.1862	0.1927	0.2362	0.2268	0.0608	0.0607	0.0624	0.1926	0.0662	0.1916	0.2763	0.0607	0.0620
Ridge λ=1	0.1923	0.1927	0.2362	0.2277	0.0610	0.0607	0.0687	0.1927	0.0847	0.1924	0.2764	0.0608	0.0667
Ridge λ=0.5	0.1926	0.1927	0.2362	0.2278	0.0612	0.0607	0.0762	0.1927	0.1019	0.1924	0.2764	0.0608	0.0723
Ridge λ=0.1	0.1927	0.1927	0.2362	0.2278	0.0633	0.0608	0.1218	0.1927	0.1535	0.1924	0.2764	0.0610	0.1040
Ridge λ=0.05	0.1927	0.1927	0.2362	0.2278	0.0657	0.0608	0.1565	0.1927	0.1673	0.1924	0.2764	0.0612	0.1259
Ridge λ=0.01	0.1927	0.1927	0.2362	0.2278	0.0827	0.0613	0.2249	0.1927	0.1765	0.1924	0.2764	0.0633	0.1627
Ridge λ=0.005	0.1927	0.1927	0.2362	0.2278	0.0989	0.0617	0.2358	0.1927	0.1769	0.1924	0.2764	0.0657	0.1676
Ridge λ=0.001	0.1927	0.1927	0.2362	0.2278	0.1496	0.0640	0.2413	0.1927	0.1771	0.1924	0.2764	0.0833	0.1699

Table D.5. CsPbBr$_3$ wrapper RMSE-CV results for a selection of modeling methods using each of the descriptors of the alkylamine ligands for comparison.

	Chain length	Molar mass	Boiling point	Enthalpy of vaporization	Density	pKa	Diffusion coefficient 20°C	ΔG agglomeration 100°C	Dipole moment	Polarizability	Melting point	^{1}H-NMR shift (terminal CH$_3$)	^{1}H-NMR shift (-NH$_2$)
Linear	1.0603	1.0603	1.0309	1.0367	1.0707	1.1576	1.0266	1.0603	1.0703	1.0604	1.0024	1.0395	1.0901
Quadratic	0.8811	0.8811	0.8737	0.8730	0.8802	1.0817	0.8835	0.8811	0.9564	0.8815	0.9175	0.9696	1.0442
Quadratic (Cross)	0.8398	0.8398	0.8689	0.8506	0.8875	1.1079	0.8668	0.8398	0.8839	0.8391	0.8599	1.0011	1.1134
SVM - RBF	0.7757	0.7755	0.7670	0.7556	0.7768	0.9755	0.7550	0.7764	0.8494	0.7725	0.7595	1.0016	0.9197
SVM - Linear	1.1452	1.1451	1.1476	1.1535	1.1384	1.1276	1.1249	1.1452	1.1332	1.1448	1.0616	1.0304	1.0716
SVM Quadratic	1.0165	1.0165	1.0614	1.0510	1.0638	1.0434	1.0444	1.0165	1.0225	1.0158	1.0085	1.1192	1.3435
SVM - Cubic	1.0858	1.0859	1.1078	1.1005	1.0881	1.6240	1.1265	1.0858	1.1986	1.0861	1.2439	1.7287	1.2162
KNN - K=3	1.0684	1.0348	0.9704	1.0920	1.0795	1.1037	1.0675	1.0012	1.0690	1.0934	1.0239	1.1286	1.1260
Ridge λ=50	1.0838	1.0529	1.0239	1.0453	1.1130	1.1130	1.1129	1.0529	1.1127	1.0631	0.9962	1.1130	1.1129
Ridge λ=10	1.0632	1.0581	1.0288	1.0353	1.1177	1.1177	1.1173	1.0579	1.1164	1.0580	1.0003	1.1177	1.1175
Ridge λ=5	1.0598	1.0591	1.0298	1.0354	1.1186	1.1186	1.1178	1.0590	1.1160	1.0587	1.0013	1.1186	1.1181
Ridge λ=1	1.0595	1.0600	1.0307	1.0363	1.1193	1.1194	1.1154	1.0600	1.1081	1.0600	1.0021	1.1194	1.1171
Ridge λ=0.5	1.0598	1.0602	1.0308	1.0365	1.1193	1.1195	1.1117	1.0601	1.1000	1.0602	1.0023	1.1195	1.1150
Ridge λ=0.1	1.0602	1.0603	1.0309	1.0366	1.1184	1.1197	1.0885	1.0603	1.0766	1.0604	1.0024	1.1195	1.1028
Ridge λ=0.05	1.0602	1.0603	1.0309	1.0367	1.1172	1.1199	1.0704	1.0603	1.0713	1.0604	1.0024	1.1194	1.0948
Ridge λ=0.01	1.0603	1.0603	1.0309	1.0367	1.1092	1.1209	1.0341	1.0603	1.0695	1.0604	1.0024	1.1185	1.0853
Ridge λ=0.005	1.0603	1.0603	1.0309	1.0367	1.1015	1.1221	1.0286	1.0603	1.0698	1.0604	1.0024	1.1174	1.0861
Ridge λ=0.001	1.0603	1.0603	1.0309	1.0367	1.0781	1.1294	1.0264	1.0603	1.0702	1.0604	1.0024	1.1095	1.0889

Table D.6. Deconvolution of PL emission spectra for a validation set of six samples. Multi-peak Gaussian fitting has been used to determine the fractional populations for different layer thicknesses (n = 1, 2, 3, 4, 5, 6, and bulk).

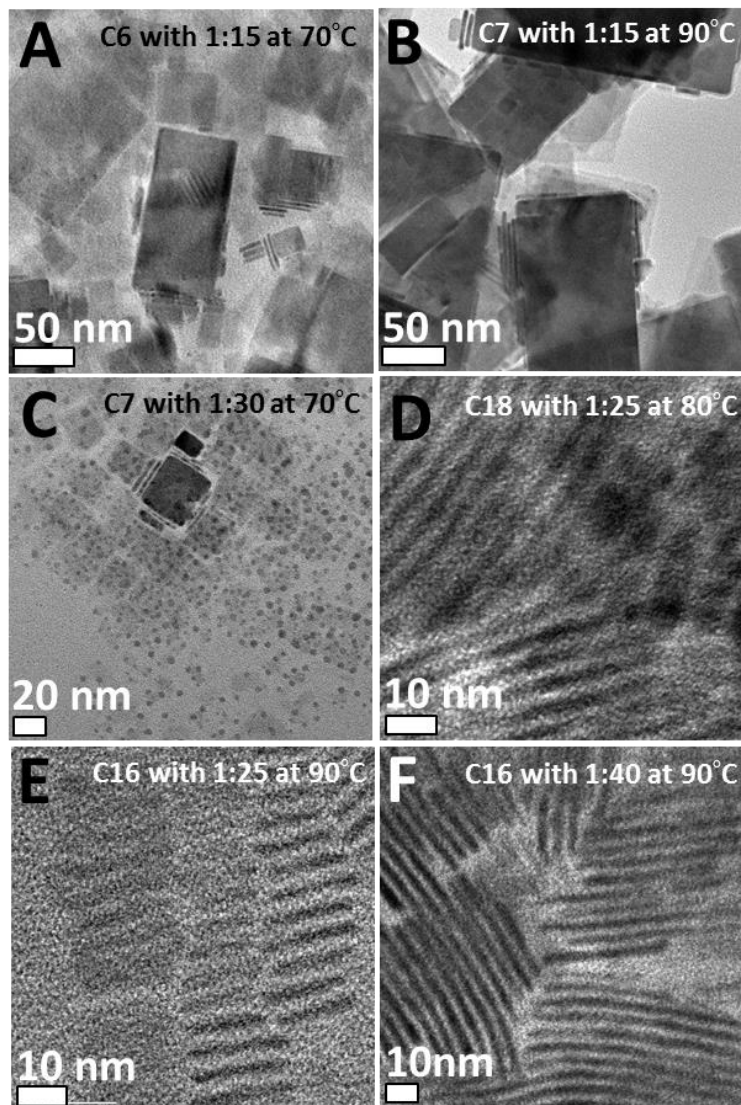| Entry	Chain-length (C_n)	T (°C)	Conc. (x)	n = 2	n = 3	n = 4	n = 5	n = 6	n = bulk	n_{avg}	TEM Thick-ness (nm)
1	6	70	1:15	-	0.030	0.101	0.135	0.334	0.400	7.2	4.0
2	7	90	1:15	-	0.128	0.175	0.195	0.166	0.336	6.4	3.7
3	7	70	1:30	0.009	0.392	0.279	0.185	0.068	0.067	4.3	2.5
4	18	80	1:25	0.059	0.246	0.306	0.119	0.187	0.083	4.6	2.9
5	16	90	1:25	0.060	0.562	0.192	0.075	0.083	0.027	3.7	2.3
6	16	90	1:40	-	0.413	0.328	0.068	0.048	0.142	4.6	2.8

Figure D.5. TEM images of CsPbBr$_3$ nanoplatelets corresponding to the validation set stabilized at different reaction conditions: A) C6 with 1:x = 1:15 at 70°C; B) C7 with 1:x = 1:15 at 90°C; C) C7 with 1:x = 1:30 at 70°C; D) C18 with 1:x = 1:25 at 80°C; E) C16 with 1:x = 1:25 at 90°C; and F) C16 with 1:x = 1:40 at 90°C.

Table D.7. Deconvolution of PL emission spectra for samples predicted to be have an n_{avg} of 3.0. Multi-peak Gaussian fitting has been used to determine the fractional populations for different layer thicknesses ($n = 1, 2, 3, 4, 5, 6,$ and bulk).

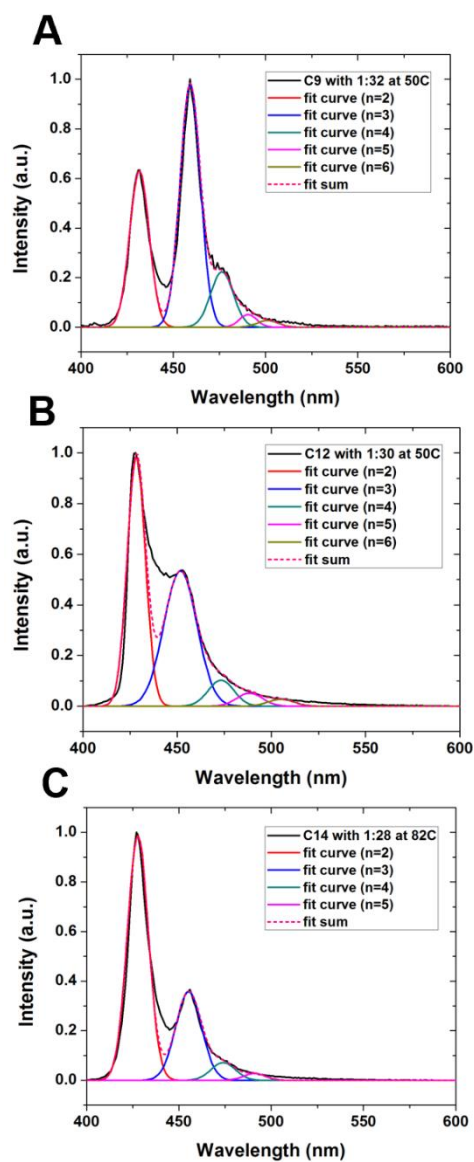| Entry	Alkylamine Chain-length (C_n)	T (°C)	Conc. (x)	$n = 2$	$n = 3$	$n = 4$	$n = 5$	$n = 6$	$n =$ bulk	$n_{avg.}$
1	9	104	1:32	0.318	0.514	0.131	0.023	0.015	0	2.90
2	12	50	1:30	0.446	0.439	0.065	0.033	0.017	0	2.74
3	14	82	1:28	0.642	0.286	0.053	0.018	0	0	2.45

Figure D.6. PL emission spectra and Gaussian peak fits for three samples predicted to have an $n_{avg.}$ of 3.0; A, B, and C correspond to entries 1, 2, and 3 in Table D.7, respectively.
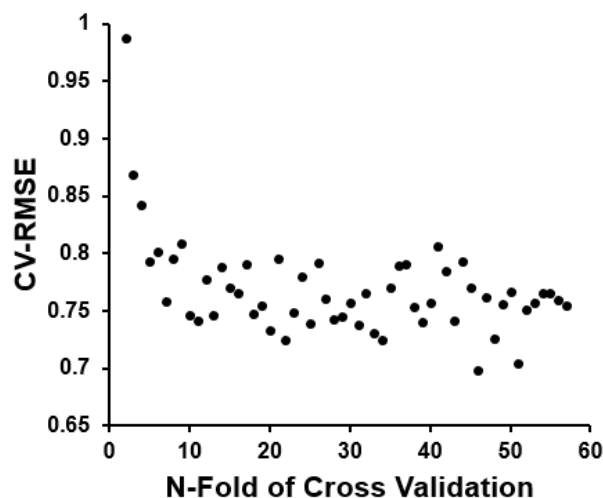
Figure D.7. Plot of cross-validation error *versus* the number of folds in cross validation for the SVM model with a radial basis function kernel using diffusion coefficient as the alkylamine descriptor.

D.1. References

[1]   W. M. Haynes, D. R. Lide, J. B. Thomas, *CRC Handbook of Chemistry and Physics : A Ready-Reference Book of Chemical and Physical Data*, 97th ed. CRC Press **2017**.

[2]   *ACD/Percepta*; Advanced Chemistry Development Inc. Toronto. **2017**

[3]   J. Cho, Y. H. Choi, T. E. O'Loughlin, L. De Jesus, S. Banerjee, *Chem. Mater.* **2016**, *28*, 6909.

[4]   D. Matulis, V. A. Bloomfield, *Biophys. Chem.* **2001**, *93*, 53.

[5]   M. D. Hanwell, D. E. Curtis, D. C. Lonie, T. Vandermeerschd, E. Zurek, G. R. Hutchison, *J. Cheminform.* **2012**, *4*, 17.

[6]   National Institute of Advanced Industrial Science and Technology, Spectral Database for Organic Compounds. http://sdbs.db.aist.go.jp (acsessed July 25, 2017)